CARDIFF
UNIVERSITY
PRIFYSGOL
CAERDYDD

*Cardiff School of Engineering*

*Hydro-environmental Research Centre*

# Physical Testing and Numerical Modelling of a Novel Vertical-Axis Tidal Stream Turbine

A thesis submitted for the Degree of Doctor of Philosophy

*March, 2014*

**Tom Harries**

**Academic Supervisors:**

Dr. Alan Kwan

Prof. Roger Falconer

# Declaration

This work has not previously been accepted in substance for any degree and is not concurrently submitted in candidature for any degree

Signed……………………………………………………(candidate) Date…………………………………..

This thesis is being submitted in partial fulfilment of the requirements for the degree of PhD.

Signed……………………………………………………(candidate) Date…………………………………..

This thesis is the result of my own independent work/investigation, except where otherwise stated. Other sources are acknowledged by explicit references.

Signed……………………………………………………(candidate) Date…………………………………..

I hereby give consent for my thesis, if accepted, to be available for photocopying and for inter-library loan, and for the title and summary to be made available for outside organisations.

Signed……………………………………………………(candidate) Date…………………………………..

# Acknowledgements

I would like to take this opportunity to thank my thesis supervisors, Dr. Alan Kwan and Professor Roger Falconer, for their invaluable support, guidance and encouragement throughout my research.

I am indebted to Paul Leach, the laboratory technician, for his guidance, expertise and patience throughout all of my laboratory work. I would also like to thank James Brammer for his assistance during laboratory data collection.

Finally I would like to thank my funders, KESS with the support of TATA Steel, for giving me this opportunity to further my knowledge, understanding, to develop new skills and enable me to carry out this research.

# Abstract

A combination of climate change, due to anthropogenic $CO_2$ emissions and concerns over energy security, due to fluctuating fuel prices, has led to the UK pushing to increase its renewable energy production. Harnessing tidal stream energy is an infant sector in the UK's renewable energy portfolio, despite the UK's large tidal stream resource, and is harnessed through deploying tidal stream energy converters. This thesis focuses on the design of a novel vertical axis tidal turbine (VATT) called CarBine which is driven by drag force and therefore has several unique advantages, including slow rotational speed, omni-directionality and a simple design. This research focused on the optimisation of the CarBine design and was split into two areas: physical testing and numerical modelling. A conventional Savonius was also analysed in both of these respects and this enabled a direct comparison of CarBine to a competing drag force driven VATT.

Physical testing measured the power of the turbines and was conducted in hydraulic flumes at both Cardiff University (CU) and IFREMER in Northern France for a range of flow conditions. Testing at IFREMER enabled the quantification of the blockage effect in the CU experiments. Physical testing resulted in the optimised design of CarBine being one with a four arm configuration. From physical testing at CU, CarBine showed inferior efficiency performance to that of the conventional Savonius, a $C_p$ of 0.117 compared to 0.225 at $U_\infty$=0.72 m/s. As a result a hybrid of both the Savonius and CarBine was tested, namely a Savonius with flaps. However, results from physical testing showed the Savonius with flaps to have inferior performance to both CarBine and the conventional Savonius, with a $C_p$ of 0.103 at $U_\infty$=0.72 m/s at CU. Numerical modelling was conducted using the commercial CFD software package, Ansys CFX. Both transient and steady state simulations along with 2D and 3D models were used to model both CarBine and the Savonius. Both the k-ε and SST turbulence models were used for comparison. The two degrees of rotational freedom present in the CarBine design resulted in CarBine being difficult to model precisely. The numerical modelling results were validated against the physical testing results and where available, 3D results showed closer validation than the 2D results.

# Table of Contents

**REFERENCES**

**APPENDICES**

# Nomenclature

| | | |
|---|---|---|
| **A** | $m^2$ | Cross-sectional area |
| **$B_D$** | m | Bucket diameter (Savonius) |
| **BFi** | m | Bucket inner flap (Savonius with Flaps) |
| **BFo** | m | Bucket outer flap (Savonius with Flaps) |
| **$B_O$** | m | Bucket overlap (Savonius) |
| **$B_t$** | m | Blade thickness (Savonius with Flaps) |
| **$C_D$** | - | Coefficient of drag |
| **$C_p$** | - | Coefficient of power |
| **$C_t$** | - | Coefficient of torque |
| **D** | m | Diameter |
| **$D_D$** | m | Disk diameter |
| **$D_O$** | m | Disk overlap |
| **$D_t$** | m | Disk thickness |
| **$F_D$** | N | Drag force |
| **Fi** | m | Inner flap thickness (CarBine) |
| **$F_L$** | N | Lift force |
| **Fo** | m | Outer flap thickness (CarBine) |
| **Fr** | - | Froude number |
| **$F_t$** | m | Flap thickness (CarBine) |
| **H** | m | Turbine height |
| **I** | % | Turbulence intensity |
| **L** | m | Characteristic Length Scale |
| **P** | W | Power |
| **$P_\infty$** | W | Freestream power |
| **R** | m | Radius |
| **Re** | - | Reynolds number |
| **$S_D$** | m | Shaft diameter |
| **T** | Nm | Torque |
| **U*** | - | Non-dimensional flow speed |

|  |  |  |
|---|---|---|
| $U_\infty$ | m/s | Freestream flow speed |
| $\overline{U}_\infty$ | m/s | Turbine cross section area averaged flow speed |
| $U_c$ | m/s | Corrected flow speed (Blockage Correction) |
| $U_t$ | m/s | Near wall flow speed |
| $U_x$ | m/s | Streamwise flow speed |
| $U_y$ | m/s | Spanwise flow speed |
| $U_z$ | m/s | Depthwise flow speed |
| $x$ | m | Streamwise direction (Cartesian coordinate system) |
| $X$ | m | Distance in streamwise direction |
| $y$ | m | Spanwise direction (Cartesian coordinate system) |
| $Y$ | m | Distance in spanmwise direction |
| $y^+$ | - | Non-dimensional wall distance |
| $z$ | m | Depthwise direction (Cartesian coordinate system) |
| $Z$ | m | Distance in depthwise direction |
| $\alpha$ | - | Distance (diameters) between T1 and T2 |
| $\beta$ | - | Bucket overlap ratio (Savonius) |
| $\gamma$ | - | Blockage Factor |
| $\varepsilon_t$ | - | Pope and Harper blockage correction |
| $\theta$ | deg (°) | Azimuth angle |
| $\lambda$ | - | Tip speed ratio |
| $\mu$ | deg (°) | Blade angle of attack |
| $\nu$ |  | Kinematic viscosity |
| $\rho$ | kg/m$^3$ | Density |
| $\tau_w$ | N/m$^2$ | Wall shear stress |
| $\phi$ | - | Aspect ratio |
| $\omega$ | rad/s | Angular velocity |
| $m$ | - | Alexander blockage correction |

# Acronyms

| | |
|---|---|
| **ADV** | Acoustic Doppler Velocimeter |
| **BSI** | British Standards Institution |
| **C** | CarBine |
| **CFD** | Computational Fluid Dynamics |
| **CFR** | Central Feed in Tariff Register |
| **CU** | Cardiff University |
| **DECC** | Department of Energy & Climate Change |
| **DNS** | Direct Numerical Solution |
| **FIT** | Feed in Tariff |
| **GDP** | Gross Domestic Product |
| **GL RC** | Germanischer Lloyd Renewables Certification |
| **HATT** | Horizontal Axis Tidal Turbine |
| **IEA** | International Energy Agency |
| **IFREMER** | French Research Institute for Exploitation of the Sea |
| **IPCC** | Intergovernmental Panel on Climate Change |
| **LES** | Large Eddy Simulation |
| **MARINET** | Marine Renewables Infrastructure Network |
| **MCT** | Marine Current Turbine Ltd |
| **MREKEP** | Marine Renewable Energy Knowledge Exchange Program |
| **Ofgem** | Office of Gas and Electricity Markets |
| **PIV** | Particle Image Velocimetry |
| **PMG** | Permanent Magnet Generator |
| **PTFE** | Polytetrafluoroethylene |
| **PTO** | Power Take-Off |
| **RANS** | Reynolds Averaged Navier-Stokes |
| **ROC** | Renewable Obligation Certificate |
| **ROO** | Renewable Obligation Order |
| **RPI** | Retail Price Index |
| **RPM** | Revolutions per minute |

| | |
|---|---|
| **S** | Savonius |
| **SCF** | Savonius with Closed Flaps |
| **SD** | Sub-domain |
| **SF** | Savonius with Flaps |
| **SIF** | Significant Impact Factor |
| **SST** | Shear Stress Transport |
| **THATT** | Transverse Horizontal Axis Tidal Turbine |
| **TSR** | Tip Speed Ratio |
| **VATT** | Vertical Axis Tidal Turbine |

# List of Figures

# List of Tables

# 1 Introduction

There is currently a global energy crisis that is predominantly due to two factors: climate change and energy security. The solution to the aforementioned problems is to reduce the demand for energy and therefore emissions through becoming more energy efficient in conjunction with harnessing indigenous sources of renewable energy. To ensure there is a global effort to resolve these issues in December 1997, the Kyoto Protocol was announced and signed by 171 countries (including the UK) as part of the United Nations Framework Convention on Climate Change; the aim of which was to commit its members to reduce their emissions through internationally binding emission reduction targets. In addition to the Kyoto Protocol the UK government has committed to internal targets, detailed in the Renewable Energy Directive to achieve 15% of its energy consumption from renewable sources by 2020 (European Parliament, 2009) in addition to supplying 30% of the electricity generation from renewable sources, targeted by the UK government’s department of energy and climate change (DECC). In 2012 the UK produced 4.1% of its energy from renewable sources (DECC, 2012a), highlighting the need for the UK government to spur on further development of technologies to harness renewable energy sources.

Of the variety of renewable energy sources available to the UK, including Wind, Biomass, Solar etc., the least developed is marine energy. Wind, biomass and ground source heat pumps technology is already being exploited at large commercial scales with the UK currently the world’s market leader in installed operating capacity of offshore wind technology (DECC, 2013a). Marine energy sources include wave energy, tidal range and tidal stream energy. Wave energy suffers from the unpredictability of wind energy whilst to date a proposal to install a tidal barrage in the River Severn in the UK was rejected partially on the basis of environmental concerns (House of Commons, 2013). However tidal stream energy is predictable and regarded as a more environmentally friendly alternative to a tidal barrage since harnessing tidal stream energy can be achieved without impounding the flow. In 2011 the UK generated 1GW/h from marine energy sources, equating to 0.003% of the total electricity generated from renewable sources (DECC, 2012b). This is a minuscule amount compared to the Carbon Trust's 2004 estimate that the UK has around 50% of Europe's tidal energy resource at around 17 TWh/year, equating to 4% of the UK's energy supply. The figure was increased during an updated resource assessment in 2011 by the Carbon Trust, predicting the resource to be close to 20.6 TWh/year. Both figures highlight the potentially large untapped tidal energy resource available to the UK.

Although the first full scale tidal stream turbine was deployed in 2003 off Lynmouth, Devon by Marine Current Turbines Ltd. there is currently no market leader in the tidal energy sector since no developer has progressed past a single full scale device deployment, despite the UK Crown Estate releasing leases for 41 wave and tidal sites for array deployment around the UK (The Crown Estate, 2013). As a result, the sector is considered to be in its infancy and is therefore still open to new technologies. This thesis is focused around a new tidal stream energy turbine, namely CarBine. CarBine is a novel vertical axis tidal stream turbine whose design was conceived at Cardiff University by Alan Kwan. Contrary to the market dominant horizontal axis tidal stream turbines, CarBine harnesses drag force as opposed to the traditionally harnessed lift force and is therefore a high torque and low angular velocity turbine.

## 1.1 Thesis Aims

The aims of this thesis are as follows:

- To quantify the performance of CarBine, a novel vertical axis tidal stream turbine, via physical testing;
- Create a framework for numerical modelling of CarBine to support design optimisation;
- Analyse the competitiveness of CarBine through comparing its performance to rival technologies.

## 1.2 Thesis Layout

The thesis is split into 13 chapters whereby each chapter commences with a brief summary of its contents. Chapters 2 through to 6 perform the literature survey. The basis of this is: the UK drivers towards a green renewable energy future (Chapter 2), the potential of marine energy in the UK and the technology available to harness it (Chapter 3), the range of tidal stream turbines in the market (Chapter 4 and Appendix A), identifying sites with favourable parameters for tidal stream turbine deployment (Chapter 5) and finally the structural considerations when operating in a harsh unforgiving environment such as the open ocean (Chapter 6). Chapter 7 provides the background, description and technological progress of CarBine whilst Chapter 8 reviews the Savonius turbine.

The methodology for both the physical and numerical modelling is split into separate chapters. In addition the results and discussion form a single chapter with a separate chapter for the physical and numerical modelling. The prime reason for dividing the results and discussion chapter into physical and numerical modelling is that the numerical modelling is based on the outcomes of the physical testing study. Finally the thesis is concluded with a common conclusion and common future work chapter for both the physical and numerical modelling.

# 2 Background & UK Energy Policy

**This chapter both elaborates on the background to the study summarised in the introduction chapter, highlighting climate change concerns, and uncertainty of energy security through the rising cost of a barrel of oil over the last century, whilst also providing an overview of the UK Energy Policy designed to aid the UK in achieving its UN and internal emission reduction targets. Particular attention is paid to the actions of the UK Government's Department of Energy and Climate Change (DECC) which is responsible for achieving the targets.**

Since the Industrial Revolution in the 1800's the use of coal as a fuel has exponentially increased, with the catalyst arguably being James Watt's invention of the steam engine in 1769, leading to efficient mining of coal; following suit was the rise in the use of oil and gas as a fuel (MacKay, 2009). Coal, oil and gas are non-renewable forms of energy-fossil fuels, thus in a human time scale they are finite energy sources and cannot be replaced at a rate to match consumption; both of these take geological time scales to form. Recently the world's population has surpassed the 7 billion mark and supplemented by numerous technological advancements, has led to big increases in the consumption of fossil fuels. With global population ever increasing and continual global technological development, demand for fuel continues to rise.

## 2.1 Energy Crisis

There are two predominant reasons as to why there is currently an energy crisis:

### 2.1.1 Side effects of the usage of fossil fuels are directly leading to climate change

The combustion of fossil fuels for energy conversion consists of the hydrocarbons found in fossil fuels reacting with oxygen, energy is thus provided in the form of heat. However one of the compounds created as a resultant of the combustion is carbon dioxide, $CO_2$. The $CO_2$ released then enters the atmosphere and heavy consumption of fossil fuels has led to high levels of $CO_2$ in the atmosphere. Other contributors to atmospheric $CO_2$ levels include change of land use (such as deforestation) and industrial processes e.g. cement manufacture. The atmospheric $CO_2$ acts as a "blanket" over the earth causing a greenhouse effect, allowing solar radiation to penetrate but containing re-radiated heat from the earth from escaping, causing an imbalance between the energy absorbed from the sun and that emitted to space, which ultimately leads to climate change. The Royal Society defines climate change as a "change in globally averaged surface temperature"(2010). Other greenhouse gases include: Methane, Nitrous Oxide, HFC, PFC and SF6 . It is this increase in temperature that concerns climatologists, since "if not mitigated, [it would] threaten the stability of the world's climate" (Trade, 2007, p. 28). Current $CO_2$ levels in the atmosphere, 456.3 ppm, are at their highest for nearly 650,000 years, and 32% of this is from power station emissions (DECC, 2012b). In 2011 in the UK, around 83% of the anthropogenic $CO_2$ emissions originate from burning fossil fuels to produce energy. If emission levels continue at today's level then they will reach double pre-industrial levels by the year 2050, at around 550 ppm, with an estimated global temperature rise exceeding $2^oC$ (Trade, 2007, p. 29).

Climate change has "significant implications for present lives, for future generations and for ecosystems on which humanity depends" (The Royal Society, 2010). If no action is taken and global temperatures rise, predicted effects of climate change include:

- 5-10% loss in global GDP;
- Threat to international peace, security and development;
- The International Panel on Climate Change (IPCC) hypothesise that climate change will result in an increase in extreme weather events (floods, droughts etc.);
- Rising sea-levels could displace millions of people in low lying countries such as Bangladesh;
- Between 75 and 250 million people in Africa will experience further pressure on scarce water resources;
- Dramatic reduction in yields, by 50% in some countries, of rain-fed agricultural land (Trade, 2007, pp. 29–30).

### 2.1.2 Energy Security

Coal and gas currently dominate the world's electrical energy supply, as seen in Figure 1c, with the demand for oil expected to increase by 50% between 2002 and 2030 (International Energy Agency, 2005). In 2010 coal (27.3%), gas (32.4%) and oil (21.4%) contributed to 81.1% of the total global electricity energy supply. The make-up of the UK's electricity energy supply in 2010 and 2011, as seen in Figure 1a and Figure 1b is dissimilar to that of the world. Figure 1b illustrates that gas and coal dominated the UK supply in 2011 with 40.7% and 29.1% of the supply respectively whereby globally the supply is dominated by 40.6% coal and only 22.2% gas. 12% of the UK electrical energy supply in 2011 was supplied from a low carbon source, whilst two thirds of that was from nuclear energy.

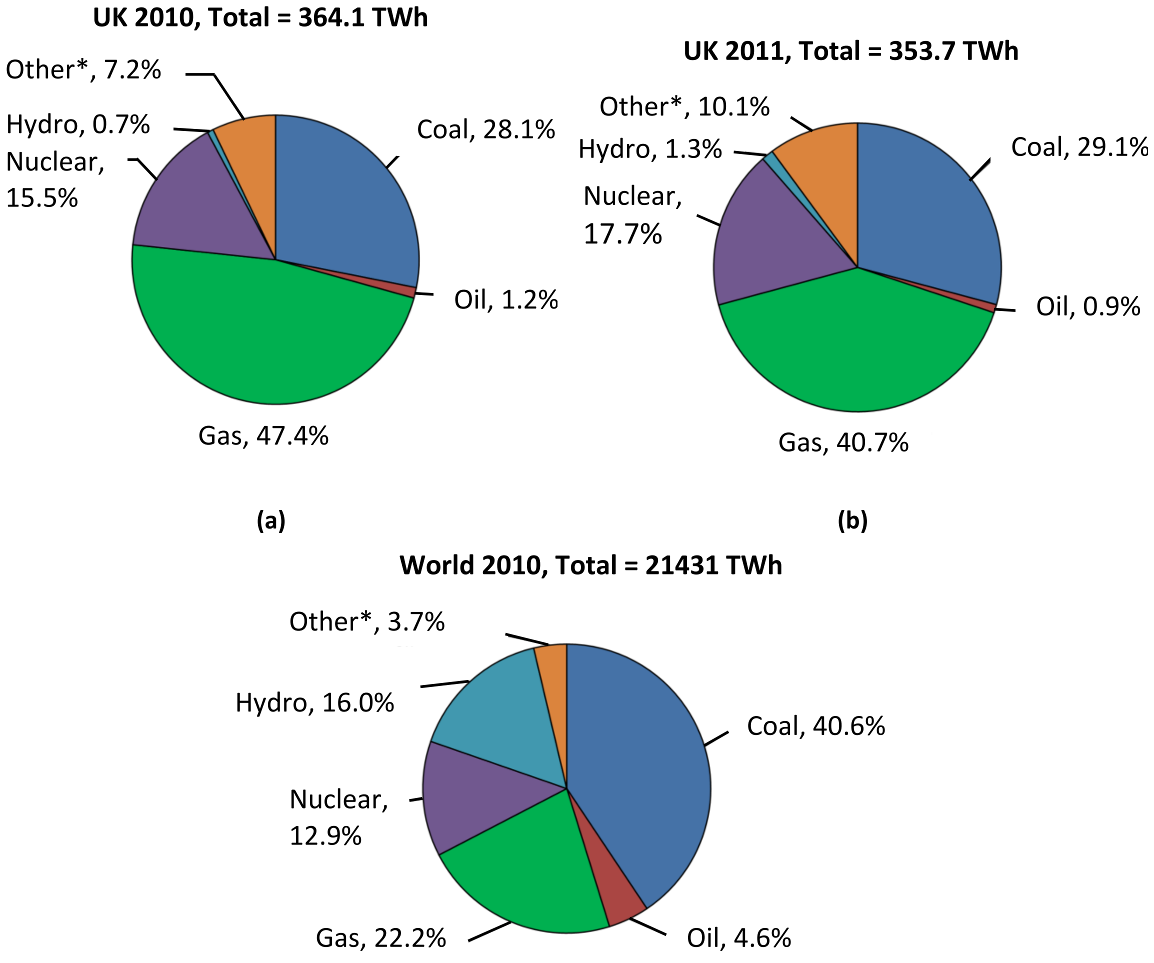

**(a)** **(b)**

**(c)**

**Figure 1 Breakdown of the electricity energy supply in (a) the UK 2010, (b) the UK 2011, (c) the world 2010, adapted from (DECC, 2012b).*Includes geothermal, solar, wind, heat, biofuels and waste.**

However nuclear energy is constantly under global scrutiny and is subjected to intense public opposition due to its major failures in the past resulting in severe consequences, such as Three Mile Island in 1979, Chernobyl 1986 and Fukushima 2011 (World Nuclear Association, 2013). The EU average is 21% electrical energy supply from low carbon sources, which leaves the UK falling behind its European counterparts (DECC, 2012b).

Although the International Energy Agency, IEA, state “global oil and gas reserves are sufficient to sustain economic growth for the foreseeable future”(International Energy Agency, 2005) the locations of the oil and gas reserves do pose significant risks and uncertainty.

- 62% of the world’s oil reserves are located in regions that are considered politically unstable, such as the Middle East and North Africa;
- The world’s top 2 exporters of crude oil are Saudi Arabia and Russia(International Energy Agency, 2013);
- 50.7% of the world’s natural gas supplies can be found in the Middle East and Africa (BP, 2014a).

There is a clear imbalance as to the location of the fuel reserves and that of areas with increasing demand; such as China who are responsible for 11% and 18% of the world’s oil and coal imports respectively (DECC, 2012b, pp. 11–15). Advances in fracking and horizontal drilling along with the discovery of large shale gas resources have enabled the U.S. to address their reliance on oil and natural gas imports (Harvey and Loder, 2013). Since 2008, oil production in the U.S. has risen by over 30% and accounts for 9.6% of global production (BP, 2014b). There are a number of risks inherent with the current scenario:

- **Long Supply lines increase risks and impact of disruptions to energy supply**. For example, the east Siberia-Pacific Ocean pipeline links the world’s largest producer of oil, Russia, with the world’s biggest energy consumer, China and is nearly 5000km in length and accounts for nearly 25% of Russia’s oil export (Bloomberg, 2013). Disruption to this supply would have major consequences in Asia.

- **Market Power**. The use of pipelines for energy transportation has led to countries having the influence to affect the reliability of supply and thus energy prices. In June 2013, a leak forced the closure in a Canadian pipeline feeding North America, leading to a sharp hike in the price of crude oil in the USA (Inquirer Business, 2013).
- **Terrorism, Accident and natural disaster.** These can increase the likelihood of supply disruptions when fuel is transported across such vast distances.

Since 2004 the UK has been an energy importer. In 2012, 43% of the energy used in the UK was imported (DECC, 2013b, p. 9); subjecting the UK to the fluctuating price of imported fuel, as seen in Figure 2. Fluctuating fuel prices leads to doubts in energy security and makes planning difficult and unpredictable for economic and strategic growth. This uncertainty over costs can present potential barriers to future business growth (Carbon Trust, 2010).

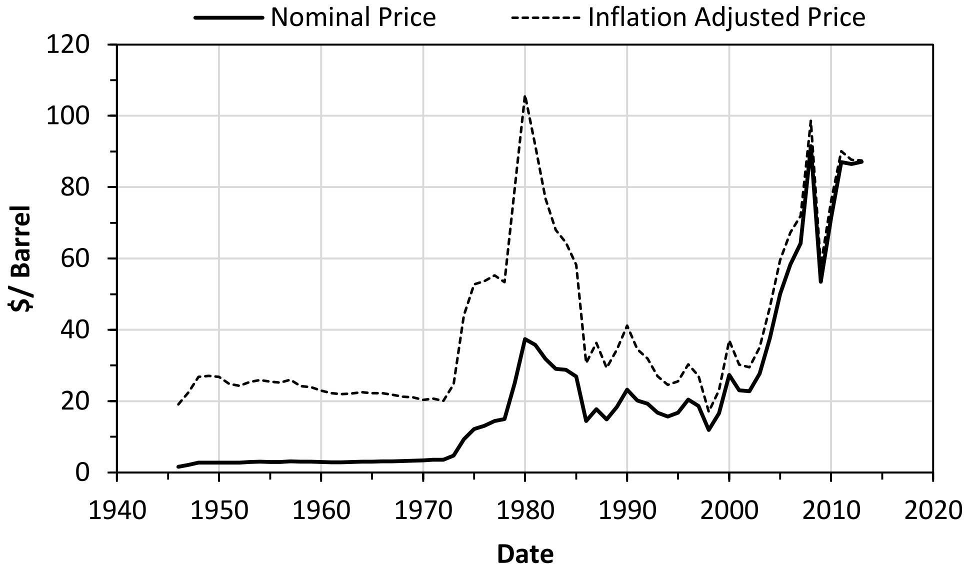

**Figure 2 The fluctuating prices of oil (InflationData.com, 2013)**

## 2.2 Energy Action

The solution to the aforementioned problems is to both reduce the demand for energy and reduce emissions through becoming more energy efficient in conjunction with harnessing renewable sources of energy. In December 1997, the Kyoto Protocol was announced and signed by 171 countries (including the UK) as part of the United

Nations (UN) Framework Convention on Climate Change; the aim of which was to commit its members to reduce their emissions through internationally binding emission reduction targets. Initially the Kyoto protocol, enforced for the first commitment period from 2005 to 2012, produced an average reduction in emissions levels (compared to 1990 levels) of 5%. The second commitment period, announced in Doha, Qatar in December 2012, provided new commitments from its participants for the period extending from 1st January 2013 to 31st December 2020, with the aim of reducing emissions by 18% (United Nations, 2013).

The renewable energy sources are those that are repeatedly available naturally unlike fossil fuels, which are a finite resource. Sources of renewable energy include: Solar, wind, wave, tidal, geothermal heat from the earth as well as wood/ crops grown specifically as fuel sources. The use of renewable energy does not result in the direct creation of $CO_2$ (initially $CO_2$ will be indirectly created as renewable energy harnessing devices are manufactured). The burning of biomass fuels does release $CO_2$ into the atmosphere but this is typically equal to the amount of $CO_2$ absorbed by the plant during growth (NREL, 2012). The availability of such renewable sources depends specifically on the characteristics, such as location, climate, land availability etc. of each country. Producing indigenous renewable energy will solve the issue of energy security, fluctuating fuel prices, provide backup if fossil fuel sources are exhausted, as well as giving the potential for exporting surplus “green” energy (Carbon Trust, 2010).

## 2.3 What is being done in the UK?

### 2.3.1 Department of Energy & Climate Change (DECC)

A government department set-up by former British Prime Minister Gordon Brown to deal with energy and climate related issues, DECC has four primary goals:

- Save energy with the Green Deal and support vulnerable consumers;
- **Deliver secure energy on way to a low carbon energy future**
    - Reform the energy market to ensure that the UK has a diverse, safe, secure and affordable energy system and incentivise low carbon investment and deployment;
- Drive ambitious action on climate change at home and abroad; and

- Manage our energy legacy responsibly and cost-effectively (DECC, 2012c).

The highlighted goal "Deliver secure energy on way to a low carbon energy future" is spurred by the government's commitment in the 2009 Renewable Energy Directive-UK to achieve 15% of its energy consumption from renewable sources by 2020 (European Parliament, 2009). Placed into perspective, this would require almost a 4-fold increase compared to the value of 4.1% achieved in 2012, as seen in Figure 3. In addition the UK government aims to achieve 30% of its electricity generation from renewable sources by the year 2020 (Wall Street Journal, 2013). The ultimate long-term target is to reduce emissions by 80% compared to 1990 values by 2050 to "help the UK become less reliant on imported fossil fuels and less exposed to higher energy prices in the future" (DECC, 2013c).

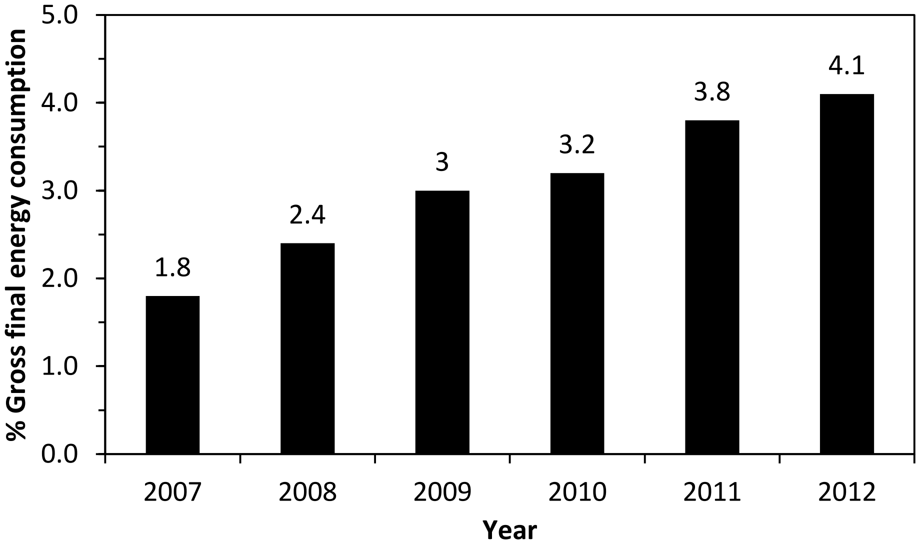

**Figure 3 % of energy derived from renewable sources in UK, calculated using methodology required by the directive**

Subsequent devolved UK administrations have their own goals.

- ***Scottish Government***

  Aiming to supply 100% of its electricity consumption (% of gross annual consumption) from renewable sources by 2020. In 2011 Scotland achieved its interim target of 31%; subsequently a new interim target of 50% has been set for 2015 (The Scottish Government, 2012).

- ***Northern Ireland Executive***

  Aiming to supply 40% of its electricity consumption from renewable sources by 2020, with an interim target of supplying 20% of its electricity consumption from renewable sources by 2015.

- ***Welsh Government***

  Does not have devolved administration goals but Wales is showing progress in renewable energy generation through granting licenses for various onshore and offshore wind farms, maintaining an interest in the Severn Estuary barrage proposal, see Section 3.2, as well as numerous tidal stream turbine proposals.

In 2011, from comparing Figure 1b with Figure 4, the UK generated 9.7% of its electricity supply from renewable sources (according to the stipulations provided in the renewable obligation (DECC, 2013d)). This leaves the UK needing a 3-fold increase in electricity generation from renewable sources by 2020 to achieve DECC's target of 30%. Figure 4 shows that harnessing wind energy was the largest contributor to the UK renewable electricity energy supply with nearly half the share at 45.6%.

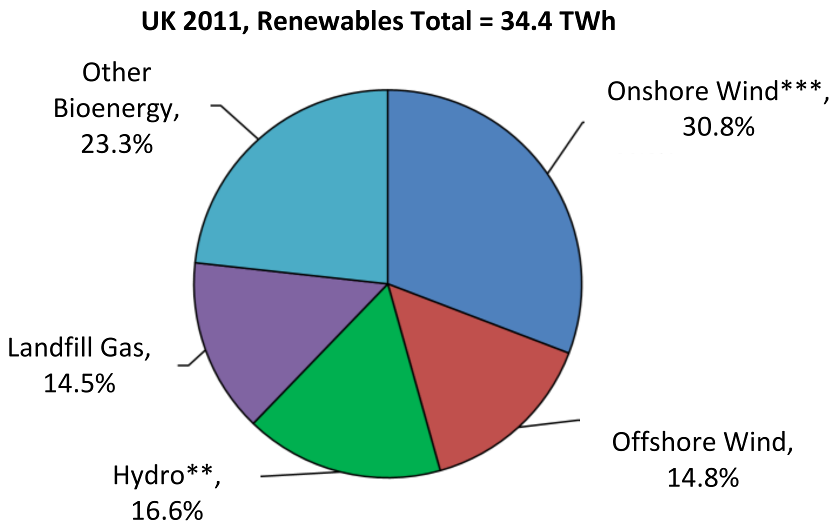

**Figure 4 Breakdown of the electricity supply from renewables in UK in 2011 (DECC, 2012b).**

****Hydro includes wave/tidal with a contribution of 0.001 TWh. ***Onshore Wind includes solar PV of 0.25 TWh.**

In the UK, during the period of July 2011-June 2012, the total electricity generation from renewables increased by 10.17% reaching 41.3TWh from an installed capacity of 15.5GW. This accounts for 11.3% of the UK's electricity generation, which is a 1.6% increase on the previous year (DECC, 2012d). The detailed breakdown of the electricity energy supply from 2012 is not yet available; however the breakdown for 2011 can be seen in Figure 4.

### 2.3.2 Renewable Energy Roadmap

In order to keep in line with the 2020 target, the government and devolved administrations (Wales, Scotland and Northern Ireland) have published a renewable energy roadmap (DECC, 2012a), designed to provide a comprehensive guide regarding the current issues facing various renewable energy sectors, and the pathways available or pathways that could be created in order to accelerate towards the designated targets. Attention is directed towards the cost-effectiveness of the available technologies, driving innovation and methods to reduce related costs over time. Eight key areas are discussed, which are technologies that are feasibly deployable coupled with favourable cost-effectiveness.

Any general renewable energy figures from the government are a combination of the eight areas below:

- Onshore wind
- Offshore wind
- **Marine energy**
- Biomass electricity
- Biomass heat
- Ground source heat pumps
- Air source heat pumps
- Renewable transport

Wind, Biomass and ground source heat pumps technology is already being exploited at large commercial scales. The UK is currently the world's market leader regarding wind technology and its deployment, with over 700 turbines currently installed on and offshore in the UK, with further deployment currently in motion. As a result, efforts are being directed towards developing the remaining sectors, such as marine energy. The aim is the decarbonisation of the UK's energy supply along with increasing the UK's energy independency. Reducing the UK's reliance upon fossil fuels will not only result in increased decarbonisation but consequently increase the security of supply and eradicate the constant fluctuating cost of fossil fuels, as seen in Figure 2. Other consequences of increased deployment of renewable energy conversion systems is the creation of new jobs in the UK in a variety of sectors, including design, management, research, manufacturing etc. The renewables sector (covering electricity and transport) currently supports around 110,000 jobs directly and in immediate supply chains. Predictions suggest the figure will rise to around 400,000 if governmental targets are met in 2020.

## 2.4 Support Instruments

To obtain the ambitious UK government 2020 target of meeting 15% of energy supply from renewable sources, the government introduced a series of financial incentives in order to motivate current UK energy suppliers to adopt a green approach as well as to entice new investment into the renewable sector. Examples of the financial incentives aimed at accelerating the supply of energy from renewable sources include the following.

### 2.4.1 Macro Generation-Renewable Obligation Certificates (ROCs)

The primary stimulant encouraging renewable energy in the UK is the allocation of Renewable Obligation Certificates (ROC), introduced in 2002 through the Utilities Act 2000. The act requires all power suppliers in Great Britain to source a specific proportion of renewable energy. This target was 3% in 2003, increasing annually to 10.4% by 2010 and 15.4% by 2015. The Renewables Obligation (RO) remains enforceable by law until 2027. The UK government deals with RO for England and Wales whilst Northern Ireland and Scotland are regulated by their respective devolved administrations.

The tradable ROCs are given to eligible renewable power generators for every MWh of green electricity that they produce. It is then compulsory for power utilities who have not met their renewable energy targets to purchase these certificates to fulfil their obligation. Alternatively they can pay a ‘buyout’ price for any shortfall. This ‘buyout’ price is stipulated by the regulators Ofgem each year. For 2013/2014 this is roughly £42.02 per ROC plus 10%, which is set to track the Retail Price Index (RPI) (UK Government, 2013). The proceeds are returned to the renewable energy producers in proportion to the number of ROCs they generate. The greater the shortfall of ROCs issued below the set target, the greater the buy-out fund. As the number of renewable generators increases the shortfall and hence the fund will decrease, however due to the 10% headroom provision (i.e. the government sets the annual ROCs target under the Renewable Obligation Order (ROO) to be 10% higher than expected) this provides additional but variable income to renewable generators Figure 5 illustrates how ROC prices have fluctuated over the period of October 2002 to October 2011, with the average price of a ROC being around £47 (On-line ROC Auction Service, 2013).

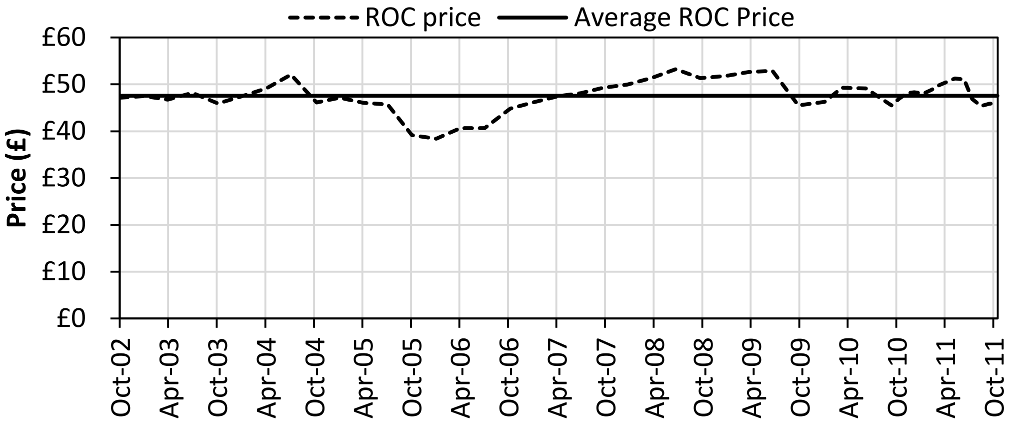

**Figure 5 Fluctuation of ROC prices over time (On-line ROC Auction Service, 2013)**

Previously the RO was technology-neutral; this has had the effect of encouraging established and profitable technologies, at the expense of emerging technologies. To address this, the Department for Business Enterprise and Regulatory Reform reformulated the RO, with the intention of 'banding' the technologies according to their stage of development. The number of ROCs provided per MWh of generation depends on the type of technology used, with infancy technology (higher risk for investors) receiving more ROCs.

### 2.4.2 Micro Generation-Feed in Tariffs (FIT) Schemes

Introduced on April 1st 2010 the FIT schemes are designed to "support organisations, businesses, communities and individuals to generate low-carbon electricity using small-scale (5 megawatts (MW) or less total installed capacity) systems" (UK Government, 2013). The Scheme works via an individual, organisation or community installing a small scale renewable micro-generation device. Depending on its capacity, the generator is registered with a licensed electricity supplier (<50 kW) or Ofgem (>50 kW). Subsequently either the supplier or Ofgem inspect the installation to ensure it satisfies FIT scheme criteria and also handles the generation data. Finally during operation, the supplier will pay the generator one of two tariffs: Supply tariff, for any electricity generated, or an export tariff for surplus energy generated which is fed into the national grid. According to the Central FITs Register (CFR), the first quarter of 2012 experienced an increase in eligible FITs installed capacity to 1090.8MW compared to 108.4 MW in the first quarter of 2011; an 11 fold increase (Ofgem, 2013).

**Comparing Figures Figure 1, Figure 3 and Figure 4 there is clearly a need to increase both the UK's renewable energy portfolio and reduce its reliance on imported fossil fuels. From the UK's renewable energy roadmap, "marine energy" is listed as one of the 8 energy sectors, yet from Figure 1 only 0.7% of the UK's energy supply is from hydro sources compared to 16% globally. Equally, considering the large potential tidal stream resource available in the UK ($\approx$17 TWh/year (Carbon Trust, 2011), more details available in Section 3.3.3), only 0.001TWh, equating to 0.003% of the UK's renewable energy supply, was harnessed in 2011. This leaves clear room for improvement and development for the emerging tidal stream industry. The infancy of the sector relative to wind harnessing technology is reflected in the UK government offering 5 ROCs/MWh of generation from tidal stream sources (see Section 2.4.1). This is designed to act as a stimulant for investment and development that should lead to a future increase in the energy generation from tidal stream sources.**

# 3 Marine Energy

**This chapter contains a description of the three forms of marine energy: wave, tidal range and tidal stream energy. In summary, wave energy suffers from intermittency, tidal range suffers from widespread environmental protests associated with the large infrastructure works, and significant environmental alterations, despite its higher power density whilst tidal stream energy is predictable and could provide base load power to the National Grid. Tidal stream turbines are expected to have minimal environmental impact during operation but care must be taken during the commissioning and decommissioning phases. The majority of the feasibly extractable UK tidal energy resource is located in Pentland Firth (Northern Scotland) around the Channel Islands and the remaining sites are primarily scattered along the western coast of the UK.**

---

The Marine Energy sector within the UK Renewable Energy Roadmap consists of wave, tidal stream and tidal range energy schemes. To date, the UK's marine sector is in its infancy and in 2011 tidal and wave energy accounted for only 1 GWh of the UKs electricity energy supply, as seen in Figure 4. The following sub-sections will describe the three methods of harnessing marine energy, in conjunction with their advantages and disadvantages, with an emphasis on harnessing tidal stream energy.

## 3.1 Harnessing Wave Energy

Waves are formed from wind action and can therefore be viewed as an indirect form of solar energy (Falcão, 2010). The power inherent in wave energy is often experienced and displayed negatively, i.e. during storm conditions at sea. A major advantage of wave power is that it increases in the winter months, which coincides with peak electricity demand. Wave energy, similar to wind energy, suffers from the unpredictable nature of the resource in various time-scales, such as wave-to-wave and seasonal. There are a variety of wave energy converters under development, including oscillating water column, oscillating body and overtopping devices.

**(a)** **(b)**

**Figure 6 Pelamis operating in Orkney (Pelamis Wave Power Ltd., 2013a) (a) in 2011 (b) in 2012 .**

Pelamis Wave Power Ltd is the developer of the Pelamis wave energy device, seen in Figure 6. Pelamis is a snake-like semi-submerged oscillating body device, whereby the movement of the 4 tubular sections via an ocean wave, is resisted by hydraulic rams. A hydraulic power take off system in each joint consists of hydraulic cylinders at the joint, which resist the wave-induced motion and pump high pressure fluid into a hydraulic motor which then drives an electrical generator (Pelamis Wave Power Ltd., 2013b).

Pelamis state that they achieved "The world's first export of electricity from an offshore wave energy converter to an onshore grid network" as well as "the supply and commissioning of the world's first multiple machine wave farm" (2013c). The first grid connected prototype test was conducted in the North Sea and in the European Marine Energy Centre, EMEC, between 2004 and 2007. The prototype was 120 m in length with a diameter of 3.5 m and a capacity of 750 kW. The wave farm consisted of 3 x 750 kW devices installed off the coast of Portugal in 2008. The farm has since been decommissioned due to the collapse of the Portuguese energy provider's parent company, Babcock and Brown (Pelamis Wave Power Ltd., 2013d). Scottish Power Renewables purchased a P2 device from Pelamis that has been operating in EMEC at the Orkney site for over 1 year, generating for 7500 grid connected hours at an output of 160 MWh (Pelamis Wave Power Ltd., 2013e).

## 3.2 Harnessing a Tidal Range

The power in a tidal range can be harnessed through the construction of an encasing structure, be it a barrage or a lagoon, to manipulate the water levels each side of the structure in order to create a pressure head difference. In the example of a barrage extending the whole width of an estuary, as the flood tide approaches the downstream side of a barrage the water level will begin to increase in comparison to the water level on the upstream side, when the difference between the water levels, the pressure head, reaches the optimum height sluice gates are opened and the water flows through turbines. Additionally, power can be generated on the ebb of the tide, as water is held back on the upstream side of the barrage and subsequently released when the pressure head between the larger upstream height and lower downstream depth is at an optimum. The UK's tidal range resource has been estimated to be around 25-30 GW which could supply 12% of today's UK electricity demand (DECC, 2013e). The tidal range resource is primarily located in the Severn, North-West England and the East coast.

A tidal barrage typically extends the width of an estuary/lake as seen in Figure 7, with schemes such as the tidal barrage in La Rance, France with a capacity of 240 MW and operational since 1966 (Wyre Tidal Energy, 2013), Sihwa in South Korea with a capacity of 254 MW and operational since 2010 (Schneeberger and VA TECH HYDRO, 2008) and the smaller scale Annapolis in Canada with a 20 MW capacity and operational since 1984 (Nova Scotia Power, 2013) . A tidal lagoon on the other hand encompasses an area of the sea through an erected sea wall and the shoreline, as seen in Figure 8.

**Figure 7 location of the proposed Hafren Power Severn Barrage scheme (Hafren Power, 2013a).**

**Figure 8 location of the proposed Swansea Bay Tidal Lagoon scheme (Tidal Lagoon Swansea Bay, 2013a).**

Since 1894 there have been developments towards erecting a barrage across the Severn estuary. In recent years investors and entrepreneurs have collaborated to form Corlan Hafren Ltd. (2013b) with the aim of securing investment to install an 18 km long barrage connecting Brean in England to Lavernock Point in Wales, as seen Figure 7.

The proposed barrage would produce 16.5 TWh annually, equating to 5% of the UK's energy demand and is the equivalent to 3 to 4 nuclear power stations or 3000 wind turbines (Hafren Power, 2013a). Studies predicting both the generating capacity and the effects of the Severn Barrage include Xia et al., (2012, 2010a, 2010b).

Recently the proposed Severn barrage has encountered economic, environmental and political obstacles. The government's energy and climate change committee, DECC, concluded that the result of a 2-year cross-governmental feasibility study of the Severn tidal scheme was that the £25 billion scheme was unproven on economic and environmental grounds. Environmental concerns raised included the loss of intertidal habitat, the potential harming of fish and concerns over the barrage's impact on flood risk (DECC, 2013e). Corlan Hafren however remain undeterred by the economic claim, citing the project would be privately backed, secure 20,000 jobs and that similar projects such as La Rance in France has had minimal long term environmental impacts (BBC, 2013a). Concluding remarks from the chief executive of Corlan Hafren on the negative government report describe: “The report is unhelpful and frustrating - we all know we have a lot more work to do and we will do it” (BBC, 2013b).

Swansea bay tidal lagoon is a proposal to erect a sand-core breakwater wall 9.5 km long, enclosing a sea area of 11.5 $km^2$, as seen in Figure 8. The proposed project generation capacity is 240 MW with an annual output of 600 GWh (Tidal Lagoon Swansea Bay, 2013b). The project timeline aims to be fully installed and generating electricity to the grid by 2017, subject to planning and licensing approval (Business Green, 2013).

Tidal range schemes possess the ability to generate a vast amount of electricity although ironically this can also be their downfall owing to their large scale, which inherently poses difficult environmental, economic and political questions. However the La Rance tidal power station, France is considered a success since the huge initial economic investment has now been offset resulting in electricity production costs of 1.8 c/kWh, less than that of nuclear power, 2.5 c/kWh (Wyre Tidal Energy, 2013).

## 3.3 Harnessing Tidal Stream Energy

### 3.3.1 The tidal cycle

The global tidal cycle is predominantly driven by changes in the ocean levels due to the astronomical gravitational interaction of the moon and to a lesser extent the gravitational influence of the sun. In collaboration with the earth's coriolis force this causes the global propagation of long wavelength wave motion-the tidal cycle. To a lesser extent other factors such as density differences (salinity and temperature) also drive tidal currents.

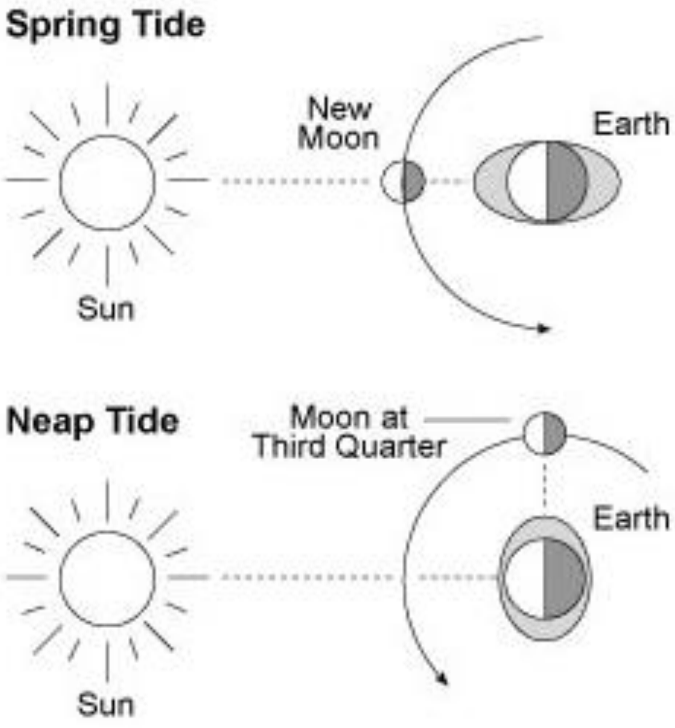

**Figure 9 Sun and moon interaction to produce neap and spring tides (Lang, 2010).**

The gravitational effects of the moon and sun causes bulges in the earth's ocean envelope on either side of the earth in line with the position of the moon as seen in Figure 9. It is the earth's rotation within these bulges that cause the semi-diurnal tidal pattern at a point, i.e. twice a day there are periods of low (ebb) and high water (flood). The semi-diurnal tidal pattern is the dominant pattern in the earth's oceans.

A combination of the earths' rotational period of approximately 24 h and the lunar cycle of approximately 28 days results in a global tidal cycle period of 24.83 h; resulting in an ebb-flood cycle period of 12.42 h. This diurnal ebb-flood cycle can be approximated by a double sinusoid as seen in Figure 10a. Combining the interaction of the moon, the sun's gravitational influence and their relative position to earth causes the spring-neap tidal cycle as seen in Figure 10b. The spring-neap cycle has a fortnightly period, which can also be approximated using a double sinusoid as seen in Figure 10b. The spring tide coincides with the moon in positions of syzygy[1], producing a larger than average tidal range, whilst the neap tide coincides with the moon in positions of quadrature[2], producing a reduced tidal range (NOAA, 2013).

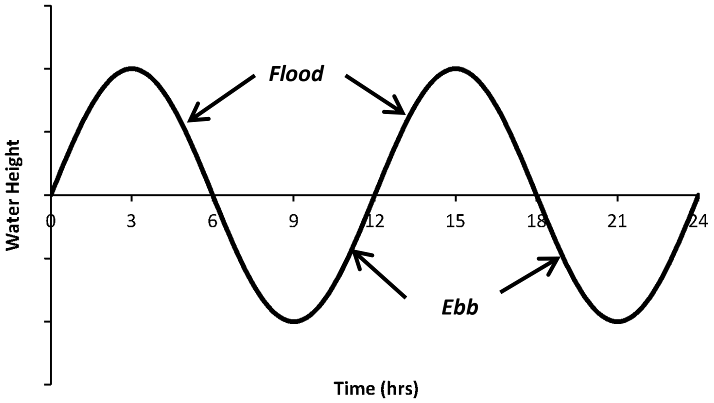

(a)

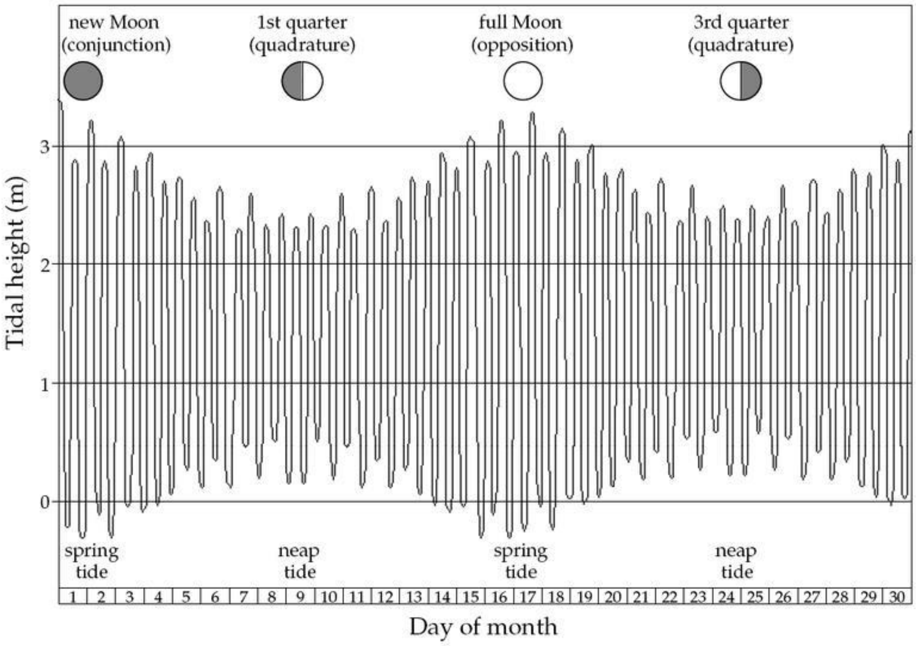

(b)

**Figure 10 (a) Semi-diurnal tidal cycle (b) Monthly spring-neap tidal cycle (University of Alberta, 2013)**

---

[1] Alignment of 3 celestial bodies

[2] The position of a celestial body at which it makes a right angle to that of the sun.

### 3.3.2 Tidal Streams

In the deep oceans off the coastal shelves the tidal streams/currents are inherently small and of the order of 0.02-0.05 m/s. However as the wave motion propagates over coastal shelves and is subjected to bathymetric and topology changes, this can result in amplified tidal amplitudes and tidal currents of an order of magnitude larger, 0.5-1.0 m/s in the case of the western European shelf (Couch and Bryden, 2006). Further amplification of tidal currents are caused due to the venturi effect when flow is forced through topologies such as channels between islands and channels between the mainland and islands, e.g. Pentland Firth (see Figure 13), Ramsey Sound, and the Channel Islands in the UK whereby due to adhering to the conservation of mass, the flow is accelerated due to the reduction in the cross sectional area in the channel compared to the open ocean. The constrained flow within the channel also results in bidirectional flow (changing direction by $180^{0}$ with the flood and ebb of the tide). A similar effect occurs in estuaries, such as the Severn Estuary, whereby the incoming tide is forced along the estuary with a reducing cross sectional area as it travels upstream, causing amplification in both the tidal range and currents.

In locations such as North-West Scotland there can be large differences in tidal phases between adjacent regions leading to amphidromic points/tidal nodes between the adjacent sites. Combined with a tidal phase difference of 4-5 hours within a short distance along a coastline, this can cause a difference in water levels either side of an amphidromic point which can drive large tidal currents. A combination of these attributes with a topographical change such as a channel between islands can lead to large amplification of tidal currents as seen in the Pentland Firth (see Figure 13) (Bryden and Melville, 2004).

**Figure 11 SeaGen - example of a tidal stream turbine (Marine Current Turbines Ltd., 2013a)**

The power available in tidal streams, see Section 0, is extracted through deploying tidal stream energy converters (TSECs). TSECs take many forms, ranging from tidal stream turbines, see Figure 11, to an oscillating hydrofoil. However the dominating form of TSECs is the tidal stream turbine which will be the focus of this study. The working principle of a tidal stream turbine is to convert the kinetic energy of tidal streams into electrical energy. Unlike the impounding nature of tidal barrages, tidal stream turbines are deployed as individual turbines, whilst several devices deployed at a site are referred to as a tidal array/farm. Further details of tidal stream turbines and their characteristics can be found in Section 4 and Appendix A.

### 3.3.3 UK Tidal Stream Resource

There are numerous reports on the assessment of the UK tidal stream resource, (e.g. Black & Veatch Consulting Ltd, (2005); DTI, (1993) and European Commission, (1996)), each with its own unique assumptions for the characteristics of the turbine used in the studies, i.e. turbine diameter, efficiency etc. Blunden and Bahaj, (2007) formed an extensive list of the resource assessments and the methods employed. The variations in these assumptions, the techniques used in the models and the quality of the model data result in varying degrees in estimations of the potential tidal stream resource in the UK. The resource assessments discussed in this section are desk studies based on secondary data source such as Admiralty tidal stream atlases, tidal diamonds etc. Early studies (such as DTI, (1993) and European Commission, (1996)) estimate only the one way interaction of tidal arrays, i.e. the array capacity based on the flow speed, whereas later studies (such as Black & Veatch Consulting Ltd, (2005) and Carbon Trust, (2011)) estimate the two way interaction of tidal arrays; thus being the array capacity based on flow speed but also the effects of array density on the flow.  As a result of the two-way interaction, Black & Veatch Consulting Ltd, (2005) and Carbon Trust, (2011), refer to a “Significant Impact Factor (SIF)” or “technical tidal resource”; thus referring to the maximum exploitable resource from a particular site prior to significant environmental impacts (such as severe reduction in tidal currents and/or tidal range) and a resource that remains economically viable to harness.

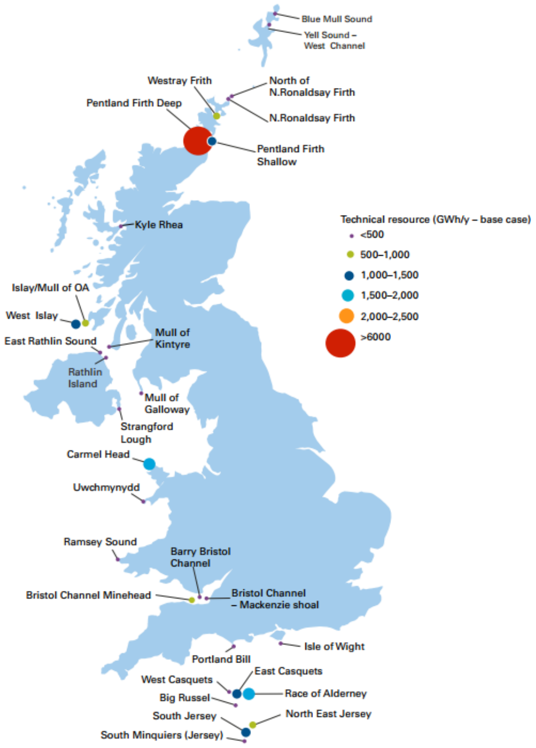

**Figure 12 Practical Tidal Resource sites around the UK, taken from: (Carbon Trust, 2011)**

It is estimated that the UK has around 50% of Europe’s tidal energy resource and a study in 2004, conducted by the Carbon Trust, estimated the UK’s technical resource at around 17 TWh/ year, which is equivalent to 4% of the UK’s energy supply .  In 2011 the UK Carbon Trust, in collaboration with Edinburgh University, conducted an updated tidal current resource study, in terms of accuracy and resolution, and suggest a total of 20.6 TWh/year could be practically extracted from 30 key tidal stream sites as seen in , without a significant impact on either the economics of energy extraction, or on the environment (Carbon Trust, 2011).  In addition, the report states that a total of 29 TWh/year could be extracted if energy extraction was prioritised over other site uses, such as fishing and shipping lanes. The 30 sites were selected based on the criteria of: mean annualised power density >1.5 kW/m$^2$ and water depth >15 m. One of the earliest studies, UK Tidal stream energy review (DTI, 1993) highlighted 42 key sites with a resource of 6.9 GW using the criteria of a mean spring tide peak flow speed of ≥2.0 m/s and excluded any site with a water depth <20 m.

The UK Renewable Roadmap (DECC, 2012a) states there is potential for deployment of wave and tidal energy devices with a capacity of 27 GW by the year 2050. However the resource is not divided equally across the UK (see  and Figure 13) with around 64% of the resource located in the Pentland Firth, North Scotland (primarily due to the presence of numerous islands, creating flow constrictions and thus increasing the available power flux density) and 20% in the Channel Islands (inducing another issue- the Channel Islands are not part of the UK and are not connecting to the UK grid). Wales in particular, with a 1200 km coastline has up to 6.2 GW estimated capacity (10 GW if including the Severn Estuary) (Welsh Government, 2012).

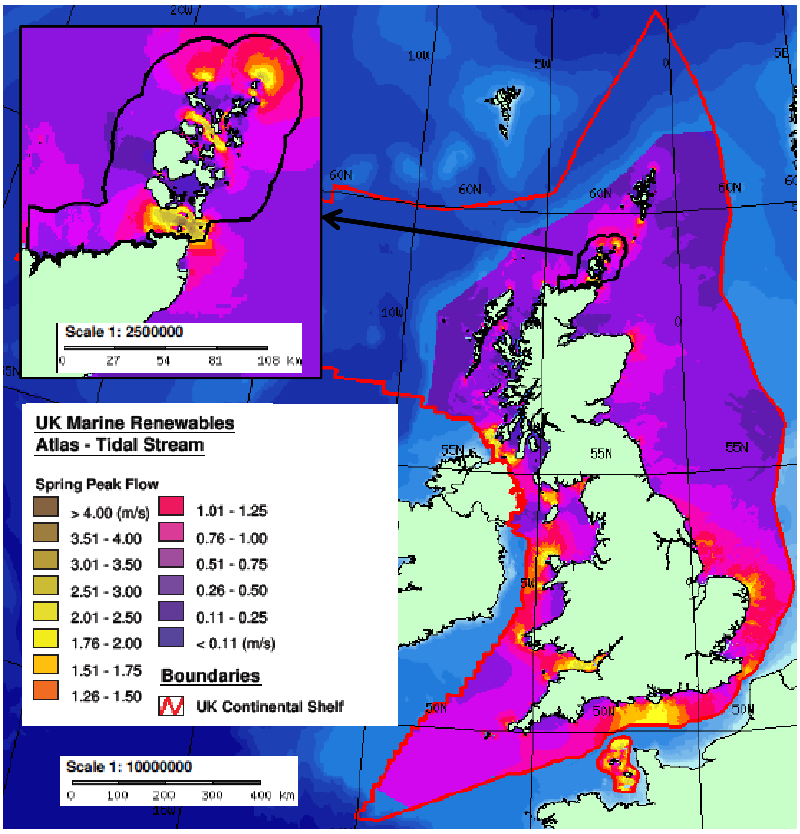

**Figure** 13 **UK (and highlighted Pentland Firth) Spring peak flow distribution Reproduced from (ABPmer, 2008)**

**Table 1 Distribution of Total UK tidal stream resource (Black & Veatch Consulting Ltd, 2005)**

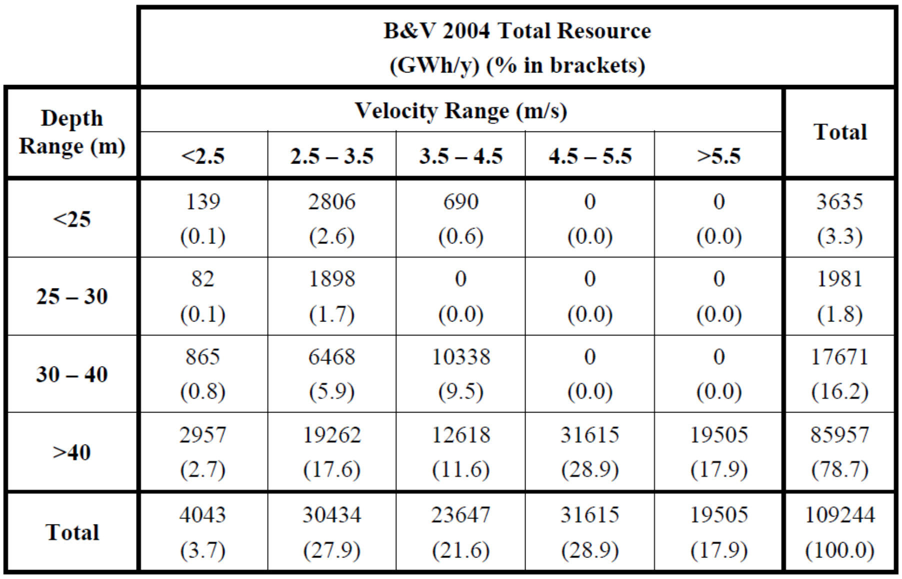

| | B&V 2004 Total Resource (GWh/y) (% in brackets) | | | | | |
|---|---|---|---|---|---|---|
| Depth Range (m) | Velocity Range (m/s) | | | | | Total |
| | <2.5 | 2.5 – 3.5 | 3.5 – 4.5 | 4.5 – 5.5 | >5.5 | |
| <25 | 139<br>(0.1) | 2806<br>(2.6) | 690<br>(0.6) | 0<br>(0.0) | 0<br>(0.0) | 3635<br>(3.3) |
| 25 – 30 | 82<br>(0.1) | 1898<br>(1.7) | 0<br>(0.0) | 0<br>(0.0) | 0<br>(0.0) | 1981<br>(1.8) |
| 30 – 40 | 865<br>(0.8) | 6468<br>(5.9) | 10338<br>(9.5) | 0<br>(0.0) | 0<br>(0.0) | 17671<br>(16.2) |
| >40 | 2957<br>(2.7) | 19262<br>(17.6) | 12618<br>(11.6) | 31615<br>(28.9) | 19505<br>(17.9) | 85957<br>(78.7) |
| Total | 4043<br>(3.7) | 30434<br>(27.9) | 23647<br>(21.6) | 31615<br>(28.9) | 19505<br>(17.9) | 109244<br>(100.0) |

**Table 2 Distribution of feasibly extractable UK tidal stream resource (Black & Veatch Consulting Ltd, 2005)**

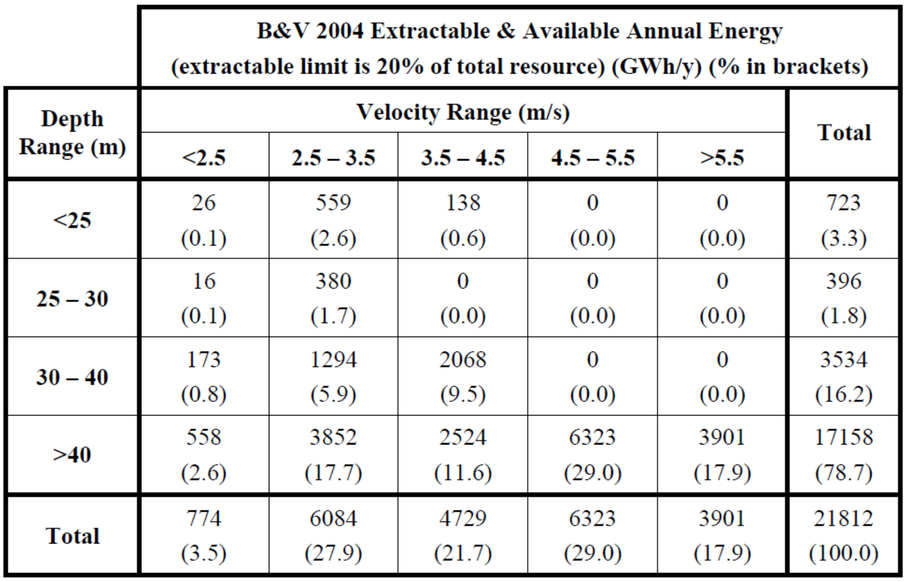

| | B&V 2004 Extractable & Available Annual Energy (extractable limit is 20% of total resource) (GWh/y) (% in brackets) | | | | | |
|---|---|---|---|---|---|---|
| Depth Range (m) | Velocity Range (m/s) | | | | | Total |
| | <2.5 | 2.5 – 3.5 | 3.5 – 4.5 | 4.5 – 5.5 | >5.5 | |
| <25 | 26<br>(0.1) | 559<br>(2.6) | 138<br>(0.6) | 0<br>(0.0) | 0<br>(0.0) | 723<br>(3.3) |
| 25 – 30 | 16<br>(0.1) | 380<br>(1.7) | 0<br>(0.0) | 0<br>(0.0) | 0<br>(0.0) | 396<br>(1.8) |
| 30 – 40 | 173<br>(0.8) | 1294<br>(5.9) | 2068<br>(9.5) | 0<br>(0.0) | 0<br>(0.0) | 3534<br>(16.2) |
| >40 | 558<br>(2.6) | 3852<br>(17.7) | 2524<br>(11.6) | 6323<br>(29.0) | 3901<br>(17.9) | 17158<br>(78.7) |
| Total | 774<br>(3.5) | 6084<br>(27.9) | 4729<br>(21.7) | 6323<br>(29.0) | 3901<br>(17.9) | 21812<br>(100.0) |

Table 1 and Table 2 indicate that the total UK tidal resource is 109.2 TWh but with the application of a SIF this becomes 21.8 TWh. Table 2 calculates the feasibly extractable energy of the total tidal resource using a SIF, previously discussed in this section. The majority of the UK's feasibly extractable tidal resource (i.e. an applied SIF), 78.7% (≈17 TWh), is found in waters of depths > 40 m. This is mainly due to the presence of greater flow speeds. Around 60% of the potential 17 TWh available at depths >40 m is from flow speeds >4.5 m/s. To the author's knowledge no testing of a tidal stream turbine has been conducted for such speeds due to the large structural loadings present on a turbine's support structure and the thrust exerted on the turbine itself at such flow speeds. Ignoring resource where the flow speeds >4.5 m/s, the potential feasibly extractable tidal resource in the UK becomes 11.5 TWh, a 53% reduction. The current market leaders for tidal stream turbines are horizontal axis tidal turbines (HATT) (see Section 4.2.1), which deploy devices with blade diameters typically in the range of 16-18 m, details on which can be found in Appendix A. With an expected minimum clearance of 5 m from blade tip to sea bed and water surface (further details of clearances in Section 5.3), the minimum depth for deployment of such devices is around 26-28 m. Using Table 2, and assuming current market leaders exploit resources of >30 m depth, this leaves an estimated resource of 1119 GWh/y (5.1% of the total resource) which is currently un-exploitable using current technology. Negating flow speeds >4.5 m/s this equates to around 10% of the total available resource.

### 3.3.4 Advantages of Tidal Stream Energy Extraction

Tidal stream energy is completely predictable; unlike wind, wave and sun, tidal power is a renewable on which one could depend; it works day and night all year round, as highlighted in section 3.3.1. Despite suffering from periods of slack tide, as seen in Figure 10, whereby the available power is zero it is possible to generate base load electricity to the National Grid. Successive high and low tides take about 12 hours to progress around the British Isles, so the strongest currents off Anglesey, Islay, Orkney and Dover occur at different times from each other; thus, together, a collection of tide farms could produce a more constant contribution to the electrical grid than one tide farm, albeit a contribution that wanders up and down with the phase of the moon (MacKay, 2009). The predictability of tidal stream energy means large factors of safety to account for storm conditions (for bed mounted devices) is not necessary, negating the need for costly over engineering in the design and manufacturing of the tidal energy converters.

Tidal stream energy could provide cost-effective and energy self-sufficiency for remote communities and islands located near economically exploitable tidal stream sites, defined by the 1993 UK Tidal Stream Energy Review as sites with an average spring tide peak flow of ≥2.0 m/s. Alderney in the Channel Island is such a place, currently subjected to the “most expensive electricity in the world” due to the high cost of importing oil and gas. Alderney Renewable Energy (ARE) Ltd aim to redress this by deploying 4 x 1 MW turbines on the seabed which would power the pumps for a pumped storage system on the island (Long Finance, 2013). Open Hydro turbines are expected to be chosen for the project since Open-Hydro own a 31% stake in ARE (Alderney Renewable Energy, 2013). An ice-plant and industrial estate on the remote Scottish island, Shetland, have plans to be powered by a 30 kW community owned tidal stream turbine from Nova Innovation Ltd (Innovation, 2012).

Currently there is major financial support from the UK government for the development of tidal stream turbine technology. In 2013 the UK government increased the number of ROCs (see section 2.4.1) given to tidal stream energy generators (as well as wave) to 5 ROCs/MWh generated until 2017 (for a single array with a capacity up to 30 MW, and 2 ROCs thereafter). This is the largest ROC/MWh granted by Ofgem for any renewable source (DECC, 2013d). Offering 5 ROCs is intended to act as a stimulus for investment into the development of tidal stream energy converters that should result in the decrease cost of energy of tidal stream over time.

### 3.3.5 Disadvantages of Tidal Stream Energy Extraction

One of the main disadvantages of tidal stream energy to date is the cost of development is high, due to the sector’s infancy. Ernst & Young estimate the capital and operational expenditure (CapEx) to be as high as £12.4 M/MW and £0.56 M/MW (per annum) respectively for pre-demonstration projects. The cost will however decrease as experienced developers edge closer to full commercialisation of the technology leading to the establishment of supply chains, with Ernst & Young estimating a reduction in CapEx and OpEx costs to £2.7 M/MW and £0.12 M/MW respectively for 10-50MW array projects. Additionally development towards full commercialisation will lead to increased confidence in the technology; aiding both the scientific and investor/developers communities. This is in contrast to one of the current advantages of tidal stream energy stated by David MacKay (2009) as “It doesn’t require high-cost hardware, in contrast to solar photovoltaic power”. It is not only the CapEx that is expected to decrease over time, but also the OpEx.

Despite the UK possessing a large tidal stream resource (see section 3.3.3), the location of prime tidal stream regions do not always coincide with areas of high electricity demand, such as in Orkney and the Channel Islands, resulting in the costly installation of a grid connection prior to the installation of a generating device and the provision of an effective transmission. This could be mitigated through government support, possibly directly via the National Grid, to supply grid connections that could later be repaid when the device(s) begin generating electricity and an income.

Despite proving renewable energy there is a risk of public opposition to the deployment of numerous devices into the sea as they could provide a negative visual impact on the surrounding environment (depending on distance from shoreline). This is not a problem for some developers, such as DCNS with their gravity base turbine Open Hydro (see Appendix A), since they are hidden from view beneath the surface. Developers such as Siemens with their SeaGen turbine could encounter opposition due to the turbine being mounted on a surface penetrating monopole as seen in (for further details see Appendix A) as well as floating tidal stream turbines close to shore.

**Figure 14 View of SeaGen from the nearby harbour (Siemens, 2012)**

Additionally there is a risk of damage to surface penetrating or near surface support structures from boats, ships etc. and vice versa as seen in June 2013 when a yacht with a crew of three crashed into Marine Current Turbine Ltd (MCT) SeaGen turbine monopole in Strangford Loch, breaking the mast of the yacht and throwing the entire crew overboard (BBC, 2013c). However no serious injuries were sustained to the crew.

This is difficult to mitigate besides providing ample warning to seafarers of the obstacles that lie ahead through signage and a lighting system.

The long term survivability of a TSEC in a harsh marine environment is an unknown factor. To date the majority of full scale prototypes are installed for a typical period of one year, with regular downtime for maintenance or changes to device configurations during the testing period, e.g. Tidal Energy Ltd plan to change the blade sizes of their full scale Deltastream turbine during their one year testing period (Tidal Energy Ltd, 2009). Although MCT's SeaGen turbine was in operation for three years (Marine Current Turbines Ltd., 2013b). Therefore the survivability of such devices for prolonged periods of time in a harsh marine environment, with life expectancies of around 25 years, is still an unknown quantity. The risks will be mitigated by the industry learning from other vastly experienced offshore industries, such as oil and gas exploration, that have engineered offshore structures to withstand the marine environment for greater than 25 years, e.g. the Beryl Alpha oil platform located over 200 miles northeast of Aberdeen has been in operation since 1976 (Drilling Contractor, 2012). Further details on survivability of devices can be found in Section 6.

Finally obtaining consents is an onerous and expensive process due to the lack of detailed scientific evidence as to the effects of tidal stream devices. A substantial amount of work must be conducted prior to seeking consent for device deployment, including detailed bathymetric studies, profiling flow conditions and detailed environmental surveys. Combined the pre-consent requirements are an expensive process and this financially exposes investors. Mitigation could be provided through collating knowledge and experience from various developers, scientists and researchers such as the National Research Council's-Marine Renewable Energy Knowledge Exchange Program (MREKEP) (Natural Environment Research Council, 2013).

### 3.3.6 Environmental Considerations

The installation of tidal stream turbines, particularly the concept of a large array, has led to widespread environmental concerns. Frid et al., (2012) conducted a study on the potential impacts of tidal stream turbines on the local environment. This includes the following.

#### *3.3.6.1 Habitat and Species:*

Affecting benthic habitats and communities composition (Lohse et al., 2008) by altering water flows and sediment dynamics (Neill et al., 2009). However tidal stream turbines are installed in areas where high current flows already cause sediment transport disturbance. The wake of a tidal stream turbine will pose both problems and opportunities. Problems lie with the deposition of sand, which may increase the mortality of seagrass beds and decrease growth rate of vegetation. However there may be opportunity for a new benthic habitat to be created in the wake of a tidal stream turbine due to the deposition of organic matter, increasing diversity and abundance of invertebrates (Widdows J. and Brinsley M., 2002). However studies also show that fish are attracted to artificial structures and therefore predation may increase in the area surrounding tidal stream turbines (Davis et al., 1982; Langlois et al., 2005).

Many researchers are concerned with fish mortality when coming into contact with rotating tidal stream turbines (Dadswell and Rulifson, 1994; Deng et al., 2011). However using the experience and mitigation techniques gained by large tidal barrages such as la Rance, see section 3.2, and full scale deployment trials of tidal stream turbines should help reduce this problem. Unlike tidal barrages, tidal stream turbines will not funnel (unless deployed in a ducting structure) organisms through the turbine structure and therefore offer the opportunity for organisms to avoid the structure.

Pelc and Fujita, (2002) claim that tidal stream turbines rotating at <50 RPM will minimise fish mortality from contact with the turbine blades. Using information available from Appendix A, a typical commercial scale tidal stream turbine has a blade radius of 9m, and would operate in flow speeds ranging from 2-4 m/s. Using the recommended maximum 50 RPM by Pelc and Fujita, (2002) and Equation (7), a typical sized tidal stream turbine should operate at a tip speed ratio (non-dimensional speed ratio of a turbine, further details in Section 0) lower than the following, for the given flow speeds:

**Table 3 Maximum TSR values to minimise fish mortality**

| | RPM: | 50 | ω(rad/s): | 5.2 | |
|---|---|---|---|---|---|
| **U(m/s)** | 2 | 2.5 | 3 | 3.5 | 4 |
| **TSR** | 24 | 19 | 16 | 13 | 12 |

Appendix A, shows that all the tidal stream turbines reviewed operated at TSR<12 which satisfies the maximum TSR values calculated in Table 3 to minimise fish mortality. However the Pelc and Fujita, (2002) results are questionable since the study analyses RPM which is not scalable. Non-dimensional parameters must be provided to enable comparison of lab-scale experiments to full-scale operations. Comparing the range of TSR values in Table 3 to Figure 15 shows they are not realistic TSR values.

Tidal stream turbines are expected to have little effect on diving seabirds since their agility is greater than the slow moving turbine blades, although questions have been raised as to whether diving birds may mistake turbine blades for prey (AWATEA, 2008). Little information is available on the potential impacts of tidal stream turbines on larger mammals such as cetaceans but it is expected that due to their echo locating ability, the chances of a collision with a tidal stream turbine is low. Tidal Energy Ltd. are deploying their Deltastream device in Ramsey Sound, West Wales which has a resident porpoise community. Post de-commissioning the results of the environmental impact on the porpoises will be made available in the public domain since it is part funded by the Carbon trust (Recharge, 2012). A reduction in potential collisions of tidal stream turbines and marine mammals such as porpoise and seals can be achieved through devices emitting a low noise to warm marine mammals of its presence, such as that utilised by Deltastream (Tidal Energy Ltd, 2009).

#### *3.3.6.2 Reproduction and Recruitment*

Unless tightly packed, it is expected that tidal stream turbines will have little impact on larval transport. The Crown Estate are funding research in the Pentland Firth, Scotland on the potential impacts of tidal stream turbines on the migratory routes of salmon (BBC, 2013d).

#### ***3.3.6.3 Noise:***

Primarily focused on noise during the installation and de-commissioning stages of a tidal stream turbine, excessive noise from activities such as piling can affect Cetaceans. This was highlighted by the effects of installation of offshore wind turbines in Denmark on porpoises. Effects included a reduction in foraging behaviour and echolocation activity (Henriksen et al., 2003; Tougaard et al., 2003). However, besides the SeaGen devices the majority of tidal stream turbines are using gravity bases or a floating arrangement, as seen in Appendix A, reducing the highlighted noise issues from installation.

# 4 Tidal Stream Turbines

**This chapter describes the performance characteristics of tidal stream turbines that will need to be measured when conducting the physical and numerical modelling of CarBine, namely the non-dimensional parameters, which enable comparisons between multiple devices: coefficient of performance and torque ($C_p$ and $C_t$) and tip speed ratio (λ). Additionally this chapter summarises the various tidal stream turbine technologies, whilst highlighting that the most mature technology is the horizontal axis tidal turbine (HATT). Finally a comparison between wind and tidal stream energy reveals that due to the increased density of water compared to wind, for equivalent power output a tidal stream turbine can be up to 5.57 times smaller than a wind turbine.**

---

The following parameters are used to describe the performance of a tidal stream turbine, the majority of which are non-dimensional terms obtained through established techniques such as the Buckingham-pi theory (Mason-Jones et al., 2012). The advantages of non-dimensional analysis are described in EquiMar, (2010a) and include:

- Scaled model results can be applied to prototype scale without scaling ratios;
- Dimensionless parameters are identical between scale model and prototype;
- Results of models at different scales can be plotted on the same diagram;
- The number of output parameters reduces.

Despite current effort from EMEC to produce guidelines on the development of a tidal turbine (EMEC, 2013a) a universal standard such as a British Standard or a European Standard for the performance characterisation of a tidal turbine does not exist. It is generally accepted within this field of research that a device's performance can be predominantly characterised by three dimensionless parameters: coefficient of performance $C_p$, coefficient of torque $C_t$ and tip speed ratio TSR, all of which are given below.

The available freestream power $P_\infty$ (W), for a turbine with cross sectional area (perpendicular to the flow) $A$ (m$^2$), placed in a moving fluid (in the absence of significant changes in depth and elevation) with undisturbed flow speed $U_\infty$ (m/s) and density $\rho$ (kg/m$^3$) is given by the equation

$$P_\infty = \frac{1}{2}\rho \int_A \left(U_\infty^3 dA\right) \tag{1}$$

Bryden and Melville, (2004) state that it is convenient to use the average flow speed across the swept area perpendicular to the flow of a flow conversion device for the $U_\infty$ component. This simplifies Equation (1) to

$$P_\infty = \frac{1}{2}\rho A U_\infty^3 \tag{2}$$

Equation (2) is further modified since a tidal stream conversion device cannot convert the total freestream power available due to losses and therefore the term $C_p$, the coefficient of power, is introduced. The $C_p$ term refers to the percentage of the total freestream power, for a given $A$ (of the device) and $U_\infty$, which the device can convert from kinetic energy of the stream of water to mechanical energy. Modifying Equation (2), to produce the power extracted by the tidal stream turbine as

$$P = \frac{1}{2}C_p \rho A U_\infty^3 \tag{3}$$

$$C_p = \frac{P}{P_\infty} \tag{4}$$

$C_p$ takes into account the losses due to the Lanchaster-Betz law and the internal mechanisms of the device. Originally accredited to the work of Betz, (1920) but later amended to include the work of Lanchester, (1915) thanks to Bergey (1979), the Lanchaster-Betz limit stipulates that for a turbine with a small cross section in comparison to the operating domain, i.e. unbounded flow, the maximum achievable $C_p$ is 16/27 or 59%. Numerical studies of the efficiency of a turbine in a tidal channel were carried out in detail by Garrett and Cummins, (2007), who state that the Lanchaster-Betz limit is achieved when the “flow speed decreases to $2/3\,U_\infty$ through the turbine and further to $1/3\,U_\infty$ as the flow expands in the turbine wake”; the theory of which is based upon the power extraction from wind by an actuator disk. In scenarios whereby the turbine cross section is large in comparison to the domain dimensions, i.e. bounded flow, blockage effects become apparent which increases the maximum achievable $C_p$, further details are found in Section 9.5.

The kinetic energy of the flow is converted to mechanical energy by tidal stream turbines through harnessing lift and/or drag forces, as seen in Section 4.1. It is the relationship of the generated lift/drag force with the lever arm of the turbine that generates the rotational torque $T$ (Nm). The non-dimensional form of the torque $T$, the coefficient of torque, $C_T$ is found by

$$C_T = \frac{T}{\frac{1}{2}\rho A U_\infty^2 R} = \frac{C_p}{TSR} \tag{5}$$

Akin to Equation (3) the power generated by a turbine can also be calculated using its angular velocity $\omega$ (rad/s) and the generated torque $T$ (Nm)

$$P = T\omega \tag{6}$$

From Equation (6) above it can be seen that the power extracted by the turbine, $P$, is a function of both $T$ and $\omega$. Therefore in order to find the maximum $C_p$ of a turbine it must undergo testing to vary $T$ and $\omega$. Since torque is related to the angular velocity a balance must be found, and hence the maximum $C_p$. A parameter devised to vary for such testing is the tip speed ratio, TSR of the turbine. The TSR is the relative speed of the turbine in relation to the freestream flow speed. The angular velocity $\omega$ (rad/s), of a turbine with radius $R$, can be expressed as a value relative to the freestream flow speed $U_\infty$ (m/s), through the non-dimensional form TSR, seen in Equation (7). Plotting $C_p$ vs. TSR enables the visual distinction of the position of the maximum $C_p$ and the corresponding TSR value, resulting in the optimum operating conditions for the turbine in order to produce maximum efficiency, as seen in Figure 15.

$$TSR = \lambda = \frac{R\omega}{U_\infty} \tag{7}$$

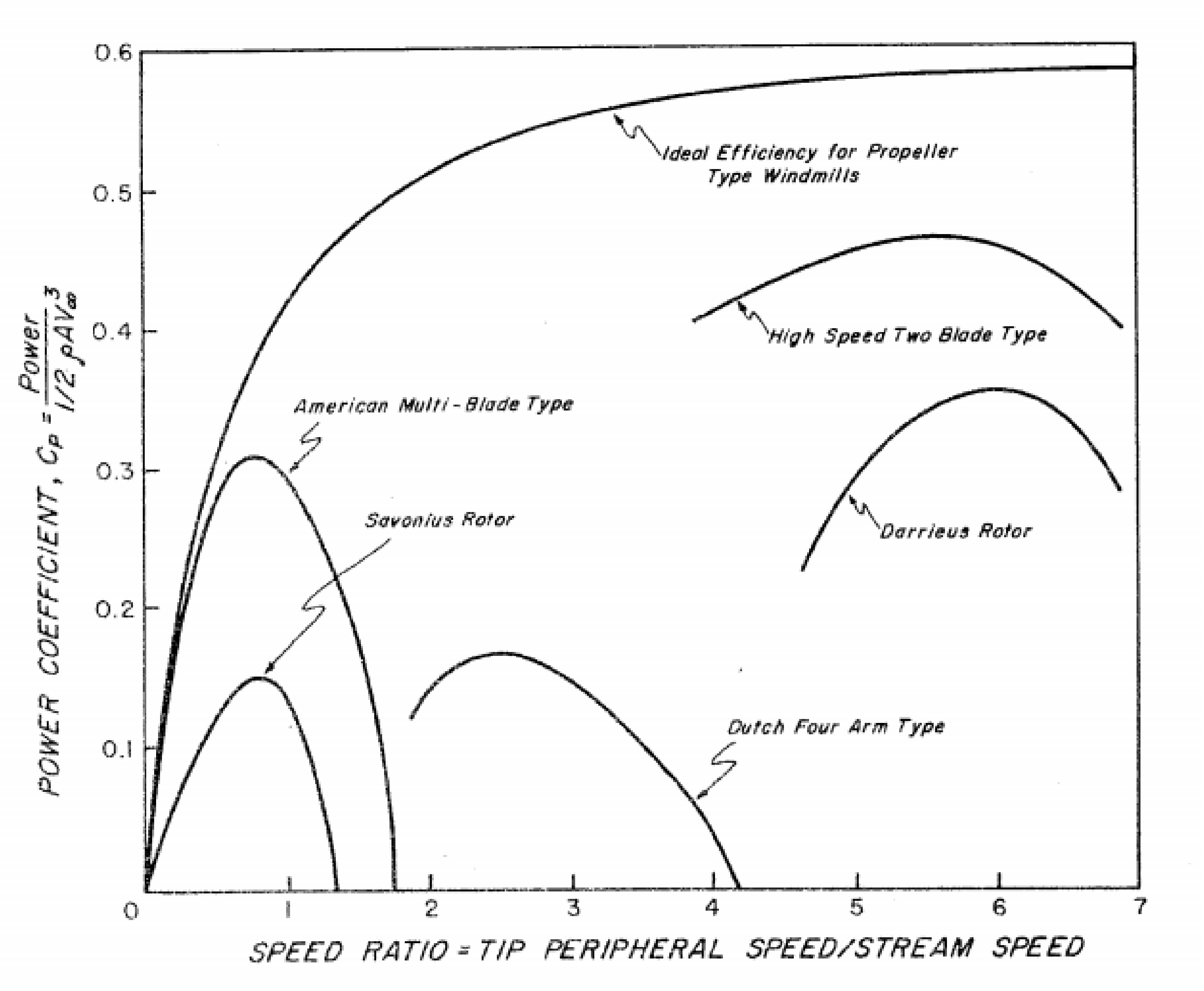

**Figure 15 $C_p$ vs. λ curves for a variety of wind turbines (Wilson and Lissaman, 1974)**

Below is a summary of terminology describing power output/ energy extraction:

- **Cut-in speed:** $U_\infty$ at which a turbine begins to generate power;
- **Rated speed:** $U_\infty$ at which a turbine is operating at its rated power;
- **Power Rating:** The maximum power output of a given turbine achieved at rated speed;
- **Capacity Factor:** Ratio of the actual energy produced in a given period compared to the theoretical maximum, based on the power rating. For a given site, the capacity factor of a tidal stream turbine can be predicted accurately due to the reliability of the tidal cycle, see Section 3.3.1.

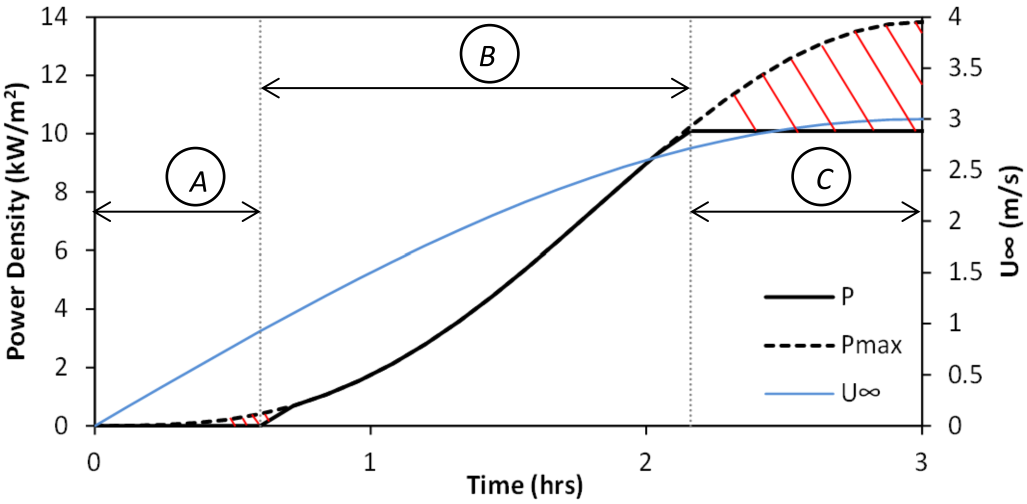

| | |
|---|---|
| **A** | **$U_\infty$ below cut-in speed, P=0** |
| **B** | **Between cut-in speed and rated speed, P=Pmax** |
| **C** | **Operating at rated speed, P<Pmax** |

**Figure 16 Power output phases for a theoretical tidal stream turbine**

Figure 16 illustrates the power output of a theoretical turbine with a cut-in speed of 1.0 m/s and rated speed of 2.7 m/s at a theoretical site with a maximum $U_\infty$ of 3 m/s for a quarter of a tidal cycle. $P_{max}$ is the maximum power available to the turbine, whilst $P$ is the power generated. The shaded areas indicate the energy that was not extracted by the turbine for both below and above the cut-in and rated speed. This equates to 12.5% of the total energy available, split into 12% for $U_\infty$above that of the rated speed and 0.5% for $U_\infty$ below the cut-in speed. The concept of a rated speed, and thus rated power, is universal for wind turbines and is dictated by economics; the value of the rated speed is chosen to minimise the cost of energy for a given site. A lower rated speed enables a lower capacity generator to be used, lowering the cost, as well as a larger capacity factor, which will be vital if tidal stream power is ever to provide base load capacity to the National Grid (Clarke et al., 2006).

## 4.1 Driving Forces

Tidal stream turbines extract energy based on two fundamental processes, which are the lift and/or drag forces exerted by the tidal streams on the turbine, causing a rotary motion which in turn drives the electrical generation subsystem. The type of force that causes the rotary motion depends upon the design of the turbine. For a drag type turbine such as the Savonius, see Sections 4.2.2.3 and Chapter 8, drag force is the predominant driving force and is therefore maximised during design. For turbines whereby lift force is the predominant driving force, such as hydrofoil turbines (the majority of HATTs), the drag force is minimised during design since it produces a negative torque to the positive torque produced by the lift force. For this reason the lift $(F_L)$-drag $(F_D)$ force ratio, $(F_L/F_D)$, is maximised in design. Generally, lower drag and higher lift forces can be achieved by producing thinner blades however this poses structural issues since thickness is a structural advantage for strength (Orme et al., 2001).

### 4.1.1 Drag Force

Drag force is the result of both pressure (or form) drag and frictional (or skin) drag and acts in the direction of the flow (Houghton and Carpenter, 2003). When frictional drag exceeds form drag an object is described as streamlined, whereas when form drag exceeds frictional drag an object is described as a bluff body. Drag force $F_D$, can be calculated using

$$F_D = {}^1/_2\, C_D \rho {U_\infty}^2 A \tag{8}$$

where $U_\infty$ (m/s) is the speed of the object relative to the fluid (further details in Section 0), density, $\rho$ (kg/m$^3$), drag coefficient, $C_D$ (-) (dependent upon the shape of the object and the Reynolds Number (Chadwick et al., 2004) and Mach Number – for low Mach numbers, i.e. <1.0 then the Mach number can be ignored) and cross sectional area perpendicular to the flow $A$ ($m^2$).

Pressure drag is the result of an imbalance in pressures upstream and downstream of an immersed object, such as a flat plate orthogonal to the flow, see Figure 17b. The imbalance of high pressure on the upstream face caused by the stagnation points (Bernoulli's principle) from the deflection of flow around the flat plate and the low pressure on the downstream face caused by the flow separation, results in a net force on the object in the direction of the flow. A larger cross sectional area perpendicular to the flow will result in a larger drag force.

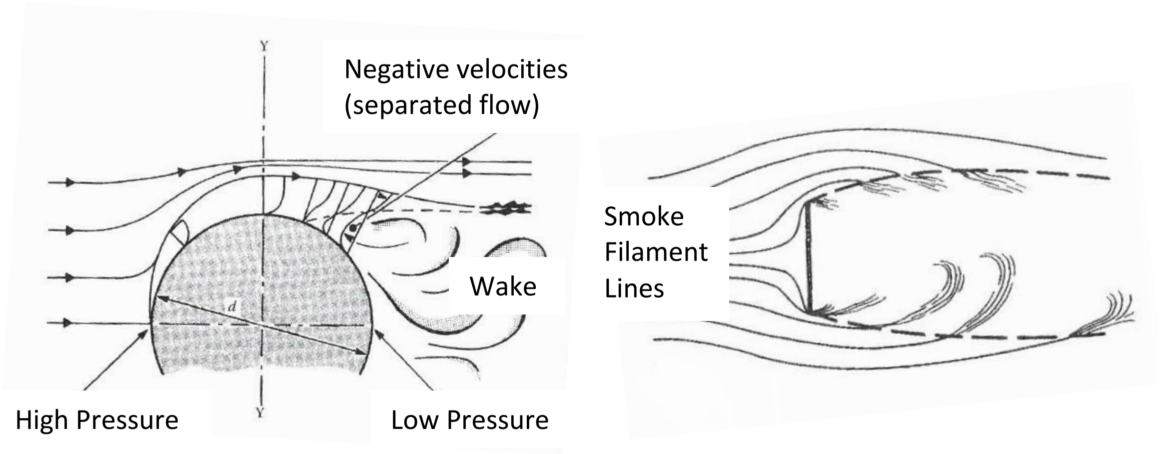

**(a)** **(b)**

**Figure 17 Flow separation (a) Cylinder (Chadwick et al., 2004) (b) Orthogonal flat plate (Houghton and Carpenter, 2003)**

The destabilising of the laminar boundary layer, whereby at a certain point the boundary layer can become detached from the object is known as the separation point and has a large impact on the pressure drag of an object; flow separation results in vortices shedding and discharging into the stream resulting in increased pressure drag. The process of flow separation is illustrated in Figure 17a: as the flow is deflected outwards around the cylinder the flow accelerates with an increasing boundary layer until it reaches a point, y-y. From this point the flow in the boundary layer is travelling slower than that of the surrounding flow, the flow in the boundary layer continues to retard to the point when it acts in the opposite direction to the surrounding flow, causing negative velocities. The negative velocities correspond to a lower pressure than that of the surrounding flow, as a result fluid is drawn into the low pressure zone within the boundary layer; this process causes eddies to form which are then drawn downstream to form the wake of the object (Chadwick et al., 2004).

Hydrofoils are designed to minimise the pressure drag through delaying the separation of the boundary layer to the blade tip, this is done through gradually changing the cross sectional area, since abrupt changes in the geometry of an object will cause detachment of the boundary layer. Changing the angle of attack of a blade to the oncoming flow, µ in Figure 18, will also change the location of the separation point. It is this sensitivity of hydrofoils to flow separation and the minimisation of pressure drag which dictates their complex and expensive manufacturing, see further details in Section 6.2.

Skin-friction drag is generated in the boundary layer and is due to the tangential shear stresses acting along the surface of an object, the magnitude of which depends on the surface roughness, characteristics of the boundary layer be it laminar, transitional or turbulent, as seen in Figure 18, and the Reynolds number. The tangential shear stresses are due directly to viscosity and act in alignment but opposing the incoming flow (Houghton and Carpenter, 2003).

Skin-friction drag is higher in a turbulent boundary layer in comparison to a laminar boundary layer. The effect of roughness on the boundary layer depends upon the degree of surface roughness of the object in relation the height of the laminar sublayer of the boundary layer. If the surface roughness protrudes the laminar sublayer into the turbulent region then this causes increased energy loss due to the formation of eddies, resulting in an increased frictional drag. If the surface roughness does not protrude the laminar sublayer of the boundary layer then there will be very little frictional drag (Chadwick et al., 2004).

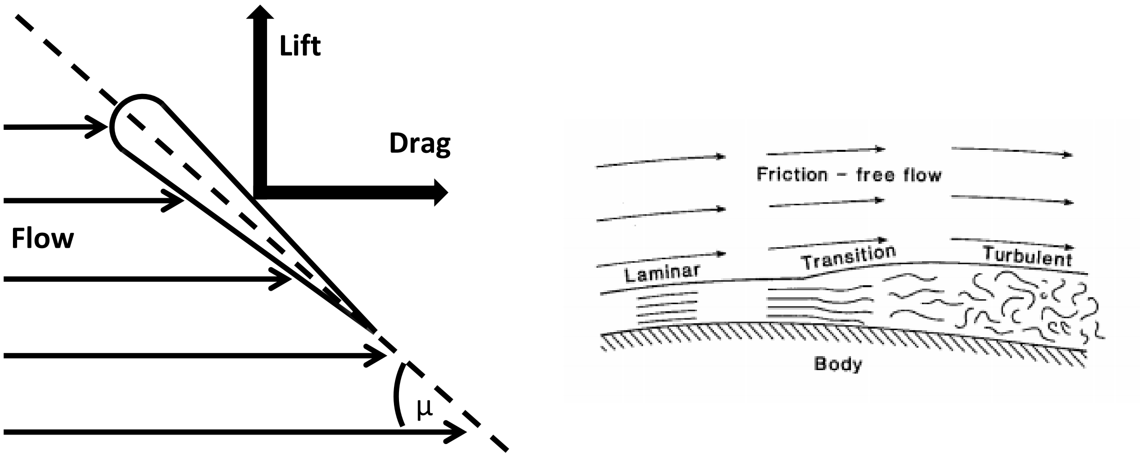

**(a)** **(b)**

**Note: Not all tidal stream turbines use hydrofoils**

**Figure 18 (a) Forces acting on a hydrofoil (adapted from (Clifford et al., 1993)) (b) Boundary layer separation**

The wake of an object is the direct result of both the loss of momentum in the flow due to the object's total drag and it's increased energy due violent eddies in the wake. Within the flow the loss of momentum appears as a reduction in the flow speed. Analysing the size and intensity of the wake of an object will indicate its form drag. Streamlined objects, such as hydrofoils, will have a smaller wake to that of a bluff body, as seen in Figure 17.

### 4.1.2 Lift Force

Unlike drag force, lift force acts perpendicular to the flow direction on an immersed object. As seen in Figure 18 lift force is generated as a result of the application of Bernoulli's theorem to the blade tip: due to the hydrofoil profile, the fluid travels faster over one side of the hydrofoil causing low pressure relative to the other side where there is higher pressure, causing an imbalance in pressure either side of the blade. The result of the pressure imbalance is a force in the perpendicular direction to the flow direction, lift force $F_L$

$$F_L = {}^{1}\!/_{2}\, C_L \rho {U_\infty}^2 A \tag{9}$$

for a fluid with undisturbed velocity, $U_\infty$, density, $\rho$ (kg/m$^3$), and lift coefficient, $C_L$ (-) (dependent upon the shape of the blade, the Reynolds Number and the angle of attack, μ) and cross sectional $A$ (m$^2$).

## 4.2 State of the Art

Below is a list of the various categories of tidal stream turbines. Since the technology can be considered to be in its infancy in comparison to wind, there are no official criteria for the individual categories and there are also numerous novel designs that fit into their own individual categories. With consideration to the amount of research that has been conducted in this field, the two main categories are horizontal axis and vertical axis tidal turbines, HATT and VATT respectively. Recent studies by Bahaj, (2011); Khan et al., (2009); King and Tryfonas, (2009) and Lago et al., (2010) have examined the various tidal stream turbines in development, however the sector's infancy means such reviews quickly become outdated. The Marine Energy Global Technology Review 2012 by Marine Energy Matters (MEM) states that globally out of the 16 technology developers that have reached full prototype/commercial scale, 30% are UK based. From a survey conducted from publicly available information, Appendix A includes details on the forerunners in tidal stream energy conversion using select horizontal, vertical and transverse horizontal axis tidal turbines mainly in UK waters.

### 4.2.1 Horizontal Axis Tidal Turbine (HATT)

HATTs are turbines whereby their axis of rotation is parallel to that of the direction of the freestream flow. Typically HATTs are perceived as "underwater windmills" since visually they are synonymous to wind turbines. HATTs usually consist of a number of blades, normally in the shape of a hydrofoil, mounted on a hub or nacelle. As a result of using hydrofoils, HATTs harness lift force for torque generation, further details can be found in Section 4.1.2. Various HATTs at different stages of the design process can be seen in Appendix A. HATTs are the most developed category of tidal stream devices reflected by HATTs majority share of grid-connected commercial scale prototypes,as seen in Appendix A. SeaFlow, a 300 kW HATT created by MCT in 2003 and installed off the coast of Devon was the world's first pilot project in open sea conditions for the extraction of energy from tidal streams (IT Power, 2013), as seen in Figure 19b.

**(a)** **(b)**

**Figure 19 Examples of HATTs (a) OpenHydro turbine (b) Raised SeaFlow turbine**

In May 2008 Open Hydro became one of the world's first grid connected HATTs (McLindon and Gray, 2008). The Open Hydro device (owned by DCNS) is a unique HATT due to its open centred design with an outer ring of blades, as seen in Figure 19a. MCTs SeaGen, as seen in Figure 11, was the world's first grid connected megawatt size device at 1.2 MW and was installed in Strangford Loch, Ireland in 2008. SeaGen is an advancement of the SeaFlow device, further details of which can be found in Appendix A. Research into HATTs is more advanced than that for other categories, with one of the main reasons being that HATTs have demonstrated the most promising performance parameters such as high $C_p$ values, see Figure 15, which is one of the key factors with respect to attracting investment since a high $C_p$ value results in greater energy extraction from a given flow.

### 4.2.2 Vertical Axis Tidal Turbine (VATT)

VATTs differ from HATTs simply by the orientation of the axis of rotation. For a VATT the axis of rotation must be perpendicular (vertical) to that of the flow direction. Due to their orientation to the flow VATT's utilise lift and/or drag force for torque generation. As previously stated, research for this type of device is not as mature as that for HATT, primarily due to their typically inferior performance with respect to $C_p$ values, as seen by the Savonius performance in Figure 15. On the contrary VATTs do present some unique advantages in comparison to HATT, which are further discussed in Section 8.1.

There is a range of different varieties of VATTs, which are outlined below.

#### *4.2.2.1 Darrieus Turbine*

Designed by G.J.M Darrieus in 1931, the Darrieus turbine comprises of a number of vertical blades (typically 3-5) shaped like a hydrofoil and held via a series of arms or sandwiched between two disks (Darrieus, 1931), as seen in Figure 20a. The Darrieus turbine is purely a lift-generating device. In the Straits of Messina (Italy) a commercial scale Darrieus turbine, namely the Kobold Turbine, was tested in 2001 (see Appendix A for further details). Further studies on the Darrieus turbine in a hydraulic environment include Antheaume et al., (2008); Gretton, (2009); Kiho et al., (1996); Li and Calisal, (2010) and Maître et al., (2013).

#### *4.2.2.2 Gorlov Turbine*

Designed in 1995 by A.M. Gorlov and an evolution of the Darrieus turbine, the Gorlov turbine is simply a Darrieus turbine with twisted/helical blades (Gorlov, 1995), as seen in Figure 20b. The twist in the blades effectively represents an infinitely staged device resulting in a steady torque output in comparison to the Darrieus style turbine. Further studies on the Gorlov turbine include Han et al., (2013) and Yang and Shu, (2012).

#### *4.2.2.3 Savonius Turbine*

Designed by Sigurd. J. Savonius at the beginning of the 20th century to harness wind energy (Savonius, 1931), the Savonius turbine is pre-dominantly a drag driven device but it also generates lift force. The Savonius turbine consists of 2 semi-circular buckets mirrored along a common axis as to form the letter S, as seen in Figure 20c. Further details can be found in Section 8.

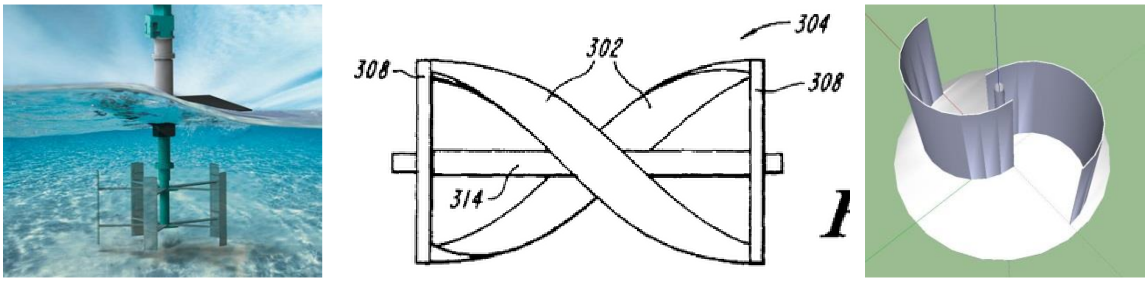

(a) (b) (c)

**Figure 20 Variety of VATTs (a)Darrieus (b)Gorlov (sideways view) (Gorlov, 1995) (c) Savonius (minus the top disk)**

Further examples of less pursued VATTs can be found in Bhutta et al., (2012) and details of commercial scale VATTs can be found in Appendix A.

### 4.2.3 Transverse Horizontal Axis Turbine (THATT)

THATTs differ from VATTs and HATTs since their axis of rotation is perpendicular in the horizontal plane to that of the direction of the freestream flow. Extensive research on a THATT device has been conducted at Oxford University, on a variant of the Gorlov turbine namely the Kepler Energy turbine (McAdam et al., 2013a, 2013b, 2013c). In the US, a THATT owned by Ocean Renewable Power Company (ORPC, 2013) namely TidGen seen in Figure 21, has been successfully deployed and grid connected in the river Maine, USA since September 2012 (Maine Sunday Telegram, 2012). TidGen is similarly based on the Gorlov style design. Further details on TidGen and the Kepler Energy turbine can be found in Appendix A.

**Figure 21 TidGen, an example of a THATT (Maine Technology Institute, 2013)**

### 4.2.4 Other types of tidal stream energy devices

#### *4.2.4.1 Venturi*

A venturi device is a housing structure for a tidal stream turbine. Based on Bernoulli's principle the venturi device accelerates the freestream flow by directing the flow through a constricted area-thus increasing the flow speed. The accelerated flow then drives the housed turbine, producing a higher power output than could be achieved in the surrounding freestream flow, see Equation (2). The Davidson-Hill venturi turbine, as seen in Figure 22b, is an example of the technology and claims to achieve an increase in efficiency of 384% compared to freestream conditions, further details available in Appendix A.

#### *4.2.4.2 Kite*

Analogous to a kite in wind, kite style tidal turbines work on the basis of a kite tethered to the sea bed. The kite consists of a hydrodynamic wing with a turbine attached below. Generating lift force from the tidal streams, the wing moves through the water on a fixed trajectory due to the tethering, typically forming a figure of eight. This causes the attached turbine to rotate, producing electricity. To the author's knowledge, Deep Green, a unique solution from the Swedish company Minesto Ltd (Minesto Ltd, 2013), seen in Figure 22a, is the only kite device currently on the market. Further details of Deep Green are available in Appendix A.

#### *4.2.4.3 Archimedes Screw*

An ancient concept, dating back to the ancient Greeks (the time of Archimedes), the screw was first used and is still used as a simple pumping device, which consists of a helical screw wrapped around a cylinder all enclosed within a larger cylinder. With the screw inclined, as the screw is turned each subsequent thread scoops up a small volume of water and this is later deposited once the thread reaches the summit of the screw. In recent times this principle has been converted to act as a tidal stream turbine. Energy is captured as the water flows through the helical device causing it to rotate (EMEC, 2013b). The Norwegian company Flumill aim to commercialise this technology with their device Flumill, as seen in Figure 22c whilst being tested at EMEC (see Section 5.5)(Flumill AS, 2013).

### 4.2.4.4 *Oscillating Hydrofoils*

Lift and drag forces are generated by the pressure differences generated over the hydrofoils by the relative motion of the tidal currents. This force is used to drive a hydraulic pump which transfers high pressure fluid to drive a motor and finally an electrical generator. These devices utilise a hydraulic power take off system as opposed to the mechanical power take off systems used by the turbine style device (University of Strathclyde, 2013). An example of this is the Stingray device, as seen in Figure 22.

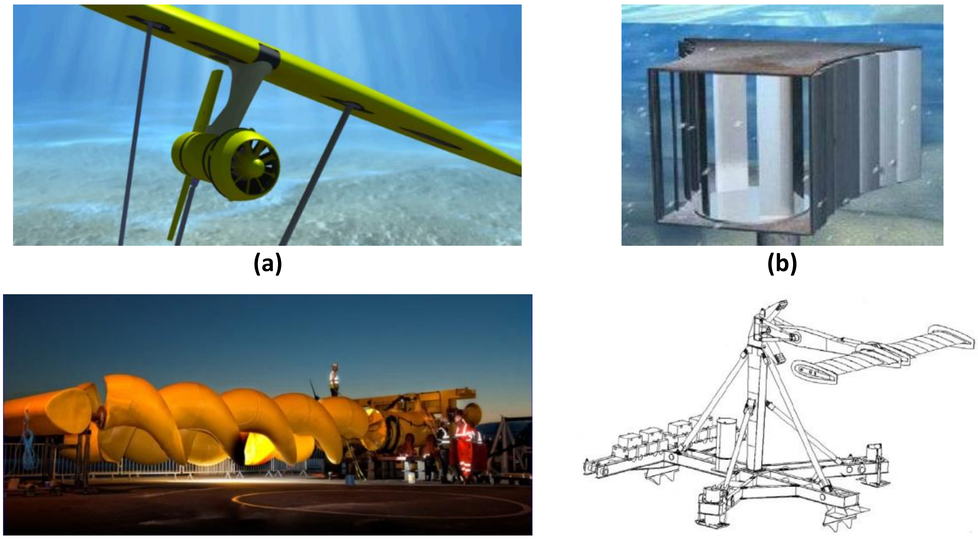
**(a)** **(b)** **(c)** **(d)**

**Figure 22 (a) An artist's impression of Deep Green (Minesto Ltd, 2013) (b)Davidson-Hill Venturi turbine (Tidal Energy Pty Ltd, 2013)(c) Flumill Archimedes screw turbine (Flumill AS, 2013) (d)Stingray device (University of Strathclyde, 2013)**

### 4.2.4.5 *Fan Belt*

The fan belt is a device whereby hydrofoils are mounted on a belt albeit on a vertically or horizontally aligned oval circuit, the water flow over the hydrofoils causes the belt to rotate and hence generate power. The belt rotates in the opposite direction when the direction of the tide changes. A vertically aligned example is the Aquanator AN-400 by Atlantis Energy Corporation, which was installed and grid connected in Australia in 2008 (Atlantis Resources Ltd, 2013a) , as seen in Figure 23a. A horizontally aligned example is the Tidal Sails device seen in Figure 23b.

**(a)** **(b)**

**Figure 23 Examples of Fan Belt turbine (a) Aquanator AN-400 (Atlantis Resources Ltd, 2013a) (b) Tidal Sails device (Tidal Sails AS, 2013)**

### 4.2.5 Supporting Structure

Similar to the number of different styles of tidal stream turbines available there are also numerous techniques for supporting or anchoring a tidal stream turbine in the harsh marine environment. Appendix A shows that tidal stream energy turbines are typically supported on a gravity base or on a floating structure. Further details of which can be found in an analysis conducted by Orme et al., (2006) and Owen and Bryden, (2005).

### 4.2.6 Tidal Turbine Array

#### *4.2.6.1 Tidal Turbine wake*

Synonymous with wind turbines, numerous tidal turbines deployed at a site are labelled as a tidal array or farm. The layout of a tidal array for a given site is based upon the wake properties of the turbine in question. The wake of a tidal turbine is divided into near and far regions (Myers and Bahaj, 2009) and is described as the region of slow moving fluid downstream of a turbine (highlighted in Figure 24a) due to the momentum drop across the rotor, the theory of which is described by the axial momentum actuator disk theory. A turbine’s wake is characterised by strong pressure/shear gradients and intense turbulent structures (Myers and Bahaj, 2009).

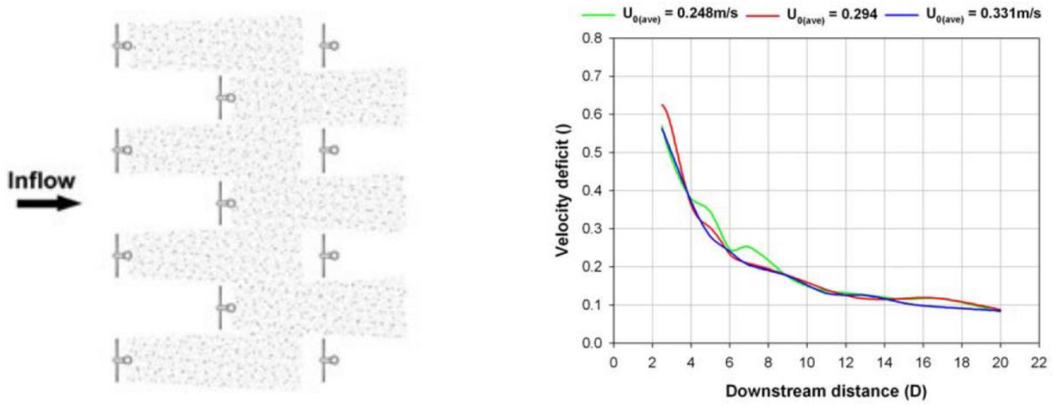

(a) (b)

**Figure 24 (a) Example of tidal array layout (wake highlighted) (Ingram et al., 2011) (b) Centreline velocity deficit downstream of a porous disk study (A. S. Bahaj et al., 2007)**

It is the far wake region that determines the inter turbine spacing, the length of which is described in terms of the number of diameters D of the turbine downstream (e.g. 10D) whereby the wake has reached an acceptable velocity deficit of the freestream flow, seen in Figure 24b. The velocity deficit $U_{def}$, is given by Equation (10) using the wake flow speed $U_w$.

$$U_{def} = {}^{U_W}/_{U_\infty} \tag{10}$$

Since the available freestream power is proportional to the cube of the freestream flow speed (see Equation (2)), placing a turbine directly downstream of another turbine would result in a large decrease in available power; since the wake recovers with increasing distance downstream there is an optimum point to place the next turbine to maximise both available power and array density, leading to larger yields for a specific site plan area. Wake recovery is achieved via the turbulent mixing mechanisms between the freestream flow either side of the wake and the flow through the turbine which acts to re-energise the wake through increasing its velocity (A. S. Bahaj et al., 2007; Nishino and Willden, 2012) Tidal array spacing has been studied for HATTs in both perpendicular and parallel directions to the freestream flow (Ahmadian and Falconer, 2012; Bahaj et al., 2011; A. S. Bahaj et al., 2007; Li et al., 2007; Mycek et al., 2013; Myers and Bahaj, 2005; Stallard et al., 2011). Bahaj et al., (2011) and Bahaj et al., (2007) concluded for a HATT that a downstream spacing in the range of 15-20D would provide a wake recovery, $U_{def}$ (compared to freestream conditions) of 85% and 92% respectively.

### 4.2.6.2 *Proposed tidal turbine arrays*

To the author's knowledge, globally there are no grid-connected commercial tidal arrays. With respect to deployment time the closest to a tidal turbine array is in the US, Ocean Renewable Power Company and their turbine TidGen (details of which can be found in Appendix A) have completed the first phase of three to deploy 18 turbines in the water around Eastport Maine, North America. The first phase consisted of the successful year long testing of one turbine (completed in July 2013), whereby the second phase aims to test a pair of devices by 2014, with the final phase comprising of 18 turbines (with consent yet to be granted) (Cox, 2013).

In the UK the Crown Estate (a property business owned by the Crown acting on behalf of the government) manages virtually the entire sea bed for up to a distance of 12 nautical miles from the UK coastline, essentially handing the Crown Estate total control over the leasing of potential tidal stream sites; the most promising of which can be seen in and Figure 13. In November 2008 the Crown Estate announced an invitation for projects from developers of tidal stream for the Pentland Firth strategic area. Subsequently by October 2012 it was announced that 1600 MW worth of leases had been granted, including five tidal stream projects and six wave energy projects. The largest of this was a 400 MW lease granted to MeyGen Ltd for an area known as the Inner Sound, located in the Pentland Firth (The Crown Estate, 2013). In November 2013, MeyGen Ltd was wholly acquired by Atlantis Resources Ltd. (Atlantis Resources Ltd, 2013b). This 400 MW was granted consent in September 2013 and becomes Europe's largest tidal turbine project and will utilise the AR1000 turbine developed by Atlantis Resources Corporation (further details can be found in Appendix A). The project will be installed in phases, with the first comprising of 9 MW, the second 86 MW and the final phase of 398 MW which consists of around 400 turbines. The first and second phases are forecasted to be operational by 2020 (BBC, 2013e).

Scottish Power Renewables announced in September 2013 that it had signed a Memorandum of Understanding for its Sound of Islay tidal array that would utilise both Alstom devices, Tidal Generation turbines and Andritz Hydro Hammerfest turbines, the HS1000 (see Appendix A for further details on the turbines). With a capacity of 10 MW, the full site deployment of the Sound of Islay tidal array is expected by 2016 ("Tidal device deal for Sound of Islay," 2013).

The Welsh government have also granted consent for the development of the Skerries tidal array off the coast of Anglesey, North Wales (Siemens UK, 2013). The Skerries tidal array is a 10 MW project consisting of five 2 MW turbines developed by Marine Current Turbines Ltd. The turbines will be a development of the SeaGen turbine, details of which can be found in Section 4.2.1 and Appendix A.

## 4.3 Tidal stream energy vs. Wind energy

Although analogies exist between wind and tidal turbines, there are distinct differences. In contrast to wind the power density of tidal stream energy is predictable and reliable. The stochastic nature of wind power generation can be seen from Figure 25.

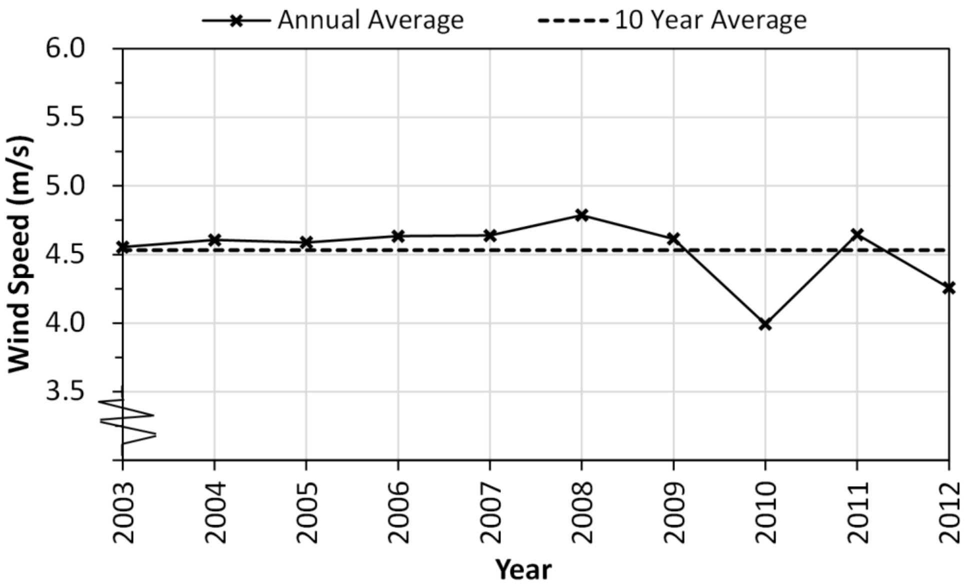

**Figure 25 Average wind speed for the UK from 2003-2012. Data source: Meteorological Office where regional wind speed data is aggregated according to wind electricity generating capacity**

Figure 25 illustrates the variation in the average UK wind speed for wind power generation over the last ten years and it is clear that the wind speed is inconsistent in each subsequent year. Since power is directly proportional to the cube of the flow speed, see Equation (1), the variation in the wind speed can be applied to the subsequent variation in the power generation. In the past three years alone the average wind speed has changed from 4.0 m/s in 2010, up to 4.6 m/s in 2011 and back down to 4.3 m/s in 2012. Comparing these variations against the 10 year average wind speed of 4.5 m/s proves the scholastic nature of wind, its unreliable nature means wind power generation cannot be used for base load electricity supply to the National Grid. In addition wind turbines are vulnerable to damage from high speed winds during storm conditions and require a cut-out speed to avoid damage, the predictability of the tidal cycle means this is unnecessary for tidal turbines.

Unlike wind the power available from tidal stream is capable of providing base load electricity supply to the grid (Clarke et al., 2006). Although at a single site the power output will vary considerably with the tidal cycle (both daily cycles and the spring-neap cycle), if the power output from numerous sites with out of phase tidal cycles were combined, this would eradicate the peaks and troughs of the power output from a single site. Clarke et al., (2006) showed that a near continuous base load supply could be supplied from combining the power output from tidal stream arrays at three Scottish coastal sites whilst also limiting the capacity of the turbines.

The predictability of tidal stream resource is a major enticement for research and development in its exploitation. Its predictability not only allows developers to predict potential outputs of devices according to the scale of a device and its sited location, but it also acts as a stimulus for investment in the field since financial gains can be confidently predicted in both the short and long term. From the consumer's point of view, power generation from the tidal stream resource reduces any uncertainty in energy security, which is a particular issue with fluctuating prices of fossil fuels but also the unpredictable nature of wind as a resource. The regularity of the peaks and troughs in power production from tidal stream allows energy companies to cater for variance in power supply through supplementing supply from other sources of renewables and/or from additional marine energy schemes, such as impoundment schemes. Due to the density of water -be it fresh or saline water-being 800 times larger than that of air (as seen in Table 4), the power density is thus orders of magnitude larger for an identical swept area and freestream velocity according to

Equation (2) and displayed in . The stated densities in Table 4 are for a nominal temperature of 20 $^{o}$C, air density is at sea level and the saline water density is that for a salinity of 35% (Hagerman et al., 2006).

**Table 4 Comparison of fluid densities.**

| Fluid | ρ (kg m$^{-3}$) |
|---|---:|
| Air | 1.225 |
| Saline water | 1025.000 |
| Fresh water | 997.000 |

However the targeted velocities for feasible wind power generation are larger than that for tidal stream, typical wind speeds reach up to 6 m/s whereas a typical tidal stream velocity for feasible power generation in the UK is around 2 m/s (MacKay, 2009). A wind flow speed of 6.0 m/s and a tidal stream flow speed of 2.0 m/s correspond to power densities of 0.13 kW/m$^2$ for wind and 4.1 kW/m$^2$ for tidal stream (an order of magnitude larger).

To illustrate the increased power density present in tidal stream compared to wind, the Enercon E-126 is currently the world's largest wind turbine with a blade diameter of 127m (de Vries, 2012), and using Equation (3) the size of an equivalent capacity tidal turbine would be:

$$P_{wind} = P_{tidal} \tag{11}$$

$$\frac{1}{2} C_p p_w A_w V_w^3 = \frac{1}{2} C_p p_t A_t V_t^3 \tag{12}$$

and assuming an equal efficiency for both the tidal and wind turbines and using the velocities from (MacKay, 2009), $V_w$=6.0 m/s and $V_t$=2.0 m/s, and the densities from Table 4, Equation (12):

$$\frac{A_w}{A_t} = \frac{\rho_t V_t^3}{\rho_w V_w^3} = 31 \tag{13}$$

An equivalent rated tidal turbine to the Enercon E-126 wind turbine with 127 m diameters blades would have a blade diameter of 22.8 m, 5.57 times smaller than that of the wind turbine.

Unlike the wind resource, the tidal stream resource is governed by both an upper and lower limit – the water's surface (wind's lower limit being the ground and tidal stream's being the seabed); restricting the available resource. In reality the upper limit of a tidal streams potential power capture area is significantly lower than the water surface, see Section 5.3. Additionally, a tidal stream turbine will be subjected to larger unwanted forces such as enhanced thrust force in comparison to a wind turbine (due to the increased density) leading to fatigue and structural integrity issues, further details in Section 6. However these issues are offset by the increased power density in tidal stream.

The Japanese firm Mitsui Ocean Development and Engineering Company, have designed a device to harness both the kinetic energy flux of wind and tidal currents. The device, SKWID – Savonius Keel and Wind Turbine Darrieus, seen in Figure 26, is a floating device which utilises a Savonius turbine to harness tidal currents and a Darrieus to harness the wind energy with a common generator. The Savonius provides not only additional power to the Darrieus but also acts as a start-up device for the Darrieus wind turbine (MODEC, 2013).

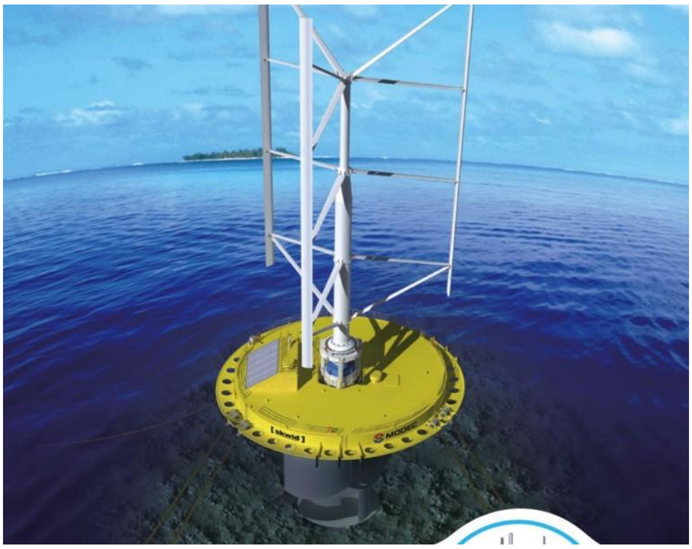

**Figure** 26 **Artist impression of a deployed SKWID device (MODEC, 2013)**

# 5 Site Identification and characterisation

**This chapter contains a summary of the key characteristics of a potential site for the harnessing of tidal stream energy: velocity, turbulence, hub-height restrictions and other factors such as shipping lanes, conservation sites etc. Finally this chapter includes a description of the European Marine Energy Centre (EMEC), a testing facility designed to enable tidal stream turbine developers to test prototypes up to full scale in a marine environment. . The standard IEC TS 62600-201 Tidal energy resource characterization and assessment (Legrand, 2009), currently accepted and under discussion by BSI, (2014), forms the basis of the velocity and turbulence sections.**

Characterising a site for the potential harnessing of tidal stream energy includes collecting data such as velocity distribution curves, a tidal ellipse, a flow shear profile etc. Throughout a whole site these attributes may not remain constant due to changes in the bathymetry and the spatial variations in the tidal flow across an entire site. The Tidal Resource Assessment (Black & Veatch Consulting Ltd, 2005) states that in order to accurately quantify the available kinetic energy flux at a particular site it requires detailed site measurements for a minimum period of a year, in conjunction with an accurate tidal stream resource model, due to:

- Flood and ebb tides are generally of different range, and the corresponding flow velocity will be of different strength;
- The first and second tidal cycles in a day also generally have different amplitudes;
- The local tidal flow pattern is not necessarily sinusoidal, but can be skewed and distorted;
- The amplitude of the 14-day spring-neap cycle varies continuously, peaking and troughing twice a year.

Other resource assessments (Bomminayuni et al., 2012; Gooch et al., 2009) suggest that detailed site measurement over a period of a month is sufficient in line with a tidal stream model. The European Marine Energy Centre, EMEC, in Orkney, Scotland is striving towards creating standards for the various aspects of power generation from a tidal stream turbine. Examples of studies on the characterisation of potentially exploitable tidal stream energy sites include, an assessment near Rose Due Island, Georgia, USA (Bomminayuni et al., 2012), an assessment of the Bristol Channel, UK (Croft et al., 2010) and an initial evaluation of the tidal stream energy resources at Portland Bill, UK (Blunden and Bahaj, 2006) and the Alderney Race, UK (Bahaj and Myers, 2004) to name a few. The following points are the primary considerations when locating sites for the deployment of tidal stream turbines: Velocity, turbulence, hub height restrictions and various additional factors.

## 5.1 Velocity

Since the available power at a specific location is the function of the velocity component cubed, see Equation (2), this can be considered to be the most important factor when choosing where to locate a tidal stream turbine. However due to the cubic law relating velocity to energy capture, a 0.05 m/s error in estimation in mean velocity can lead to errors of up to 6% in energy estimation (for rated velocities in the range of 1.5-2.5 m/s) (Black & Veatch Consulting Ltd, 2005), meaning accurate velocity data is vital for accurate power predictions. When characterising the velocity at a particular site both the mean and maximum flow speeds are quoted whereby the EMEC Tidal energy resource characterisation and assessment states that a flow speed can only be considered a maximum flow speed if the speed is sustained for a minimum of 10 minutes (Legrand, 2009), whilst other studies have used a period of five minutes (Gooch et al., 2009). The maximum flow speed is typically used for preliminary identification of sites. However it is also important when considering the loadings on the device. The mean flow speed is typically used in order to gain an approximation of the available power at a site through calculating the mean power density, W/m$^2$, using Equation (2). In the past, tidal diamonds obtained from admiralty charts (The United Kingdom Hydrographic Office, 1993) gave an indication of the flow speed and direction at discrete points and served as an initial parameter for identifying areas of potentially high power density; however they are based on too broad a spatial resolution to enable site specific energy capture calculations. Velocity distribution curves, typically over a period of one month (Batten et al., 2008) to incorporate numerous spring and neap tides, are used to display and quantify the available resource at a site, as seen in Figure 27, and are used to calculate the useful proportion of the tidal cycle available for power production from a particular tidal stream turbine, dependant on the cut-in speed and rated speed of the device, see Section 0.

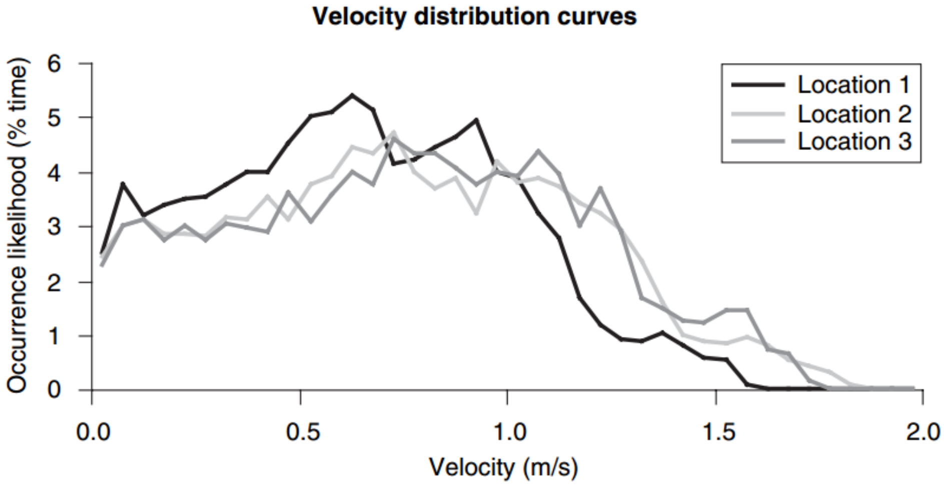

**Figure 27 Velocity Distribution curves for 3 different sites 1km apart from a 1 month harmonic analysis (Legrand, 2009)**

A time series tidal ellipse illustrates the changing direction of flow over a number of tidal cycles, as seen in Figure 28a. Tidal ellipses are an indicator of the bi-directionality of a tidal regime at a given site, whereby a perfectly bi-directional site would have an asymmetry of zero degrees. Figure 28a illustrates a tidal cycle with an asymmetry of around $10^o$. Tidal ellipses are particularly important for the non omni-directional tidal stream turbines, particularly HATTs. A significant variance in the direction of the tidal streams between low and high tide can dictate whether or not an HATT requires a yawing device; since the design of hydrofoils are sensitive to the incoming angle of the flow. Asymmetrical tidal streams can indicate complex geometry in the near region, increasing the variability of the tide which could lead to more costly “micrositing” measures in line with increasing complications for the deployment of a tidal array at a site (Gooch et al., 2009).

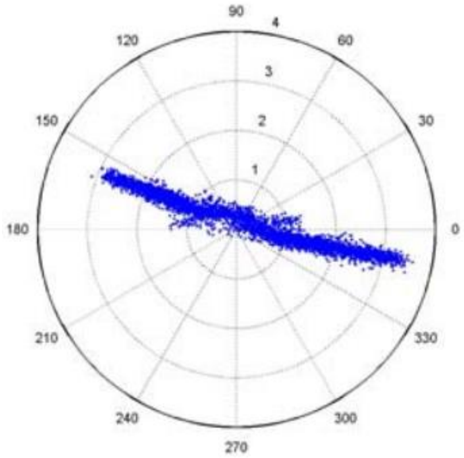

(a)

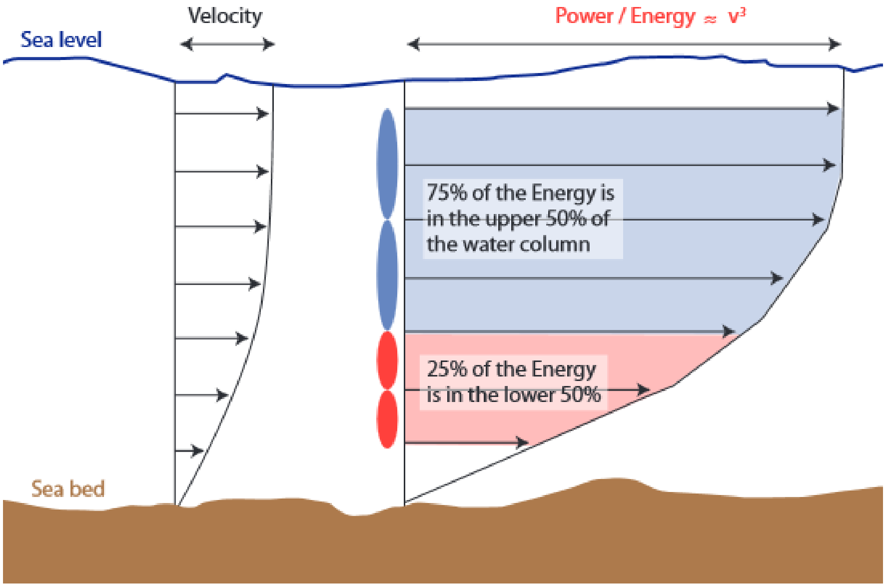

(a)

**Figure 28 (a) Example of a tidal ellipse from an EMEC test site (McCann et al., 2008) (b) Vertical power and velocity distribution in a water column (Fraenkel, 2011)**

Understanding the vertical variation in flow speed at a potential site (shear profile) is vital from a structural viewpoint, with regards to foundation design and supporting structure. It is also important from a mechanical viewpoint, with regards to the variation in axial forces acting on the turbine and for determining a desirable hub-height. Non uniform shear profiles are imparted on the flow due to the frictional effect of the bathymetry and the free surface. Previous studies (Legrand, 2009; McCann et al., 2008; Peterson and Hennessey, 1978) demonstrate the shear profile of a site can be approximated from a known surface velocity, using Equation (14).

$$U(z) = U_{\infty}\left(\frac{z}{d}\right)^{\frac{1}{\alpha}} \tag{14}$$

where $U(z)$ is the flow speed (m/s) as a function of depth $z$ (m), $U_{\infty}$ is the freestream flow speed (m/s), $d$ is the total depth (m) and $\alpha$ is an empirical constant (assumed to be 7). Various studies have experimented with values of $\alpha$ and conclude that it is site specific and is typically, 7 (Peterson and Hennessey, 1978), 10 (Legrand, 2009) or 5 (McCann et al., 2008). Figure 28b shows the power distribution with a non-uniform velocity profile, with 75% of the available power present in the upper 50% of the water column.

## 5.2 Turbulence

It is known from the study of wind turbines that turbulence poses a problem for both the operating efficiency ($C_p$) and causes material fatigue of a device which reduces its lifespan (Thomson et al., 2010). Turbulence is the fluctuating component of the flow speed $u'$, above or below the mean streamwise flow speed $\overline{U}_{\infty}$, and the instantaneous flow speed $U_{\infty}$ is

$$U_{\infty} = \overline{U}_{\infty} + u'_{\infty} \tag{15}$$

For site characterisation, turbulence is typically represented as the ratio of the fluctuating flow speed component to the mean flow speed, termed the turbulence intensity, $I$ (-,%) (Gaurier et al., 2013) where $u$, $v$ and $w$ represent the streamwise, spanwise and depthwise flow speed respectively.

$$I = \sqrt{\frac{u'^{2}_{\infty}}{\overline{U}^{2}_{\infty}}} = \sqrt{\frac{u'^{2} + v'^{2} + w'^{2}}{\overline{U}^{2} + \overline{V}^{2} + \overline{W}^{2}}} \tag{16}$$

Wind energy sites have levels of turbulence intensity in the range of $I$= 0.1 to 0.12 (Black & Veatch Consulting Ltd, 2005). An investigation into turbulent effects in Puget Sound, USA (Thomson et al., 2010) concluded that the levels of turbulence were of similar magnitude to that of wind energy sites, with $I$=0.1. Similarly characterising an

EMEC tidal site, McCann et al., (2008) found that turbulence intensity decreased with increasing flow speed. At slack water ($U_\infty$=0.818 m/s), $I$=0.177 whilst at peak flow ($U_\infty$=1.882 m/s) $I$=0.101; again of similar magnitude to that of wind energy sites. Turbulence levels cannot be estimated at a site, and must be measured using high frequency data recording equipment, since changes in the bathymetry can increase turbulence and therefore each site is unique. Norris and Droniou, (2007) defines a site as “turbulent” if a flow sample has a 1 m/s difference between the maximum and minimum readings within a centred 10 minute sample.

## 5.3 Hub Height restrictions

Since the resource is bounded by a lower (sea bed) and upper (water surface) there is a finite height in which to locate a tidal stream turbine, which in turn is site-dependant. The water depth at a site therefore dictates the maximum rotor height. Croft et al., (2010) conducted a case study for the deployment of a tidal stream turbine in the Bristol channel and state numerous factors which dictate the maximum rotor height in addition to the water depth. The Bristol Channel is a busy shipping lane, thus a minimum under-keel clearance between vessels and the proposed rotor was required. A minimum clearance depth of 11 m from the rotor to the sea surface has been suggested by the Chamber of Shipping. When discussing water depth attention must be paid to the depth at the point in time being discussed, i.e. at highest or lowest astronomical tide (HAT/LAT), wave peak/trough, storm surge level etc. Croft et al., (2010) used LAT as the chart datum level. The EMEC guideline for tidal resource assessment (Legrand, 2009) recommends that a minimum clearance of 5 m from the LAT be used to account for recreational activities and to minimise turbulence and wave loadings on the tidal stream turbines. The guideline also states that a clearance of 5 m or 25% of the water depth from the sea bed should be designed for to minimise turbulence and shear loading from the boundary layer.

## 5.4 Additional Factors

Additional factors to consider whilst analysing the available resource is the realistic availability of the resource with respect to its current usage, i.e. locations which satisfy the conditions required for tidal stream energy capture may coincide with busy shipping lanes, areas of high environmental interest or prime fishing locations to name a few. All factors contribute in potentially lowering the realistic available resource. Marine Scotland et al., (2012) provides guidance on such issues, with detailed studies of such considerations in the Pentland Firth, Scotland. Figure 29 illustrates the tidal stream resource available at the Pentland Firth Outer Sound, Scotland, and it can be seen that the site has tidal streams of up to 2 m/s, sufficient for potential economical energy extraction, whereas Figure 30 is identical to Figure 29 but with additional layers of data including shipping lanes (ranging from passenger ships to cargo ships), location of shipping vessels and conservation sites. It is clear from Figure 29 and Figure 30 that the high velocity tidal stream sites coincide with various other commercial activities; therefore potential deployment of tidal stream turbines at this site would have to provide a compromise for continued use by the various commercial industries, and continued protection of conservation zone whilst producing renewable electricity for Scotland.

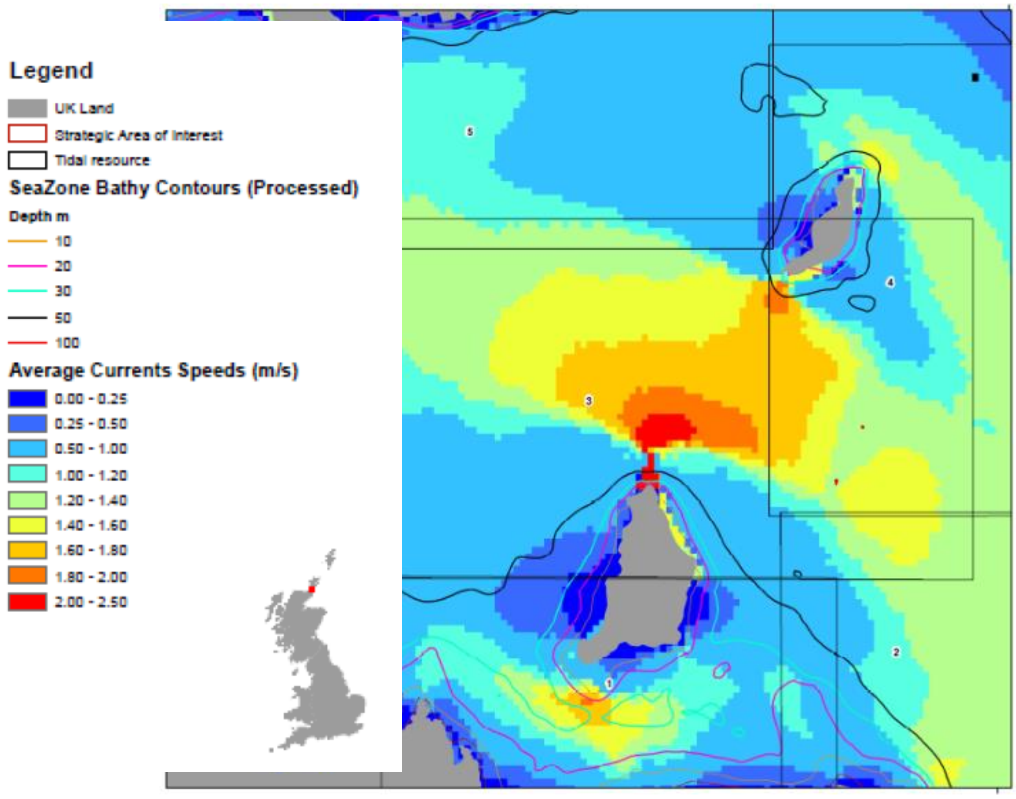

**Figure 29 Average flow speed at Pentland Firth Outer Sound, Scotland. Reproduced from (Marine Scotland et al., 2012).**

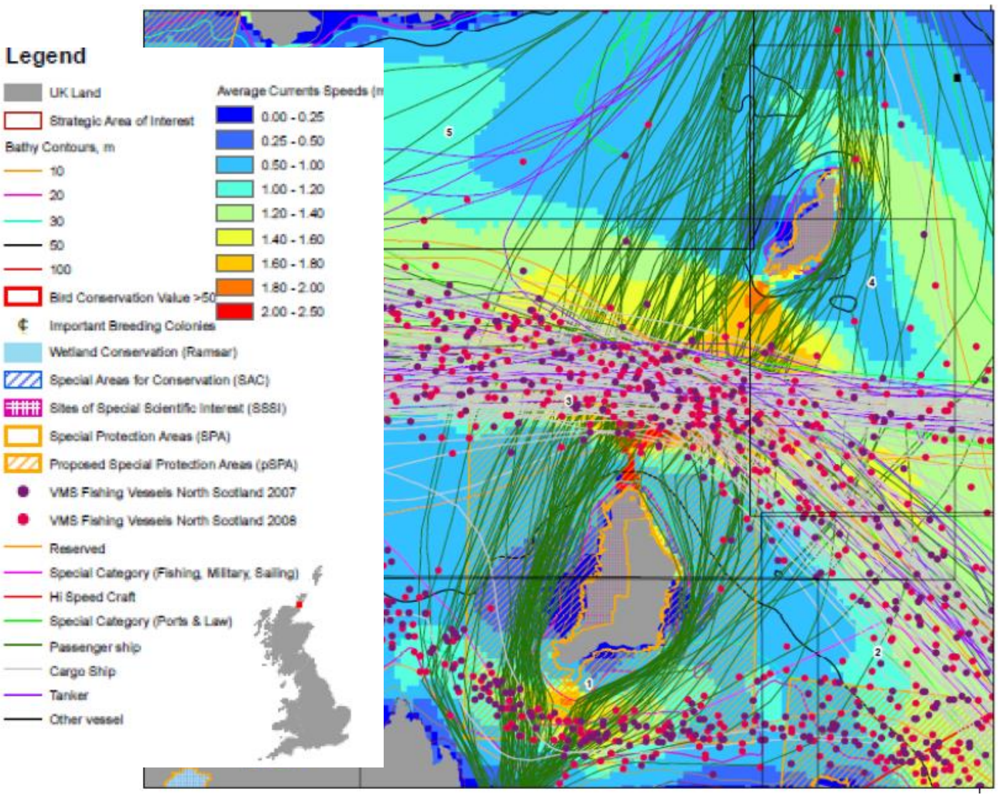

**Figure 30 Average current speed and local uses of the tidal stream resource at Pentland Firth Outer Sound, Scotland. Reproduced from (Marine Scotland et al., 2012).**

## 5.5 European Marine Energy Centre (EMEC)

Established in 2003 and situated in Orkney, Northern Scotland, EMEC is the world's first testing facility for wave and tidal energy devices in open sea conditions. EMEC currently houses 14 full scale test berths, 8 for tidal stream turbines and 6 for wave energy converters (EMEC, 2013c). EMEC was founded as a direct result of a recommendation of the House of Commons Science and Technology Committee in 2001 with the aim of accelerating the development of marine energy technology. Funding was acquired from a grouping of public sector organisations, to date funding has reached £30 million. In 2013 an £8m extension to a pier in off Kirkwall, Orkney meant EMEC had constructed Scotland's longest commercial deep-water berth (including installing a 1000 tonne crane), granting easier access to EMEC for marine energy developers (BBC, 2013f; EMEC, 2013d). Bryden and Norris, (2007) includes further details of the facilities available at EMEC.

### 5.5.1 EMEC Tidal Energy test site

The EMEC tidal energy test site is located in the Fall of Warness off the island of Eday, in the Orkneys, Northern Scotland as seen in Figure 31. Peak spring tides at the site reach 4 m/s and the tidal test site consists of an area 2 km wide and 4 km in length, with 7 test berths available ranging in depth from 12-50 m. There are 11 kV subsea cables (connected to a transformer supporting grid connection) present at each of the berths. In order to characterise the flow conditions at the test site there are several current meters in deployment with the ability to measure both the current speed and direction. EMEC has offices located in Stromness that are connected to the test site via a network of fibre optics, allowing real time data acquisition and analysis of individual devices, with areas dedicated to separate developers. As a result of DECC funding, a tidal test site for scaled tidal stream turbines was installed at EMEC in Shapinsay Sound, north-east of Kirkwall. This test site offers more benign conditions, with peak spring tides near 2 m/s with water depths of 21-25 m. See Appendix A for devices that have conducted testing at EMEC.

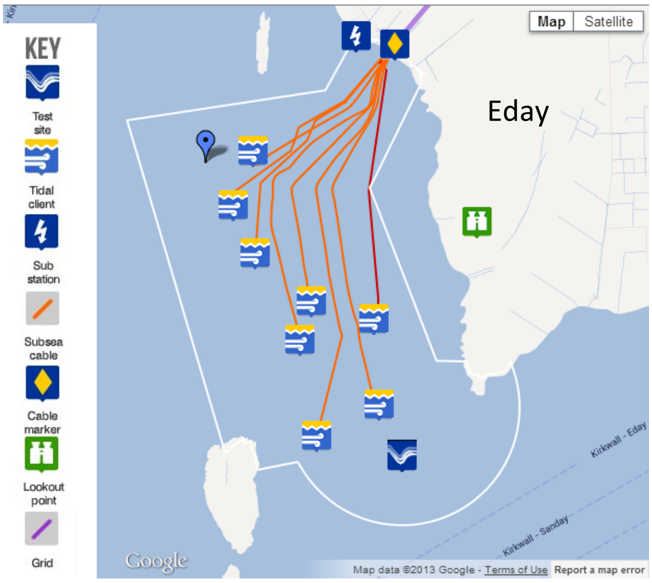

**Figure 31 EMEC's tidal stream turbine test site, adapted from (EMEC, 2013e)**

# 6 Structural Considerations

**This chapter describes the structural issues facing the developers of tidal stream turbines. Cavitation is an effect to be designed against for a turbine in a water environment alongside corrosion and biofouling. The choice of materials for a tidal stream turbine must be able to withstand the environmental conditions, withstand the turbine loadings, be a feasible cost and ideally have a low embodied $CO_2$/ high recyclable content. Dependant on the chosen material, be it typically steel or composite, issues can be caused by corrosion (for steel) and/or biofouling (since turbines are likely to be installed in the euphotic zone). This chapter describes the various methods used to mitigate corrosion for steel components, such as coatings, cathodic protection and galvanising and similarly antifouling coatings to mitigate biofouling.**

---

At time of writing there are no industry standards or codes directly applicable to the design of a tidal stream turbine, and indirectly applicable codes include the code for the design of offshore wind turbines (Det Norske Veritas, 2007). Germanischer Lloyd Renewables Certification (GL RC) provides certification for the integrity, safety, know-how to stakeholders and confidence to investors of marine energy converters; based on Argyriadis, (2008). The tidal stream turbine developers to obtain GL RC include: Tidal Generation Ltd, Voith Hydro Ocean Current Technologies and Kawasaki have applied (GL Renewables Certification, 2013). EMEC, funded by the Scottish Government and the Department for Business, Enterprise and Regulatory Reform, compiled 12 guides with the collaboration of academics, developers, utilities etc. to facilitate the development of marine energy converters, six of which are being put forward to the International Electrotechnical Commission for global adoption as industry standards (EMEC, 2013a). The guides describing structural design include Argyriadis, (2008); Davies, (2009) and Starling, (2009). Davies conducted a review of “the available certification schemes for wave and tidal stream renewable energy installations” for TATA Steel (Davies, 2012), using the numerous referenced certification schemes mentioned throughout this section.

## 6.1 Cavitation

An effect with damaging consequences, cavitation occurs when the local pressure falls below the vapour pressure of the water. It typically occurs due to a change of velocity (such as that in the vicinity of tidal turbine blades). This causes the entrained gas bubbles in the liquid to implode, with calculations suggesting the implosions create shockwaves in the region of 415 MPa (Roberge, 2013a). These implosions can have the effect of damaging surface films on a blade, such as anti-fouling and/or corrosion protection layers. Cavitation can be predicted by comparing the local pressure to the cavitation number $\sigma$, also known as the pressure coefficient, and is found by

$$\sigma = \frac{P_T - P_V}{0.5\rho V^2} \tag{17}$$

where $P_T$ is the local pressure around the blade, $P_V$ is the freestream pressure and $V$ is the reference velocity, typically at the blade tip (the local pressure will vary along the length of the blade) and is found using Equation (18).

$$V = \sqrt{(U_\infty^2 + \omega^2 R^2)} \tag{18}$$

Bahaj et al., (2007b) and Batten et al., (2008, 2006) have studied the potential onset of cavitation in laboratory testing of an HATT in a cavitation tunnel. Bahaj et al., (2007b) found that the onset of cavitation occurred at a cavitation number of 0.9, which relates to TSR values of above 7. When reduced to 0.4 there is cavitation along 10-15% of the blade. The higher the cavitation number the lower the risk of cavitation, and therefore from Equation (17) it can be seen that the cavitation number can be increased through lowering $V$ which as seen in Equation (18) is through lowering the TSR (the $\omega^2 R^2$ term) of the turbine. Therefore slowly rotating turbines, such as drag type turbines like CarBine and the Savonius turbine, are unlikely to encounter any cavitation issues.

## 6.2 Materials

Choosing the materials for the manufacturing of the components of a tidal stream turbine is based around several factors, as explained by Ocean Flow Energy Ltd managing director Graeme Mackie, who described to Reinforced Plastics their choice of materials for their Evopod device (further details of the device can be found in Appendix A) “We use composites on our machines where lightness, strength and corrosion resistance are prime requirements, which at present is mainly the rotors”. Further he explains, “Non-dynamic elements are in steel. One factor that has powerfully affected our material choice was the high galvanic corrosion we experienced with earlier trial steel structures placed in fast currents. This was more severe than we expected” (Marsh, 2009). An elaboration of said factors plus additional factors influencing the choice of materials to be used in the manufacturing of a tidal stream turbine can be found below.

### 6.2.1 Strength (Load bearing capacity, pressure variation & Fatigue)

The chosen material must be able to withstand the calculated main load conditions for the chosen device both on its blades and its structure, for an HATT this includes high levels of torque on the turbine blades which cause the rotation, Mx, bending moment due to the thrust, My, and yaw moments on the blades, Mz, (blade root bending moments), torsional and shear forces. A turbine blade is subjected to tensile forces on its upstream face and compression force on its downstream face. The harshness of the marine environment can be characterised by the range of unsteady dynamic loads that both the turbine’s blades and structure are subject to, including:

- **Variation in tidal flow speed and temporal distribution, see Section 5.1.**
- **Variation in tidal flow direction, see Section 5.1.**
- **Vertical shear profile of the flow, see Section 5.1.**

  During one revolution the blades of a turbine will experience a variation in the mean freestream velocity and therefore the magnitude of turbulent fluctuations. Consequently the velocity fluctuations on a turbine blade, for HATT or VATT, are larger than at a static section of the structure since the blades are travelling through multiple turbulent eddies in one revolution, resulting in unsteady loading on the blades (Milne et al., 2010).

- **Yaw Angle**

  The yaw angle is the misalignment of the turbine blades to the flow in the longitudinal direction. Milne et al., (2010) showed from numerical analysis that for a HATT, a yaw angle of up to $10^0$ proved insignificant in terms of fatigue and ultimate loading.

- **Turbulence**

  A numerical study by McCann, (2007) showed strong correlation between fatigue loading and levels of turbulence intensity based on the blade root bending moment, concluding that for levels of turbulence intensity >14% fatigue loading would dictate the blade root design. The importance of turbulence on turbine loading is further highlighted by numerical analysis conducted by Milne et al., (2010).

- **Additional loads from wave loading**

  Additional loading applies to tidal turbines located within the active wave base. The wave base is defined as half the wavelength of the wave in question, due to wave energy dissipating exponentially with depth. The extreme load case for wave action was set for a 50 year wave event equating to a significant wave height of 10 m in McCann, (2007), which resulted in a wave base of 5 m. Applying this load case to any location means any turbine with blade tips located beneath the upper 5m depth of water will be immune to wave loading.

- **Unsteady wake of support structure and turbine**

  The above factors subject the turbine to cyclic loading and unloading that can ultimately lead to fatigue failure method of a material. Davies, (2012) stipulates that fatigue design should be based on the appropriate S-N curves, but these will not be covered in this brief review. Fatigue loading is a focus of recent research (Davies et al., 2013; McCann, 2007; Milne et al., 2011) since in the past turbines have been over-designed by a factor of up to 30% to ensure durability, leading to excessive costs and additional weight (Marsh, 2009).

### 6.2.2 Weight (Inc. strength-weight ratio and stiffness-weight ratio)

Unlike wind turbines, the manufacturing of tidal turbines is concerned with both the dry weight and the submerged weight of the turbine. The dry weight of a turbine determines the transportation from dock to site as well as the installation methods to be used. Turbines such as SeaGen, weighing 1,000 tonnes, was transported dry and installed using a crane barge with a capacity of 3,300 tonnes, as seen in Figure 32a. Openhydro's 1 MW device, weighing 400 tonnes, was also transported dry and installed at EMEC using a uniquely commissioned heavy lift barge (costing $5 million), (Elphick, 2008), as seen in Figure 32b.

(a) (b)

**Figure 32 (a) Rambiz barge installing SeaGen (Marine Current Turbines Ltd., 2013b) (b) OpenHydro Installer barge at the Bay of Fundy (OpenHydro, 2013)**

Transportation and installation vehicles such as the heavy lift barges above have an extremely expensive daily rate which has led to many developers designing turbines with neutral buoyancy to enable the device to be towed to site and subsequently anchored using ballasting techniques.

(a) (b)

**Figure 33 Tidal Generation Ltd turbine Installation (a) Nacelle (b) Foundations (Alstom, 2013)**

Tidal Generation Ltd turbine tows its buoyant nacelle to the site using small boats (around 20 m long), as seen in Figure 33a, the turbine is then installed using a remotely operated vehicle (ROV) a winch and a patented clamping mechanism, negating the need for heavy lift barges; however the foundation would require a heavy lift crane barge, as seen in Figure 33b. This enables significant time saving and efficient maintenance. The use of composite materials such as carbon or glass fibre, provide a high strength-weight and stiffness-weight ratio in comparison to steel, enabling carbon fibre components to maintain the structural integrity of steel whilst being considerably lighter, as seen in Table 5. High stiffness is vital when utilising hydrofoils in the design of a tidal stream turbine since the blade deformation will alter the hydrodynamic properties of the blade and ultimately affect the power output of the turbine.

**Table 5 Mechanical properties of various materials, adapted from (Babu et al., 2006)**

| Material | Stiffness | Tensile strength | Density |
|---|---|---|---|
| | *GPa* | *MPa* | *g/cm³* |
| **Steel** | 30 | 190 | 7.5 |
| **Glass-fibre** | 73 | 3500 | 2.54 |
| **Carbon-fibre** | 350 | 4000 | 1.75 |

### 6.2.3 Durability

In order to produce competitive lifetime cost of electricity, the life expectancy of tidal stream turbines is expected to be around 20-25 years. To ensure such a prolonged period of time it is vital the materials used have taken into account fatigue loading, the effects of corrosion either using passive or active measures, as seen in Section 6.3 as well as marine growth/biofouling. Debris in the oceans will typically be floating or travelling along the seabed, and avoiding/designing for collisions will affect the durability of a tidal stream turbine. There is little that can be done for floating devices to avoid collisions (besides considerations in the structural design) with debris however for submerged tidal stream turbines the EMEC guideline (Davies, 2009) recommends avoiding the upper 5 m (from the LAT) and the lower 5 m or 25% (whichever is greatest) to minimise the risk of damage with collisions from debris. A study by Bibeau et al., (2009) on a 5 kW Darrieus style tidal stream turbine in the Winnipeg River, Canada discovered that the risk of collision from ice in the winter posed significant structural risk to the turbine, with blades being damaged and suffering losses in operational efficiencies as a result.

### 6.2.4 Cost

If the desired strength, weight and durability of a structure can be achieved by numerous materials, ultimately the cheaper material will succeed, since reducing manufacturing costs will result in cheaper cost of electricity. The manufacturing process of producing composites such as carbon fibre is slow and energy intensive leading to them being more expensive than steel (US Department of Energy, 2013).

### 6.2.5 Embodied $CO_2$ intensity

Although the embodied $CO_2$ intensity is unlikely to feature as the deciding factor in the choice of material, it is a significant factor nonetheless. Embodied $CO_2$ intensity refers to the $CO_2$ emissions expended in the creation of a construction material. The life cycle assessment of a structure is based on the embodied $CO_2$ of its various parts according to the principles of BS EN 15978. When referring to a renewable energy generator, such as a tidal stream turbine, although green energy is produced with no greenhouse gases emissions initially there will be a $CO_2$ outlay for the projects whole life-cycle, including construction materials, manufacturing, component transport, installation, maintenance, decommissioning and recycling (Douglas et al., 2008).

Douglas et al., (2008) studied the whole life cycle of the SeaGen turbine and concluded that large reductions in the $CO_2$ payback period can be performed through utilising materials with a high recyclable efficiency. The embodied $CO_2$ for the SeaGen turbine in the study was lowered by 26% as a result of the recycling credits. Through using data from wind farm studies, values of 90% and 100% can be applied to the recyclability of steel whereas plastic and composites go into landfill (Vestas, 2006). The breakdown of the materials used in the manufacturing of the SeaGen turbine from MCT can be seen in Figure 34.

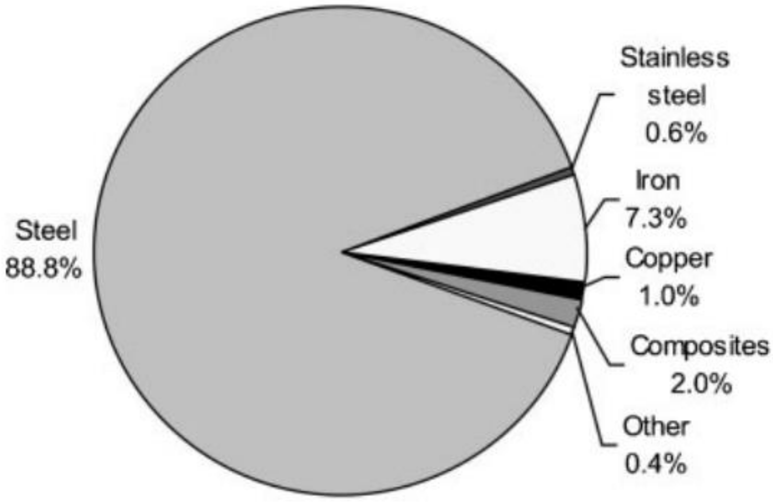

**Figure 34 Breakdown of SeaGen materials by mass (Douglas et al., 2008)**

Figure 34 shows that the dominant material used in the manufacturing of SeaGen was steel; this is primarily due to the 54.6 m tall surface penetrating monopole supporting SeaGen. Each rotor blade consisted of 800 kg of composite material. The composite material consists of glass fibre, foam and epoxy resin with some carbon fibre used in the blades. Steel is accountable for 68 % of the embodied $CO_2$ but is also responsible for 85% of the recycling credits. Although responsible for only 2% of the overall mass, composites account for 7.8% of the embodied $CO_2$. Therefore when comparing embodied $CO_2$ for different materials, particularly for steel and composites which are likely to compete for the main components of the turbine, it is steel that entails less embodied $CO_2$ since it can nearly all be recycled post decommissioning unlike composites which are sent to landfill.

### 6.2.6 Steel vs. Composites

The dominant material used in the manufacturing of tidal stream turbines is steel, as illustrated in the example in Figure 34. Steel is typically used for the support structure, nacelle and hub of turbines e.g. in the design of the 2 MW Tidalstream device which uses S355 structural steel plate, the nacelle and structure for the world's largest tidal stream turbine, the AK-1000 by Atlantis Resources Corporation and the gravity base structure of OpenHydro; whereas composite materials are used for the manufacturing of the blades. Steel was originally tried as a blade material however composites such as glass fibre and carbon fibre, with their lower rotational inertia due to their reduced weight in comparison to steel, enabled quicker speed up (lift turbines typically rotate at TSRs >6 for wind and TSRs >3 for tidal stream) and enhanced self-starting ability which was vital for wind turbines aiming to capitalise on gusts of wind. Composite blades also have a higher fatigue level than steel (Babu et al., 2006). This design principle has seen been applied to tidal stream turbines. However for high torque drag force dominant turbines, such as the Savonius (see Sections 4.2.2.3 and 8 for more details), quick speed up is not an issue since they typically rotate at a TSR ≤1 and inherently possess self-starting ability. The hydrofoil blades of both the SeaGen and Tidal Generation ltd turbines were manufactured by Aviation Enterprises Ltd, and comprised of a hollow carbon fibre composite box spar as the main load bearing member, along with carbon ribs and a glass fibre composite envelope bonded to this skeleton; with an epoxy resin used throughout (Aviation Enterprises Ltd., 2013). Blades for the AR-1000 turbine were manufactured from glass reinforced plastic (Atlantis Resources Corporation, 2013). The detailed manufacturing of the blades from composites and the difference in material properties between glass and carbon fibre composites can be found in McEwen et al., (2012) and Mohan, (2008). Structural performance is achieved using a composite via the long fibres ensuring longitudinal stiffness and strength whilst the resin is responsible for improved fatigue performance, particularly responsible for fracture toughness, delamination strength and out of plane strength and stiffness of the composite as well as resistance to hydrolytic attack (Mishnaevsky Jr, 2012).

**Table 6 Comparison of the properties of Steel and Composites**

| Properties | Steel | Composites |
|---|---|---|
| High Strength | X | X |
| Low Weight | | X |
| High Durability | X* | X |
| Low Cost | X | |
| Low Embodied $CO_2$ | X | |

***If applied with anti-corrosion protection**

There are known examples of structural failure during full scale testing of tidal stream turbines, all of which are HATTs. On the 18th July 2008 in the Strangford Loch, Northern Ireland, two of the blades on one of SeaGen's 600 kW rotors were damaged, MCT attributes the failure to a computer fault in the control system and state this fault can only occur during the commissioning phase and had no adverse effects on the environment or wildlife (Sea Generation Ltd., 2008).  In June 2010 in the Bay of Fundy, Canada the 400 tonne OpenHydro turbine had to be withdrawn as two of the blades had broken, as detected by an underwater camera.  Upon retrieval it was discovered that all 12 blades had broken off the turbine (Boslet, 2010; Energy for Students, 2012).

## 6.3 Corrosion

An inherent issue with deploying a structure in the marine environment is corrosion which can cause severe problems to the durability and integrity of a steel structure. Corrosion reduces the thickness of a metal which in turn reduces the mechanical strength of the structure, impacting its structural safety and its performance.  Used on a tidal stream turbine, corroded metal will lead to a reduced operational life and/or costly maintenance unless anti-corrosion techniques are applied, whether it be active or passive.  Nowadays the learning curve and expertise of offshore industries such as shipping, oil and gas exploration and offshore wind development means the risk of corrosion can be mitigated via corrosion protection.  Corrosion design guidance specifically for tidal stream turbines can be found in Davies, (2009) in addition to the "Corrosion Protection" report by the Health & Safety Executive, (2002) and the British Standard for guidance on corrosion in a marine environment (British Standard, 2012). GL RC's guidelines for marine energy converters state the need for corrosion design but provide no guidance (Argyriadis, 2008).

### 6.3.1 Process

An electrochemical process, corrosion requires the simultaneous presence of water and oxygen.  The process involves the surface of the material acting as both an anode and a cathode.  Firstly iron becomes oxidised in the presence of water with the iron acting as an anode.  The ferrous ions released as a result of the oxidisation travel through the metal to a location where the surface of the material is in contact with oxygen (in the form of dissolved oxygen) and water; resulting in a cathodic reaction. This reaction takes place on the surface of the metal reducing the oxygen to produce hydroxide ions.  The hydroxide ions from the cathode and ferrous ions from the anode then react resulting in ferrous hydroxide.  Which when further oxidised produces hydrated ferric oxide, red rust (Fullick and Fullick, 2000; TATA Steel et al., 2013a). During the process, water acts as the electrolyte, a solution containing ions, which facilitates the conduction of electricity. Pure water is a weak electrolyte, a poor conductor, as it contains a small amount of ions whereas saline water which is roughly 4% common salt is a strong conductor. As a result, metal corrodes at a faster rate in saline water but this rate is affected by the chloride content and temperature of the water (Roberge, 2013b). In addition to salinity, corrosion rates are also affected by immersion depth, steel composition and pH levels (Ting et al., 2011). The chemical equation for the corrosion of iron can be seen below

$$Fe + 3O_2 + 2H_2O = 2Fe_2O_3H_2O \tag{19}$$

$$Steel + Oxygen + Water = Hydrated\ Ferric\ Oxide\ (rust) \tag{20}$$

Initially the corrosion rate (current flow) is at its greatest then the rate decreases with time. After a period of time polarisation occurs which is the depletion of oxygen molecules in the electrolyte immediately adjacent to the cathode surface which stifles the corrosion process as well as the formation of a film on the surface of the metal; resulting in a uniform loss of metal across the entire material, namely general corrosion. However new reactive anodic regions can also be formed, reigniting the corrosion process. When the corrosion of a region is not stifled and continues to ingress into the material, this is called pitting corrosion. Pitting corrosion occurs when the material is subjected to continually wet conditions, leading to it being a major structural consideration when designing tidal stream turbines. Galvanic corrosion occurs when two dissimilar metals are in contact either physically or electrically (via an electrolyte such as seawater). The anode and cathode members are distinguished by their relative positions in the galvanic series (which measures their electrical potential). The difference in the electrical potentials of the dissimilar metals causes a flow of electrons between the two which accelerates the corrosion of the anode member. Galvanic corrosion is the basis of cathodic protection, further details in section 6.3.3.

### 6.3.2 Erosion-Corrosion

Besides being immersed in a strong electrolyte, tidal stream turbines with parts manufactured from metals will also suffer from different erosion- corrosion rates due to the water flow speed. A study by Efird, (1977) showed that corrosion rates in copper base alloys can be increased in the presence of moving water as they are susceptible to a critical surface shear stress. At a critical flow speed, the protective surface film on the material degrades resulting in accelerated corrosion rates. The critical flow speed varies dependant on the material as seen in Figure 33. Erosion rates of materials are increased due to localised turbulence caused by the increased roughness of the material due to corrosion, further exaggerated by pitting. The increased turbulence can also be caused by the surface degradation of the metal caused by cavitation, see Section 6.1.

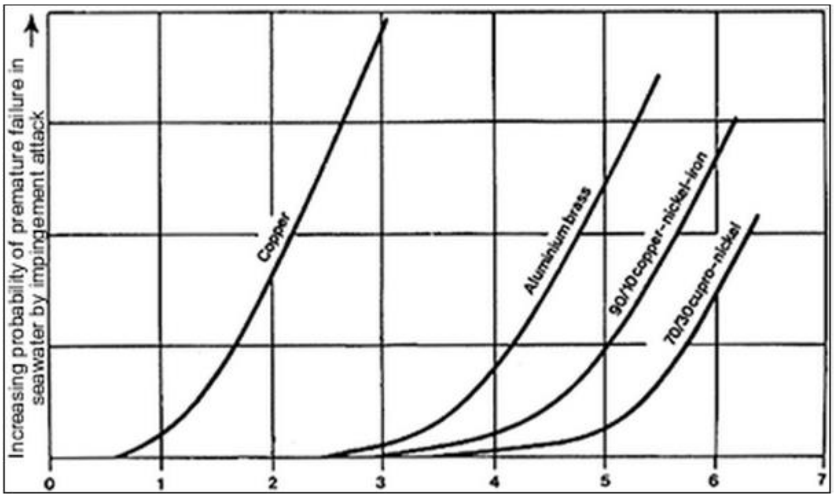

**Figure 35 Erosion corrosion rate (impingement) vs. Flow speed in seawater for various copper alloys (Gilbert, 1978)**

Corrosion allowance/over engineering is a passive technique that entails designing the corrosion prone component to be thicker than necessary for load bearing, i.e. providing a sacrificial thickness to the component. When a corrosion allowance is designed in collaboration with a coating, 6mm is added to the wall thickness to cover a coating with an operating life of 20 years (Det Norske Veritas, 2007). Corrosion allowance will however add additional weight to the structure and could therefore affect stability issues (for floating devices) as well as altering installation and maintenance procedures. Regular inspections must be carried out to confirm the corrosion rates used in the design process.

### 6.3.3 Corrosion Mitigation Techniques

Metals can be designed for corrosion either passively by corrosion allowance or actively by coatings, cathodic protection or galvanising.

#### *6.3.3.1 Coatings*

Involves coating the metal with a protective layer to inhibit exposure to water and oxygen. However any abrasion or scratch that exposes the metal beneath will lead to corrosion. Coatings for the marine environment are typically epoxy based paint systems comprising of numerous layers and should have good abrasion and ultraviolet resistance. Paints consist of:

- Pigment-Solid particles;
- Binder-Oil or resin which provides cohesion and a protective film;
- Solvent-Dissolves the binder, reducing its viscosity, providing easier application.

According to Davies, (2009) painted coatings tend to have a design life of between 5-10 years, compared to the expected life period of a turbine of 20 years coatings will therefore need to be reapplied.

(a)

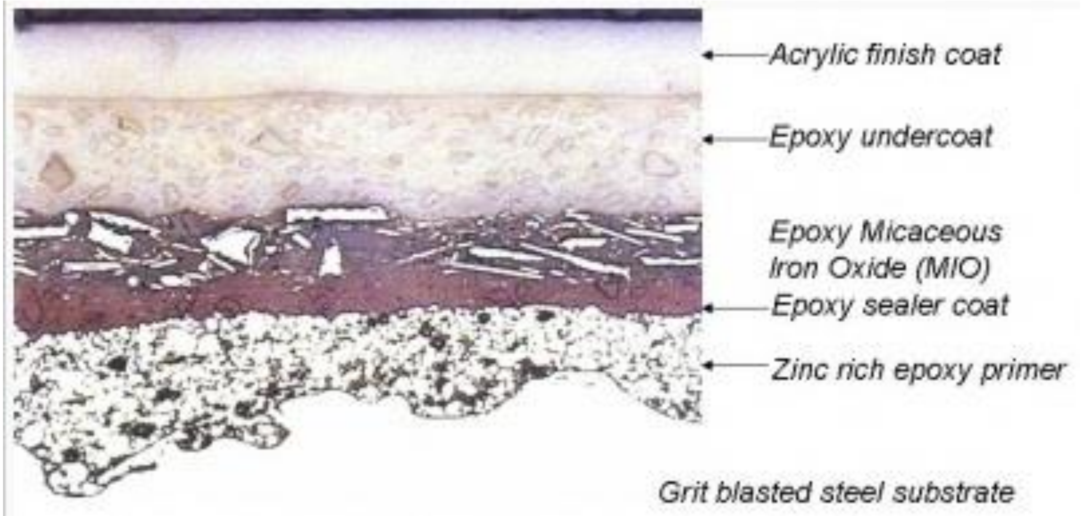

**(b)**

**Figure 36 (a) schematic of paint coating layers (b) example of paint coating layers; adapted from (TATA Steel et al., 2013b)**

Figure 36 shows anti-corrosion coating consists of several layers; a primer, intermediate layers and a finish coat, each with a specific function. The prime layer provides both corrosion inhibition for metals and an adhesive layer for subsequent coats. Prime layers are typically zinc-rich polymers which act as cathodic protection if the coating is damaged and the steel is revealed. The intermediate layer mainly provides the thickness for the coating with a thicker coating roughly equating to a longer life. High levels of pigmentation within an intermediate layer can reduce the permeability of the layer to oxygen and water which reduces the coatings' susceptibility to corrosion. The finish coat provides the aesthetical finish as well as the first defence against weather and sunlight. The preparation of the steel and the application process, such as steel and ambient temperature and humidity are important in achieving the desired performance from the coating (TATA Steel et al., 2013c). Paint application methods and the pre-treatment of the steel will not be covered in this review, but details can be found in TATA Steel et al., (2013d). The standard for coatings, surface inspection, application and inspection for offshore structures is the NORSOK M-501 (NORSOK standard, 1997).

#### *6.3.3.2 Cathodic Protection*

The cathodic protection technique works by placing the metal to be protected in contact with a material that oxidises more readily, such as zinc, aluminium or magnesium. The process uses the principles of galvanic corrosion; causing the iron to act as a cathode instead of anode resulting in the sacrificed material such as zinc corroding instead of the iron. The sacrificial anode, in this example zinc, will need to be replaced regularly when general corrosion occurs. Davies, (2009) states that Cathodic protection should only be used for fully submerged zones and should be designed for a period commensurate of the design life of the turbine or for periods between dry-docking maintenance. The 54.6 m tall monopole used to support the SeaGen turbine was partially aluminium cathode protected (Douglas et al., 2008). The use of cathodic protection on the OpenHydro turbine can be seen highlighted in Figure 37. An in situ experiment (Polagye and Thomson, 2010) of the corrosive potential of various tidal stream turbine materials was conducted at a possible turbine deployment site, Puget Sound in Washington. The results showed that structural steel, with sacrificial nodes, suffered reduced (but not eliminated) surface oxidation after three months in comparison to that of unprotected structural steel.

**Figure 37 OpenHydro support structure with sacrificial anodes (circled) (Snohomish County Public Utility District, 2012)**

#### *6.3.3.3 Galvanising*

Galvanising is essentially a combination of a coating and cathodic protection. Galvanised steel is typically covered with a layer of zinc, which protects the steel from exposure to water and oxygen but if the protective layer is scratched, cathodic protection ensures that the zinc will corrode and not the iron since it oxidises first. To galvanise steel the component is dipped in a bath of molten zinc, the coating is durable, tough, abrasion resistant and provides cathodic protection, the average coating thickness is 85 µm (TATA Steel et al., 2013c). There are limitations to the size of components that can be hot dip galvanised.

#### *6.3.3.4 Stainless Steel*

Unlike carbon steel, stainless steel is a less readily corrosive metal. For marine application, the 316 stainless steel grade is recommended since it contains molybdenum which provides higher resistance to pitting corrosion in a chloride environment (such as seawater). Despite its corrosion resistance properties, stainless steel can cost up to 5 times more than carbon steel[3] (MEPS (International) Ltd, 2014).

#### *6.3.3.5 Summary*

The type of corrosion protection required will dependent on the zone(/s) in which the tidal stream turbine is situated:

- Atmospheric zone-coatings;
- Splash zone-either corrosion allowance or coatings or both. Cathodic protection is redundant in this zone due to lack of continuous contact with the electrolyte (seawater);
- Inter-tidal zone-no details provided but can be assumed to be identical to splash zone;
- Submerged zone-external structure via cathodic protection, internal structure via cathodic protection, coatings or corrosion allowance (or a combination);
- Buried zone-no details provided (not a concern for gravity base and floating systems) (Health & Safety Executive, 2002).

---

[3] based on a price comparison of hot rolled steel plates, using April 2014 prices

Since the majority of tidal stream turbines are fully submerged (gravity base) or floating, it is the splash and submerged zones which are of interest. Health & Safety Executive, (2002) describes the splash zone as part of the structure between the level of the 50-year (average) wave superimposed on the highest astronomical tide and 3 metres below the lowest astronomical tide. Tidal stream devices will also be subjected to different zones at different periods of their life cycle, as seen in Table 7. Table 7 shows that for a floating system it satisfies both the splash zone and the submerged criteria, resulting in potentially two difference corrosion prevention techniques on a common component.

**Table 7 Corrosion zones experienced by gravity based and floating tidal stream turbines**

| Life-cycle | Floating System | Gravity system |
|---|---|---|
| ***Manufacturing*** | Atmospheric | Atmospheric |
| ***Transportation*** | Submerged & Splash | Atmospheric |
| ***Installation*** | Submerged & Splash | Splash |
| ***Operating*** | Submerged & Splash | Submerged |

***Note: Maintenance and decommissioning assumed the same as transportation and installation***

Figure 38 shows that the rate of corrosion various markedly with depth relative to the mean low and high tide. The highest rate of corrosion is found in the splash zone due to continuous contact with highly aerated sea water and the abrasive effects of spray, sea waves and tidal action. Corrosion rates of 0.9 and 1.4 mm/yr have been reported at Cook Inlet, Alaska and in the Gulf of Mexico, respectively (Powell and Michels, 2006). In the submerged zone the rate of corrosion decays with increasing depth. This is proportional to the decay in oxygen levels as depth increases. The maximum corrosion rate in the submerged zone is found just below the surface and is due to high levels of aeration from tidal action.

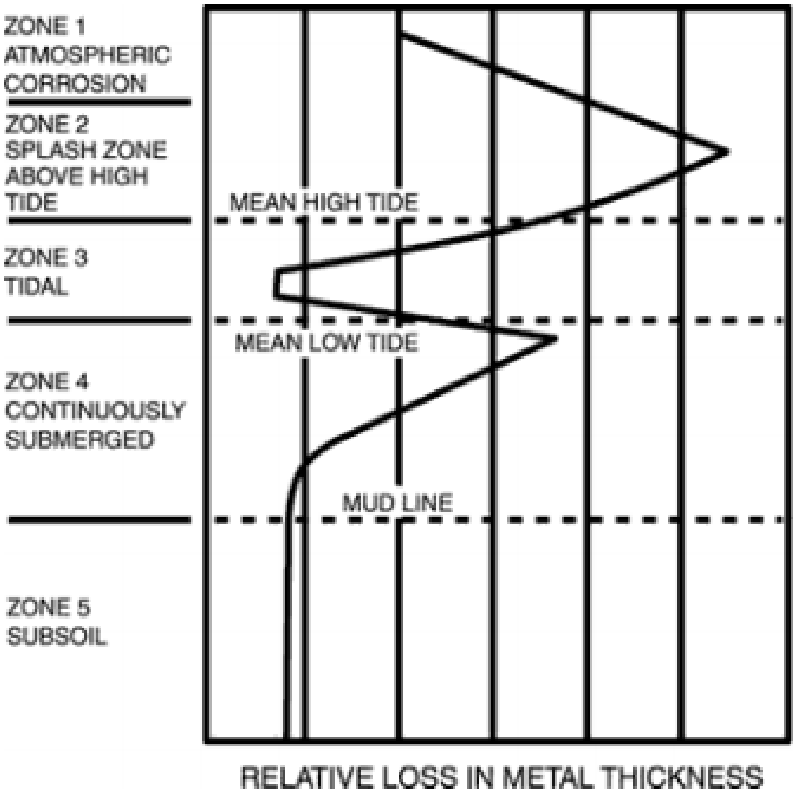

**Figure 38 Profile of the Thickness Loss Resulting from Corrosion of an Unprotected Steel Structure in Seawater (Powell and Michels, 2006)**

## 6.4 Biofouling

Immersed components of a tidal stream turbine are susceptible to biofouling; the presence of marine communities, such as barnacles and weeds growing on operational components of the turbine. Tidal stream turbines consist of both static (structure) and dynamic (blades) components, each prone to attack from different organisms. Barnacles are known to adhere to propellers and once adhered, they are known to resist rotational movement. Most weeds will fall off moving objects quickly, but some species such as the Brown weed can withstand high flow speeds. Slime, a conglomerate of algae, forms an ideal layer for further algae growth and is typically found on stationary objects (“Boat Painting Guide,” 1997, “OECD Marine Fouling Catalogue,” 1965; Orme et al., 2001). Figure 39a below illustrates biofouling on the submerged zone of the ScotRenwables turbine, SR250 whilst installed at the EMEC test facility. Whilst Figure 39b shows the growth of barnacles and other marine life on the supporting structure of the TidGen turbine deployed in Eastport, Maine in North America.


(a) (b)

**Figure 39 Biofouling on the (a) SR250 turbine (Scotrenewables, 2013) (b) Clean Current turbine (Clean Current, 2007)**

The photic zone is the layer of the ocean that receives sunlight, the upper 80m of which is termed the euphotic zone, which receives sufficient illumination for photosynthesis to occur. It is within this region that 90% of marine life is present (Encyclopedia Britannica, 2013). Since tidal turbines are expected to be deployed in similar depths, biofouling of the turbine is a design issue.

**Table 8 Marine growth depth profile, adapted from (Det Norske Veritas, 2007)**

| Depth below mean water line /m | Marine growth thickness per exposed surface /mm |
|---|---|
| 0-10 | 50 |
| 10-20 | 45 |
| 20-25 | 65 |
| 25-35 | 90 |
| >35 | 80 |

Biological factors such as temperature, salinity, oxygen content, pH value, flow speed and seasonal variations will affect the variety of species and growth rate at a particular site. The majority of these factors vary with depth, Table 8 shows the change in marine growth with increasing depth. The greatest thickness of marine growth is found at a depth of 25-35 m which is a prime location for a tidal stream turbine. Biofouling is therefore of prime concern to developers.

Biofouling on performance sensitive blades, particularly hydrofoils (see Section 4.1), can drastically effect the hydrodynamic properties of the blades and hence its efficiency. The growth of marine communities on blades will introduce large drag forces, a problem which has been recorded in the shipping industry since the first century AD (Vance, 2013). Orme et al., (2001) investigated the effect on lift and drag of an aerofoil (with a section similar to that used on MCT's SeaGen) subjected to various degrees of biofouling, with marine communities simulated via small conical shapes extruded on the test blade to mimic barnacles. The testing revealed that the drag coefficient of the blade increases with increasing barnacle size and the lift coefficient is reduced with the presence of barnacles, regardless of size. The presence of barnacles reduces the lift to drag ratio by a factor of six. Marine growth on a floating turbine leads to an increase in mass; this will alter the hydrodynamic stability of such a device. Batten et al., (2008) approximated the effect of biofouling on the performance of a turbine using hydrofoils through increasing the section drag coefficient by up to 50%. Results show that for an increase drag coefficient of 50%, the $C_p$ does not vary for TSRs ≤4 but at higher TSRs the peak $C_p$ decreases by 6-8%.

Antifouling coatings can be applied to offshore structures to inhibit the growth of marine communities. There are typically two varieties of anti-fouling coatings:

- ✓ **Leaching mechanism,** where a hydrophilic coating releases biocides, this prevents the settlement of organisms on a material for the duration of the scheme life (International Marine, 2013a).
- ✓ **Foul release mechanism** is where a biocide-free hydrophobic coating, relying on a smooth low friction surface, is applied to which organisms have difficulty attaching. If organisms manage to attach, the connection is normally so weak that a modest flow speed or component movement (such as a rotating blade) would release the organism (International Marine, 2013b)

An in situ experiment on the potential of biofouling of various tidal stream turbine materials was conducted at a possible turbine deployment site, Puget Sound in Washington (Polagye and Thomson, 2010). The testing concluded that composite materials such as Glass fibre and Carbon fibre experienced minimal biofouling during a

10 month test period (which is a limited time period in comparison to a 20 year life expectancy of a turbine) with and without an antifouling coating (a variety of which were tested). The study also showed that biofouling is more dominant on rougher surfaces (which can be caused by corrosion), edges or within crevices. Population of a rough area, edge or crevice from biofouling causes shaded areas for further growth and hence spreading across an entire material can follow. Therefore minimising the risk of biofouling prior to the use of coatings can be achieved via reducing the number of sharp edges and crevices and providing corrosion resistance. Plymouth Marine Laboratory (PML) are collaborating with tidal stream turbine developers, such as DCNS (OpenHydro) and Alstom, with long term in-situ testing at EMEC of the various anti-fouling coating systems available (Vance, 2013).

**In conclusion, the choice of material and anti-corrosion technique is a balance between the CapEx and OpEx. The research suggests that to minimise OpEx then a light structure should be used, i.e. constructed of composites, which will enable lower capacity vessels to be used with higher availability and lower costs than specialist offshore installation vessels, such as the Rambiz (see** Figure 32**a), thus reducing the OpEx. Despite the use of composites increasing the CapEx, it would avoid the problem of corrosion, therefore increasing the expected lifetime and reducing the risk of future maintenance due to excessive corrosion. The advantage of reduced maintenance, and thus OpEx, should outweigh the initial higher CapEx incurred through using composites. Although manufacturing the entire turbine out of composites may be excessive, since large structural elements could use ordinary steel with adequate corrosion protection this will reduce cost but add ballast weight since a structure manufactured entirely of composites could be buoyant. For a bed mounted design, a buoyant/semi-buoyant structure would require ballasting. It is unlikely a large proportion of stainless steel would be utilised in the construction of a turbine since its high cost compared to ordinary steel (see section 6.3.3.4) makes it comparable to that of the cost of composites but without the benefit of reduced weight. The use of stainless steel is likely to be restricted to that of smaller components such as bearings.**

# 7 “CarBine”

**This chapter contains a detailed description of CarBine-a novel drag type tidal stream turbine, its working principles and a list of potential advantages. A theoretical estimation of a drag type wind turbine of this type by Manwell estimates the $C_p$max/λ=0.08/0.33 (Manwell et al., 2009). A review of the preliminary studies of CarBine has been conducted, which predominantly consist of proof of concept testing. Comparing the current development of CarBine to various industry standards, for stages of development of a tidal stream turbine, leads to CarBine requiring both dynamic physical testing and numerical modelling to be conducted. The closest competing technology to CarBine discovered is the Hunter Turbine, developed at Queen Mary University, London.**

## 7.1 Description

CarBine, a combination of “Cardiff” and “turbine”, was devised on the basis of utilising the enhanced potential drag force (see Equation (8)) present in water in comparison to wind (due to the greater density of water, see Table 4), in the form of a VATT; contrary to the market leading HATTs and certain VATTs (such as the Darrieus) that are harnessing lift force. CarBine consists of a series of flat rectangular panels which are either closed or open, see Figure 40.

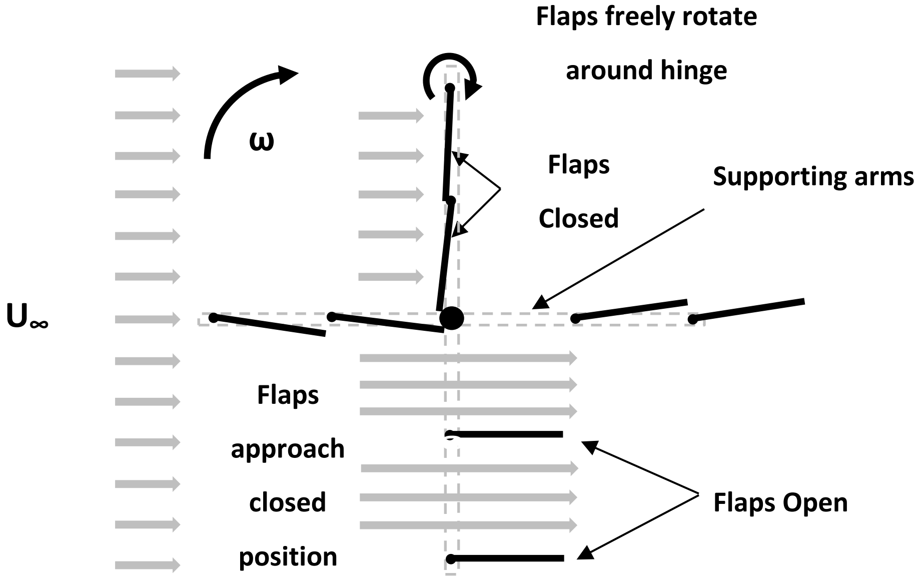

Figure 40 CarBine schematic (example of a 4 Arm configuration-90$^o$ phase)

When closed i.e. on one half of revolution, the flaps act as bluff bodies generating form drag in the direction of the flow (positive moment), see Figure 41a, whereby when open i.e. the flaps are parallel to the flow and act as streamlined bodies generating minimal frictional drag force (negative moment), see Figure 41b, and no form drag. Figure 42 also displays an estimation of a transition zone, where the closed flaps begin to open and rotate to the open position. The net result is a rotary motion in the positive direction, as seen in Figure 42.

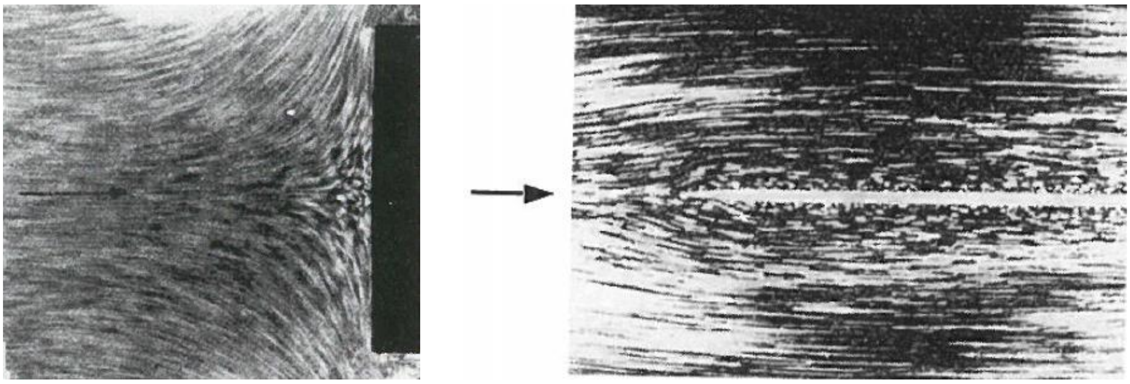
(a) (b)

**Note: Aluminium particles have been sprinkled on the surface of the water to make the streamlines visible. The length of each particle streak is proportional to the flow speed.**

**Figure 41 Snapshot of flow (a) Flat plate orthogonal to flow (b) Flat plate at zero incidence (Prandtl and Tietjens, 1931)**

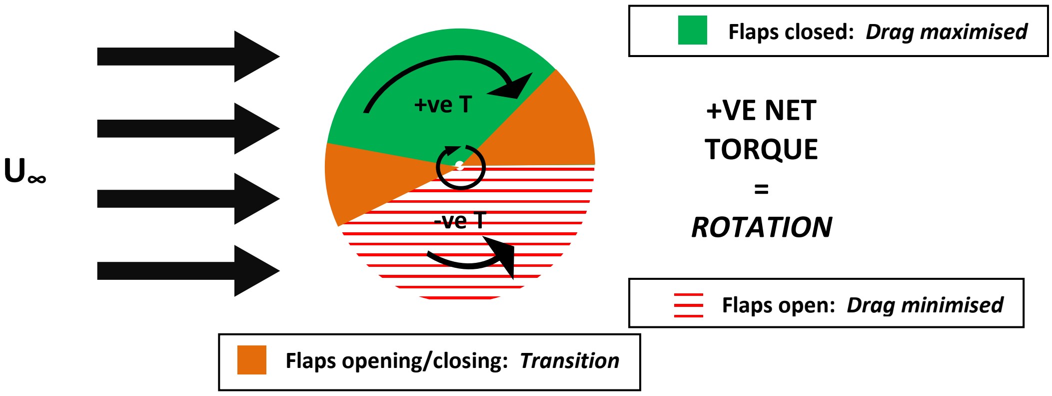

**Figure 42 Principles of CarBine**

Arguably a derivation of the Savonius turbine principles, see Section 8, whereby the Savonius is based on a larger drag coefficient for the generating side (concave) than the non-generating side (convex) to produce an average net positive torque, CarBine is designed with the aim of maximising the net positive torque through focusing on reducing the negative torque arising from the non-generating side. CarBine’s unique feature, similar to the slatted blade approach (see Section 8.4.1), is to allow the flaps on the non-generating side to open; reducing their negative drag since they are allowed to align with the flow. Permitting flow to travel unopposed through one half of CarBine produces the possibility of increased array densities in comparison to that of HATTs, as seen in Figure 43.

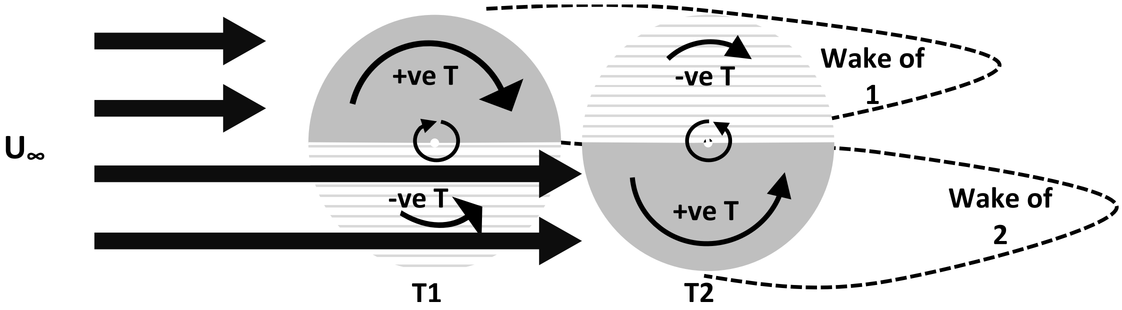

**Figure 43 Example of a CarBine unit**

## 7.2 Performance of a theoretical drag type turbine

Based on a turbine that is driven solely by drag force, akin to the drag driven windmills used in the Middle East over a thousand years ago, Manwell et al., (2009) calculated the theoretical $C_p$-λ curve of a wind turbine consisting of flat plates whereby the returning blades are shielded from the flow (Figure 44), using the following equations:

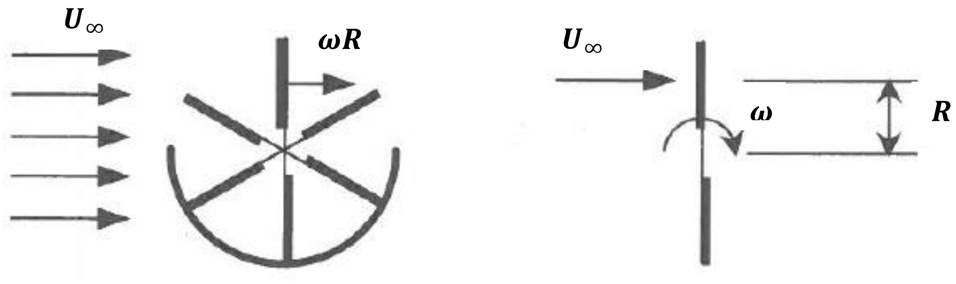

**Figure 44 Drag type turbine (Manwell et al., 2009)**

$$F_D = C_D\left[\frac{1}{2}\rho(U_\infty - \omega R)^2 A\right] \tag{21}$$

Similar to Equation (8), Equation (21) splits the relative velocity term into its components: freestream velocity $U_\infty$ and angular velocity of the turbine $\omega R$, as seen in Figure 44. Manwell et al use a $C_D$ value of 1.1 for a 3D flat plate perpendicular to the flow. However NASA, (2013) states that during wind studies a flat plate had the largest $C_D$ from a variety of shapes with a value of 1.28, seen in Table 9. The values in Table 9 were obtained empirically for identical flow conditions (i.e. constant Re) and the cross-sectional area opposing the flow, A.

**Table 9 $C_D$ for various shapes (NASA, 2013)**

| Shape | $C_D$ |
|---|---|
| Flat plate – *perpendicular to the flow direction* | 1.28 |
| Airfoil | 0.045 |
| Sphere | 0.07-0.5 |
| Bullet | 0.295 |
| Prism | 1.14 |

Table 9 shows that a flat plate would generate almost 30 times more drag force than that of an airfoil; quantifying the streamlined nature of an airfoil in comparison to other shapes. Using Equation (6), Equation (21) becomes

$$P = C_D\left[\tfrac{1}{2}\rho A(U_\infty - \omega R)^2\right]\omega R = (\rho A U_\infty^3)\left[\tfrac{1}{2}C_D\lambda(1-\lambda)^2\right] \tag{22}$$

To produce a $C_p$-λ chart for a turbine with a frontal area of 2A (i.e. the width of 2 flaps, see Figure 44) then Equation (22) is combined with Equation (3) to give

$$C_p = \left[\tfrac{1}{2}C_D\lambda(1-\lambda)^2\right] \tag{23}$$

Equation (23) shows that for TSR ($\lambda$) values of 0 and 1 the $C_p$ value is 0. Therefore for a solely drag type turbine the available range of TSRs are $0< \lambda <1$, as illustrated in Figure 45. As seen in Figure 45, the maximum $C_p$ for a drag type wind turbine according to Manwell et al., (2009) is 0.08 whereas according to the figures from NASA, (2013) the maximum $C_p$ is 0.095, both occur at $\lambda=0.33$. However the theory does not make any allowance for the variation in $C_D$ during a revolution. As an arm sweeps an entire revolution the angle of the blades with the incoming flow will vary and hence the $C_D$ value as well as a varying frontal area; both contributing to a varying torque and hence power output. Additionally the theory does not account for any interaction between blades on adjacent arms which could potentially increase the maximum available power, since more than one arm could be supporting blades generating positive torque at any one instance and therefore increasing the overall torque and power output. Conversely introducing multiple arms could cause a reduction in power output since the blades on arms moving into the “positive region” could have a shadowing effect on other blades also located in the “positive region”; in addition to increasing the negative torque as a result of multiple open blades moving against the freestream flow. Applying this theory to CarBine, a theoretical maximum $C_p$ value of less than 0.10 means CarBine would not be competitive in the marketplace with HATTs that possess $C_p$ values greater than 0.4 (see Figure 15 for $C_p$-λ curves for various horizontal wind turbines). However since CarBine will comprise of multiple arms the performance of CarBine is unknown. Although CarBine is not expected to achieve efficiencies as high as conventional HATTs based on the above theory, a review of typical $C_p$ values for the Savonius turbine (see Figure 50) has found an average $C_p$≈0.15, indicating there is promise for a drag-type turbine. Furthermore CarBine does possess an array of unique advantages compared to HATTs as seen in Section 7.3.

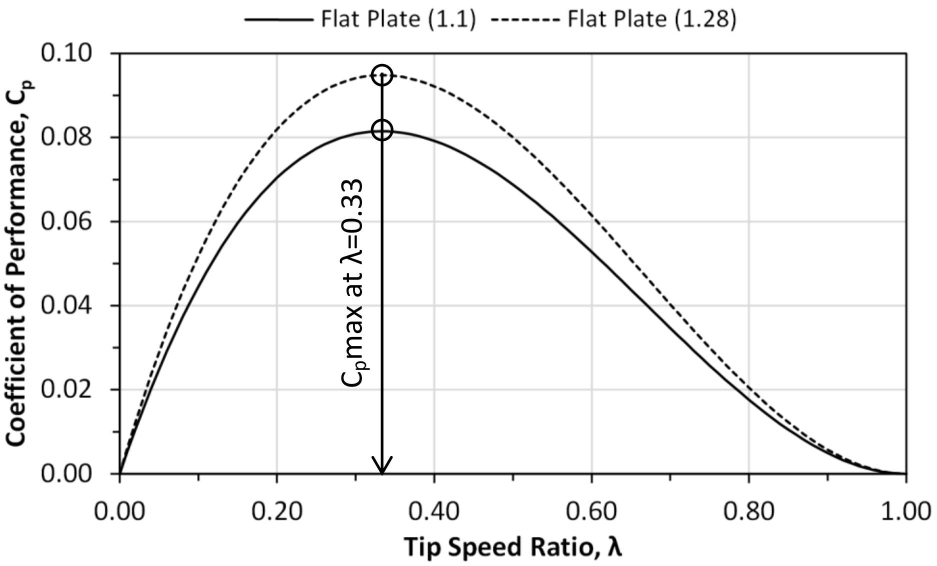

**Figure 45 Theoretical $C_p$-λ for a drag type turbine using Equation (23)**

## 7.3 Potential advantages and disadvantages of CarBine

- ✓ **Omni-directionality**

  Negating the need for a yawing system will reduce the unit cost price of the turbine and avoid any issues of misalignment which can induce fatigue issues and a reduction in turbine $C_p$ (Maganga et al., 2010), see Section 6.2.1.

- ✓ **Simple, robust blade design**

  Unlike the market leading HATTs, CarBine does not use hydrofoils which are expensive due to the precision engineering required, see Section 6.2.6. This again reduces the overall price of each unit.

- × **Numerous moving parts**

  Despite a simple blade design, for each blade CarBine will require pivot points to permit rotation. Such connections are likely to require bearings which in turn will increase both the cost and maintenance intervals.

- ✓ **Slow operating speed**

  Operating at a low TSR should drastically reduce the environmental impact, such as damage to marine life and the surrounding ecosystem (see Section 3.3.6.1) which is a crucial aspect in obtaining relevant licenses prior to deployment. It is expected that the final design will operate at a TSR of around 0.33 (see Figure 45) i.e. the turbine will rotate at less than half the speed of the surrounding fluid. In comparison HATTs operate at TSRs of up to 20 times that of CarBine (A.S. Bahaj et al., 2007b; Jo et al., 2012; Maganga et al., 2010; Wu et al., 2012).

- × **Large power take-off components**

  Operating at such a low speed (TSR<1), CarBine will require a large step-up gearbox in order to gain the speed-up required to match to a high speed off-the-shelf generator. Conversely CarBine could use a bespoke direct drive generator but the slow operating speed will require a large generator. Both options are expensive and add considerable weight to the final design.

- ✓ **Self-starting**

  CarBine generates large values of torque due to the high $C_p$ value of the flat blades, see Section 7.2, which would overcome any internal frictional loads enabling it to be self-starting. This negates the need for a supplementary starting mechanism; further reducing the components required and simplifying the manufacturing process. It also enables CarBine to harness power even from the low velocities present around slack tides (although power density is low, as seen in Section 0).

- ✗ **Complex braking system**

  Unlike HATTs, during emergency shutdown conditions CarBine will be more difficult to brake since it harnesses drag force. HATTs either yaw the blades parallel to the flow to prevent any lift force from generating or yaw the blades to an unfavourable pitch. CarBine however will either need a complex release system whereby all blades are released to be parallel to the flow and therefore cannot generate torque or would require a large breaking system.

- ✓ **Larger area for deployment**

  CarBine can operate semi-submerged, enabling potential for both tidal as well as river/estuarine application; this hugely increases the accessible market available to CarBine. This shallow water resource is a key area in which the developers of HATTs cannot exploit, see Section 3.3.3. As seen in Table 1 and Table 2, an estimated 1116 GWh/year of extractable energy is available in water depths <30 m around the UK, equating to 5% of the total UK tidal stream resource.

- ✓ **Stackable**

  Since CarBine is a VATT, it has the ability to stack numerous devices both vertically and horizontally-potentially creating a tidal fence, such as that hypothesised by Blue Energy Canada Inc. (2013) with their Blue Energy turbine (see Appendix A for further details). The ability to stack CarBine turbines vertically enables a multi-stage turbine to be created with potentially a smooth power output. As seen with the Savonius turbine in Section 8.3.2, multi-stage turbines enable torque fluctuations in a single stage turbine to be eradicated through offsetting the angle of subsequent vertically stacked turbines to even out the peak and troughs in torque output.

- ✓ **Reduced likelihood of Cavitation**

  Since CarBine is a slow rotating turbine, (peak $C_p$ occurring at a TSR<1) the likelihood of cavitation is very small, see Section 6.1 for further details.

- ✓ **Cheaper to manufacture**

  An amalgamation of the aspects mentioned above all leads to a significant reduction in manufacturing costs of the CarBine units in comparison to the currently deployed HATTs.

- ✓ **Denser array spacing**

  The principle of generating power from only one half of CarBine enables a unique advantage of overlapping CarBine turbines, as seen in Figure 43, which potentially enables denser array spacing in comparison to HATTs. A denser array spacing results in an increased value of $W/m^2$ of tidal stream, less ancillary equipment (e.g. cables) and easier array maintenance. This is achieved, for example through aligning two Carbines’ along the axis of the streamwise direction of the flow, namely CarBine 1 and 2, see Figure 43. CarBine 2 is located behind CarBine 1 and is driven in the counter direction to CarBine 1; resulting in the generating side of CarBine 2 being located in the undisturbed through flow from CarBine 1. The non-generating side of CarBine 2 is thus located in the wake of CarBine 1, further reducing its negative torque (since torque is proportional to the square of the flow speed, see Equation (8)). Since two CarBines can be positioned very close to each other, depending on how the power is taken off a CarBine, e.g. through a perimeter ring connection rather than off the central shaft, two CarBines can also drive a single generator positioned between two CarBines. This would be a significant cost saving since the drive train of a tidal stream turbine, can be up to 13% of the total capital cost. Based on a study by (Binnie Black & Veatch, (2001) on MCTs SeaGen turbine.

  This is a unique advantage of CarBine since every reviewed turbine in Appendix A utilises their entire swept area for power generation, with the unusable wake of conventional HATTs typically stretching for greater than 10D, see Section 4.2.6.1. If a CarBine unit consists of 2 CarBine’s aligned along the axis of the flow then the $C_p$ of the unit would be double that of a single CarBine since there will be 2 turbines operating for the same swept area as a single CarBine. Doubling the $C_p$ of CarBine in this manner would increase its competitiveness in the HATT dominated market.

## 7.4 Stages of Development

Stages of development are designed to provide a rigid structure for the development of tidal stream turbines from concept to commercial scale. At each stage there are a series of gates which “open” if the gate criteria are met; this ensures that uncertainty in predicted performance of a tidal stream turbine has been reduced within the stage. DECC recommends the structure provided in the “Tidal current Energy Device Development and Evaluation Protocol”, created by the Sustainable Energy Research Group in Southampton University (2008) as a framework for development, whereas EMEC recommend the structure provided by Nielsen, (2010) which was created for the Danish Energy Agency. However the stages in Nielsen, (2010) are based on Nielsen and Meyer, (1997) whilst the DECC stages in (University of Southampton, 2008) are loosely based on Technology Readiness Levels used by NASA for developing new technology (Mankins, 1995). These are summarised below in Table 10 and illustrated in Figure 46. The DECC protocol focuses heavily on costing and uses cost of energy as the final gate at each stage, to emphasise that progression to the next level is only viable if market competitive costs are being achieved. The DECC protocol (University of Southampton, 2008) will be used to describe the development of CarBine since it provides both a detailed breakdown of the stages and all associated gates in the form of a flow diagram (indicating key decision points), as well as accounting specifically for “novelty” subsystems- described as “the extent to which the design of the subsystem components represents a significant departure from the body of existing knowledge within the offshore, marine and wind industries”. MARINET (Marine Renewables Infrastructure Network) also provides an example of a structured development plan (MARINET, 2013a), which is again based on Mankins, (1995). Due to the lack of existing knowledge, CarBine can be classed as a novel hydrodynamic subsystem. Each stage is split into the criteria for each of the subsystems as well as criteria for complete system integration. Subsystems in the protocol are categorised as:

- Hydrodynamic subsystem-includes mechanism of converting fluid kinetic energy to mechanical energy;
- Power take-off system- includes mechanical energy to electrical energy, as described in Section 4;
- Reaction Subsystem-supporting structure and foundations.

**Table 10 Stages of Development and CarBine status (University of Southampton, 2008)**

| Stage | Description | CarBine Status |
|---|---|---|
| **1** | *(Scope of Protocol begins here)*<br>Tidal-current energy conversion concept formulated<br>• Explain concepts for the subsystems:<br>• List the major components;<br>• Identify R&D requirements for Stages 2-3, in addition to the minimum requirements;<br>• Provide documentation for standard, off the-shelf components used within their specification and not requiring further testing. | **Complete*** |
| **2** | Subsystem testing at intermediate scale, including:<br>• Computational Fluid Dynamics;<br>• Finite Element Analysis;<br>• Dynamic analysis. | **In Progress** |
| **3** | Subsystem testing at large scale | |
| **4** | Full-scale prototype tested at sea | |
| **5** | Commercial demonstrator tested at sea for an extended period.<br>(Scope of protocol ends here) | |

***Stage 1 gate for the hydrodynamic subsystem insists on a predicted maximum $C_p$>0.3. The predicted $C_p$ is lower, see section 7.2, but the additional benefits of CarBine seek to outweigh this issue, see section 7.3.**

For the hydrodynamic subsystem, the DECC protocol (University of Southampton, 2008) defines the minimum research and development required based on the novelty of the device, as seen in Figure 46. Figure 46 describes the research and development required for CarBine, this will act as the scope for this study, including:

- Model testing of hydrodynamic subsystem, 1/20 scale, see Section 9;
- Suitable CFD analysis, see Section 10.

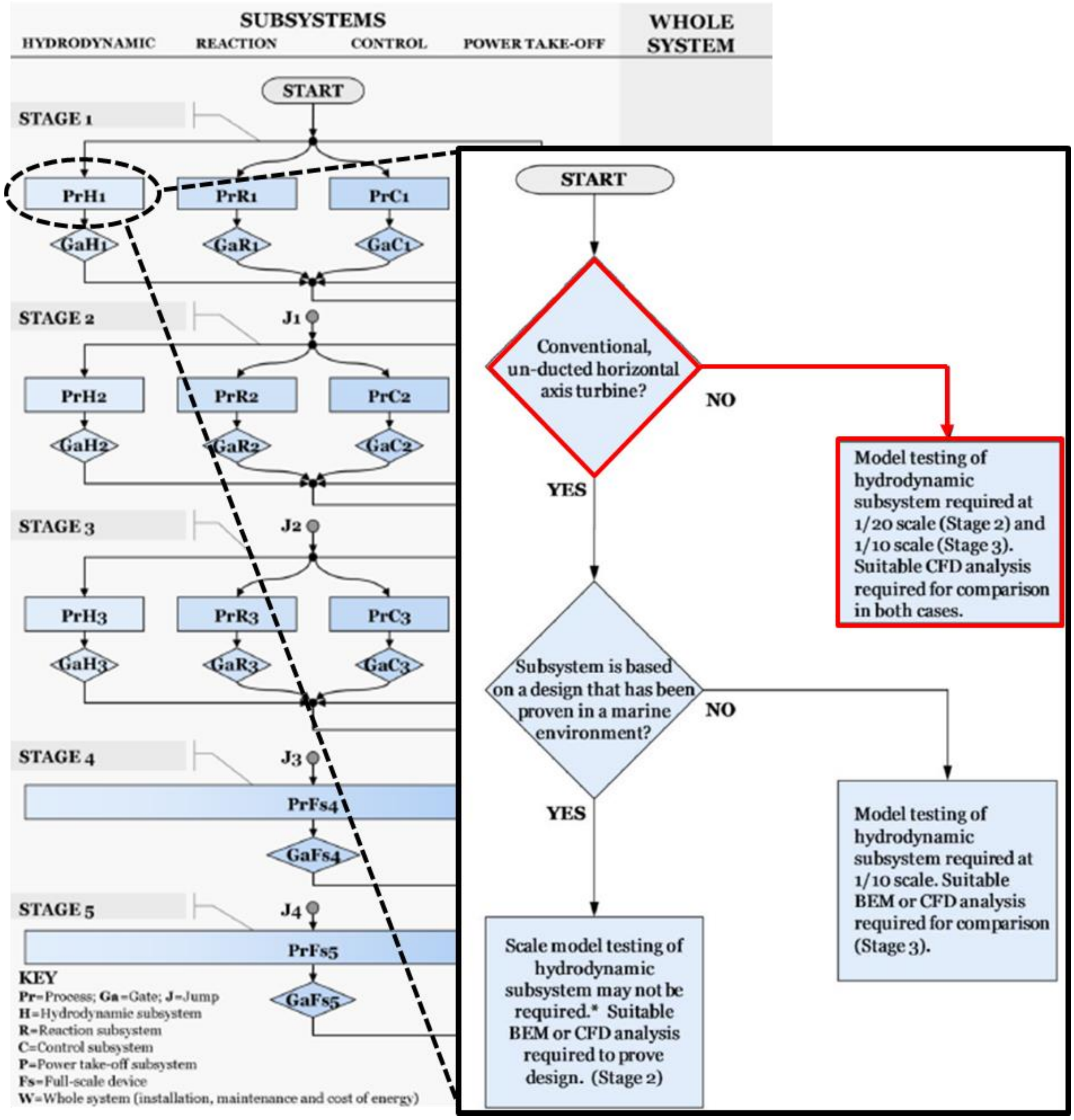

**Figure 46 Highlighted decision process for CarBine subsystem from complete stages of development schematic**

**(University of Southampton, 2008)**

## 7.5 Preliminary CarBine studies

Initial proof of concept testing of CarBine was conducted at the Cardiff University School of Engineering (Challans, 2009; Chrysafis, 2008). Chrysafis, (2008) conducted both laboratory scaled testing, using CarBine prototype 1 (see Figure 47a), and CFD modelling using Fluent (details on CFD method available in Section 10). For both the laboratory and CFD study, a 3-arm configuration of CarBine was used. The laboratory studies were based upon measuring the static torque of CarBine every $45^o$ using a newton meter in flows ranging from 0.3-0.5 m/s and measuring ω using a stopwatch. Using the static torque value over an entire rotation and the freewheeling angular velocity, the calculated performance values of CarBine (using (3) and (7))) were $C_p$/TSR ≈ 0.25/0.64. The CFD study used a similar technique to the laboratory study besides that a static 2D model of CarBine was modelled every $10^0$ and a TSR of 0.8 was used; the calculated performance values of CarBine were $C_p$/TSR ≈ 0.38/0.8. Although the study proved the concept of CarBine with regards to its working principles, it did not really provide meaningful results with regards to performance since no load was applied to the turbine during testing and therefore a range of TSRs could not be tested with corresponding efficiency values to produce a performance curve.

Challans, (2009) supplemented the laboratory studies conducted by Chrysafis, (2008) through applying a load to CarBine, through causing the turbine to lift a weight via a pulley. Through measuring the height to which the weight was lifted and the time taken for the turbine to rotate a fixed amount, it was possible to obtain some performance data. For freestream velocities ranging from 0.33-0.52 m/s performance values of $C_p$≈0.22 were achieved. CarBine prototype 2 was manufactured (see Figure 47b), and produced $C_p$ values of 0.22-0.3 for flow speed ranging from 0.33-0.5 m/s. Challans, (2009) also collected extensive data on the velocity profiles of the turbine wake. Since a range of loadings were not applied to the turbine, an entire $C_p$/TSR chart could not be drawn meaning it cannot be said whether the performance data corresponds to the peak performance of CarBine. Nonetheless it gives a promising indication of CarBine’s efficiency and provides the foundation for further investigation. An elaboration on the differences between CarBine prototype 1 and 2 can be found in Section 9.3.

**(a)** **(b)**

**Figure 47 CarBine prototypes (a) 1 (Chrysafis, 2008) (b) 2 (Challans, 2009)**

### 7.5.1 Competing technologies

Although CarBine is a novel drag-type VATT, there are competing comparable technologies in the marketplace. With regards to performance, CarBine will need to be competitive and show advantages over the simple traditional drag type (supplemented by a small degree of lift force) VATT-i.e. the Savonius; the Savonius turbine is reviewed in detail in Section 8.

#### *7.5.1.1 Hunter Turbine*

Designed at Queen Mary, University of London, the Hunter turbine is a drag type turbine (see Figure 48a). Similar to CarBine, the Hunter turbine generates torque via flaps which open and close based on their relative position to the flow. Unlike CarBine, the Hunter turbine flaps close around a rigid central cylinder as opposed to being supported by arms and aligning to the flow. Laboratory testing and CFD studies (Li and Calisal, 2010; Yang and Lawn, 2011) have been conducted on the turbine, with a peak performance of $C_p$/TSR=0.15/0.67.

#### *7.5.1.2 FlipWing*

The FlipWing turbine by HydroVolts inc. is similar to CarBine in the sense that it is a drag type turbine that consists of a series of flaps which both open and close depend on the their relative position to the flow, as seen in Figure 48b; however there is no further detail available on the device. Unlike CarBine, FlipWing is a THATT and therefore does not benefit from omni-directionality (Hydrovolts, 2012).

#### *7.5.1.3 TIDENG Offshore turbine by TIDENG*

The TIDENG Offshore turbine by TIDENG, seen in Figure 48c, operates through releasing a series of 6 flaps to generate positive torque but withdrawing the flaps from the flow when they begin to generate negative torque. The turbine base is constructed of concrete and would be towed into place and then ballasted with water and sand to create a gravity base for the turbine. The shape of the base is designed to increase the local flow speed to 1.3-2 times that of the freestream flow speed (TIDENG, 2013). There is no further detail available on the turbine. Like the Flipwing turbine, the TIDENG offshore is a THATT turbine and does therefore not benefit from omni-directionality, it is also similar to the hunter turbine in the fact that the flaps are concealed around a central cylinder during part of a revolution.

(a) (b) (c)

**Figure 48 (a) Hunter Turbine (b) FlipWing (c) TIDENG Offshore**

# 8 Review of the Savonius turbine

**This chapter contains a detailed review of the Savonius turbine – a VATT. The Savonius is considered the industry's leading drag type turbine and will therefore be used as a benchmark for the performance of CarBine. A review of the many permutations of the Savonius has been compiled resulting in an optimum configuration comprising of a single stage, 2 bucket with overlap and end plates. An average of numerous experimental studies of the Savonius in both an aerodynamic and hydraulic environment lead to performance results of $C_p$max/λ=0.17/0.77.**

The conventional Savonius turbine was designed by Sigurd. J. Savonius, at the beginning of the 20th century, to harness wind energy (Savonius, 1931); it is a vertical axis (also referred to as a cross flow) tidal turbine-VATT. The simple design consists of two semi-circular vertical offset opposing sections (buckets) such that they form the letter S, see Figure 49.

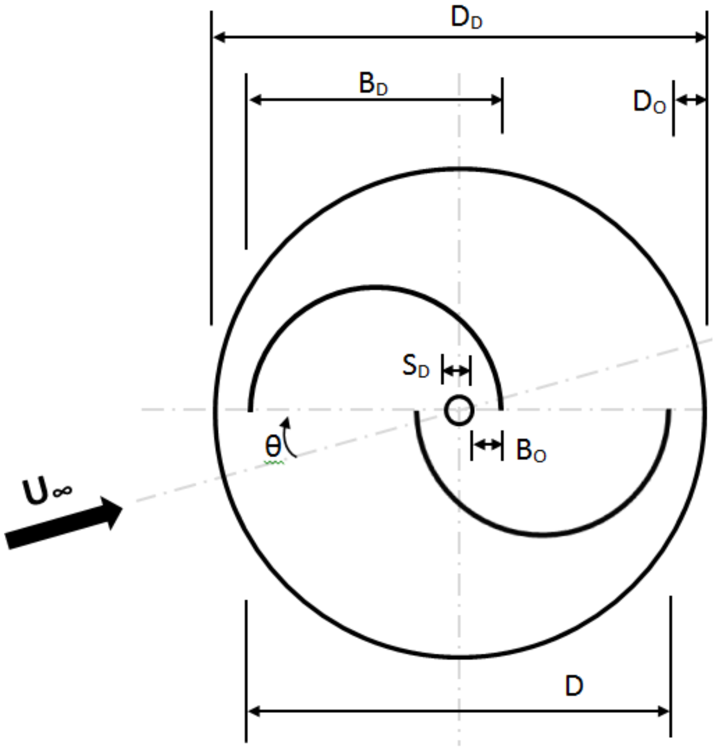

Figure 49 Savonius schematic

Table 11 Savonius design parameters for Figure 49

| Symbol | Description |
|---|---|
| $D_D$ | Disk Diameter |
| D | Diameter |
| $B_O$ | Bucket overlap |
| $S_D$ | Shaft diameter |
| $B_D$ | Bucket diameter |
| $D_O$ | Disk overlap |
| θ | Azimuth angle |

The basic principle governing the motion of the Savonius is the difference between the drag coefficient of the concave side of a bucket and its convex side. The turbine rotates due to a net positive torque. This has given rise to the Savonius being regarded as a drag type device. Previous studies have concluded that lift forces are also prominent in torque generation for a conventional Savonius turbine (Akwa et al., 2012; Fujisawa and Gotoh, 1994; Nakajima et al., 2008). Torque generation from a turbine harnessing a hybrid of drag and lift forces would be able to exceed the limiting efficiency of 0.08 predicted for a drag type (for a flat plate) turbine (Manwell et al., 2009), see Section 7.2. The literature review conducted for the performance of the Savonius Turbine discovered that the majority of research has been conducted for the use of a Savonius turbine in a wind environment, however in recent years there has been an increase in the number of investigation of the Savonius turbine in a hydraulic environment.

## 8.1 Advantages of the Savonius turbine

Although the Savonius suffers from lower efficiency values than a conventional HATT, it does however benefit from a number of key advantages.

### 8.1.1 Omni-directionality

The Savonius has the ability to rotate irrespective of the direction of the flow, negating the following issues:

- Miss-alignment issues during installation-which for conventional HATTs can be severely detrimental to performance;
- Requirement of a yawing device;
- Variations in flow direction during a tidal cycle has no effect on performance of the Savonius; and
- Variation in flow direction during a tidal cycle does not produce any unforeseen loadings or fatigue issues, see Section 6.

Irabu and Roy, (2011) and Nakajima et al., (2008) conducted laboratory studies on a Savonius with its axis or rotation perpendicular in the horizontal plane (not the vertical plane) to that of the fluid flow direction i.e. acting as a THATT, see Section 4.2.3. However this orientation does not benefit from omni-directionality.

### 8.1.2 Simple and cheap design

Conventional HATTs require profiled, precision engineered (usually composite, see Section 6.2) blades whereas the Savonius blades are simple and thus can be manufactured cheaper. Its simpler design also leads to increased robustness. The cheap and low technicality of the Savonius blades have led to the design being used as water pumps in poor countries and at isolated sites (Rabah and Osawa, 1996; Valdès and Raniriharinosy, 2001).

### 8.1.3 High Starting Torque / High Coefficient of Torque

Possessing high starting torque has resulted in the Savonius turbine acting as a start-up turbine for other devices with low start up torques. However some studies conclude for angles from $135^o<\theta<165^o$ and $315^o<\theta<345^o$ the Savonius suffers from negative starting torque (Fujisawa and Gotoh, 1994; Hayashi et al., 2005; Kamoji et al., 2009a, 2009b; Menet, 2002). The high starting torque of the Savonius has led to it being used as a self-starting mechanism for higher efficiency turbines with low starting torques, such as a Darrieus style turbine. Kyozuka, (2008) showed that the Savonius only improves the characteristics of a Darrieus when used during start-up, if connected to the Darrieus during full operation it will prove detrimental to the performance, with reductions in the Darrieus $C_p$ of up to 30%, since the wake of the Savonius alters the flow field for the Darrieus blades.

### 8.1.4 Low rotational speed

Savonius turbines operate at low TSRs in comparison to HATTs which operate at high TSRs. Figure 15 shows $C_p$ vs. $\lambda$ curves for a variety of wind turbines (Wilson and Lissaman, 1974) and Figure 50 shows that at peak efficiency a Savonius turbine operates at a TSR ≈0.8-0.9, whereas HATTs operate at TSR>6 (A.S. Bahaj et al., 2007b; Jo et al., 2012; Maganga et al., 2010; Wu et al., 2012). Low operating speeds incur structural and environmental advantages.

## 8.2 Disadvantages of the Savonius turbine

### 8.2.1 Low efficiency values

The Savonius suffers from lower efficiency values than HATTs, as seen in Figure 15. Typical HATTs have $C_p>0.4$ (A.S. Bahaj et al., 2007b; Jo et al., 2012; Maganga et al., 2010; Wu et al., 2012)., whereas Figure 15 indicates a $C_p$ of 0.15 for the Savonius turbine. Figure 50 also highlights the low efficiencies of the Savonius, with an average efficiency of 0.17.

### 8.2.2 Large dynamic torque variation

The torque generated is a function of the azimuth angle of the turbine. At varying azimuth angles the geometry opposing the incoming flow changes and each change in geometry has its own coefficient of drag and lift. Due to the change in the azimuth angle and the corresponding geometrical change, the torque generated continuously varies throughout a complete rotation (Kyozuka, 2008).

### 8.2.3 High weight to power output

Unlike conventional HATTs the Savonius turbine occupies its whole swept area with material. According to Wilson and Lissaman, (1974) this leads to the Savonius requiring thirty times more surface than that of a conventional HATT for the same power.

## 8.3 Design techniques to improve the performance of the Savonius

The conventional Savonius turbine is an inherently simple design. However reviews on the Savonius (Akwa et al., 2012; Menet and Bourabaa, 2004; Zhao et al., 2009) have shown there are numerous ways in which to alter/ increase the performance of the device. Within the literature there is no universal agreement on the efficiency of a Savonius turbine as seen in the variety of peak $C_p/\lambda$ values shown in Figure 50, due to the numerous possible variations of the geometry, the test conditions (including blockage inherent in hydraulic testing and closed section wind testing, see Section 9.5) as well as the variation on Reynolds number dependant on testing in wind/hydraulic environment.

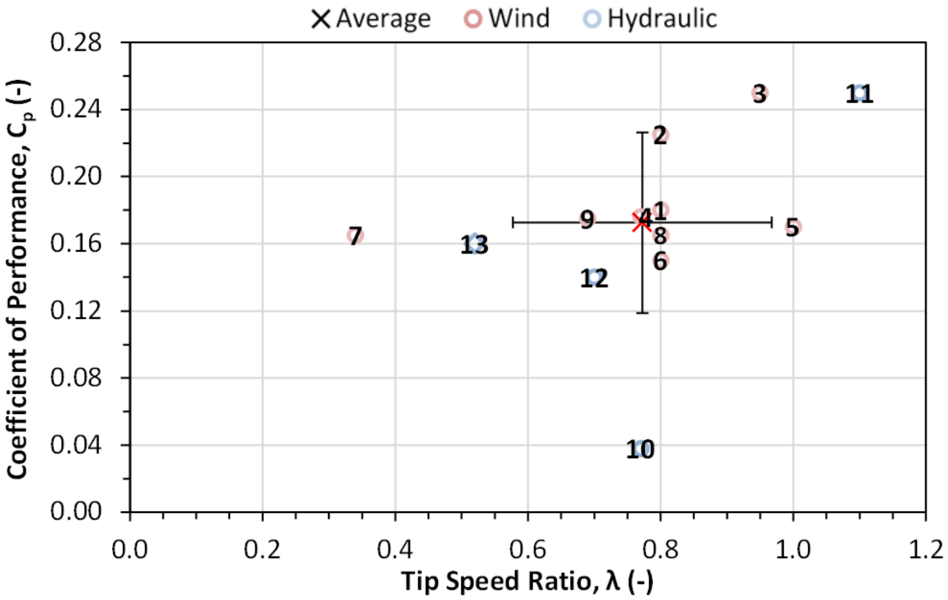

***Notes:***
***The values used are a combination of both stated values and values read from figures.***
***Values are only used for conventional Savonius turbine, i.e. 1 stage, 2 semi-circular buckets and a combination of the various factors listed in section 8.3 below.***
***Error bars for the average data point indicates the standard deviation.***

**Figure 50 Peak $C_p/\lambda$ for various experimentally tested Savonius turbines**

**Table 12 Key for Figure 50 and associated values $C_p/\lambda$**

| # | W/H | $C_p/\lambda$ | | # | W/H | $C_p/\lambda$ | |
|---|---|---|---|---|---|---|---|
| **1** | W | 0.18/0.8 | Dobrev and Massouh, (2011) | **8** | W | 0.165/0.8 | Zhao et al., (2009) |
| **2** | W | 0.225/0.8 | Sheldahl et al., (1978) | **9** | W | 0.175/0.69 | Kamoji et al., (2009b) |
| **3** | W | 0.25/0.9 | D'Alessandro et al., (2010) | **10** | H | 0.038/0.77 | Khan et al., (2008) |
| **4** | W | 0.176/0.77 | Kamoji et al., (2009a) | **11** | H | 0.25/1.1 | Nakajima et al., (2008) |
| **5** | W | 0.17/1.0 | Fujisawa and Gotoh, (1994) | **12** | H | 0.14/0.7 | Golecha et al., (2011) |
| **6** | W | 0.15/0.8 | Wilson and Lissaman, (1974) | **13** | H | 0.16/0.52 | Kyozuka, (2008) |
| **7** | W | 0.165/0.34 | Altan and Atılgan, (2010) | | | | |

The following key geometrical parameters have been identified as having the largest effect on performance.

### 8.3.1 Number of buckets

Studies (Saha et al., 2008; Sheldahl et al., 1978; Zhao et al., 2009) showed that increasing the number of buckets from 2-3 lead to a decrease in the efficiency of a

Savonius, since air striking on the generating blade can be deflected on to the concave surface of the following blade causing negative torque thus decreasing the turbine performance.

### 8.3.2 Multi-stage design

The majority of studies (Akwa, 2010; Golecha et al., 2011; Hayashi et al., 2005; Menet, 2002) state that increasing the number of stages (i.e. multiple offset turbines stacked on top of one another along the axis of rotation, two stage would be offset by $90^{o}$ and three stage by $120^{o}$) reduces the torque variation; however it is detrimental to the efficiency of the Savonius. Golecha et al., (2011) measured a 61% and 7.7% reduction in $C_p$ value for a three stage and two stage Savonius respectively, and hypothesized that the reduction could be due to the presence of the intermediate plates (between the stages) which affects the flow distribution. Khan et al., (2008) also discovered that while testing Savonius turbines with 1-3 stages, a two stage design provided the lowest torque variation, whilst the single stage design exhibited the highest efficiency value.

### 8.3.3 Bucket shape

Furthermore to the multi-stage turbine design, inducing a twist angle to the bucket geometry produces a helical shaped blade which acts as an infinite multi-stage semi-circular blade design. Kamoji et al., (2009a) compared a two bucket helical Savonius turbine with a twist of 90° to a conventional Savonius turbine. Results showed that both had almost the same $C_P$ (0.174) however the helical Savonius turbine possessed positive static coefficient for all azimuth angles ($0^\circ \leq \theta \leq 180^\circ$). Mohamed et al., (2011) altered the blade geometry of the Savonius using evolutionary algorithms to create an “optimal” blade, in the presence of an obstacle shielding the returning blade. The results show an increase in efficiency of around 15% compared to the classical Savonius in the presence of an obstacle. Saha and Rajkumar, (2006) showed an increase in $C_p$ value from 0.11 (with semi-circular blades) to 0.14, using helical shaped blades. As opposed to designing a helix shaped blade, Abraham et al., (2012) designed a blade which differs from the conventional Savonius in that there is a straight section which connects the two curved ends which are not semi-circular; however no detailed results of the performance of the device are available. Nevertheless introducing a twist into the Savonius bucket shape eradicates one of its key advantages, which is that of a simple blade design.

### 8.3.4 Overlap ratio, β

The overlap ratio $\beta$ is defined as

$$\beta = \frac{B_O}{B_D} \tag{24}$$

where $B_O$ is the blade overlap and $B_D$ is the blade diameter as shown in Figure 49. Introducing an overlap ratio allows a portion of fluid from the generating blade to be deflected onto the concave side of the non-generating blade; resulting in a reduction in the difference in pressure between the concave and convex side of the non-generating blade and hence lower drag force. This overall produces an increased net torque, and enhanced performance values. Recommended values of β vary from 0-0.2 for increased $C_t$ values but then a decrease in $C_t$ between 0.3 and 0.5 (Saha et al., 2008), to a monotonic increase in torque as β is increased from 0 to 0.5 (Fujisawa, 1992). These contradicting suggestions do share a common feature and that continually increasing β will eventually lead to decreased performance, in this case above a value of 0.2 or 0.5. The reason is that the projected area of the attacking blade decreases as β increases, until eventually the torque generated by the attacking blade reduces, leading to inferior performance. Akwa et al., (2012) concluded that an overlap ratio of 0.15 enhances the max $C_P$ value to 0.316 in comparison to the conventional Savonius turbine with a max $C_P$ of around 0.25 with an overlap ratio of 0.0.

### 8.3.5 Inclusion of stators

Studies (Golecha et al., 2011; Mohamed et al., 2011) showed the effects of introducing an obstacle/ curtain/ deflector plate to shield the convex blade of a conventional Savonius turbine. Shielding the returning convex blade which produces the negative torque should theoretically increase the performance of the shielded turbine. Mohamed et al., (2011) showed that positive starting torque was achieved at all angles for a shielded turbine and an increase from a max $C_P$ of 0.17 for a conventional

Savonius to a max $C_P$ of around 0.25 for a shielded turbine. Using a deflector plate Golecha et al., (2011) experienced an increase of 50% for $C_P$ to a value of 0.21 in comparison to an unshielded turbine. Altan and Atılgan, (2010) used a “curtain”, which acted as both a shield to the returning blade and a duct, to increase the oncoming wind speed. The results showed a 100% increase in performance when comparing the curtain design to the no-curtain design. However such a design not only loses its omni-directionality but also poses significantly more environmental concerns than a conventional Savonius.

### 8.3.6 End Plates

Introducing end plates, i.e. circular plates fixed to both the upper and lower side of the Savonius turbine, has been shown to increase the performance of a Savonius turbine. Ushiyama et al., (1982) increased the $C_P$ from a maximum of 0.16 to just above 0.20 through including end plates. This study and others (Akwa et al., 2012; Menet and Bourabaa, 2004) recommend negligible thickness of the end plates in comparison to the turbine height as well as a diameter of around 1.1 times the diameter of the rotor, further increase in the plate diameter will lead to an increase in the rotor’s inertia.

### 8.3.7 Aspect Ratio

The aspect ratio φ is regarded as a key criterion for improving the performance of a Savonius rotor. Various studies (Khan et al., 2008; Ushiyama et al., 1982; Zhao et al., 2009) have been conducted regarding the aspect ratio, with the majority in agreement that an aspect ratio of 1.0 and above improves the efficiency of a conventional Savonius turbine (Ushiyama et al., 1982). Zhao et al., (2009) varied φ from 1 to 7 for a helical blade Savonius rotor and concluded that the optimum aspect ratio is equal to 6.

$$\varphi = \frac{H}{D} \tag{25}$$

## 8.4 Performance Augmentation Techniques

### 8.4.1 Dynamic Blades

Some studies aimed to augment the performance of the Savonius turbine through designing dynamic buckets. The techniques vary from permitting the entire bucket to swing during a revolution to splitting the buckets into a series of flaps. The principle is to reduce the degree of negative drag experienced by the returning bucket, i.e. the non-generating bucket. The one-way flapped design works through the flaps remaining closed whilst the concave face of a bucket is facing the flow whereas it would open once the convex face of the bucket is facing the flow; with the aim of increasing the net torque in comparison to a conventional Savonius turbine design.

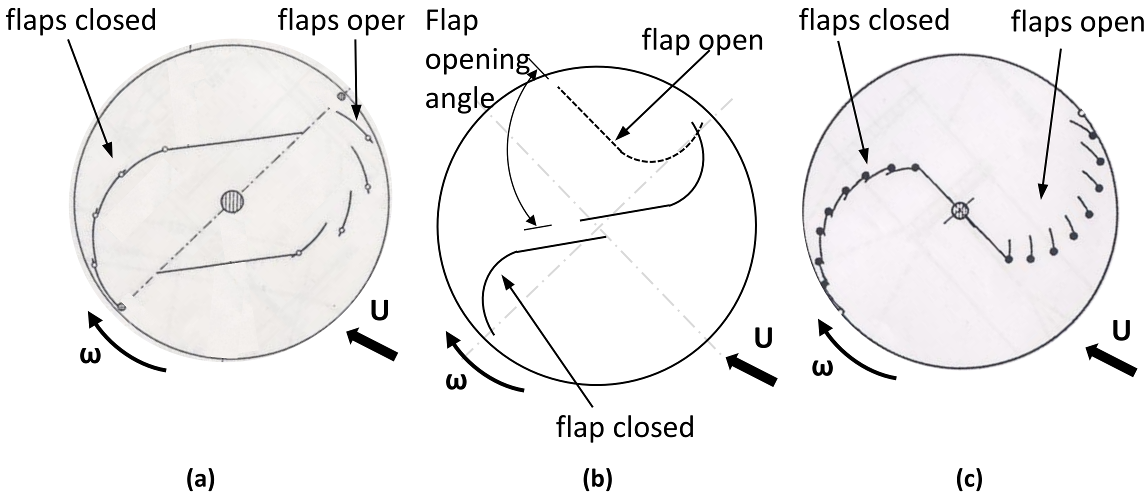

**Figure 51 Schematic of modified Savonius turbines used for (a) Tabassum and Probert, (1987), (b) Aldoss and Najjar, (1985), (c) Reupke and Probert, (1991)**

Tabassum and Probert, (1987) tested a modified Savonius, formed by a straight portion and a curved section for each bucket, as seen in Figure 51b. Rather than a rigid bucket, the buckets comprised of four flaps each. The static torque of the modified flapped Savonius with varying maximum opening angle of the flaps was compared to that of a rigid modified Savonius. The results show that the flapped modified Savonius, for all flap opening angles, eradicated the negative torque experienced by the modified rigid Savonius at $0^o \leq \theta \leq 5^o$ and $165^o \leq \theta \leq 180^o$ and showed an increase of starting torque over an entire cycle of over 30%. Specifically the modified flapped Savonius with flaps opening to a maximum of $60^o$ achieved the maximum static torque and displayed enhanced static torque performance in the regions of $0^o \leq \theta \leq 30^o$ and $60^o \leq \theta \leq 150^o$. The peak in performance of both the modified flapped Savonius and the Savonius were similar and occurred at $\theta = 50^o$.

Aldoss and Najjar, (1985) investigated dynamic buckets, whereby buckets (with similar shape to those tested by Tabassum and Probert, (1987) were hinged on their outside edge and allowed to rotate depending on their orientation to the flow, as seen in

Figure 51a; aimed at minimizing the form drag on the non-generating bucket and maximising the drag on the generating bucket. The optimum rotated angle for the generating bucket was found to be $13.5^o$ whereas the optimum rotated angle for the non-generating bucket was found to be $50^o$. The turbine $C_p$ was increased to 0.24 in comparison to 0.18 for the rigid design.

Reupke and Probert, (1991) investigated the performance of a flapped modified Savonius, trialling an arrangement of four and eight flaps for each bucket with no central gap as seen in Figure 51c, which were subsequently compared to baseline data from a rigid modified Savonius. Unlike the rigid configuration it was discovered that both the four and eight flap configurations were self-starting. During testing it was discovered that at TSR values below 0.70±0.05 both flapped configurations could not sustain a given load and suddenly dropped to TSR values of ≈0.3 and ≈0.4 for the four flap and eight flap respectively, leaving a large range of unobtainable TSR values, and splitting the efficiency curves into two sections. The flapped configurations obtained higher torque coefficients than the rigid configuration however they achieved much lower $C_p$ values, 0.04±0.015 compared to 0.15±0.02 for the rigid configuration. It was observed that as the turbine gained speed, i.e. at the upper TSR values the flaps would lock in place due to the centrifugal forces, leading to increased acceleration, indicating the turbine performs better without the flaps. It was hypothesised that this could be due to the fact that a Savonius turbine is not solely a drag device and that the lift force normally generated is absent in the case of the modified turbine. In addition the flow impacting the generating bucket could be disrupted by the opening of the flaps on the non-generating bucket.

Despite the research on flapped buckets resulting in inferior performance to rigid buckets, Reupke and Probert, (1991) suggested that this is partly due to the large velocities encountered in wind and subsequently this performance augmentation technique has not been thoroughly tested in water where the encountered velocities are considerably lower.

### 8.4.2 Valve Aided

Saha et al., (2008) introduced a non-return valve into the centre of conventional Savonius buckets. The valve would remain close whilst the concave face of a bucket is facing the flow whereas it would open once the convex face of the bucket is facing the flow, allowing wind from the convex side to the concave side of the returning bucket, thus reducing the difference in pressure either side of the bucket resulting in reduced form drag; thus enhanced net torque. The study showed that for a 3-bucket 2-stage Savonius configuration, the inclusion of the valves did increase the $C_p$ from 0.26 to 0.31.

# 9 Physical Testing

**This chapter contains a detailed description of the methodology used to capture performance data of CarBine during physical testing. The physical testing was conducted at two separate laboratories, namely at Cardiff School of Engineering (CU) and at the French Research Institute for Exploitation of the Sea (IFREMER) in Boulogne-sur-mer, France. Initial design optimisation of CarBine was carried out at CU whereas testing at IFREMER was designed to quantify the blockage effect present at CU. This chapter describes both the development of the various prototypes to be tested, including CarBine, a conventional Savonius and a Savonius with flaps in addition to the mechanical power take-off system. An uncertainty analysis of the various performance parameters measured using the mechanical power take-off system revealed uncertainties <2% for $C_p$, $C_t$ and λ.**

---

Scaled testing of a tidal stream turbine, including proof of concept testing, can be carried out using physical models in a controlled environment, such as a hydraulic flume. A scaled model is a smaller representation of the envisioned full scale turbine. The advantages of scale model testing include:

- Obtaining proof of concept;
- Establishing key performance data, such as $C_p/\lambda$ curves (see Section 0);
- Optimising design parameters, such as angle of attack for lift-type turbines (Bahaj et al., 2007b; Mason-Jones et al., 2012);
- Parameterisation of novel designs that are difficult to model numerically;
- Validating numerical models, see Section 10; and
- Providing confidence for potential investors.

## 9.1 Scaling of flow conditions (Re and Froude)

In order to extrapolate results from a scaled model to full scale the laws of similitude must be adhered to. EquiMar, (2010a) states that for complete similitude between the scaled model and the full scale there exists three levels of similarity to be satisfied:

- **Geometric Similarity**-the prototype geometric dimensions must be scaled;

- **Kinematic Similarity**-all (fluid and model) velocity ratios must be the same at both model and prototype scale, such as TSR; and
- **Dynamic Similarity**-all (fluid and model) force ratios, such as Froude, Reynolds, Cauchy, Weber and Euler must be constant.

It is simple to achieve geometric and kinematic similarity however dynamic similarity is difficult. Of the force ratios mentioned above, Froude number (the ratio of kinetic to potential energy in the flow) Fr, or Reynolds number (ratio of inertial to viscous forces) Re, are assessed, seen in Equations (26) and (27), since the others are barely affected by scale effects for tidal stream turbine testing.

The Froude number is defined as

$$F_r = \frac{U_\infty}{\sqrt{gZ}} \tag{26}$$

where $Z$ (m) is the depth of the water and $g$ (m/s$^2$) is the acceleration due to gravity. The Reynolds number is defined as

$$R_e = \frac{U_\infty L}{\nu} \tag{27}$$

where $L$ (m) is a characteristic length scale. For flow characterisation $L$ is taken as the hydraulic mean depth of the flow, for a uniform channel this is taken as the depth $Z$ (m). For turbine characterisation this is typically taken as the diameter of the turbine D (m) for a drag-type turbine or as the chord length of the hydrofoil section for a lift-type turbine (since Reynolds number significantly impacts the lift coefficient). $\nu$ (m$^2$/s) is the kinematic viscosity. Mason-Jones et al., (2012) conducted a non-dimensional analysis on the performance parameters of a tidal turbine and showed that P, $C_p$ and $C_t$ are all functions of Re, but also stated that for high Re (>$10^6$) it is not unusual for these parameters to become independent of Re. The turbines in this study will be tested for a range of Re to check for Re independency. From Equation (27), if $L$ (which is taken as D in the case of turbine characterisation) and ν are kept constant then varying the Re is achieved through testing at various flow speeds, $U_\infty$.

The difficulty in achieving dynamic similarity is encountered whilst simultaneously trying to maintain Fr and Re similitude for flow characterisation, since they cannot be scaled together. Therefore only a realistic Fr or Re number can be adhered to during testing, providing a compromise between free surface effects (Fr) and local blade effects (Re) (McAdam et al., 2010).

To apply Froude similarity between scale model (s) and full scale prototype (f), Equation (26) becomes

$$\frac{U_f}{\sqrt{gZ_f}} = \frac{U_s}{\sqrt{gZ_s}} \tag{28}$$

Rearranging Equation (28) to make $U_m$ the subject gives

$$U_s = U_f\sqrt{\beta} \text{ where } \beta = \frac{z_s}{z_f} \tag{29}$$

Similarly, to apply Reynolds similarity between scale model and prototype, Equation (27) becomes

$$\frac{U_f L_f}{\nu} = \frac{U_s L_s}{\nu} \tag{30}$$

Rearranging Equation (30) to make $U_m$ the subject gives

$$U_s = U_f\beta \text{ where } \beta = \frac{L_f}{L_s} \tag{31}$$

Table 2 shows the UK tidal stream have depths ranging from 25 m< Z <40 m and the spring peak flow with magnitudes ranging from 2.5 m/s< $U_\infty$ <5.5 m/s. The extremities of these ranges will be used to provide a guideline for achieving dynamic similarity for flow characterisation between a scale model for the CU facility (details of the facility can be found in Section 9.2.1) and full scale prototype.

**Table 13 Scaling of Froude Number**

| | | f | s | f | s |
|---|---|---|---|---|---|
| **Scale Factor* (f/s)** | | 10 | | 16 | |
| **Z** | **m** | 25 | 0.5 | 40 | 0.5 |
| **U∞** | **m/s** | 2.5 | **0.35** | 2.5 | **0.28** |
| **Fr** | **-** | 0.16 | | 0.13 | |
| **Z** | **M** | 25 | 0.5 | 40 | 0.5 |
| **U∞** | **m/s** | 5.5 | **0.77** | 5.5 | **0.62** |
| **Fr** | **-** | 0.35 | | 0.28 | |

**Table 14 Scaling of Reynolds Number**

| | | f | s | f | s |
|---|---|---|---|---|---|
| **Scale Factor* (f/s)** | | 10 | | 16 | |
| **v** | **$m^2/s$** | $1.13 \times 10^{-6}$ | | $1.13 \times 10^{-6}$ | |
| **L** | **m** | 25 | 0.5 | 40 | 0.5 |
| **U∞** | **m/s** | 2.5 | **125** | 2.5 | **200** |
| **Re** | **-** | $5.5 \times 10^7$ | | $8.8 \times 10^7$ | |
| **L** | **m** | 25 | 0.5 | 40 | 0.5 |
| **U∞** | **m/s** | 5.5 | **275** | 5.5 | **440** |
| **Re** | **-** | $12 \times 10^7$ | | $19 \times 10^7$ | |

**based on the water depth (Z or L)*

From Table 13 and Table 14, Froude number ranges from $0.13 \leq Fr \leq 0.35$ with corresponding model equivalent velocities $0.28$ m/s$\leq U_s \leq 0.77$ m/s whilst Reynolds number ranges from $5.5 \times 10^7 \leq Re \leq 19 \times 10^7$ with corresponding model equivalent velocities $125$ m/s$\leq U_s \leq 440$ m/s. Since the facility at CU can produce a maximum flow speed of around 1.7 m/s it is clear that Reynolds number similarity is impossible, whilst Froude number similarity for the range of conditions stated above is technically achievable. However despite the corresponding freestream flow speed for Froude similarity to a full scale prototype of 5.5 m/s being a realistic flow speed, it's above the anticipated maximum spring peak flow speed for economically feasible energy extraction of around 4.5 m/s (see Section 3.3.3). Bahaj et al., (2007) undertook a scaling analysis for the scaled model testing of an HATT and concluded that achieving Re similarity between a scaled and full scale model would result in a 100 mm diameter turbine rotating in excess of 1500 RPM. This is both unobtainable from a design point of view and is unfeasible with regards to hydrodynamics since it would entail large pressure gradients and induce excessive swirl into the surrounding flow. Bahaj et al., (2007) also concluded that maintaining Re similitude was impossible since the facility was not able to produce the high flow speeds that would be required. As a result, in both examples only Fr similarity was undertaken.

## 9.2 Test Facilities

In order to test a scale model of CarBine two testing facilities were identified: the flume in the hydraulics laboratory at Cardiff School of Engineering (herein referred to as CU) and the hydraulic flume at IFREMER (French Research Institute for Exploitation of the Sea) in Boulogne-sur-mer, France. The opportunity to test CarBine at IFREMER was provided by MARINET (Marine Renewable Infrastructure Network), an EU funded initiative, with aim to accelerate the development of marine renewable energy technologies, particularly wave, wind and tidal (MARINET, 2013b). An application was submitted and accepted in 2012 for a fully funded, transnational access to the test facility IFREMER for a period of 5 days.

Initial testing of CarBine and design optimisation was carried out at CU. Testing at IFREMER was then required to enable quantification of the blockage effects (see Section 9.5) whilst testing CarBine at CU, and to enable the testing of a two stage CarBine.

### 9.2.1 Cardiff University School of Engineering Hydraulic Flume (CU)

The hydraulic flume at CU is a re-circulating bi-directional hydraulic flume driven by an axial flow impeller powered by an electric motor with the return pipeline located underneath the flume, seen in Figure 52.

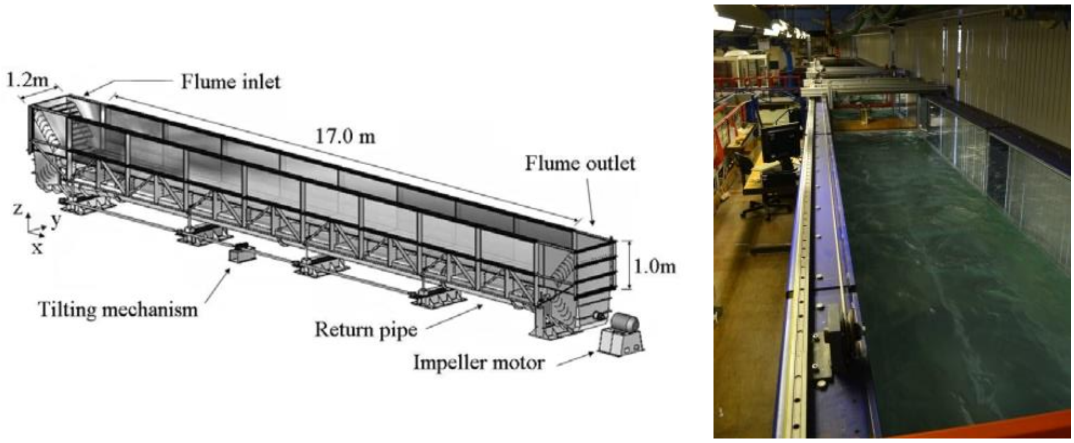

(a) (b)

**Figure 52 Hydraulic flume at CU (a) 3D view (Rauen et al., 2008) (b) working image**

The flume walls and bed are made of glass to enable visualisation of the flow. Access to the flume is achieved through an elevated walkway located along one side of the flume with plan access to the flume achieved via working tables suspended between the flume walls. To the author's knowledge, Challans, (2009) and Chrysafis, (2008) conducted the only previous testing of a tidal turbine using this facility, details of which are found in Section 7.5.

### 9.2.2 IFREMER Hydraulic Flume (IFREMER)

The hydraulic flume at IFREMER is a re-circulating hydraulic flume driven by an axial flow impeller that is powered by an electric motor, seen in Figure 53. The working section of the flume is located below the working platform, seen in Figure 53b. A side view of the working section can be accessed via a viewing window located at a lower level, seen in Figure 53c. Installation of equipment, e.g. a turbine is achieved via a travelling crane running above the flume. Previous testing of tidal turbines conducted at IFREMER include (Davies et al., 2013; Germain, 2008; Gregory et al., 2007; Maganga et al., 2009; Myers and Bahaj, 2009).

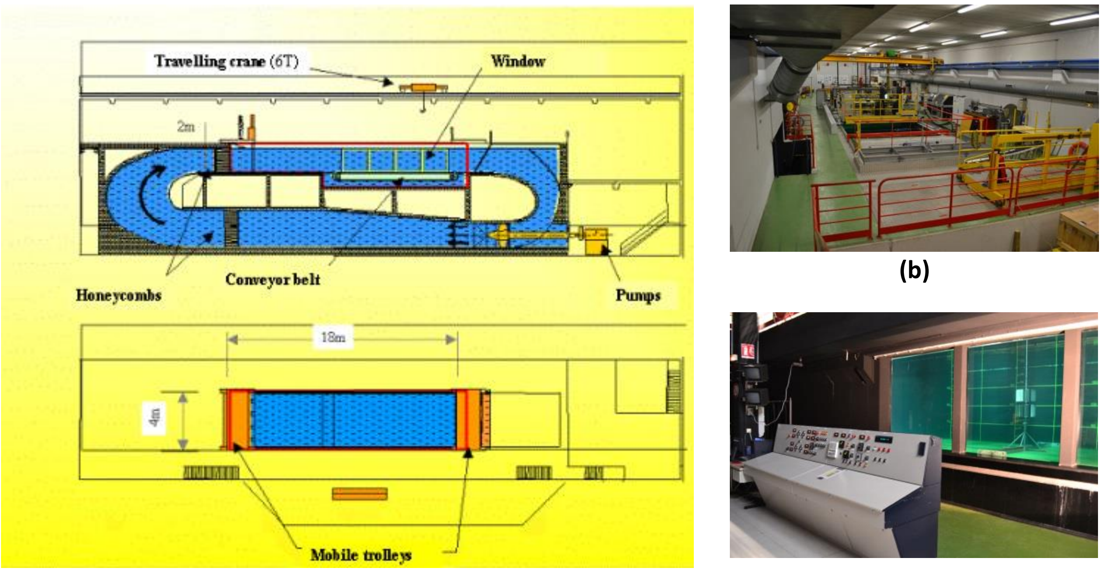

(b)

(a)

(c)

**Figure 53 Hydraulic Flume at IFREMER (a) Schematic (Germain, 2008) (b) working image (c) viewing section**

### 9.2.3 Working section dimensions and flow parameters for hydraulic flume at CU and IFREMER

Figure 54 and Table 15 show the working section dimensions and flow parameters of both the flume at CU and IFREMER.

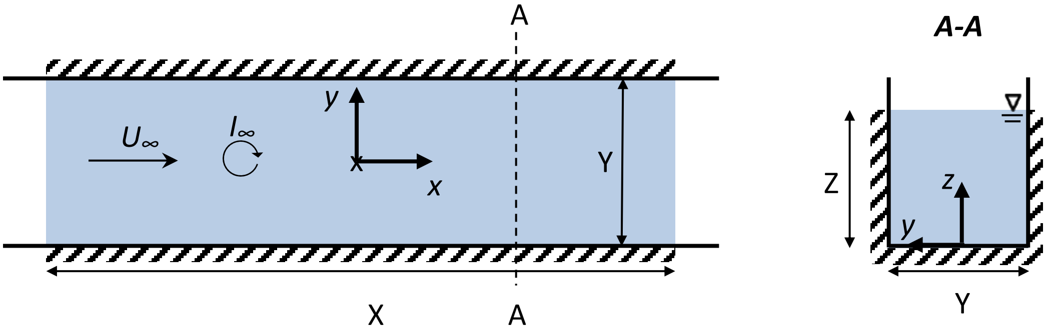

Figure 54 Hydraulic flume working section, with co-ordinate system

Table 15 Flume working section parameters for CU and IFREMER (Gregory et al., 2007)

| Symbol | Description | Units | CU | IFREMER |
|---|---|---|---|---|
| X | Length | (m) | 17 | 18 |
| Y | Width | (m) | 1.2 | 4 |
| Z | Depth | (m) | 0.5 | 2 |
| $U_\infty$ | Maximum flow speed | (m/s) | ≈1.7 | 2.2 |
| $I_\infty$ | Turbulence Intensity | % | ? | 5-25 |

## 9.3 CarBine Prototypes

Table 16 illustrates the evolution of CarBine's prototypes from prototype 1 (Chrysafis, 2008) to prototype 2 (Challans, 2009) to the current study, prototype 3. Prototypes 1 and 2 were based on a fixed 3-arm configuration, i.e. a $120^0$ phase angle; however other phase angles have yet to be tested. Prototypes 1 and 2 were also not designed with consideration to fitting a testing rig and testing at high flow speeds. Prototype 3 overcomes the issues faced with prototypes 1 and 2 (as described in Table 16) but in addition the disk supports enable numerous phase angles to be tested for CarBine. Rather than supported by fixed arms, holes can be drilled through the disks to enable the positions and the number of the flaps and thus the phase angle to be varied. Changing the phase angle will lead to optimisation of the design of CarBine.

Table 16 CarBine prototype development

<<<< Prototype Development

| | |
|---|---|
| **1**<br>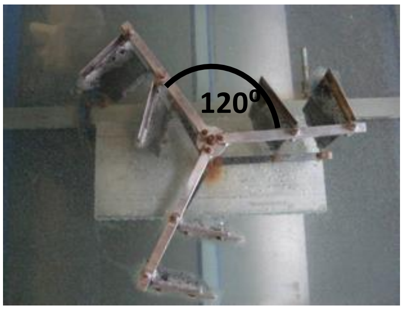<br> <br>**Figure 55 CarBine prototype 1 (Chrysafis, 2008)** | • Initial proof of concept.<br>• Fixed 3 arm configuration.<br>• Aluminium construction.<br>• Flaps movement restricted to 90°.<br>• Prototype begun to rust during testing.<br>D=0.4m; H=0.25m |
| **2**<br>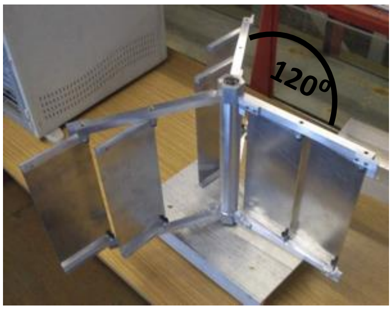<br> <br>**Figure 56 CarBine prototype 2 (Challans, 2009)** | • Increased robustness.<br>• Thicker vertical shaft, providing increased stiffness.<br>• Flaps can rotate up to 180°.<br>• Fixed 120° phase configuration.<br>D=0.4m; H=0.25m |
| **3**<br>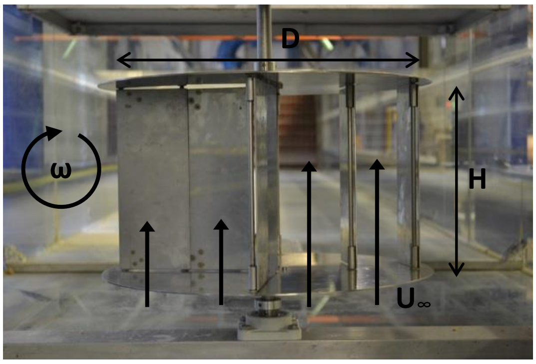<br> <br>**Figure 57 CarBine prototype 3** | • Constructed with non-corrosive material – stainless steel.<br>• Shaft is housed within waterproof stainless steel bearings.<br>• Designed as a "kit". Supporting disks rather than arms enables inter-changeable flap configurations.<br>• Increased stiffness on vertical shaft. Due to two sets of bearings, one at base and one at top of shaft, to restrict horizontal movement.<br>D=0.4m; H=0.25m |
| • Increased stiffness allows testing at higher flow speeds.<br>• Each flap rotates about a steel rod that is the length of the flap, permitting free rotation of flap with minimal friction.<br>• Longer shaft enables connectivity with turbine performance testing apparatus. | |

### 9.3.1 Prototype 3

Due to the range of performance values obtained from a literature review for experimentally tested Savonius turbines, seen in Figure 50, it was decided that testing an equally scaled Savonius with identical flow and blockage conditions at the same facility would provide direct comparison of CarBine and the Savonius. Therefore in addition to creating CarBine prototype 3, the designs of which can be seen in Figures 60 and 61, a Savonius turbine was also constructed which enabled a benchmark comparison of CarBine to a conventional drag type turbine. The design of which was a result of the Savonius review in Section 8 and is detailed in Figure 59 and Table 17.

The experimental models were designed and manufactured at Cardiff University. Both the geometry of the turbine and the Savonius were of equal swept area. A rotor diameter of 400mm and height of 250mm were chosen as a balance between maximising the generated torque (to reduce the influence of losses from the PTO on the results) and ensuring the blockage factor was kept to a minimum. The geometry of both models was sandwiched between 2 2mm thick disks. This not only ensured consistency in the flaps/bucket support between the turbine and the Savonius but also facilitated changes to the phase angle of CarBine that lead to design optimisation. The turbine and all its fixings were manufactured from stainless steel.

The variable during testing of Carbine was the angle between adjacent arms, the phase angle, seen in Figure 60. For each configuration, each arm supported 2 flaps. 2 flaps per arm was chosen since having a singular flap per arm would restrict the minimum phase angle, since flap collisions could occur for a phase angle <$90^o$ due to the larger sweep circle of a single flap. Each flap, cut from 2mm stainless steel sheet was hinged upon an axis extending the height of the turbine. Each axis was tapped and screwed to the disk at each end. From Figure 59a, the rotation of the inner flap Fi is restricted by stoppers positioned adjacent to the central shift whereas the rotation of the outer flap Fo is restricted by the axis of Fi. The length of each flap was 250mm, a clearance of 1mm was maintained between both the top and bottom edge of each flap by the inclusion of washers. During testing, both CarBine and Savonius configurations were aligned to ensure $\theta=0^o$ corresponded to an arm/bucket being aligned parallel and facing the direction of the flow, as seen in Figure 59.

Additionally a Savonius turbine with flaps (SF) was constructed, as seen in Figure 59c. Each bucket of the SF comprised of two flaps and two rigid sections. In Figure 59c the flaps are drawn as broken lines whilst the rigid sections are drawn as solid lines. Two equally sized flaps comprise the middle third of each bucket. When closed the flaps complete the full bucket shape, whereas when opened, the flaps reduce the pressure on the returning bucket through allowing the flow to pass through. The bucket dimensions of the SF are identical to the Savonius prototype, detailed in Table 17. The SF will act as a hybrid combining the principles of CarBine and the conventional Savonius. The aim of the SF is to increase the performance of the Savonius by reducing the negative torque experienced by the returning bucket of the Savonius through incorporating flaps into the buckets, similar to the work reviewed in Section 8.4. To the author's knowledge this design alteration has not previously been tested in a hydraulic environment. Ultimately a direct comparison can therefore be made between two turbine designs incorporating flaps: a purely drag force harnessing turbine, CarBine and a turbine harnessing lift and drag forces, Savonius. To enable direct comparison between turbine designs all prototypes are designed with equal swept areas, seen in Figure 59d and Table 17. A two stage CarBine (stacked along the z-axis) was also tested at IFREMER, the design of which will be a result of the design optimisation of CarBine during testing at CU. The aim of the two stage CarBine was to reduce the variation in power output during a revolution as discussed in Section 8.3.2. The dimensions of each stage of the turbine were identical to that found in Table 17 besides the height H which was equal to 2H for the two stage turbine.

All prototypes were housed between the same supporting disks and share the same support structure for each testing facility, eradicating any variances between the various prototypes besides their fundamental designs. During testing at CU the prototype was fixed in the flume through positioning the turbine shaft within a waterproof bearing housed in a horizontal stainless steel bar lying on the flume bed which was attached to pre drilled holes on the flume walls, see in Figure 58a. The holes along the flume walls were spaced at 1 m apart therefore enabling the position of CarBine in the streamwise direction to be altered when conducting the array study see Section 9.4.3.3. Due to the increased depth Z at IFREMER ($Z_{IFREMER}=4Z_{CU}$) a different support structure had to be used. Similar to CU, the support structure at IFREMER was also fixed to a horizontal bar lying across the width Y of the flume, seen in Figure 58b. For both CU and IFREMER the base was installed first and the turbine subsequently lowered into position until the shaft connected with the bearing in the base. At IFREMER a diver was required to install the support structure and guiding cone was used atop of the support structure to simplify guiding the turbine into position.

**Table 17 Prototype dimensions for CarBine, Savonius and SF**

| Dimension | ALL | Dimension | CarBine (C) | Savonius (S) | Savonius with Flaps (SF) |
|---|---|---|---|---|---|
| **D** | 0.4 | **Fi** | 0.1 | - | - |
| **$D_D$** | 0.42 | **Fo** | 0.1 | - | - |
| **$D_O$** | 0.01 | **$B_D$** | - | 0.235 | 0.235 |
| **$S_D$** | 0.02 | **$B_O$** | - | 0.035 | 0.035 |
| **H** | 0.25 | **BFi** | - | - | $(\pi B_D/6)=0.123$ |
| **$D_t=B_t=F_t$** | 0.002 | **BFo** | - | - | $(\pi B_D/6)=0.123$ |

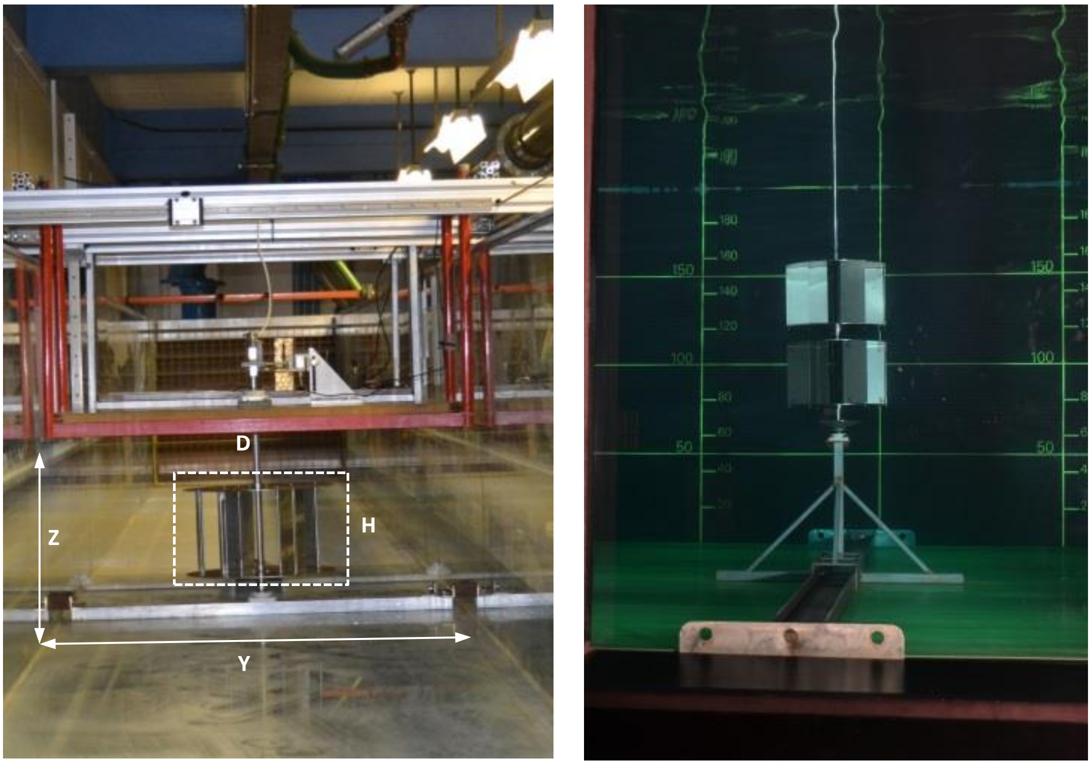

(a) (b)

**Figure 58 Supporting structure for (a) CU (b) IFREMER**

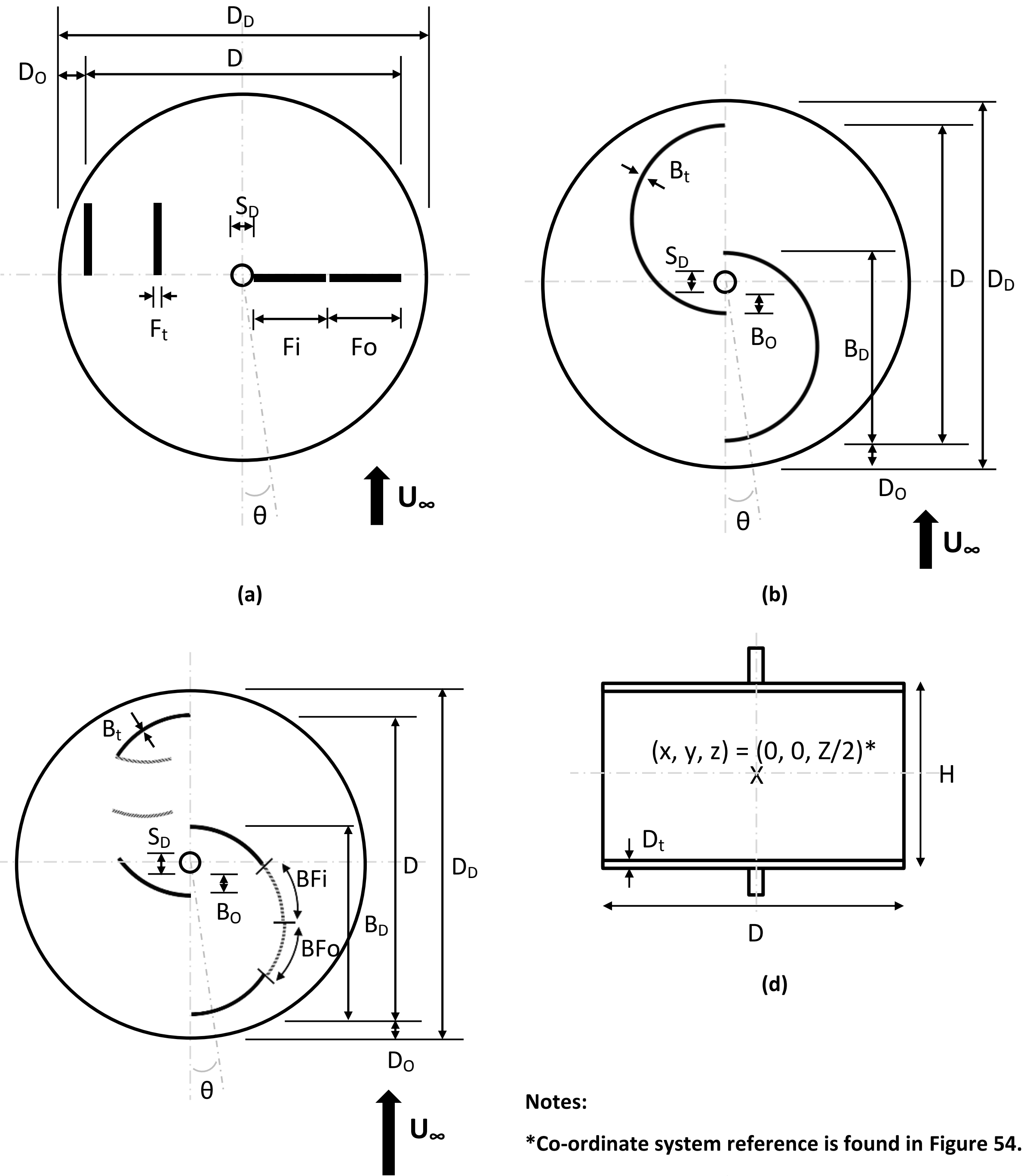

**Notes:**

***Co-ordinate system reference is found in Figure 54.**

**For clarity only a 180$^0$ phase CarBine is shown in (a) further details of CarBine configurations can be found in Figure 60.**

**Savonius with flaps (c)-flaps shown by broken line.**

**Dimension values can be found in Table 17.**

**Figure 59 Prototype schematic (a) CarBine (b) Savonius (c) SF**

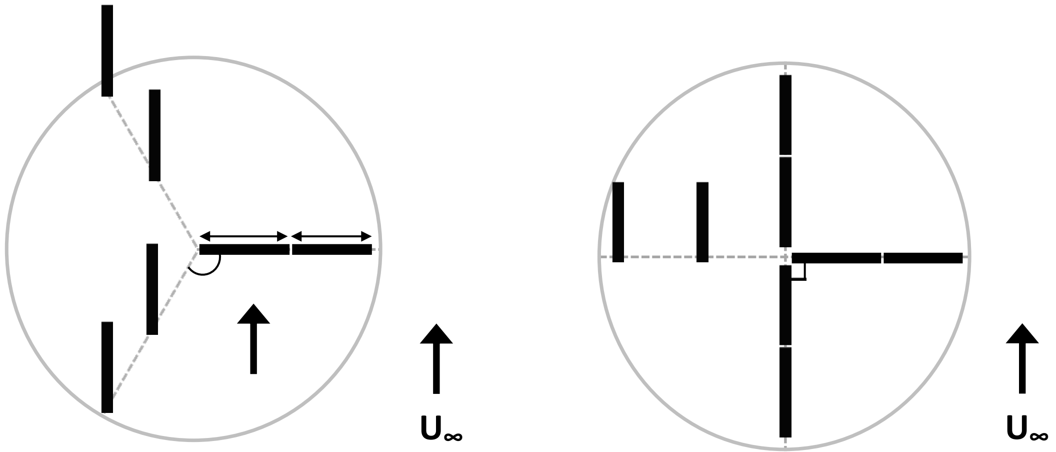

*“3 Arm CarBine”* **(C3)**

*“4 Arm CarBine”* **(C4)**

**(a)** **(b)**

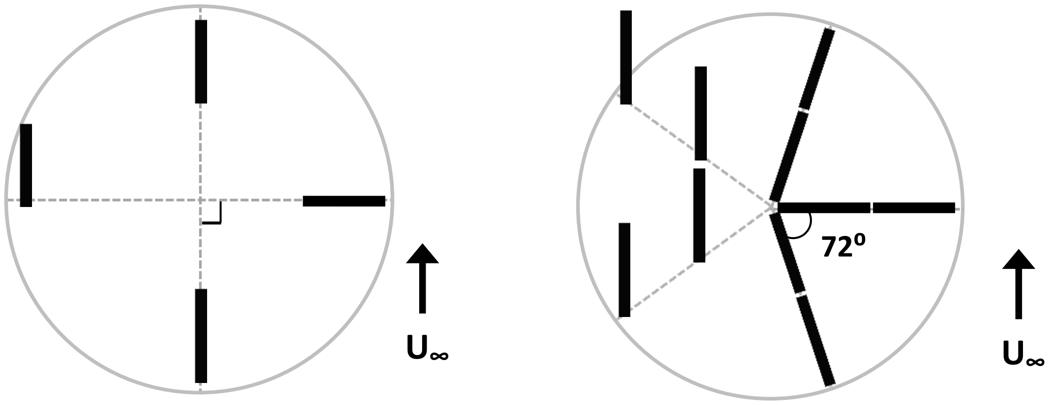

*“4 Arm outer flaps only”* **(C4O)**

*“5 Arm CarBine”* **(C5)**

**(c)** **(d)**

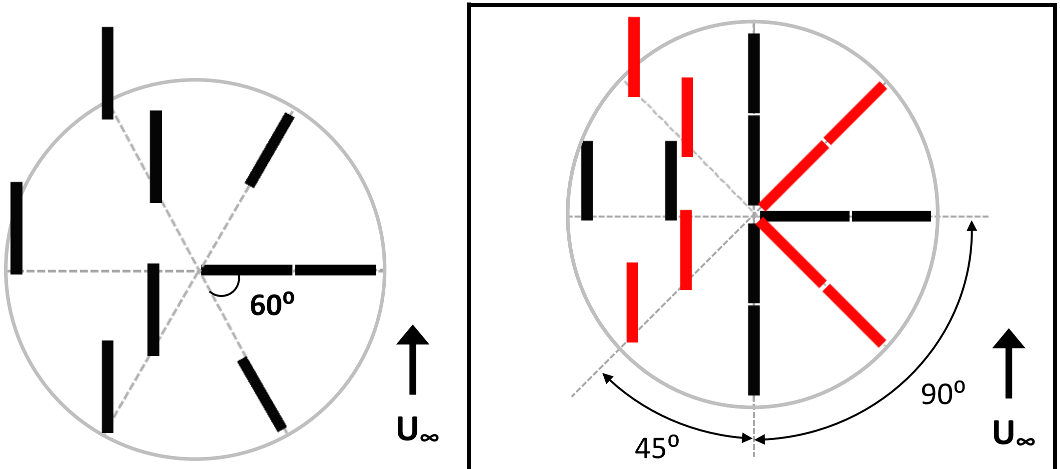

*“3 Arm + 3 Offset CarBine”* **(C3+3)**

*“2 Stage 4 Arm 45° Offset”* **(C4_2)**

**(e)** **(f)**

**Notes:**
**All flaps have equal dimensions, details found in Table 17.**
**(e) is the closest representation of a 6 arm CarBine without flaps colliding.**
**(f) was tested at IFREMER only.**

**Figure 60 CarBine configurations for physical testing (a) C3 (b)C4 (c)C4O (d)C5 (e)C3+3 (f)C4_2**

## 9.4 Experimental Programme

Based on Section 0, characterising the performance and finding the optimum operating point of a tidal stream turbine ($C_p$max/λ) is achieved through measuring the following parameters: $U_\infty$, T and ω which will result in the calculation of $C_p$, λ and $C_t$.

### 9.4.1 Velocity Measurements, $U_\infty$

#### *9.4.1.1 Acoustic Doppler Velocimeter (ADV)*

In order to measure the performance of the turbine prototypes an accurate measurement of the freestream flow speed $U_\infty$, within the flume was required prior to the installation of a turbine, as described in Sections 0 and 5.1. At CU there was a volumetric flowmeter located within the re-circulating pipe of the flume however a more accurate velocity measurement was required at the precise future location of the turbine within the flume working section: x, y, z=[0, -0.2≤y≤0.2, 0.25≤z≤0.75]m (co-ordinate system shown in Figure 54). At IFREMER detailed flow measurements for the proposed flume conditions were already available (Gaurier et al., 2013) and therefore were not needed to be collected again during this study.

The flow speed at CU was controlled through varying the pump power, pp(%) of the axial flow impeller. An initial study was carried out to identify the flow characteristics of the flume for various pump powers, using a Nortek Vectrino which is an acoustic doppler velocimeter (ADV). Using the ADV resulted in 3D point measurements (streamwise $U_x$, spanwise $U_y$ and depthwise $U_z$) of the flow speed within the test section. The ADV was used for flow profiling within the test section, measuring vertical and horizontal profiles of the flow speed for a range of pump powers. The freestream velocity $U_\infty$ is calculated as a resultant of the three velocity components measured using the Vectrino ADV, using

$$U_\infty = \sqrt{U_x^2 + U_y^2 + U_z^2} \tag{32}$$

The non-dimensional velocity $U^*$ is calculated from the freestream velocity $U_\infty$ and the turbine cross-section area averaged freestream velocity $\overline{U}_\infty$ using

$$U^* = \frac{U_\infty}{\overline{U}_\infty} \tag{33}$$

The ADV consists of 4 receiving transducers and a transmit transducer and measures the flow speed based on Doppler effect. The ADV transmits pairs of sound pulses into the water and based on the changed pitch of the echoes (the Doppler shift) it can determine the flow speed. Since sound will not reflect off water, seeding particles were introduced to the water to provide a medium for the reflection of the sound pulses. Since the particles possess similar density to that of water, they remain suspended in the flow and travel at the speed of the water. Thus the measured velocity was equal to that of the water.

The Vectrino software displays the real time data acquisition and also analyses various parameters to ensure accurate data collection, including Signal to Noise ratio (SNR) and Correlation (%). The user guide (Nortek AS, 2009) provides guidelines on achieving the desired values for these parameters and recommends values of >15 and >90% for the SNR and correlation respectively. The Nortek ADV captures the streamwise $U_x$, spanwise $U_y$, and depthwise $U_z$, velocity components of the flow at a maximum sampling rate of 200 Hz. A time independency study was carried out to determine the sampling period and it was determined that a sampling period of 120 s for each data point was a sufficient compromise of both accuracy and time expense.

A detailed profile of the flow was obtained through measuring both the vertical and horizontal flow profiles at the location of where the turbines were to be placed, x,y=[0,0](m). Vertical profiles were taken every 100 mm for -500≤y (mm)≤500, with each vertical profile consisting of 8 data points, z=[75, 125, 175, 225, 250, 310, 375, 410](mm). Equal intervals between the vertical profile data points was the initial aim, however there are locations whereby the correlation levels dip below 50% due to interference from the glass bed of the flume, termed weak spots (Nortek AS, 2002).

When these points were incurred the ADV was moved to a nearby vertical position where the effect was absent.

All results obtained using the Vectrino ADV were analysed using the WinADV software (Wahl, 2012). The software was used for batch processing of the ADV results and for filtering anomalous data due to the low signal strength based on the following criteria:

a) De-spiking and removal of communication errors ; and
b) Using (a) and Correlation > 70% with SNR>10%.

Wahl, (2000) provided guidance on the criteria for filtering and the general use of WinADV. Further visualising of the freestream flow was achieved through contour plots which were drawn using TechPlot.

#### *9.4.1.2 Particle Image Velocimetry (PIV)*

PIV is a technique for measuring fluid flow and unlike commonly used flow measurement apparatus such as Acoustic Doppler Velocimeters (ADVs) which result in point measurements of velocity, PIV has the ability to undertake global velocity measurements. In addition PIV is non-intrusive, measuring the velocities of small seeding particles from images captured by a camera from above the water as opposed to a submerged probe which invariably interfered somewhat with the flow of water it was measuring. PIV has transformed the qualitative analysis of particle flow visualisation to that of a quantifiable flow analysis. PIV has widely been used to capture two velocity components, namely streamwise velocity component $U_x$, and spanwise velocity component $U_y$, of fluid flow. Stereoscopic techniques can be utilised to obtain the third component $U_z$ (Prasad, 2000). The results of PIV are comparable to output of computational fluid dynamics, i.e. the ability to plot large eddy simulations and real-time velocity vector/contour maps (Dobrev and Massouh, 2012).

The basic principle of a PIV system is the acquisition of a velocity flow field from images of flow on a chosen plane, in which small seeding particles are illuminated. A typical PIV system comprises of several sub-systems: a tracer particle seeded flow, a high sensitivity high speed CCD camera, a light source for illumination of the tracer particles on a chosen plane and a computer for data acquisition and extraction of information of tracer particle positions (Prasad, 2000). The post processing of these images using specialist PIV software calculates the velocity magnitudes of the particles and produce a vector field. The target area for the PIV images is illuminated via a light sheet emitting light pulses at a given interval. The camera, positioned perpendicular to the light sheet, captures images of the target area for each light pulse. The PIV analysis software uses two successive image frames and measures the distance travelled by particles from one frame to the next. The velocity is indirectly calculated from the distance travelled in a given time period of a tracer particle in successive images.

A PIV system was designed and tested within the CU flume. However, issues arose due to the light sheet. The aim was to achieve a thin collimated light (≈5mm) with the camera's depth of field set to a similar depth, since thick light sheets leads to out of plane particles being measured leading to errors in cross-correlation between successive image frames. However due to the width of the CU flume the light sheet suffered excessive diffraction prior to reaching the test window in the centre of the flume, this resulted in a thick light sheet leading to errors in the analysis software. The PIV system's light source was therefore deemed inadequate for use in the CU flume. An investigation using the PIV and static Savonius configurations was carried out in a smaller flume at the same laboratory but since this had not become directly relevant to the outcome of this study, it can be found in Appendix B. The investigation was also published in the proceedings of the 35th International Association for Hydro-Environment Engineering and Research (IAHR) World Congress (Harries et al., 2013).

### 9.4.2 Power Take-off (PTO), T and ω

The PTO in laboratory testing is used to measure the power generated by the turbine through causing the turbine to do work by applying a measured negative torque to oppose the torque generated from the hydrodynamic forces. This enables the TSR of the turbine to be varied so that performance curves such as, $C_p$-λ can be drawn and the peak operating condition ($C_p$max/λ) found, see Section 0. As opposed to commercial operating turbines whereby power is transmitted to the national electricity grid, during laboratory testing the power generated is typically dissipated via a series of resistors (when using an electrical PTO) or via heat through applied friction to a disk brake (when using a mechanical PTO). Studies using an electrical PTO, typically consisting of a generator and a series of resistors include Abraham et al., (2012); Bahaj et al., (2007a, 2007b) and Yuen et al., (2009) and studies using a mechanical PTO, typically utilising a dynamometer and a disk brake include Armstrong et al., (2012); Han et al., (2013) and Shiono et al., (2002). Some studies use a PTO system whereby the turbine is driven for a range of fixed angular velocities using a motor/servomotor, rather than the turbine rotating due to the hydrodynamic forces acting upon it (Li and Calışal, 2010; Maître et al., 2013; McAdam et al., 2013b; O'Doherty et al., 2009). This system will not be adopted since this study aims to quantify the P, T and ω of CarBine as a function of the rotated angle θ; to enable analysis on the variability of the power output for different configurations.

#### *9.4.2.1 Electrical PTO*

For this study initially an electrical set-up was trialled. As seen in Figure 61 the system consisted of a synchronous permanent magnet generator (PMG) connected vertically in line with the turbine shaft, the PMG converts mechanical power into electrical energy. Connected to the PMG was an electrical circuit consisting of a series of resistors and a digital multimeter.

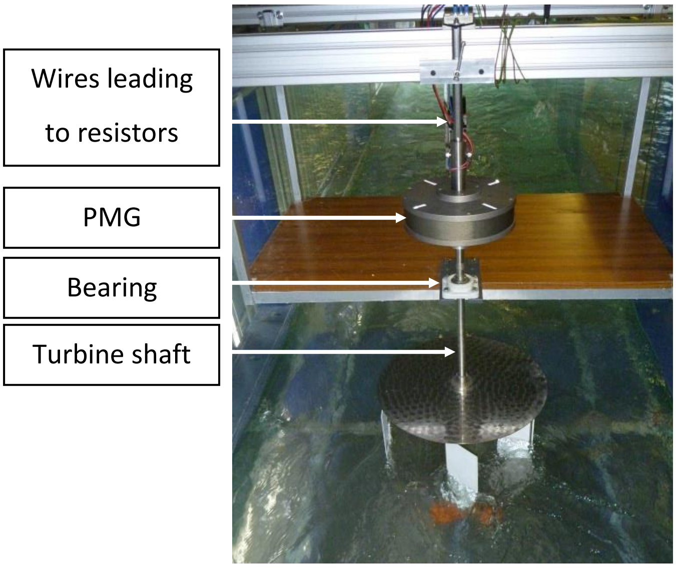

**Figure 61 Electrical PTO system**

A load was applied to the PMG in order to vary the TSR of the turbine. Loading was applied via a series of resistors. Decreasing the resistance R (ohms) resulted in an increase in current I (amps), which in turn increases the torque induced by the PMG on the turbine shaft. In order to allow the turbine to rotate with the minimum load, theoretically an infinite amount of resistance would be applied to the circuit in order to create almost free-wheeling conditions, i.e. the maximum TSR, of the turbine. Prior to undertaking studies on the turbine the torque constant K' of the generator was obtained. This was achieved via coupling the generator to a lathe and subjecting it to known angular velocities. The linear gradient of the voltage V versus ω plot is the torque constant, K'. The torque of the turbine was subsequently calculated using Equation (34).

$$T = K'I \tag{34}$$

However from initial trials only a small range of TSRs could be obtained using the system since the operating angular velocity of the turbine was not within the rated speed range of the generator. As a result when loading was applied to the turbine, the lower angular velocity meant the turbine could not overcome the internal friction within the PMG. Inherent losses in a PMG are described in detail in Yuen et al., (2009). In order to overcome this issue and continue using an electrical PTO a gearing system would be required. A tachometer was used to measure the angular velocity of the turbine for the electrical PTO. The tachometer operated through attaching reflective strips to the surface of the rotating PMG. Upon each revolution the laser from the tachometer reflected off the strip and caused the tachometer counter to increase. The output from the tachometer could be either in rpm or as a counter. Initially the RPM setting was trialled, which gave an average rpm but the accuracy was not sufficient to capture small changes in TSR. Subsequently the counter mode was used with 8 reflective strips on the rotating surface along with a stopwatch. This enabled the angular velocity to be measured over a fixed time interval and was accurate to an eighth of a revolution. In turn this enabled the differences in angular velocity for small variations in TSR to be measured. This PTO method only provided a time averaged value for the generated torque and does not synchronise with the tachometer, therefore the changing torque and angular velocity with rotated angle could be measured. As a result a mechanical PTO system was designed and used.

#### *9.4.2.2 Mechanical PTO*

To overcome the issues faced with the electrical PTO method, a mechanical PTO system using a disk brake was manufactured at CU. The components of the PTO system can be seen in Figure 62 and Table 18. The load applicator consists of a fixed brake caliper comprising of two polytetrafluoroethylene (PTFE) pads (shown in red in Figure 63) which lie above and below the disk brake. As seen in Figure 63 an increase in the applied load is achieved through turning the screw of the caliper, which in turn applies greater friction to the brake disk through the PTFE brake pads and reduces the rotational speed-lowering the TSR from free-wheeling conditions, i.e. max TSR, when no load is applied. The generated torque is directly measured by a 50 N range load cell on a 100 mm lever arm. The angular velocity is measured by an in-line shaft quadrature encoder with 2000 pulses per revolution resulting in the rotated angle being measured every $0.18^{o}$. Data from the encoder and load cell is streamed to a desktop PC through a USB connection via a Labjack data logger, at a frequency of 100 Hz for a sampling period of 120 s; resulting in a sample of 12000 values. This system synchronises both $T$ and $\omega$ data with respect to rotated angle, $\theta$. For the

CarBine array study since two turbines would be tested an additional, identical mechanical PTO was manufactured.

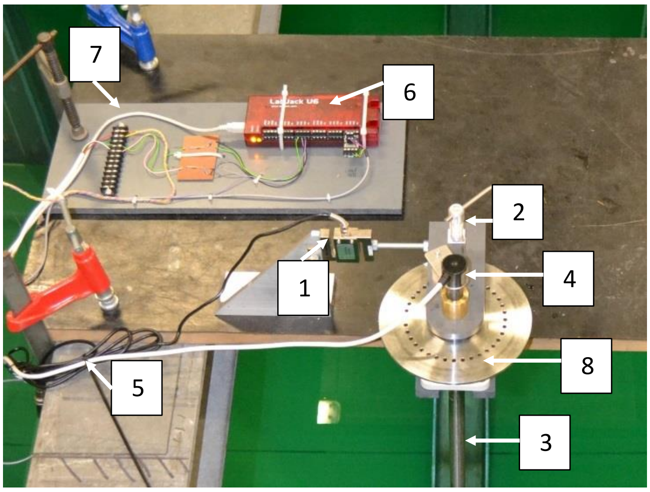

| Component | Description |
|---|---|
| 1 | Load Cell |
| 2 | Load Applicator |
| 3 | Turbine Shaft |
| 4 | Encoder |
| 5 | Data cables to Labjack |
| 6 | Labjack |
| 7 | Data cable to PC |
| 8 | Brake Disk |

**Figure 62 The PTO system being used at IFREMER**

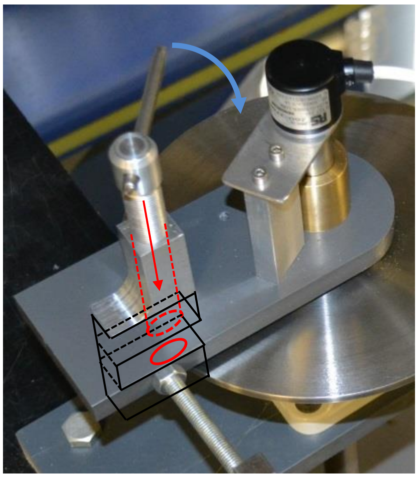

**Figure 63 Details of brake caliper and pads (component 2 from Figure 62)**

### *9.4.2.3 Data Acquisition Software*

The data was viewed, manipulated and recorded in real-time using Daqfactory Express software. Figure 64 displays the CarBine data acquisition program user interface that was created for the testing and Table 19 includes key descriptions of the interface and program. The output of the program is a csv file for each data point, e.g. for dynamic testing this will be for each TSR and for static testing this will be for each azimuth angle, see Section 9.4.3 for further details. The csv file is then inserted and analysed using a performance analysis template created on Microsoft Excel; meaning the measured data is analysed and performance curves for the turbine are updated in real time during testing.

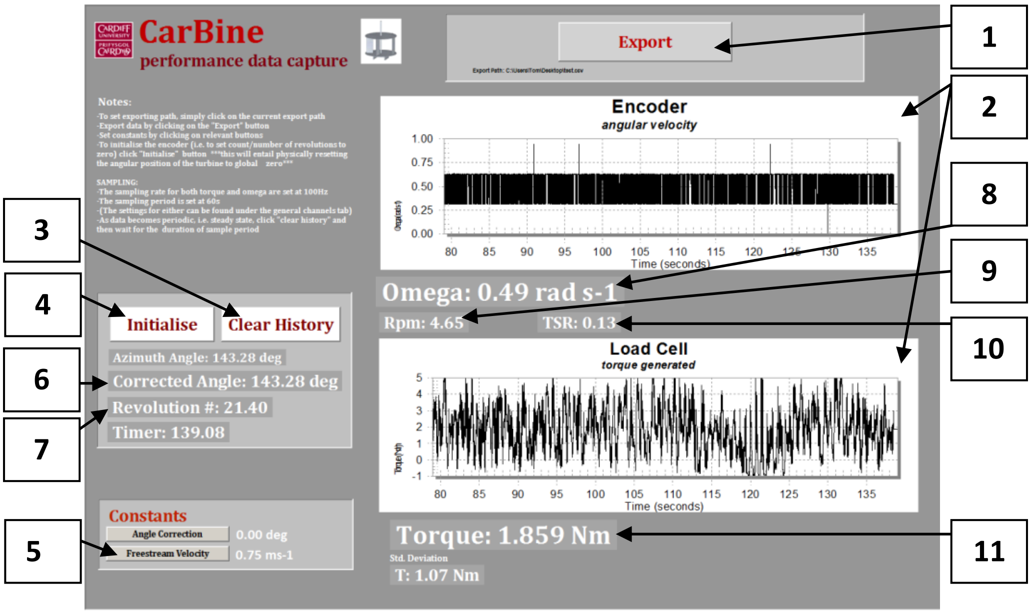

Export Path: C:\Users\Tom\Desktop\test.csv

Notes:
-To set exporting path, simply click on the current export path
-Export data by clicking on the "Export" button
-Set constants by clicking on relevant buttons
-To initialise the encoder (i.e. to set count/number of revolutions to zero) click "Initialize" button ***this will entail physically resetting the angular position of the turbine to global zero***

SAMPLING:
-The sampling rate for both torque and omega are set at 100Hz
-The sampling period is set at 60s
-(The settings for either can be found under the general channels tab)
-As data becomes periodic, i.e. steady state, click "clear history" and then wait for the duration of sample period

Azimuth Angle: 143.28 deg
Corrected Angle: 143.28 deg
Revolution #: 21.40
Timer: 139.08

Angle Correction 0.00 deg
Freestream Velocity 0.75 ms-1

Omega: 0.49 rad s-1
Rpm: 4.65
TSR: 0.13

Torque: 1.859 Nm
Std. Deviation
T: 1.07 Nm

**Figure 64 Data Acquisition user-interface for CarBine testing**

**Table 19 Key and descriptions for Figure 64**

| Key | Description |
|---|---|
| 1 | Clicking "Export" will results in the previously logged 1200 data points being exported to the directory stated below the button as a .csv file. |
| 2 | Both charts change in real-time and contain only the previous 1200 data points i.e. 120 s sample period at a sampling frequency of 100Hz. |
| 3 | "Clear History" is clicked in between readings to ensure no previous data is stored and subsequently logged for the next data set |
| 4 | Clicking initialise is done at the beginning of the experiment only. This sets the absolute angular position of the turbine. This also resets all of the variables. |
| 5 | "Freestream Velocity" is user inputted and is used to calculate the TSR (10) |
| 6 | Calculates the azimuth angle, θ:<br>*AZIMUTHANGLE.AddValue((((E1[0]/2000))*360))-(floor(((E1[0]/2000)))*360))* |
| 7 | Calculates the number of revolutions during the current sampling period:<br>*NOREVS.AddValue(abs(E1[0]/2000))* |
| 8 | Calculates ω (rad/s):<br>*OMEGA.AddValue((((((E1[0] - E1[1])/(E1.time[0] - E1.time[1]))/2000)*60)*((2*Pi())/60)))* |
| 9 | Calculates the RPM:<br>*RPM.AddValue((((E1[0] - E1[1])/(E1.time[0] - E1.time[1]))/2000)*60)* |
| 10 | Calculates the mean TSR over the sampling period:<br>*Mean(((0.2*omega)/velocity)[0,1200])* |
| 11 | Calculates the generated T (Nm):<br>*((Value*-370.15)*0.1)+56.004*<br>Value -raw reading from the load cell<br>370.15 –value from load cell calibration data sheet provided by supplier<br>56.004 -value for offsetting T to zero at beginning of testing |

**Notes: [0] and [1] refer to the current and previous sample point respectively; E1 and T1 are the raw values obtained from the encoder and load cell respectively; Refer to LabJack application guide (AzeoTech Inc., 2009) for details on the code used**

### 9.4.3 Data Collection Procedures

The following sub-sections include the details of the procedures adhered to during both dynamic and static testing of the turbine prototypes. Dynamic testing was required in order to gain the following performance curves: $C_p$ vs. λ, $C_t$ vs. λ and curves of T vs. θ and ω vs. θ for the peak operating condition ($C_p$max/λ). Static testing was required in order to quantify the self-starting ability of the prototypes through producing $C_t$ vs. θ curves.

#### 9.4.3.1 *Dynamic Testing*

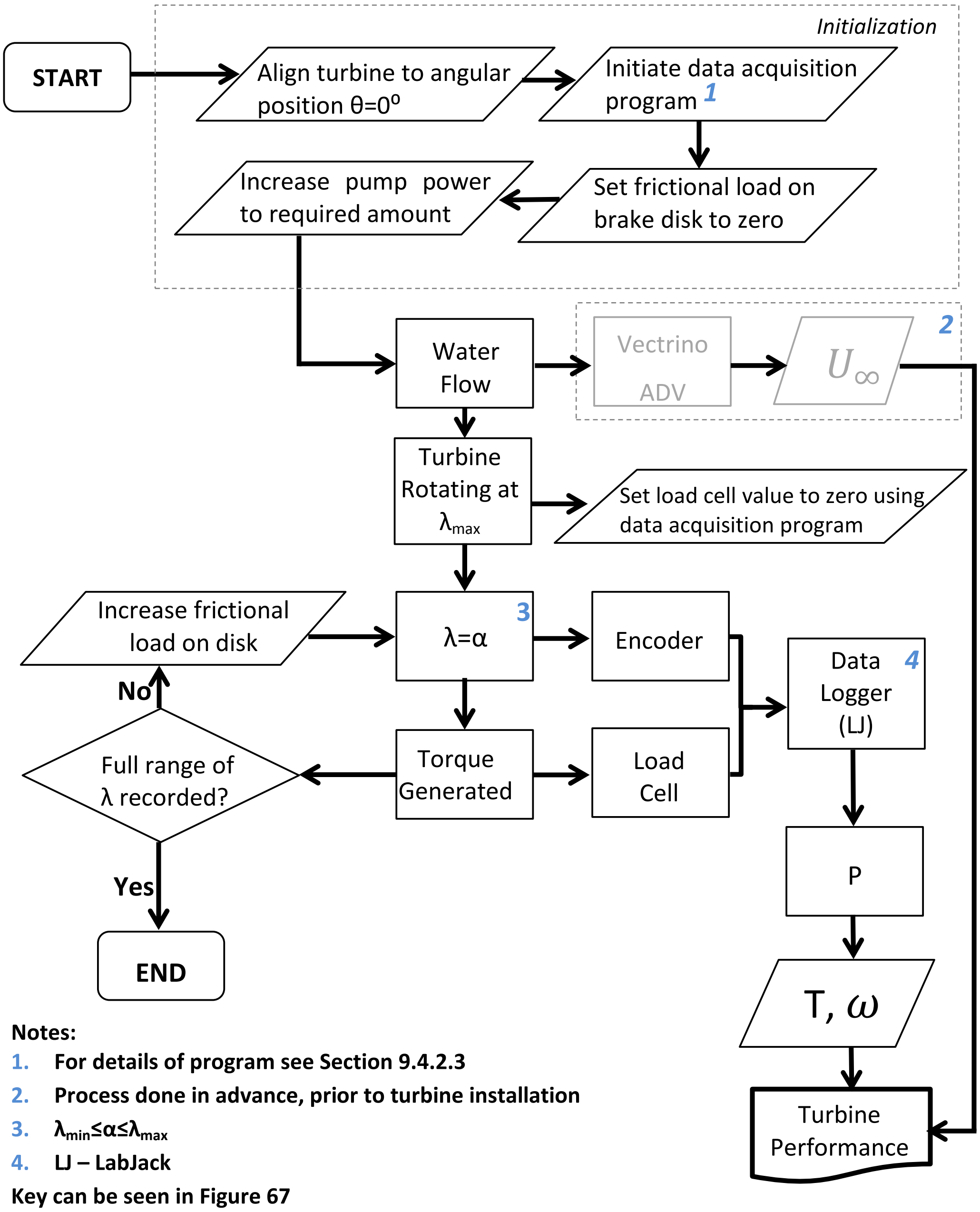

Notes:
1. For details of program see Section 9.4.2.3
2. Process done in advance, prior to turbine installation
3. $\lambda_{min} \leq \alpha \leq \lambda_{max}$
4. LJ – LabJack

Key can be seen in Figure 67

Figure 65 Flowchart of experimental data capture for dynamic testing

**Figure 66 Key for flow diagrams**

For a given turbine and U∞, a data set will consist of 10 data points ranging from $\lambda_{max}$ to $\lambda_{min}$ that are collected using the data capture process for dynamic testing described in Figure 65. Data capture begins with the turbine operating at $\lambda_{max}$ at which the reading on the load cell is reset to 0 Nm, because whilst operating at $\lambda_{max}$ the turbine has no load applied (T=0 Nm) and is rotating at freewheeling conditions. Since no power is generated at the freewheeling condition (see Equation (6)), the inherent residual value in the load cell must be zeroed to enable all values of generated torque for subsequent λ values to be made relative to that at freewheeling conditions. After recording the data for the current operating condition further load is applied to the turbine, this is repeated 10 times until the turbine reaches $\lambda_{min}$, beyond which the turbine stalls. Dissemination of the data will provide curves for $C_p$ vs. λ, $C_t$ vs. λ and curves of T vs. θ and ω vs. θ for the peak operating condition ($C_p$max/λ) for a given prototype and U∞. Comparing the results of various CarBine configurations will support design optimisation.

### 9.4.3.2 *Static Testing*

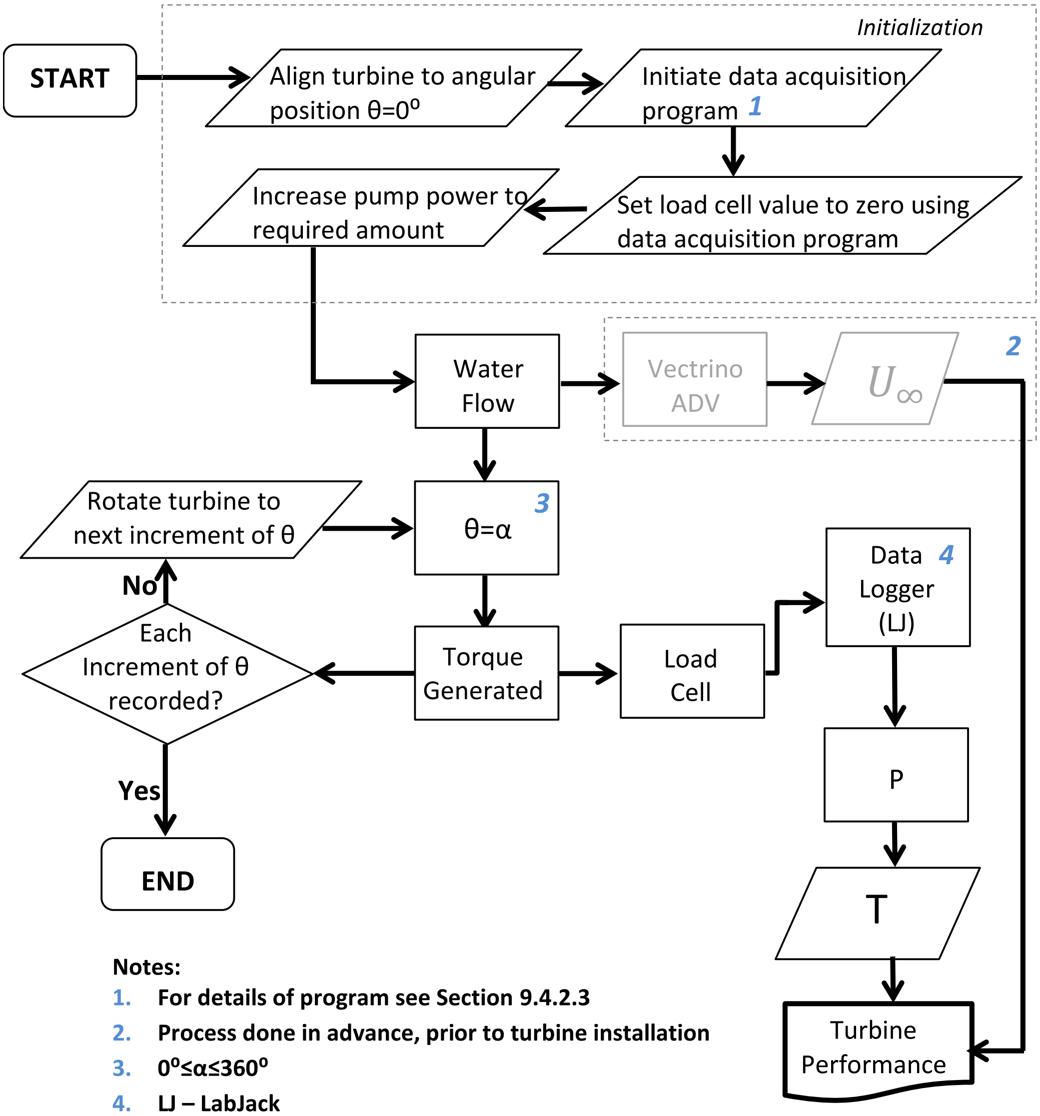

**Notes:**

1. **For details of program see Section 9.4.2.3**
2. **Process done in advance, prior to turbine installation**
3. **$0^o \leq \alpha \leq 360^o$**
4. **LJ – LabJack**

**Key can be seen in Figure 67**

**Figure 67 Flowchart of experimental data capture for static testing**

Unlike the dynamic testing no load applicator is used during the static testing, instead holes were drilled in the disk brake at $10^o$ increments. The disk brake could then be locked in place at each of the increments for $0^o \leq \theta \leq 360^o$, the data collection process of which is illustrated in Figure 67. Dissemination of the data will provide the curve for $C_t$ vs. θ for a given prototype and $U_\infty$.

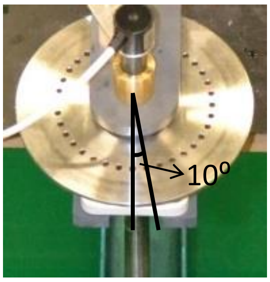

**Figure 68 Brake disk static increments**

#### *9.4.3.3 2 CarBine array testing*

Figure 43, shows that CarBine has the potential advantage of dense array spacing. For physical testing of such an array, two identical CarBine prototypes were manufactured for testing at CU, as seen in Figure 69. The study was based on the results of design optimisation of CarBine from the dynamic and static testing with regards to the optimum phase angle and number of flaps. From Figure 70 CarBine 1 operated at its optimum λ (based on $C_p$max/λ) whilst performance data was captured for CarBine 2 at varying streamwise X, and spanwise distances Y, downstream of CarBine 1. CarBine 2 was also tested for rotation in both the clockwise A (identical to CarBine 1) and anti-clockwise B direction. Both CarBine 1 and 2 were identical in size and configuration. The data capture procedure for CarBine 2 in the array testing was identical to that for the dynamic testing shown in Figure 65 besides that CarBine 1 was also operating upstream of CarBine 2 at its optimum λ. The λ of CarBine 1 was regulated using the load applicator and monitored using the data acquisition program, seen in Figure 64. Other twin turbine interaction studies include Aldoss and Obeidat, (1987); Golecha et al., (2012) and Li and Calışal, (2010). However these studies use larger separation distances than perceived for this study, using distances ranging from 3D to 8D separation in the streamwise direction, whereas this study is looking at distances from 1D to 4D. Golecha et al., (2012) concluded that for a pair of in line Savonius turbines, the downstream turbine achieves similar efficiencies to that of the upstream turbine at a distance of 8D; the aim of CarBine is to reduce this distance.

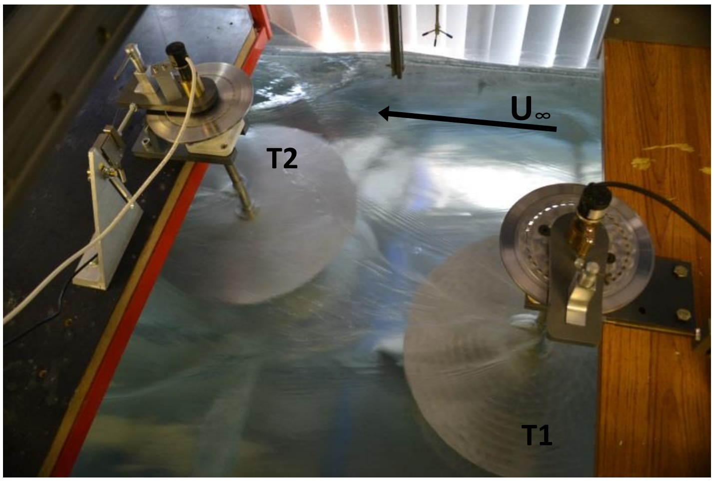

**Figure 69 Image of CarBine array testing at CU**

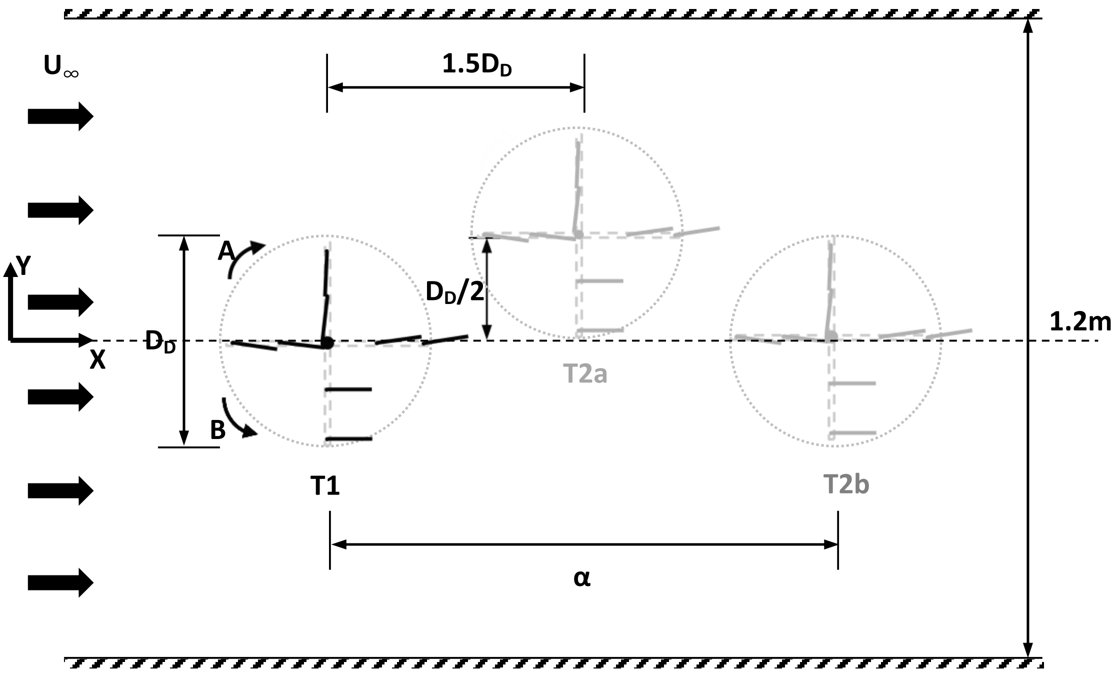

Figure 70 Schematic of two CarBine array study

## 9.5 Blockage Effect

Inherent in flume testing of turbines (wind or hydraulic), a solid blockage effect is the result of the reduction in the working section area for the flow to pass through due to the presence of a turbine. Adhering to Bernoulli's principle, the reduction in area produces an increase in the freestream flow speed in the vicinity of the turbine. The blockage factor $\gamma$, is calculated using the area ratio

$$\gamma = \frac{A}{ZY} \tag{35}$$

Using Table 15, Table 17 and Equation (35) the blockage factor, $\gamma$, at both CU and IFREMER are as follows

$$\gamma_{CU} = \frac{HD_D}{ZY} = \frac{(0.25 \times 0.4)}{(0.5 \times 1.2)} = 0.17 \tag{36}$$

$$\gamma_{IFREMER} = \frac{HD_D}{ZY} = \frac{(0.25 \times 0.4)}{(2 \times 4)} = 0.01 \tag{37}$$

Studies using wind tunnels by Maskell, (1963); Pankhurst and Holder, (1952); Pope and Harper, (1966) recommend $\gamma = 0.01 - 0.1$ for tunnel testing but for larger area ratios they produced blockage factors which are used to correct the undisturbed flow speed to account for the blockage effect; examining Equations (36) and (37), a blockage correction factor is therefore required for the CU results but not for the IFREMER results. A review of the wind tunnel blockage correction methodologies can be found in Ross and Altman, (2011). Since power is directly proportional to the cubed of the undisturbed velocity, failing to account for the flow acceleration caused by the blockage could result in exaggerated performance results. Studies that have accounted for blockage effects in their results include A.S. Bahaj et al., (2007b); Chen and Liou, (2011) and Kumbernuss et al., (2012). Whelan et al., (2009) conducted both a numerical and physical model study of the blockage effect and found $C_p$max and the range of λ to be reduced by 50% for an unblocked case compared to a $\gamma$ =0.64. The techniques most applicable to this study are the Pope and Harper and the Alexander method (based on the Maskell method).

### 9.5.1 Pope and Harper method

The Pope and Harper method calculates a corrected flow speed $U_c$, accounting for blockage, using the following equation

$$U_c = U_\infty(1 + \varepsilon_t) \tag{38}$$

where $\varepsilon_t$ is a correction factor for “wind tunnel models of unusual shapes”, and is calculated as follows

$$\varepsilon_t = \frac{1}{4}\frac{A}{ZY} \tag{39}$$

This technique is based upon a fixed swept area but the swept area of both CarBine and the Savonius varies during a revolution. For estimation purposes, the maximum swept area during a revolution will be used for both CarBine and Savonius, which occurs at θ=90$^o$, to calculate the blockage factor.

### 9.5.2 Alexander method

As an adaption of the Maskell method, Alexander and Holownia, (1978) compared the blockage effects of a flat plate and a Savonius bucket perpendicular to the flow, making this method directly applicable to this study.

$$\frac{U_c^2}{U_\infty^2} = \frac{1}{1 - m(\gamma)} \tag{40}$$

where $m$ is a correction factor determined using $\gamma$ and Figure 71. Using Figure 71, for testing at CU with $\gamma = 0.17$, $m$ ≈2.3 for the Savonius and $m$ ≈2.6 for the flat plate.

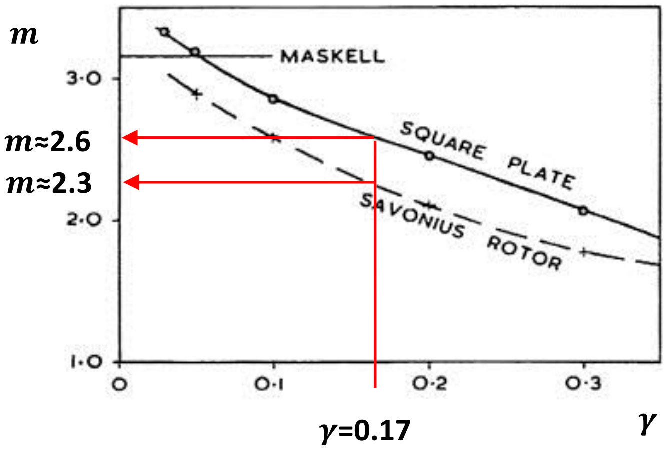

**Figure 71 Flat Plate and Savonius relationship of m vs. S/C (Alexander and Holownia, 1978)**

## 9.6 Uncertainty Analysis

For this study the uncertainty analysis was conducted using EquiMar, (2010b) and Gan, (2004) as a guide. An uncertainty analysis identifies the largest sources of uncertainty in an experimental programme, which once identified can then be reduced if deemed unacceptable. “Bias limits are defined by the bound that the magnitude of the true value of experimental bias is expected to be less than, 95% of the time” (EquiMar, 2010b, p. 7). The combined uncertainty approach is not a statistical evaluation but is based upon an assimilation of documentation relating to components of the experiment such as calibration certificates, data sheets and instrument specifications. The approach, similar to that of McAdam et al., (2013b) assumes a root mean square propagation of the errors in the multiplied data reduction equations of $C_p$, $C_t$ and λ. Other approaches to uncertainty analyses can be found in Moffat, (1988).

A combined uncertainty approach was used to provide the bias limits for the performance parameters: $C_p$, $C_t$ and TSR. A breakdown of the entire process is described for the uncertainty analysis of $C_p$, whilst only the summary of the results are provided for both $C_t$ and TSR.

### 9.6.1 Coefficient of Performance, $C_p$

A summary of the process used for the uncertainty analysis of $C_p$, found in EquiMar, (2010b, pp. 26–27), is as follows

1. Set-up the data reduction equation (DRE) in the form $C_p=f(x_1, x_2, x_3,\ldots, x_n)$.
2. Calculated the total derivative of the function f with respect to some variables, and divided through by the differential
3. Calculated an approximation of the equation by substituting in the finite difference $\Delta x_{1\ldots n}$ then divided through by the original expression f. This gave the expression for the fractional changes in $C_p$ due to small changes in $x_1$, $x_2$, $x_3,\ldots, x_n$.
4. Obtained nominal values and bounds (sourced from documentation, certificates, instrumentation data sheets etc.)
5. Once coefficients were calculated (using equation from step 3), a root square sum of the form of the law of propagation of uncertainty provided the bias limits for y.
6. Formed the data reduction equation (DRE) in the form $C_p=f(x_1, x_2, x_3,\ldots, x_n)$.

$$C_p = \frac{2T\omega}{\rho A U_\infty^3} = \frac{2(Fl)\omega}{\rho(HD)U_\infty^3} \tag{41}$$

7. Calculated the total derivative of the function f with respect to some variable. Then divided through by the differential. Calculated an approximation of the equation by substituting in the finite difference $\Delta x_{1\ldots n}$ then divided through by the original expression f. This gave the expression for the fractional changes in $C_p$ due to small changes in $x_1, x_2, x_3,\ldots, x_n$.

$$\Delta C_p = \frac{\partial C_p}{\partial F}\Delta F + \frac{\partial C_p}{\partial l}\Delta l + \frac{\partial C_p}{\partial \omega}\Delta\omega + \frac{\partial C_p}{\partial \rho}\Delta\rho + \frac{\partial C_p}{\partial H}\Delta H + \frac{\partial C_p}{\partial D}\Delta D + \frac{\partial C_p}{\partial U_\infty}\Delta U_\infty \tag{42}$$

$$\Delta C_p = \frac{2l\omega}{\rho HDU_\infty^3}\Delta F + \frac{2F\omega}{\rho HDU_\infty^3}\Delta l + \frac{2Fl}{\rho HDU_\infty^3}\Delta\omega - \frac{2Fl\omega}{\rho^2 HDU_\infty^3}\Delta\rho - \frac{2Fl\omega}{\rho H^2 DU_\infty^3}\Delta H - \frac{2Fl\omega}{\rho HD^2 U_\infty^3}\Delta D - \frac{6Fl\omega}{\rho HDU_\infty^4}\Delta U_\infty \quad \textbf{(43)}$$

$$\frac{\Delta C_p}{C_p} = \frac{\Delta F}{F} + \frac{\Delta l}{l} + \frac{\Delta\omega}{\omega} - \frac{\Delta\rho}{\rho} - \frac{\Delta H}{H} - \frac{\Delta D}{D} - \frac{3\Delta U_\infty}{U_\infty} \quad \textbf{(44)}$$

8. Nominal values and bounds (sourced from documentation, certificates, instrumentation data sheets etc.) were tabulated. Once coefficients were calculated (using equation from step 3), a root square sum of the form of the law of propagation of uncertainty provided the bias limits for $C_p$.

**Table 20 Sensitivity Analysis for $C_p$ performance parameter**

| | Units | Nominal | Bound | Source | Coefficient | $\Delta C_p/C_p$ | $\Delta C_p$ | % |
|---|---|---|---|---|---|---|---|---|
| F | N | 10 | ±5.0 x $10^{-2}$ | Load Cell documentation (±0.05% of rated output) | 5.0 x $10^{-3}$ | 5.0 x $10^{-3}$ | 7.5 x $10^{-4}$ | 0.5% |
| L | m | 0.1 | ±1.0 x $10^{-4}$ | Manufacturing machine tolerances (±0.01mm) | 1.0 x $10^{-3}$ | 1.0 x $10^{-3}$ | 1.5 x $10^{-4}$ | 0.1% |
| ω | rad/s | 3.14 | ±1.6 x $10^{-3}$ | Encoder documentation (2000 pulses/revolution) | 5.1 x $10^{-4}$ | 5.1 x $10^{-4}$ | 7.7 x $10^{-5}$ | <0.1% |
| ρ | Kg/$m^3$ | 998.2 | ±0.04464 | (ITTC, 2008) | 4.5 x $10^{-5}$ | 4.5 x $10^{-5}$ | 6.8 x $10^{-6}$ | <0.1% |
| H | m | 0.25 | ±1.0 x $10^{-4}$ | Manufacturing machine tolerances (±0.01mm) | 4.0 x $10^{-6}$ | 4.0 x $10^{-6}$ | 6 x $10^{-7}$ | <0.1 |
| D | m | 0.4 | ±1.0 x $10^{-4}$ | Manufacturing machine tolerances (±0.01mm) | 25 x $10^{-4}$ | 25 x $10^{-4}$ | 3.8 x $10^{-4}$ | 0.25% |
| $U_\infty$ | m/s | 0.75 | ±3.75 x $10^{-3}$ | (Nortek AS, 2009) (±0.5% measured value) | 5 x $10^{-3}$ | 15 x $10^{-3}$ | 2.3 x $10^{-3}$ | 1.5% |
| **$C_p$** | **-** | **0.15** | **±0.0024** | **Root Square Sum** | **-** | **0.016** | **0.0024** | **1.6%** |

*Notes: Machine manufacturing included a guillotine, rotary table, milling machine and a lathe; all with similar tolerances*

Through examining the above table the bias limits for $C_p$ for this data point is ±1.6% and the most influential variable on the final result is $U_\infty$ with an uncertainty of 1.5% with the uncertainty of the other variables <0.5%. This level of uncertainty was deemed acceptable.

### 9.6.2 Tip Speed Ratio, λ

Following the procedure outlined in Section 9.6.1, Equation (7) becomes

$$\Delta\lambda = \frac{\partial\lambda}{\partial R}\Delta R + \frac{\partial\lambda}{\partial\omega}\Delta\omega + \frac{\partial\lambda}{\partial U_\infty}\Delta U_\infty \tag{45}$$

$$\Delta\lambda = \frac{\omega}{U_\infty}\Delta r + \frac{r}{U_\infty}\Delta\omega - \frac{r\omega}{U_\infty^2}\Delta U_\infty \tag{46}$$

$$\frac{\Delta\lambda}{\lambda} = \frac{\Delta r}{r} + \frac{\Delta\omega}{\omega} - \frac{\Delta U_\infty}{U_\infty} \tag{47}$$

**Table 21 Sensitivity Analysis for λ performance parameter**

| | Units | Nominal | Bound | Source | Coefficient | Δλ/λ | Δλ | % |
|---|---|---|---|---|---|---|---|---|
| R | m | 0.20 | ±1.00 x $10^{-4}$ | Manufacturing machine tolerances (±0.01mm) | 5.00 x $10^{-4}$ | 5.00x $10^{-4}$ | 4.00 x $10^{-4}$ | 0.05 |
| ω | rad/s | 3.00 | ±1.60 x $10^{-3}$ | Encoder documentation (2000 pulses/revolution) | 5.33 x $10^{-4}$ | 5.33 x $10^{-4}$ | 4.26 x $10^{-4}$ | 0.05 |
| $U_\infty$ | m/s | 0.75 | ±3.75 x $10^{-3}$ | (Nortek AS, 2009) (±0.5% measured value) | 5.00 x $10^{-3}$ | 5.00 x $10^{-3}$ | 4.00 x $10^{-3}$ | 0.50 |
| **λ** | **-** | **0.8** | **±0.004** | **Root Square Sum** | **-** | **0.005** | **0.004** | **0.5%** |

*Notes: Machine manufacturing included a guillotine, rotary table, milling machine and a lathe; all with similar tolerances*

Through examining Table 21 the bias limits for λ for this data point is ±0.5% and the most influential variable on the final result is $U_\infty$ with an uncertainty of 0.5% with the uncertainty of the other variables <0.5%. This level of uncertainty was deemed acceptable.

### 9.6.3 Coefficient of Torque, $C_t$

Following the procedure outlined in Section 9.6.1, Equation (5) becomes

$$C_t = \frac{2T}{\rho A U_\infty^2 R} = \frac{2(Fl)}{\rho (HD) U_\infty^2 R} \tag{48}$$

$$\Delta C_t = \frac{\partial C_t}{\partial F}\Delta F + \frac{\partial C_t}{\partial l}\Delta l + \frac{\partial C_t}{\partial \rho}\Delta \rho + \frac{\partial C_t}{\partial H}\Delta H + \frac{\partial C_t}{\partial D}\Delta D + \frac{\partial C_t}{\partial U_\infty}\Delta U_\infty + \frac{\partial C_t}{\partial R}\Delta R \tag{49}$$

$$\begin{aligned}\Delta C_t = {} & \frac{2l}{\rho H D U_\infty^2 R}\Delta F + \frac{2F}{\rho H D U_\infty^2 R}\Delta l - \frac{2Fl}{\rho^2 H D U_\infty^2 R}\Delta \rho - \frac{2Fl}{\rho H^2 D U_\infty^2 R}\Delta H \\ & - \frac{2Fl}{\rho H D^2 U_\infty^2 R}\Delta D - \frac{4Fl}{\rho H D U_\infty^3 R}\Delta U_\infty - \frac{2Fl}{\rho H D U_\infty^2 R^2}\Delta R\end{aligned} \tag{50}$$

$$\frac{\Delta C_t}{C_t} = \frac{\Delta F}{F} + \frac{\Delta l}{l} - \frac{\Delta \rho}{\rho} - \frac{\Delta H}{H} - \frac{\Delta D}{D} - \frac{2\Delta U_\infty}{U_\infty} - \frac{\Delta R}{R} \tag{51}$$

**Table 22 Sensitivity Analysis for $C_t$ performance parameter**

| | Units | Nominal | Bound | Source | Coefficient | $\Delta C_t/C_t$ | $\Delta C_t$ | % |
|---|---|---|---|---|---|---|---|---|
| **F** | N | 10 | ±5.0 x $10^{-2}$ | Load Cell documentation (±0.05% of rated output) | 5.0 x $10^{-3}$ | 5.0 x $10^{-3}$ | 1 x $10^{-3}$ | 0.56 |
| **L** | m | 0.1 | ±1.0 x $10^{-4}$ | Manufacturing machine tolerances (±0.01mm) | 1.0 x $10^{-3}$ | 1.0 x $10^{-3}$ | 2 x $10^{-4}$ | 0.11 |
| **ρ** | Kg/m$^3$ | 998.2 | ±0.04464 | (ITTC, 2008) | 4.5 x $10^{-5}$ | 4.5 x $10^{-5}$ | 9 x $10^{-6}$ | <0.1 |
| **H** | m | 0.25 | ±1.0 x $10^{-4}$ | Manufacturing machine tolerances (±0.01mm) | 4.0 x $10^{-6}$ | 4.0 x $10^{-6}$ | 8 x $10^{-7}$ | <0.1 |
| **D** | m | 0.4 | ±1.0 x $10^{-4}$ | Manufacturing machine tolerances (±0.01mm) | 25 x $10^{-4}$ | 25 x $10^{-4}$ | 5 x $10^{-4}$ | 0.28 |
| **$U_\infty$** | m/s | 0.75 | ±3.75 x $10^{-3}$ | (Nortek AS, 2009) (±0.5% measured value) | 5 x $10^{-3}$ | 15 x $10^{-3}$ | 3 x $10^{-3}$ | 1.7 |
| **R** | m | 0.2 | ±1.0 x $10^{-4}$ | Manufacturing machine tolerances (±0.01mm) | 5 x $10^{-4}$ | 5 x $10^{-4}$ | 8.9 x $10^{-5}$ | <0.1 |
| **$C_t$** | **-** | **0.178** | **±0.011** | **Root Square Sum** | **-** | **0.015** | **0.0027** | **1.5%** |

*Notes: Machine manufacturing included a guillotine, rotary table, milling machine and a lathe; all with similar tolerances*

Through examining Table 22 the bias limits for $C_t$ for this data point is ±1.5% and the most influential variable on the final result is $U_\infty$ with an uncertainty of 1.7% with the uncertainty of the other variables <0.6%. This level of uncertainty was deemed acceptable.

# 10 Physical Testing-Results & Discussion

**This chapter contains the results from the physical testing measured at both CU and IFREMER. The results include the flow measurements and the performance of various CarBine configurations (C), a conventional Savonius (S) and Savonius with flaps (SF). At CU the turbines were tested at 4 different $U_\infty$: 0.77 m/s, 0.93 m/s, 1.07 m/s and 1.22 m/s whilst at IFREMER they were only tested at 0.75 m/s. Both dynamic ($C_p$ vs. λ, $C_t$ vs. λ and T, ω vs. θ) and static ($C_t$ vs. θ) testing was conducted at both facilities. The highest performing CarBine configuration was C4 with $C_p$max/λ=0.132/0.441, S achieved the greatest $C_p$max/λ=0.266/1.051, whereas introducing flaps to the Savonius proved detrimental to performance, with SF achieving $C_p$max/λ=0.103/0.626. Testing at IFREMER proved the results from CU are subjected to a high degree of blockage with $C_p$max for C4, S and SF falling by 43%, 56% and 55% respectively when tested at IFREMER.**

## 10.1 Flow measurements

This section provides the results from the flow field measurements for freestream conditions for both CU and IFREMER flumes.

### 10.1.1 CU flume

A summary of the freestream conditions used for testing can be seen in Table 23. Both $U_\infty$ and I in Table 23 are calculated for the measured flow within the swept areas of the turbines using Equations (32) and (16), whereas Re and Fr are calculated using Equations (27) and (26). Table 23 shows the range of conditions tested with the lowest pump power corresponding to a $U_\infty$=0.77 m/s and I=7.6% and the highest pump power corresponding to $U_\infty$=1.22 m/s and I=8.8%.

Table 23 Freestream conditions for testing at CU

| Pump Power (%) | $U_\infty$ (m/s) | I (%) | Re $\times10^4$(-) | Fr (-) |
|---|---|---|---|---|
| **25** | 0.769 | 7.622 | 29.4 | 0.347 |
| **30** | 0.929 | 7.443 | 35.5 | 0.420 |
| **35** | 1.073 | 7.742 | 41.0 | 0.485 |
| **40** | 1.215 | 8.788 | 46.5 | 0.549 |

The pump power was capped at 40% since a further increase in pump power created large surface waves in the flume which would induce unwanted additional loading on the turbine during testing. Section 9.1 details the flow speed requirements for Froude number similarity between a scaled model and a full scale prototype and this is achieved for scaled model Froude numbers in the range of $0.13 \leq Fr \leq 0.35$, which is achieved at a pump power of 25% with Fr=0.35.

Figure 72a shows the results of the filtering methods used for the ADV data from CU. It is clear that both filtering methods have very little effect on the results which implies accurate data collection. Figure 72a also displays curves for the 7th and 10th power law, using Equation (14) and discussed in Section 5.1, but they do not fit the measured data.

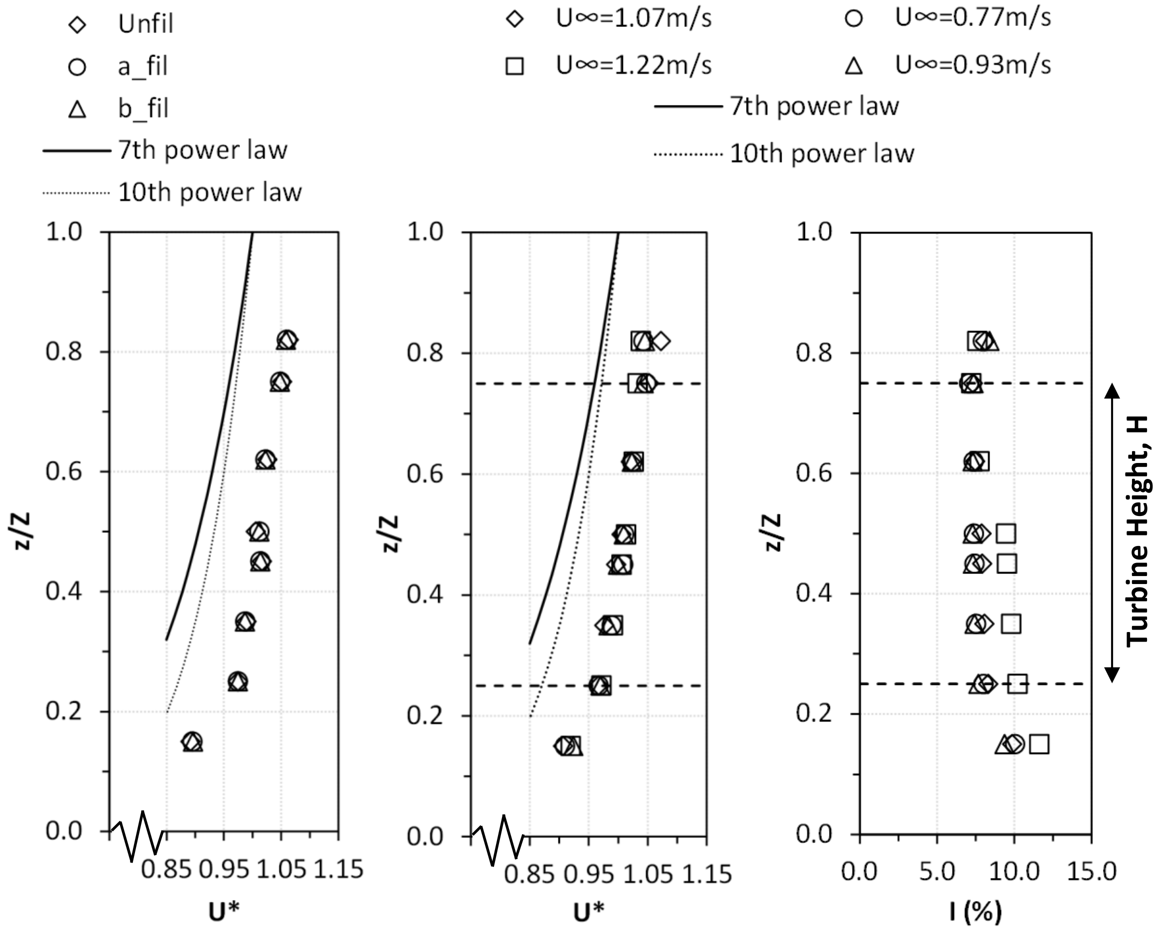

(a) (b) (c)

**Figure 72 CU ADV width averaged vertical flow profiles at x,y=[0,0]m (a)filtering methods (b)U∞ (c)I**

As expected and as seen by the theoretical 7th and 10th power law curves for $U_{\infty}$=0.77 m/s, Figure 72b shows that the flow speed increases in a parabolic form as z/Z increases; however the vertical flow profiles do not fit the theoretical power law curves. All 4 flow conditions possess similar width averaged vertical profiles at the turbine location but slight differences arise near the bed and surface of the flow. Figure 72b shows that for $U_\infty$=0.77, 0.93 & 1.07 m/s the turbulence intensity, I decreases as z/Z increases from 0 to 0.35 and then remains roughly steady. However the turbulence intensity for $U_\infty$=1.22 m/s decreases from 0 to 0.35, remains steady until 0.5 and then decreases from 0.6 onwards. The turbulence intensity is similar for $U_\infty$=0.77, 0.93 & 1.07 m/s at the turbine location but the turbulence intensity for $U_\infty$=1.22 m/s is higher by up to 3%. Figure 73 shows that the depth averaged profiles for all four flow conditions lie on top of one another and that the flow speed is constant across the turbine location y/Y=-0.2 to y/Y=0.2 but reduces as y/Y approaches the flume walls.

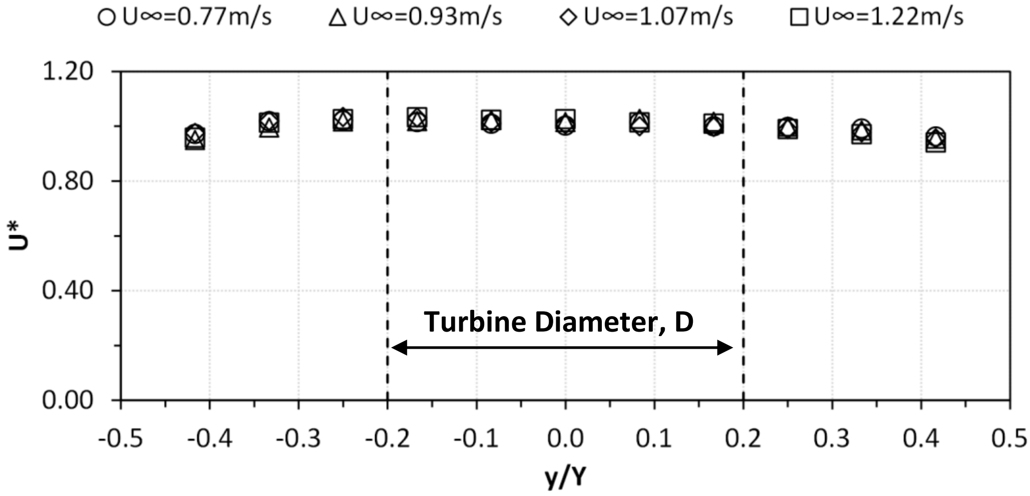

**Figure 73 ADV Depth averaged velocity profiles at x,z=[0,0]m**

Figures 75 to 78 show the contour plots of flume cross sections for all the ADV data points for both U∞ and I for the four flow conditions. The entire area of each of the figures corresponds to the flume cross section and in each of the figures the swept area of the turbine is highlighted. Due to the geometry of the probe, the distance of the sample volume from the probe (50 mm) and the presence of a free surface there exists a border of unobtainable data. Each of the flow speed contour plots illustrates reduced flow speed near the flume bed and increase in flow speed near the surface. The turbine area in each of the flow speed figures contains no severe gradient in flow speed as seen in Figure 72a and Figure 73. The turbulence intensity figures vary in distribution for each of the flow conditions and do not mirror the flow speed contours. For $U_\infty$=0.77 m/s (Figure 74b) and $U_\infty$=0.93 m/s (Figure 75b) the turbulence intensity is at its highest near the flume bed z/Z<0.2, whereas it's at its lowest on one side from y/Y=0.2-0.4; this results in only a small variation, <2%, in turbulence intensity in the turbine area. For $U_\infty$=1.07 m/s (Figure 76b) and $U_\infty$=1.22 m/s (Figure 77b) the turbulence intensity is at its highest near the flume bed z/Z<0.2, whereas it's at its lowest in the upper half from z/Z>0.5; this results in only a small variation, <2%, in turbulence intensity for $U_\infty$=1.07 m/s in the turbine area but up to 4.5% for $U_\infty$=1.22 m/s.

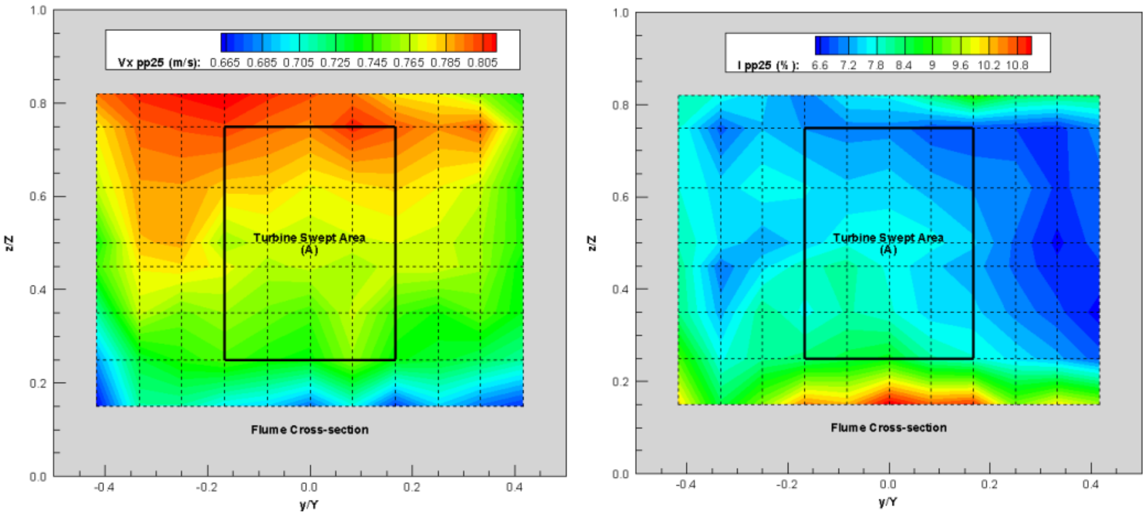

(a) (b)

**Figure 74 $U_\infty$=0.77 m/s ADV contour plots (a) $U_\infty$ (m/s) (b) I(%)**

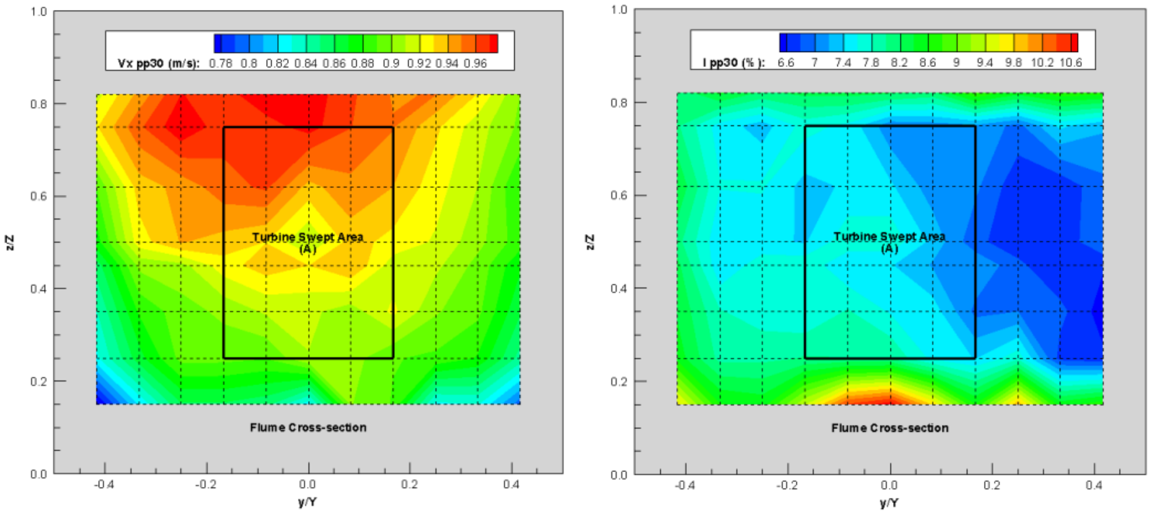

(a) (b)

**Figure 75 $U_\infty$=0.93 m/s ADV contour plots (a) $U_\infty$ (m/s) (b) I(%)**

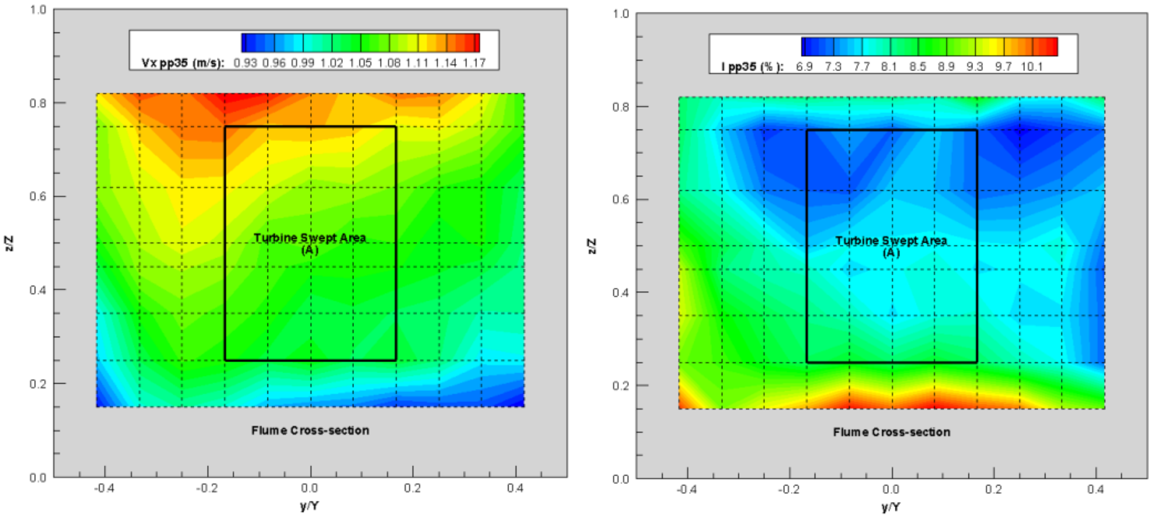

(a) (b)

Figure 76 $U_\infty$=1.07 m/s ADV contour plots (a) $U_\infty$ (m/s) (b) I(%)

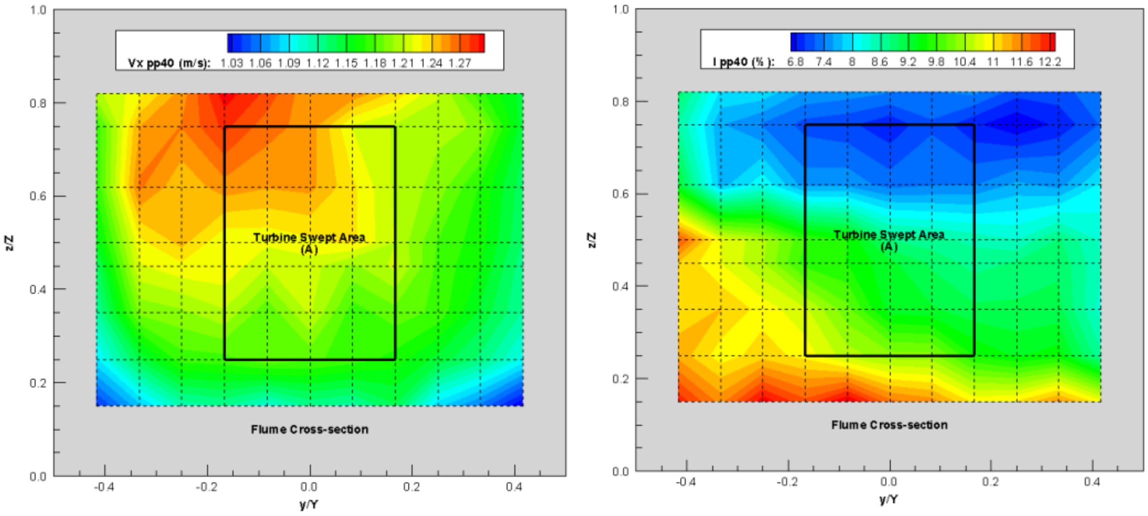

(a) (b)

Figure 77 $U_\infty$=1.22 m/s ADV contour plots (a) $U_\infty$ (m/s) (b) I(%)

### 10.1.2 IFREMER

Figure 78a compares the $U_\infty$ from CU and IFREMER, where the CU data is an average of the width averaged vertical profile for the four flow conditions from Figure 72b. It can be seen that the IFREMER profile has a steeper gradient than the CU profile with the flow speed in both profiles increases as depth from the bed increases. The steeper gradient of the IFREMER profile means it has smaller variation along the height of the turbine compared to the CU profile. Figure 78b shows that both the IFREMER and CU profiles have similar gradients but the turbulence intensity at IFREMER is 2.9% whereby the average turbulent intensity at CU is 7.6%. Detailed figures for comparisons between the CU and IFREMER freestream conditions are found in Table 24.

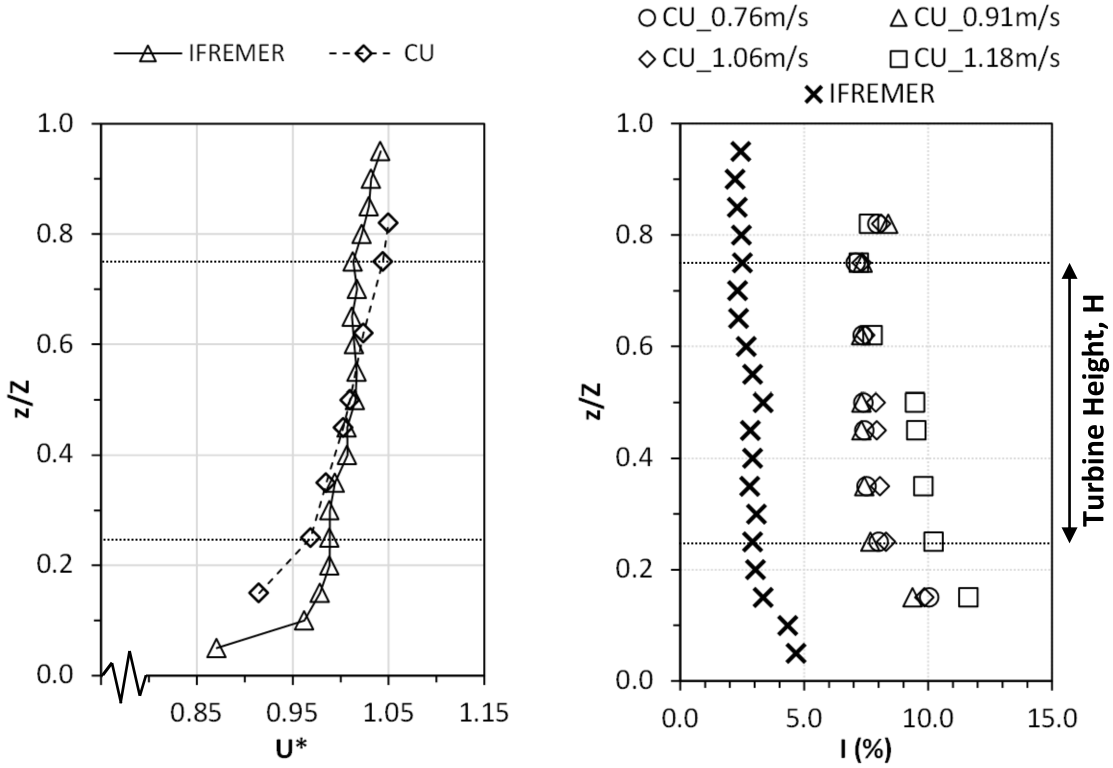

Z

(a) (b)

**Figure 78 Vertical profiles, IFREMER vs. CU (a) $U_\infty$ (b) I**

**Table 24 Freestream conditions, CU vs. IFREMER**

| | $U_\infty$ (m/s) | I (%) | Re (x10$^4$) | Fr (-) |
|---|---|---|---|---|
| **CU** | 0.769 | 7.622 | 29.4 | 0.347 |
| **IFREMER** | 0.750 | 2.914 | 114.8 | 0.169 |

**Note: Re calculated using depth as the characteristic length scale**

## 10.2 Scaled model testing

For data analysis, Equations (3)-(7) were used where Torque, T and angular velocity, ω were averaged over the entire sampling time. Flow conditions, including the freestream flow speed $U_\infty$ that were used in data analysis are found in Table 23. This section will include a summary of the performance of various CarBine and Savonius configurations for both the CU and IFREMER testing facilities. Detailed results, including the peak operating condition $C_p$max/λ and accompanying T, ω, P and $C_t$ values for each individual configuration can be found in Appendix C.

### 10.2.1 CU Testing

#### *10.2.1.1 CarBine Results*

Figures 80 and 81 show the performance results of the various CarBine configurations (detailed in Figure 60) for a range of freestream flow speeds $U_\infty$=0.77-1.22 m/s; the accompanying Re and Fr numbers can be found in Table 23. Each CarBine configuration has a colour indicator whilst each flow speed has a different symbol. Besides for C4O all configurations were tested at all 4 flow speeds, C4O was only tested at a single flow speed as an indicator to the importance of including an inner flap.

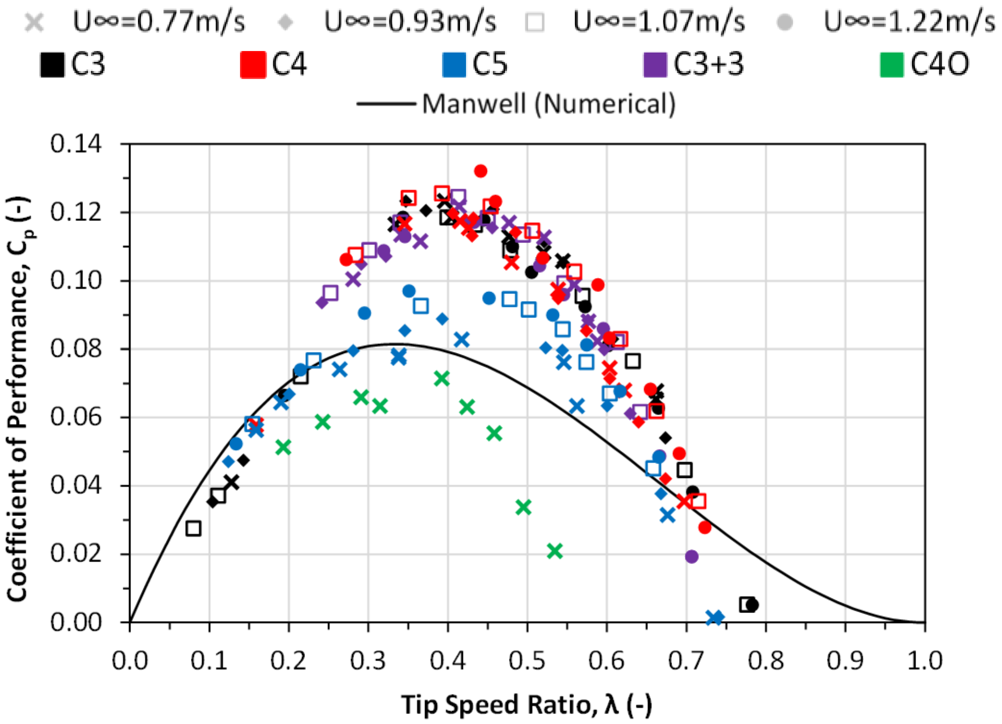

**Note: key for the CarBine configurations (e.g. C3) can be found in Figure 60**

**Figure 79 Performance results ($C_p$ vs. λ) for various CarBine configurations**

Each $C_p$ vs. $\lambda$ curve in Figure 79 displays a rising limb from $0 \leq \lambda \leq 0.4$ to a broad peak at $\lambda \approx 0.4$ and a falling limb from $0.5 \leq \lambda \leq 0.8$, besides C4O whose falling limb is steeper, $0.4 \leq \lambda \leq 0.6$. The curves for the C3, C4 and C3+3 configurations lie on top of one another with very similar peak $C_p\text{max}/\lambda$ values of around 0.125/0.4. The curves for C5 are of a lower magnitude than C3, C4 and C3+3, but the C4O curve possesses the lowest $C_p\text{max}/\lambda$ value. This indicates that for a double flap per arm configuration 4 is the maximum permissible number of flaps before performance is sacrificed. The exact $C_p\text{max}/\lambda$ values for each configuration for each flow speed are found in Appendix C. The highest recorded $C_p$ value is for C4 at $U_\infty$=1.22 m/s and is equal to $C_p\text{max}/\lambda$=0.132/0.441. Comparing C4 and C4O for $U_\infty$=0.77 m/s, the inclusion of an inner-flap provides C4 with an 86% higher $C_p\text{max}$ value than C40 due to the additional generated torque. For each CarBine configuration the $C_p$-$\lambda$ curves appear to be independent of Re, which is unexpected since for all flow conditions Re<x$10^6$ (Mason-Jones et al., 2012). Figure 79 shows that C3, C4, C5 and C3+3 display a similar rising "limb" to that of the Manwell numerical prediction (see Section 7.2) however only the C40 configuration has a $C_p\text{max}/\lambda$ which lies beneath the Manwell curve, all the other configurations have higher $C_p\text{max}/\lambda$ values than the Manwell prediction. Similarly each configuration's $C_p\text{max}$ value lies at a higher $\lambda$ than that predicted by Manwell (0.33). The highest recorded $C_p\text{max}/\lambda$=0.132/0.441 for C4 at $U_\infty$=1.22 m/s and is 65% higher than the $C_p\text{max}$=0.08 predicted by Manwell. The achievement of greater $C_p$ values than the maximum hypothesised by Manwell is likely to be due to the multiple flapped design of CarBine. Unlike in Manwell's prediction, whilst CarBine incorporates a phase angle <180° (i.e. >2 arms), there is always more than 1 flap generating torque and therefore power; it is the additional torque from multiple flaps that is likely to be the main reason as to CarBine exceeding Manwell's prediction. An optimum number of arms is achieved, in this case 4 (C4), above which performance reduces (as seen for C5). This reduction in performance could be as a result of excess shadowing from numerous arms being present in the "positive region" at any one point, hence reducing the unobstructed frontal area of generating arms and thus reducing the generated torque and power. Surprisingly, unlike Manwell's prediction, the returning CarBine flaps, i.e. in the non-generating region, are not shielded from the flow and therefore the CarBine $C_p$ would be further increased if a shielding mechanism was incorporated to reduce the negative torque from returning flaps due to skin friction drag.

The only turbine with comparable geometry to CarBine in the literature is that of the Hunter Turbine, see section 7.5.1.1. The Hunter Turbine design has 6 flaps equally spaced ($60^0$ phase) and hinged on a revolving drum. Experimental results by Yang and Lawn, (2011) show that this design achieved a $C_p max/\lambda \approx 0.18/0.44$, whilst Tidal Flow Power Ltd., (2013) states that for any flow condition a representative $C_p max/\lambda = 0.15/0.67$. Using the value from Tidal Flow Power Ltd., (2013), and comparing to the highest performing CarBine, C4 at $U_\infty = 1.22$ m/s operating at $C_p max/\lambda = 0.132/0.441$, the Hunter Turbine achieves a 36% higher $C_p$max value than CarBine. Both turbine designs operate at an identical $\lambda = 0.44$ for peak operating conditions. Since both turbines operate solely based on harnessing drag force, it is of no surprise that the $\lambda$ at optimum conditions coincide, however the distribution of their respective $C_p$-$\lambda$ curves are different. The $\lambda$ range for the Hunter Turbine is $0.33 \leq \lambda \leq 0.48$ whilst for the C4 CarBine configuration it is $0.25 \leq \lambda \leq 0.75$. The main difference is that the CarBine $C_p$-$\lambda$ curve has a broader peak and has a shallower falling "limb" whilst for the Hunter Turbine there is a sharp drop in the performance after reaching peak operating conditions at $\lambda = 0.44$, dropping to $C_p/\lambda = 0.068/0.48$.

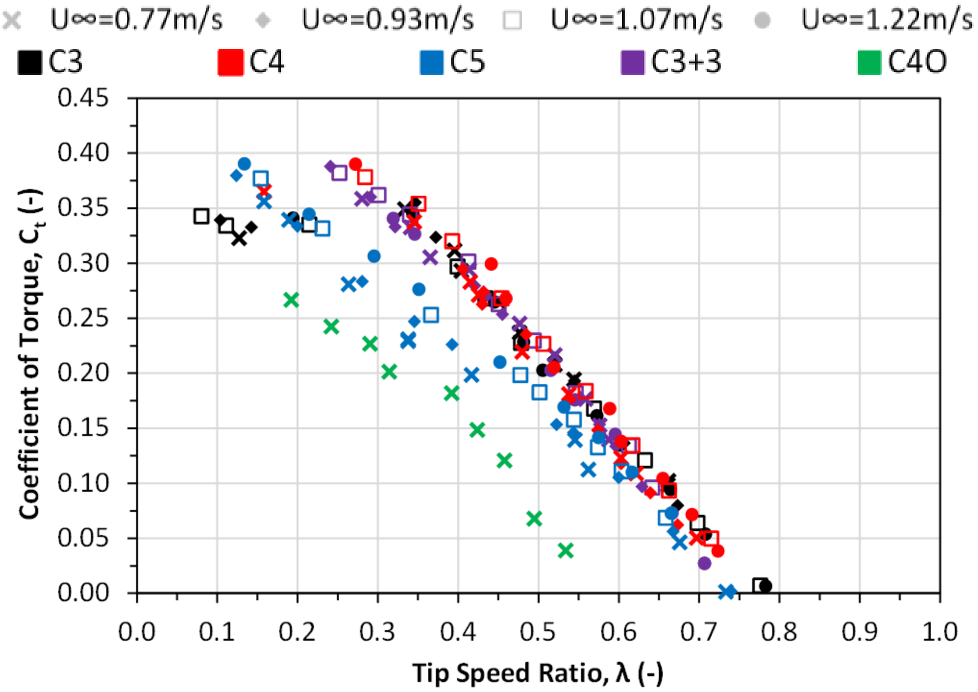

**Figure 80 Performance results ($C_t$ vs. $\lambda$) for various CarBine configurations**

Figure 80 shows that for the lower λ range, 0.1≤λ≤0.3, the $C_t$ for all configurations plateaus and then linearly decreases with increasing λ for 0.3≤λ≤0.8. Similar to Figure 79, the peak $C_t$ value for C3, C4 and C3+3 are of similar magnitude $C_t$≈0.375 with similar gradient for the falling limb whilst the peak $C_t$ value for C5 is similar to that of C3, C4 and C3+3 its falling limb has a shallower gradient. Figure 1b illustrates that a CarBine configuration with a greater than 90° phase angle (i.e. greater than 4 arms) proves detrimental to the magnitude of generated torque. For $U_\infty$=0.77 m/s, the Ct at $C_p$max/λ for C4 is equal to 0.283 whereas for C40 it is equal to 0.182, a 64% decrease in $C_t$. For $U_\infty$=0.77 m/s, C3, C4 and C3+3 have similar $C_t$ values at $C_p$max/λ, 0.312, 0.283 and 0.295 respectively. For each CarBine configuration the $C_t$-λ curves appear to be independent of Re. The $C_t$ that coincides with $C_p$max/λ for each flow speed and configuration can be found in Appendix C.

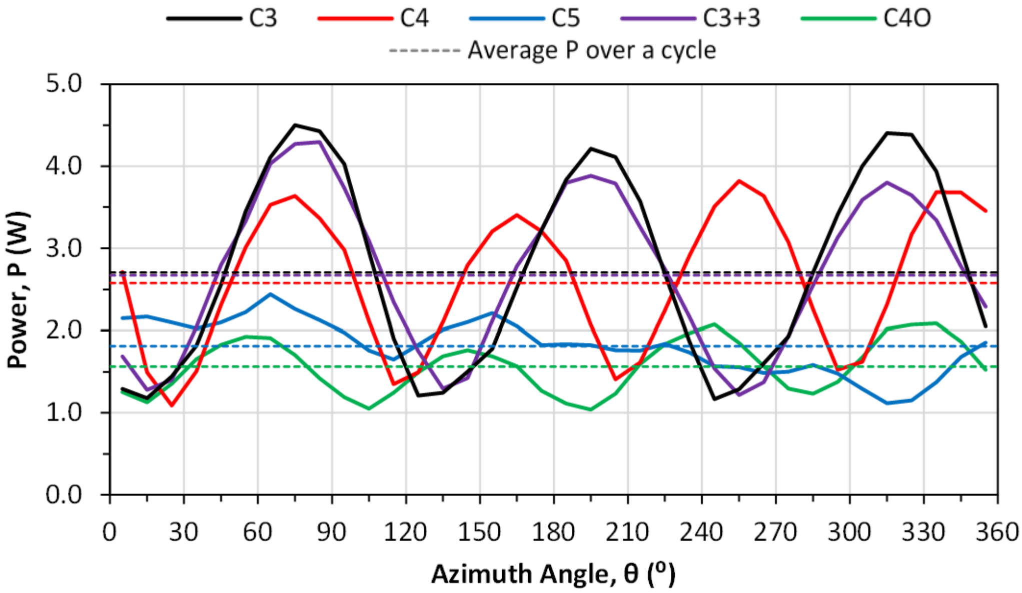

**Figure 81 Power curves at $C_p$max/λ operating point for CarBine configurations at $U_\infty$=0.77 m/s**

Figure 81 shows both the power fluctuation and average power during a revolution for each of the CarBine configurations for $U_\infty$=1.22 m/s. The average power P over a revolution for each CarBine configuration is indicated by the broken line with the configuration's corresponding colour. As expected each configuration has a repeating pattern based upon its phase angle, i.e. C4 has a period of 90°. As similarly illustrated in Figure 79, C3, C4 and C3+3 generate the greatest power at 2.7 W whereas C5 and C4O generate 1.8 W and 1.6 W respectively. For the first phase of each configuration the peak power output occurs at $65^o \leq \theta \leq 75^o$ for all configurations. The periodic behaviour equal to the number of arms is also reflected in the results of the Hunter Turbine (Yang and Lawn, 2011), with the 6 flap configuration displaying a $60^o$ period with Pmax occurring at $10^o$, considerably earlier than that of the CarBine configurations seen in Figure 81.

**Table 25 Average $C_t$ and standard deviation σ, for CarBine starting torques from Figure 81**

| CarBine | C3 | C4 | C5 | C3+3 | C4O |
|---|---|---|---|---|---|
| $\overline{P}$ | 2.703 | 2.574 | 1.814 | 2.669 | 1.564 |
| **σ** | 1.170 | 0.839 | 0.321 | 0.968 | 0.321 |

Besides the average power of an entire cycle, the variation in power during a cycle is an important parameter in power generation. Power fluctuation is a direct result of torque fluctuation (see Equation (6)), whereby fluctuating torque causes unsteady loading on the turbine blades and shaft and induces vibration which could lead to severe failure, jeopardising the life span of the turbine (Li and Calışal, 2010). Ideally the generated power would be smooth with no fluctuations therefore requiring minimal power conditioning. The power fluctuation for each configuration in Figure 81 is quantified using the standard deviation and show in Table 25. Table 25 shows that C3 has the largest power fluctuation in a cycle, followed closely by C3+3. C4 has a lower power fluctuation than C3 and C3+3, however C40 has the lowest power fluctuation of all. Both power fluctuation and the average power in a revolution decrease with decreasing phase angle.

Figure 82 shows the starting torque for one revolution for each of the CarBine configurations. The starting torque follows a similar pattern to that of the power output seen in Figure 81 with the each configuration having a repeating pattern based upon its phase angle. The $C_t$ is positive for the entire cycle for each of the configurations implying they are all self-starting. C4 has the lowest variation in $C_t$ during an entire cycle whilst C3 has the highest variation. C40 achieves higher values of $C_t$ for the first $20^o$ of each phase angle than C4 but from $40^o \leq \theta \leq 90^o$ C4 generates higher $C_t$ values than C40. The highest $C_t$ value, 1.3, is achieved by C3+3 at $\theta=90^o$ whilst the lowest, 0.5, is achieved by C5 at $\theta=150^o$ (however this data spike is not present during the other phases of C5). Ignoring the data spikes at θ=150$^{0}$ for C5 and at θ=240$^{0}$ for C3, it is the C4 and C40 configurations that achieve the lowest $C_t$ values during a revolution, $C_t$≈0.7, for each phase.

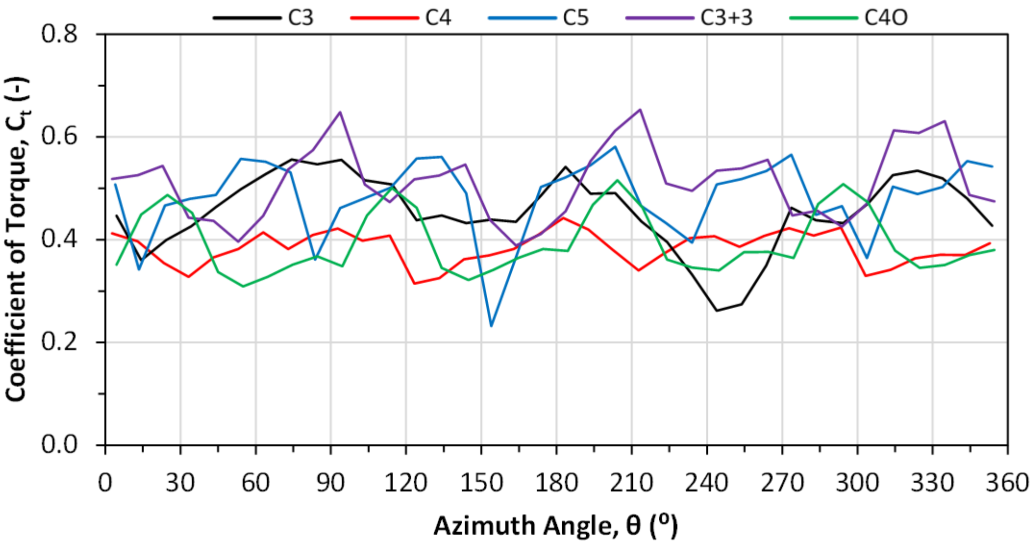

**Figure 82 Starting torque performance ($C_t$ vs. θ) data for various CarBine configurations**

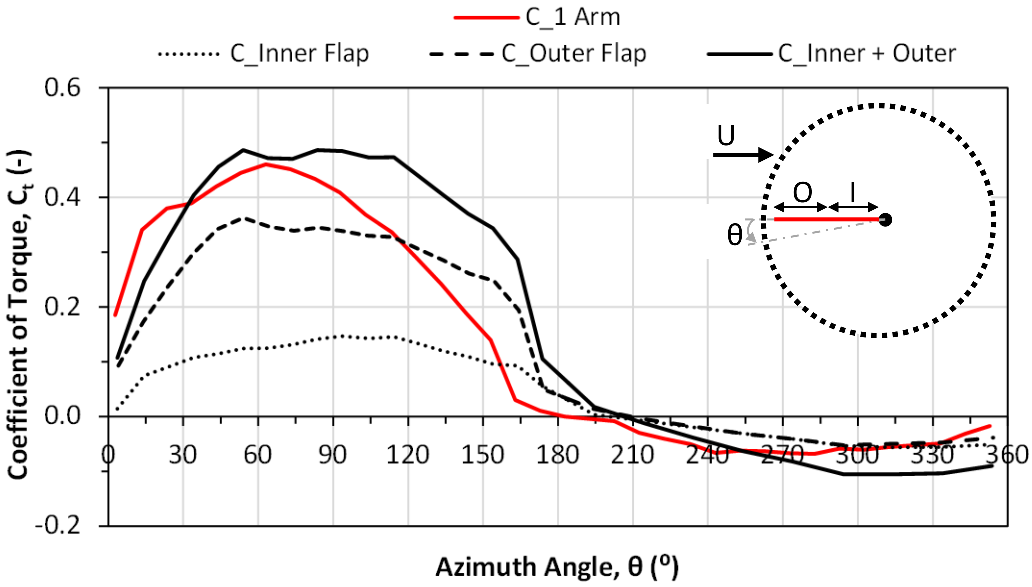

**Figure 83 Starting torque performance data for a single arm CarBine**

Figure 83 shows the static results from testing of a single arm CarBine, consisting of both an inner and outer flap (C_1 Arm), an outer flap only (C_Outer Flap), an inner flap only (C_Inner Flap) and the summation of the inner flap and outer flap data (labelled as C_Inner+Outer). As expected the C_1 Arm produces the highest $C_t$ compared to C_Inner Flap and C_Outer Flap only and all configurations display negative $C_t$ for $180^o \leq \theta \leq 360^o$. Similarly C_Outer flap generates greater $C_t$ than C_Inner flap, again expected since C_Outer flap has double the lever arm compared to C_Inner Flap. Peak $C_t$ for C_1 Arm, C_Outer flap and C_Inner flap occur at $\theta=63^o$, $54^o$ and $84^o$ respectively where C_1 arm exhibits a sharper peak than both C_Inner and C_Outer.

Surprisingly, both C_Inner flap and C_Outer flap generate greater $C_t$ than C_1 Arm for $165^o \leq \theta \leq 190^o$ which shows that when an inner and outer flap operate in tandem a negative interaction is observed for this range. Similarly C_Outer flap generates greater $C_t$ than C_1 Arm for $120^o \leq \theta \leq 190^o$ again showing that the inclusion of an inner flap produces a negative interaction. The negative interaction experienced by C1_Arm for the aforementioned range of θ is highlighted by the results of C_Inner + Outer. C_Inner + Outer summate the $C_t$ from C_Inner Flap and C_Outer Flap to produce the idealised curve if no interaction between the inner and outer flap was present. As seen in Figure 83 this results in greater $C_t$ being produced for $30^o \leq \theta \leq 190^o$ compared to C_1 Arm where interaction between the inner and outer flap is present. However positive interaction between the inner and outer flaps is present for $120^o \leq \theta \leq 190^o$ since C1_arm produces greater $C_t$ than that of C_Inner + Outer. For $180^o \leq \theta \leq 360^o$, C_1 Arm, C_Outer Flap and C_Inner flap produce similar magnitudes of $C_t$; however C_Inner + Outer produces the lowest $C_t$, showing that positive interaction must be present for C_1 Arm to reduce the negative $C_t$.

#### *10.2.1.2 Savonius Results*

Figure 84 shows the performance results of the various Savonius configurations (detailed in Figure 59) from tests in CU for a range of freestream flow speeds $U_\infty$=0.77-1.22 m/s, the accompanying Re and Fr numbers of which can be found in Table 23. Each Savonius configuration has a colour indicator whilst each flow speed has a different symbol, in addition the peak operating condition ($C_p$max/λ) for each configuration are highlighted by larger symbols.

Figure 84 shows that both the Savonius (S) and the Savonius with closed flaps (SCF) have a rising limb from $0.6 \leq \lambda \leq 1.0$, before reaching a broad peak whereby $C_p$max is achieved at λ≈1.0 and then a falling limb from 1.0≤λ≤1.6. However the Savonius with flaps (SF) has a shorter rising limb of 0.55≤λ≤0.65, peaks earlier ($C_p$max) at around λ=0.7 and a shorter falling limb from 0.7≤λ≤1.05. SF does not have a clear peak, the $C_p$-λ curve is split into two parts, whereas S and SCF have clear plateaued peaks for each flow condition.

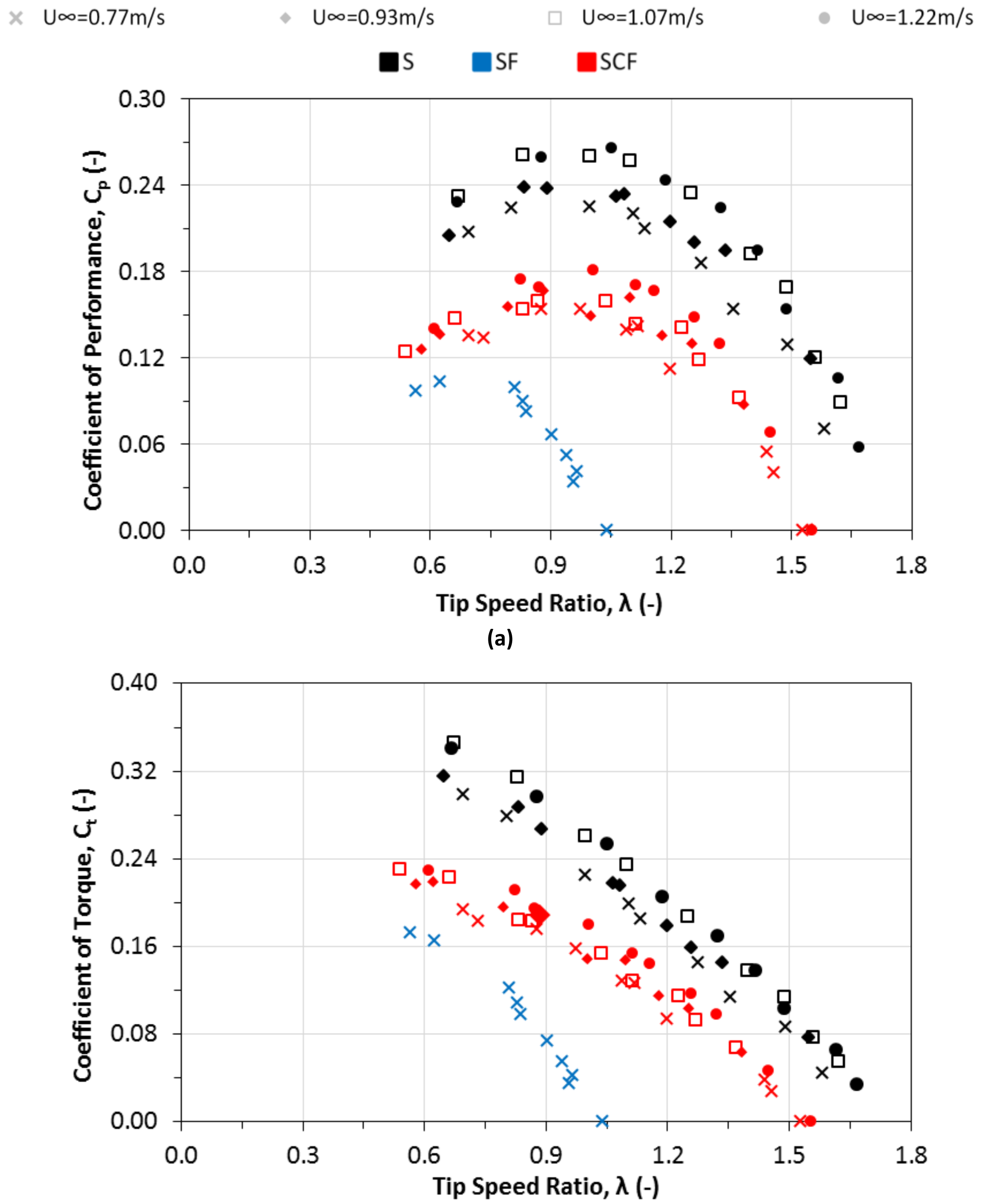

**(a)**

**(b)**

**Note: $C_p$max/λ operating point is highlighted in bold and by a larger symbol for each configuration**

**S-Savonius, SF-Savonius with flaps, SCF-Savonius with closed flaps**

**Figure 84 Performance results for Savonius configurations (a)$C_p$ vs. λ (b)$C_t$ vs. λ**

The expected performance enhancement of S through the inclusion of flaps to form SF was not found, conversely the opposite occurred; the performance of SF achieved only 38% of the performance of S at $C_p$max for $U_\infty$=0.77 m/s. As a result the flaps of SF were pinned closed to create a Savonius with closed flaps (SCF). SCF had equal dimensions to S but the buckets were not as smooth due to the presence of 2 joints for the flaps and would therefore provide a more accurate comparison of performance for SF. As seen in Figure 84a SCF achieves a considerably lower $C_p$max for all flow conditions, 0.18, to that of S, 0.26-a 69% decrease in performance. SF displayed inferior performance to SCF, $C_p$max/$\lambda$=0.10/0.62 compared to $C_p$max/$\lambda$=0.15/0.88 for $U_\infty$=0.77 m/s which is a 33% reduction in $C_p$max, thus the flaps have a negative impact on the performance of a conventional Savonius. For both S and SCF the $C_p$-$\lambda$ curves for the range of $U_\infty$ are a function of Re. An increase in Re shifts the curves upwards leading to an increase in the $C_p$max values, which is unexpected since for all flow conditions Re<x$10^6$ (Mason-Jones et al., 2012). Exact $C_p$ values can be found in Appendix C.

Figure 84b shows that for S and SCF the $C_t$ increases with decreasing $\lambda$, for the entire range of $\lambda$. The slope for S is steeper than that of SCF and it therefore achieves higher $C_t$ values. For SF the data is split into two parts, the predominant part is a linearly rising $C_t$ with decreasing $\lambda$ from $0.8\leq\lambda\leq1.05$ with a further part with rising $C_t$ but with a shallower slope for $0.55\leq\lambda\leq0.65$. For $U_\infty$=0.77 m/s SF has a shallower slope than that of SCF however for the $C_p$max/$\lambda$ operating point SF and SCF have similar values of $C_t$, 0.165 and 0.175 respectively. The $C_t$ for S at $C_p$max is 0.225, 36% higher than SF and 29% higher than SCF. For all flow speeds the $C_t$ at $C_p$max/$\lambda$ for both the Savonius and SCF varies between $0.8\leq\lambda\leq1.1$.

Both the varying and average power during a revolution for each of the Savonius configurations are shown in Figure 85. The average power P over a revolution for each Savonius configuration is indicated by the broken line with the configuration’s corresponding colour. All configurations display a sinusoidal power output over a revolution with a period equal to the phase angle of 180°. S generates the greatest power at 4.93 W, the SCF generates 3.37 W whilst SF generates the lowest amount of power at 2.26 W. All configurations generate maximum power at angles of $\theta$=65°, 235$^o$. For both S and SCF the minimum generated power occurs at angles of around θ=140$^o$, 320$^o$ but occurs later at angles of θ=155$^o$, 345$^o$ for SF.

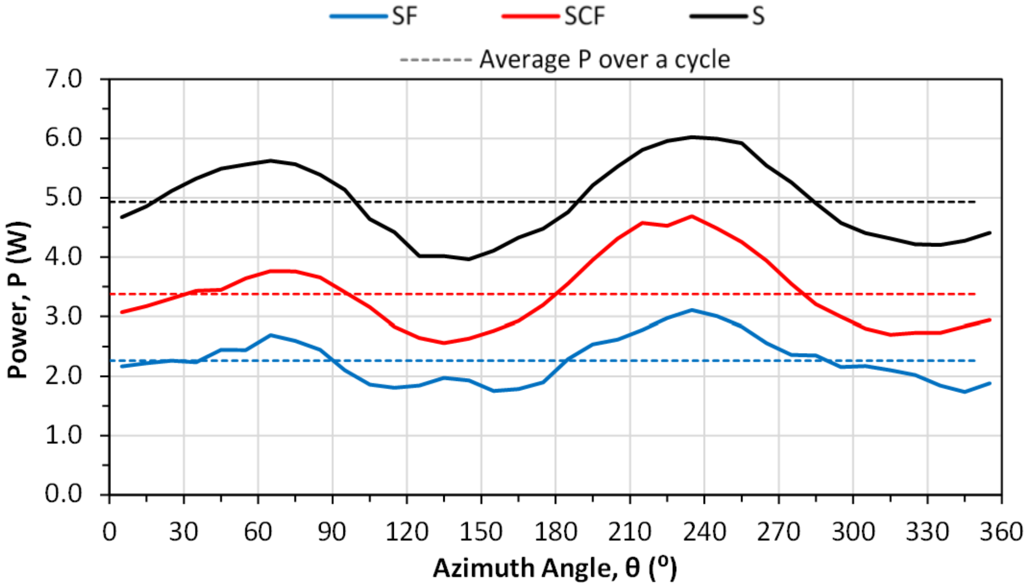

**Figure 85 Power curves at $C_p$max/λ operating point for Savonius configurations at $U_\infty$=0.77 m/s**

Figure 86The varying T and ω over a cycle for the Savonius configurations at their optimum operating points for $U_\infty$=0.77 m/s can be seen in Figure 86. Torque is displayed as a complete line whereas omega is displayed with a broken line with the configuration's corresponding colour. Similar to the power output in Figure 85, T and ω follow a rough sinusoidal pattern during a revolution for each of the Savonius configurations. The SF curves for both T and ω are the least smooth of the configurations, particularly for 105$^o$≤θ≤165$^o$ and 285$^o$≤θ≤345$^o$ whereby T and ω (unlike for the other configurations) reduce at a shallower gradient than that of the other configurations. The highest values of peak T and ω (1.4 Nm and 4.25 rad/s) are achieved by S whilst SF achieves the lowest (0.9 Nm and 3.4 rad/s). Peak T and ω values occur for 45$^o$≤θ≤65$^o$ and 225$^o$≤θ≤245$^o$ for each of the configurations. It can be seen that SF and SCF have similar torque output over an entire cycle, SCF only 6% higher than SF, yet the averaged angular velocity of SCF is 40% higher than that of SF. Using (6) this explains how SF and SCF have similar $C_t$ values at $C_p$max/λ (seen in Figure 84b) yet SCF has a higher power output (see Figure 85) and therefore $C_p$ than the SF due to its higher angular velocity. Comparing S and SCF, S has a 28% higher averaged T and 14% higher averaged ω than SCF over an entire revolution.

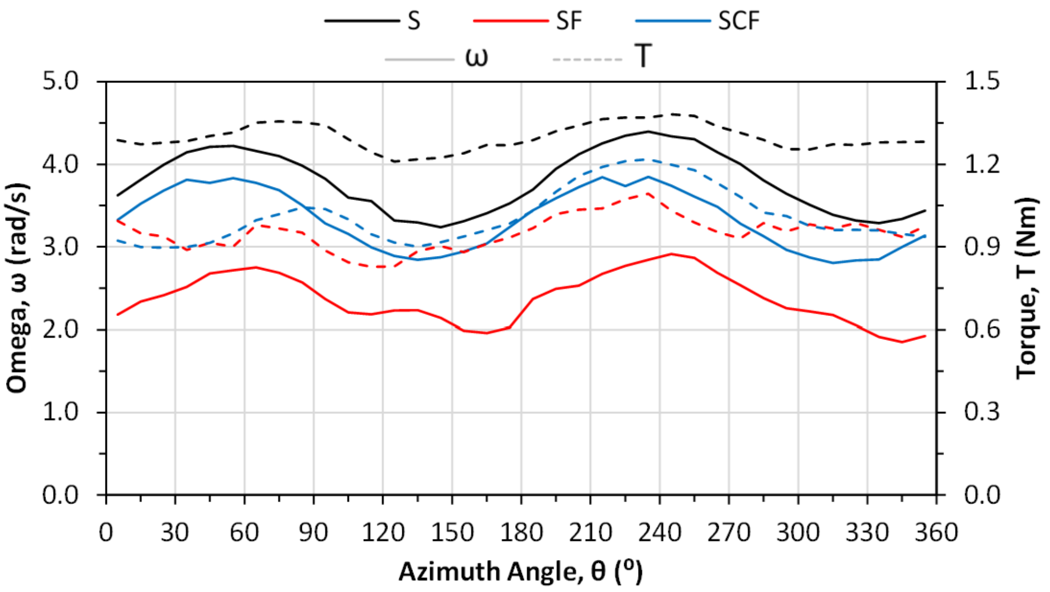

Figure 86 T and ω at $C_p$max/λ operating point for Savonius configurations at U∞=0.77 m/s

#### *10.2.1.3 CarBine vs. Savonius Results*

Figure 87 shows the $C_p$-λ and $C_t$-λ curves for all turbine configurations for testing at a flow speed of $U_\infty$=0.77 m/s. This flow speed was chosen since it is the lowest flow speed whereby an entire λ range could be recorded and satisfies the Fr scaling (see Section 9.1). Additionally at $U_\infty$=0.77 m/s the free surface behaviour remained steady however as $U_\infty$ increased surface waves became apparent, which created additional unwanted loading on the turbines. Each turbine configuration has a colour indicator whilst the results from CU and IFREMER are differentiated by different symbols.

Figure 87a highlights the superior performance of the conventional Savonius, $C_p$max=0.225, compared to the highest performing CarBine configurations, 82.9% greater than C3 (0.123), 92.3% greater than C4 (0.117) and 84.4% greater than C3+3 (0.122). Unlike the CarBine configurations which operate at a low λ range 0.2≤λ≤0.7 the conventional Savonius operates at a higher λ range, 0.7≤λ≤1.6. The SF has a lower $C_p$max/λ=0.10/0.62 than that of the C3, C4 and C3+3 but higher than that of the C5 and C4O. Figure 87b shows that for C3, C4 and C3+3 the $C_p$max/λ operating points occur at higher $C_t$ values ($C_t$≈0.3) compared to that of the conventional Savonius, $C_t$=0.22; therefore generating larger torque whilst operating under optimum conditions. Although the Savonius generates lower torque than the C3, C4 and C3+3 it does rotate at over double the speed, λ= 1.0 compared to λ=0.4. Despite CarBine configurations possessing greater $C_t$ values at optimum conditions it is the doubling of the angular velocity that leads to the greater performance of the Savonius compared to CarBine (see (6)). Since the CarBine configurations operate for a shorter λ range than the Savonius configurations, $C_t$ therefore declines at a steeper rate with increasing λ.

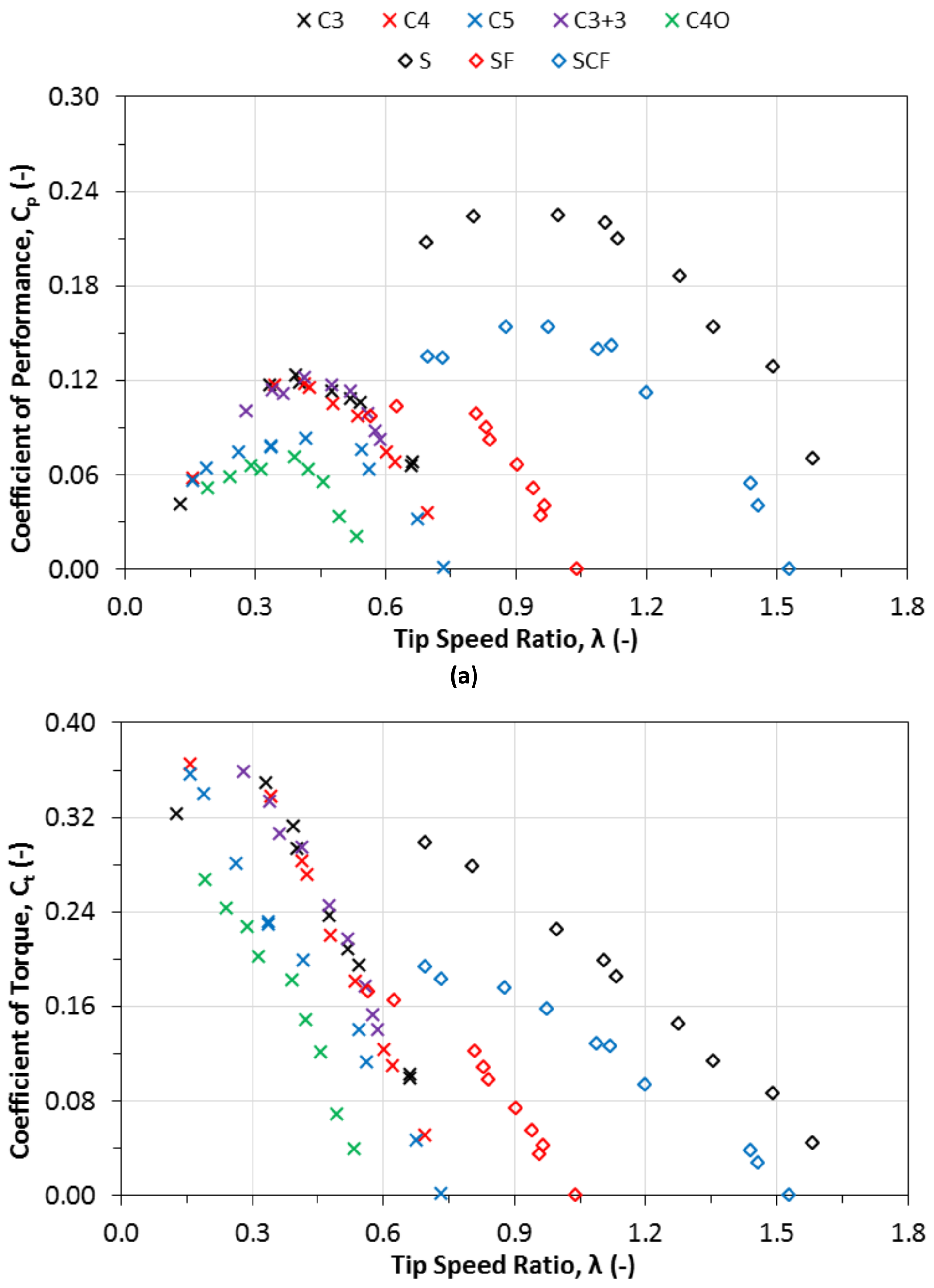

(a)

(b)

**Note: $C_p$max/λ operating point is highlighted in bold and by a larger symbol for each configuration**

**Figure 87 Performance results for CarBine and Savonius configurations for $U_\infty$=0.77 m/s (a)$C_p$ vs. λ (b)$C_t$ vs. λ**

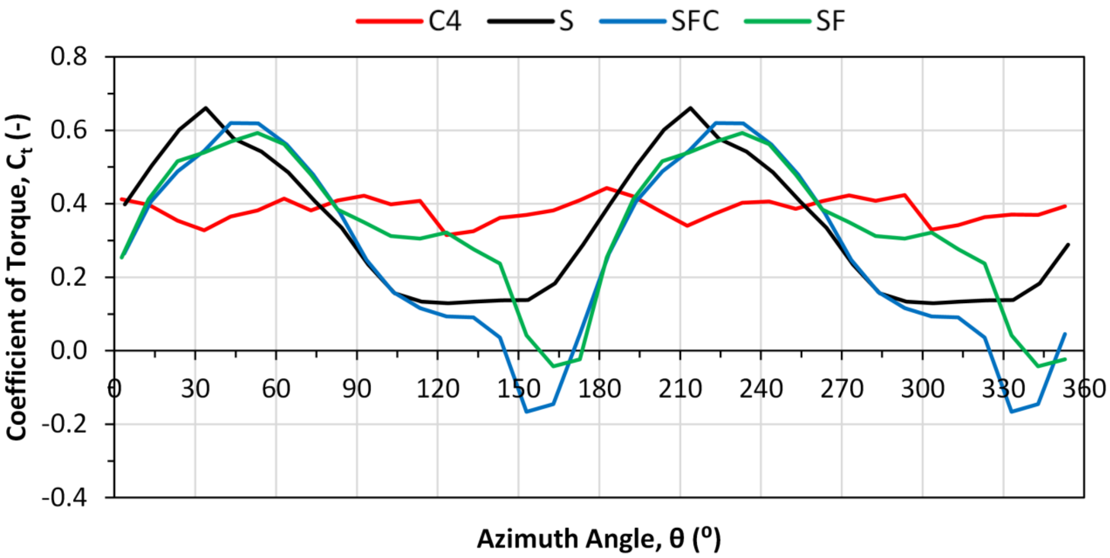

**Figure 88 Comparison of starting torque for CarBine and Savonius configurations**

Figure 88 shows the starting torque behaviour of the Savonius configurations and the optimised CarBine configuration, C4. Both S and C4 generate positive torque during the entire cycle implying they are both self-starting, whereas SCF generates negative $C_t$ at $140^o \leq \theta \leq 170^o$ and SF generate negative $C_t$ at $160^o \leq \theta \leq 170^o$. The negative $C_t$ generated by SF and SCF implies they are not self-starting at these particular angles. The Savonius configurations exhibit similar behaviour with their rising limbs and have similar peaks at $C_t \approx 1.3$ for $\theta \approx 45^o$ and also share similar falling limbs until they reach $\theta = 90^o$, for $90^o \leq \theta \leq 180^o$ the Savonius configurations differ. For SCF the $C_t$ continues to decrease for $90^o \leq \theta \leq 180^o$ at a similar gradient as that for $45^o \leq \theta \leq 90^o$ however the $C_t$ for SF decreases at a shallower gradient than SCF, generating larger positive torque than SCF for $90^o \leq \theta \leq 160^o$. Unlike the SF and SCF the Savonius does not decrease linearly from $90^o \leq \theta \leq 180^o$, the Savonius decreases until $\theta = 105^o$ and then plateau's at $C_t = 0.1$ for $105^o \leq \theta \leq 160^o$. C4 has a lower variation in $C_t$ than that of all the Savonius configurations. S generates the largest $C_t = 0.7$ whilst SFC generates the lowest $C_t = -0.15$. The behaviour of S in Figure 88 is mimicked by the studies of Irabu and Roy, (2011) and Nakajima et al., (2008). In Nakajima et al., (2008) $C_t$ displays exactly the same behaviour besides plateauing at a lower $C_t$ than in Figure 88. Whereas in Irabu and Roy, (2011) the $C_t$ displays a shallower falling limb and a sharp change from falling limb to rising limb for the next phase, rather than the plateauing effect seen for $105^o \leq \theta \leq 160^o$ in Figure 88 and Nakajima et al., (2008). Unlike for S in Figure 88

Fujisawa and Gotoh, (1994) and Hayashi et al., (2005) found $C_t$ to be negative for $125^o \leq \theta \leq 180^o$ and $140^o \leq \theta \leq 170^o$ respectively. Comparing SF and SCF using Figure 88, both have similar starting torque performance for $0^o \leq \theta \leq 90^o$ and $170^o \leq \theta \leq 180^o$ but from $90^o \leq \theta \leq 170^o$ SF displays superior performance with $C_t$ falling at a shallower rate as θ increases compared to SCF. This behaviour is identical to that seen by Tabassum and Probert, (1987) whose SF consisted of a semi-circular portion of 4 flaps and a rigid inner straight region as seen in Figure 51a. However unlike the study by Tabassum and Probert, (1987) whose SF experienced no negative $C_t$ the SF in this study did experience negative $C_t$ at $160^o \leq \theta \leq 170^o$. A similar comparison can be made to the data from Reupke and Probert, (1991) where compared to the SCF their SF configuration (seen in Figure 51c) experiences no negative $C_t$ and improved $C_t$ for $90^o \leq \theta \leq 180^o$.

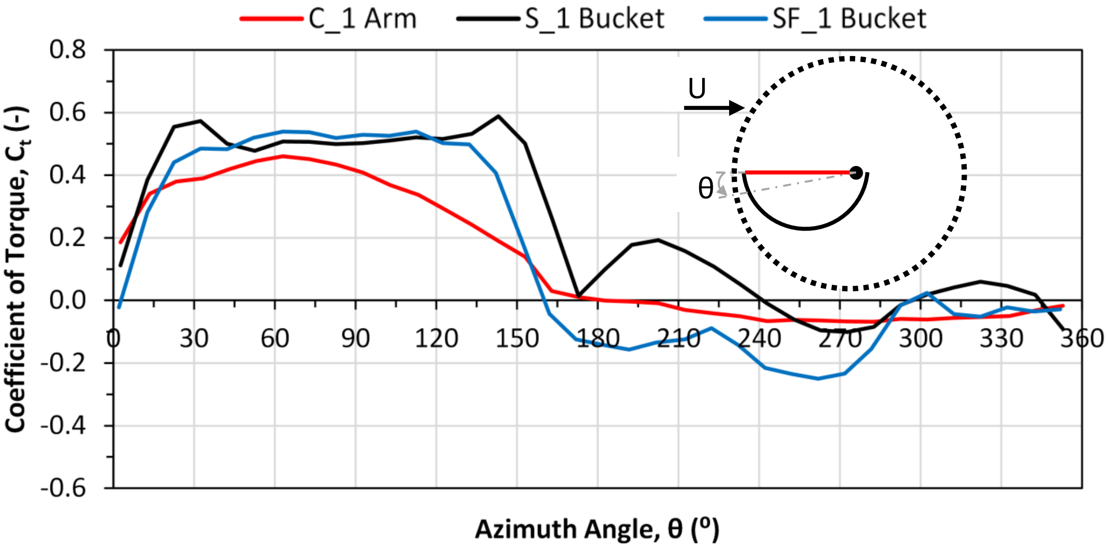

**Figure 89 Starting torque performance data for both CarBine 1 arm and Savonius 1 bucket**

Figure 89 shows the results from static testing on both a 1 arm CarBine (C_1 Arm) i.e. inner and outer flap, a 1 bucket Savonius (S_1 Bucket) and a 1 bucket Savonius with flaps (SF_1 Bucket). Since this analysis studies 1 blade of each of the configurations it does not account for interaction between numerous blades. Each of the configurations generate positive $C_t$ for $0^o \leq \theta \leq 160^o$ whilst the 1 bucket Savonius continues generating positive $C_t$ until $\theta=240^o$ and the 1 arm CarBine continues until $180^o$ after which the flaps open. For both S and SF $C_t$ rises linearly for $0^o \leq \theta \leq 45^o$, the $C_t$ then plateau's for $45^o \leq \theta \leq 135^o$ and then decreases to $C_t=0$ for $135^o \leq \theta \leq 160^o$. The

CarBine $C_t$ rises slower than the Savonius configurations for $0^o \leq \theta \leq 60^o$ before reaching its peak, $C_t$=0.45, before gradually decreasing to $C_t$=0 for $60^o \leq \theta \leq 180^o$. The Savonius generates the largest $C_t$ of the three configurations, $C_t$≈0.59 at θ=30°, 145°.

Once the CarBine flaps are open they generate negative $C_t$ for $180^o \leq \theta \leq 360^o$ with the lowest $C_t$=0.05 at θ=285°. The 1 bucket SF generates negative $C_t$ for $160^o \leq \theta \leq 360^o$ besides a small positive generation at θ=300°. However for $180^o \leq \theta \leq 360^o$ the 1 bucket Savonius only produces negative $C_t$ at $240^o \leq \theta \leq 300^o$. At θ=200°, the Savonius 1 bucket generates a $C_t$=0.2 which is 30% of the maximum $C_t$ generated for the $0^o \leq \theta \leq 180^o$. Although there are numerous studies on the Savonius turbine, both aerodynamic and hydraulic, few have measured the starting torque of a single bucket. The distribution displayed in Figure 89 was also found by Irabu and Roy, (2011) and Kyozuka, (2008). The data from Irabu and Roy, (2011) however shows no negative $C_t$ for $180^o \leq \theta \leq 360^o$ unlike the negative $C_t$ found in Figure 89. Similar to Figure 89, the results from (Kyozuka, 2008) displayed a peak $C_t$ of just below 0.6 and displayed the 2 instances of positive $C_t$ either side of a section of negative $C_t$ for $180^o \leq \theta \leq 360^o$. However the positive $C_t$ was of smaller magnitude, ≈0.05 compared to 0.2, whilst the negative $C_t$ was of larger magnitude to that found in Figure 89, ≈-0.25 compared to -0.1.

Although SF generates similar values of $C_t$ as S for $0^o \leq \theta \leq 180^o$, as hoped, the anticipated reduction in negative $C_t$ for $180^o \leq \theta \leq 360^o$ through the inclusion of flaps in SF compared to S did not occur. Conversely the inclusion of flaps produced inferior performance, for SF compared to S for $180^o \leq \theta \leq 360^o$; eradicating the positive $C_t$ generated by S resulted in generation of only negative $C_t$ for SF. The positive $C_t$ generated by S for $180^o \leq \theta \leq 240^o$ and $300^o \leq \theta \leq 345^o$ can only be attributed to the generation of lift force , since drag force can only be negative for $180^o \leq \theta \leq 360^o$ since the bucket is moving against the flow direction. It is this lift generation contrary to the expected negative $C_t$ for $180^o \leq \theta \leq 360^o$ that is the reason as to why S can operate at $\lambda > 1.0$ whereas CarBine configurations cannot (see Figure 87a). The eradication of the lift force present in S through the inclusion of flaps to create SF was also measured by Reupke and Probert, (1991).

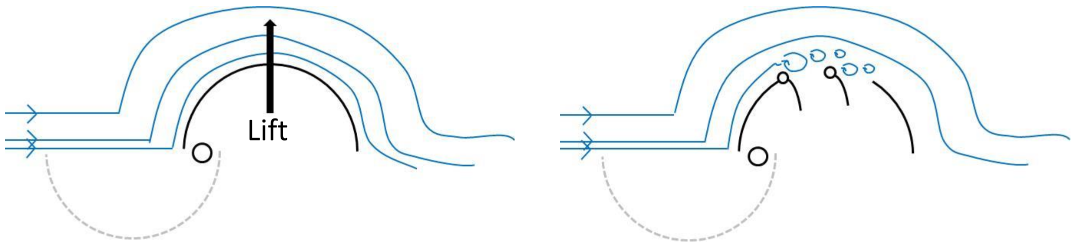

(a) (b)

**Figure 90 Hypothesised flow streamlines at θ=180$^o$ (a)S (b)SF**

The hypothesised streamlines drawn in Figure 90 could be used to explain why S displays positive $C_t$ and greater $C_t$ than SF for certain angles during 180$^o$≤θ≤360$^o$; although SF should be subjected to a reduced negative drag force compared to S since the pressure differential either side of the returning bucket is reduced due to the open flaps. It can be seen from Figure 90a that the smooth streamlined surface of S leads to attached flow and the generation of lift force; whereas in Figure 90b the presence of the joints connecting the flaps to the rigid section of the bucket creates an obstacle, this leads to separation of the attached flow resulting in no lift generation, leaving solely the additional negative drag force hence negative $C_t$. The processes of attached and separated flow are described in further detail in Section 4.1.

### 10.2.1.4 2 Turbine array

The CarBine configuration C4 achieved the highest $C_p$ value of all the CarBine configurations for all flow conditions during testing at CU, $C_p$max/λ=0.132/0.441, and was therefore used as T1 (see Figure 70) during this study. Throughout data collection T1 operated at λ=0.441. A summary of the results for C4 can be found in Appendix C and Section 10.2.1.1. For this study all tests were carried out for the flow speed $U_\infty$=0.77m/s, details of which can be found in Table 23.

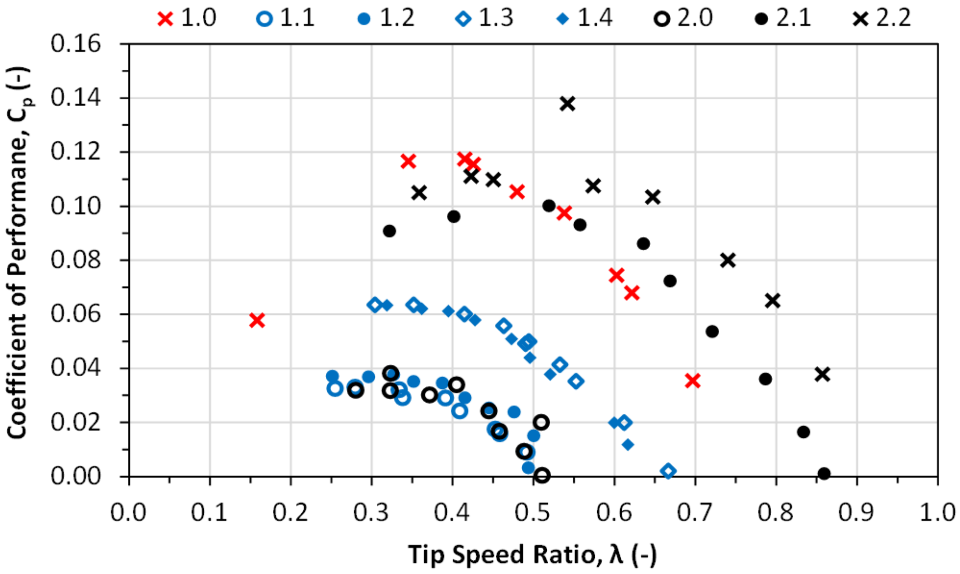

**Note: description of the various cases is found in Table 26**

**Figure 91 $C_p$ vs λ for Carbine 2 turbine array testing**

Table 26 describes the various cases tested during this study and also provides a performance summary of the results for each case whilst Figure 91 shows the $C_p$-λ curves for each case. Identical results were expected for Cases 1.0 and 1.1 since both cases are for two separate but identical C4 turbines tested in isolation. Table 26 and Figure 91 show that unsurprisingly there is minimal difference between cases 1.0 and 1.1, $C_p$max/λ=0.117/0.415 compared to $C_p$max/λ=0.112/0.439; both curves lie on each other besides case 1.0 having a slightly higher peak. The turbine in Case 1.1 was used as T2 for the remainder of the results. The arrangements tested for the 2 turbine array are split into tandem (along the x-axis) and oblique (offset in the y-direction by 0.5D) arrangements as seen in Figure 70. Cases 2.0-2.3 comprise the tandem arrangement whereby Cases 3.0-3.2 comprise the oblique arrangement.

For the tandem arrangements in cases 2.0-2.3, whereby T2 lies on the same x-axis as T1 (i.e. in the wake of T1) the power output of T2 is low, the highest being for case 2.3, P=1.612 W which is 34% lower than case 1.1, P=2.452 W. This was expected since T2 lies in the wake of T1, and follows the results by Golecha et al., (2012) who showed that for 2 Savonius turbines aligned along the direction of flow the performance of T2 (using same notation as this study) increases as the distance between T1 and T2 increases before reaching the performance of T1 at 4D downstream. However in this study, at 2D and 4D downstream T2 only reaches 38% and 66% of the performance of T1 respectively, regardless of the rotational direction of T2.

**Table 26 Performance results for CarBine 2 turbine array study**

| | **Operating Conditions** | | | | **Performance results** | | | | | |
|---|---|---|---|---|---|---|---|---|---|---|
| **Case** | **T1** | **T2** | | | **$C_p$** | **$C_p/C_{p1.1}$** | **λ** | **P** | **T** | **ω** |
| | ***ω (a/b)*** | ***T2a/T2b*** | ***α*** | ***ω (a/b)*** | **-** | ***%*** | **-** | ***W*** | ***Nm*** | ***rad/s*** |
| **1.0** | a | - | - | - | 0.117 | 104 | 0.415 | 2.574 | 1.632 | 1.577 |
| **1.1** | - | T2a | 1.5 | a | 0.112 | 100 | 0.439 | 2.452 | 1.471 | 1.667 |
| **2.0** | a | T2b | 2 | a | 0.040 | 36 | 0.291 | 0.801 | 0.794 | 1.106 |
| **2.1** | a | T2b | 2 | b | 0.042 | 38 | 0.282 | 0.921 | 0.858 | 1.073 |
| **2.2** | a | T2b | 4 | a | 0.074 | 66 | 0.343 | 1.631 | 1.253 | 1.302 |
| **2.3** | a | T2b | 4 | b | 0.074 | 66 | 0.353 | 1.612 | 1.200 | 1.343 |
| **3.0** | a | T2a | 1.5 | a | 0.042 | 38 | 0.345 | 0.911 | 0.695 | 1.312 |
| **3.1** | a | T2a | 1.5 | b | 0.108 | 96 | 0.370 | 2.360 | 1.678 | 1.406 |
| **3.2** | b | T2a | 1.5 | b | 0.124 | 111 | 0.452 | 2.709 | 1.576 | 1.719 |

**Notes: For table parameters refer to Figure 70; Performance results for T1 can be found in Section10.2.1.1 under "C4"; For Case 1.1 there is no T1**

For the oblique arrangements, Cases 3.0-3.2 are all set at 1.5D downstream and at a 0.5D offset in the y-direction. Cases 3.0 and 3.1 differ in that T2 rotates in the opposite direction to T1 for case 3.1, this results in case 3.1 achieving a 159% greater power output than Case 3.0 and only a 4% reduction in power compared to Case 1.1. However Case 3.2 is the optimum arrangement and the only arrangement of the entire study to have a positive interaction causing Case 3.2 to exceed the power generated by Case 1.1, P=2.709 W a 11% improvement compared to Case 1.1. For Case 3.2 both T1 and T2 rotate in the same direction but in the opposite direction to the default direction (see Figure 70). The generating side of T2 operates in the wake of the non-generating side of T1. This optimum oblique arrangement was also found by a numerical study (Sun et al., 2012) for a simulation of 2 Savonius turbines and unlike this study, T2 was offset by 1D and T1 and T2 operated at equal and constant TSRs. The results showed a 25% increase in the $C_p$ of T2 compared to the $C_p$ of the isolated T1. Although this is higher than the 11% in this study, if the offset distance was changed to 0.5D the increase in performance is expected to be lower due to the negative interaction of the wake of the returning blade of T1 on the performance of T2.

### 10.2.2 IFREMER Testing

The CarBine C4 achieved the highest $C_p$ value of all the CarBine configurations during testing at CU, $C_p$max=0.132, and was therefore used as the CarBine design during testing at IFREMER. In addition to the C4 configuration a 2 stage C4 turbine (along the z-axis), C4_2, was constructed with an offset angle between the 2 stages of 45°, seen in Figure 60 (there is no CU data for the C4_2 configuration). The freestream flow conditions for testing at CU and IFREMER can be found in Table 24.

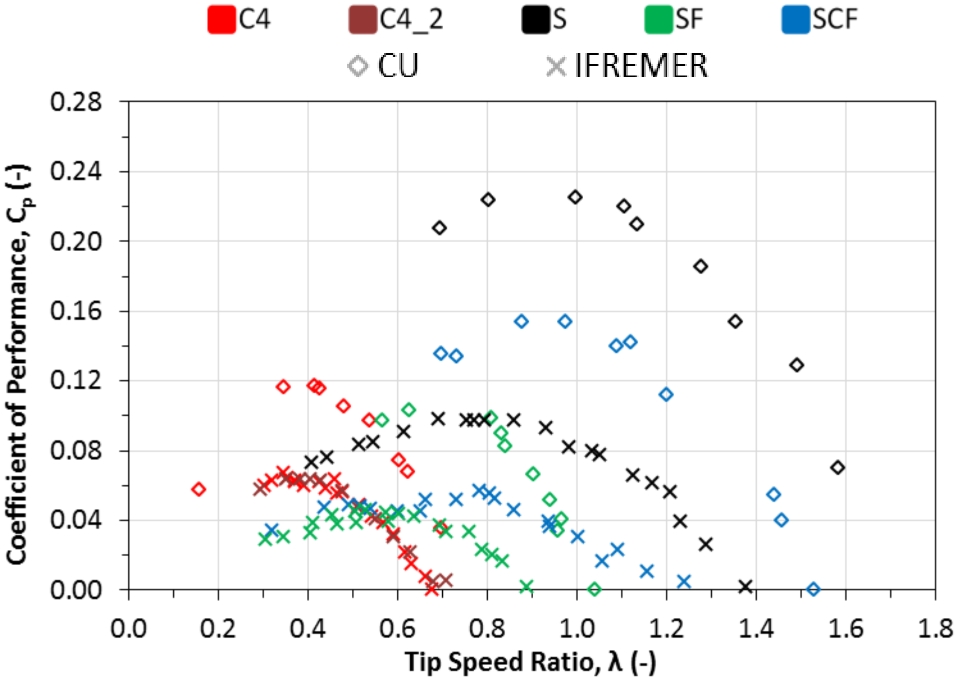

**Note: $C_p$max/λ operating point is highlighted in bold and by a larger symbol for each configuration**

**$U_\infty$=0.77 m/s for CU testing and $U_\infty$=0.75 m/s for IFREMER testing**

**Figure 92 Performance results ($C_p$ vs. λ) for CU vs. IFREMER**

Figures 93 and 95 show the $C_p$-λ and $C_t$-λ curves for the turbine configurations tested at both CU and IFREMER. Each turbine has a colour indicator whilst a different symbol is used to differentiate between results from CU and IFREMER. The peak operating condition for each turbine is highlighted by a larger symbol. Figure 92 shows that there is a decrease in the $C_p$max value for each of the configurations when tested at IFREMER compared to the value achieved while testing at CU, exact values can be found in Appendix C. SCF showed the largest decrease in $C_p$max (75%), then Savonius (56%), SF (55%) and C4 (43%). In addition there is also a reduction in the corresponding λ value for the $C_p$max as well as the configurations achieving lower $\lambda_{max}$ values (freewheeling conditions). As a result the $C_p$-λ for each of the configurations has been shifted downwards and to the left.

As expected the reduction in both $C_p$max and the range of λ experienced by all the tested turbines in IFREMER compared to CU can be attributed to the effects of blockage (see Section 9.5). Such a reduction was also found by (Whelan et al., 2009) who experienced a drop in $C_p$max of around 50% for an unblocked case compared to a highly blocked case. C4 experiences the lowest reduction in $C_p$max at IFREMER compared to CU. This could be due to CarBine allowing the freestream flow through half of its swept area, compared to S which provides a solid blockage for the entire swept area and SF which provides a solid blockage for 5/6 of its swept area; resulting in blockage factors of 16.6%, 13.9% and 8.3% respectively, as seen in Figure 93. At CU this would result in a smaller acceleration of the fluid due to blockage when testing C4 since the area available for the flow to pass through is larger. The lower degree of solid blockage by SF compared to S was also reflected at IFREMER with SF experiencing less of a decrease in performance (55%) compared to S (56%). At $C_p$max S and SF are rotating at more than double the rotational speed of C4, as discussed by (Chen and Liou, 2011) at higher values of λ a rotating turbine will act as more of a solid wall-inducing a greater degree of blockage to the flow, (until a limiting value of λ is reached) which would also explain why S and SF experience a larger decrease in performance at IFREMER compared to C4.

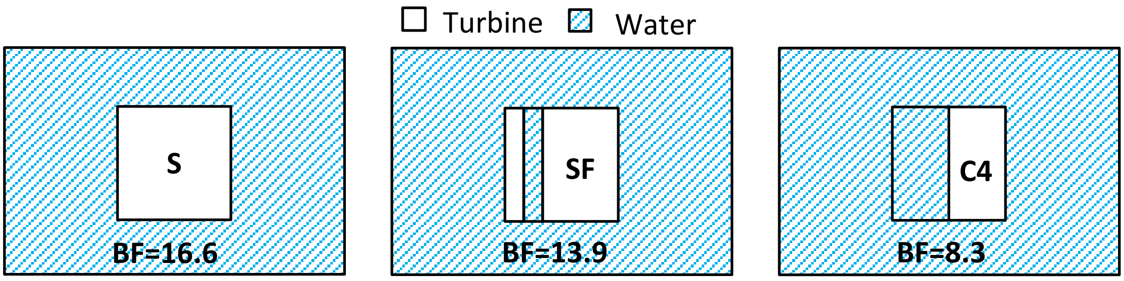

**Figure 93 Blockage factors at CU for S, SF and C4. $U_\infty$ is going into the page.**

Despite the downwards shift in the $C_p$-λ curves, the CU and IFREMER data exhibit similar distributions for each of the configurations. Unlike during the CU testing, C4 achieves a greater $C_p$max value, 0.067, than that of both the SF (0.046) and SCF (0.057) but is still 32% lower than that of the Savonius (0.098). Unlike studies on a multiple staged Savonius, see Section 8.3.2, CarBine exhibited minimal decrease in the $C_p$max value for the 2-stage, C4_2 design compared to the single stage C4. The C4_2 configuration displays an almost identical distribution to that of the C4 configurations, with $C_p$max/λ=0.064/0.405 and 0.067/0.346 respectively.

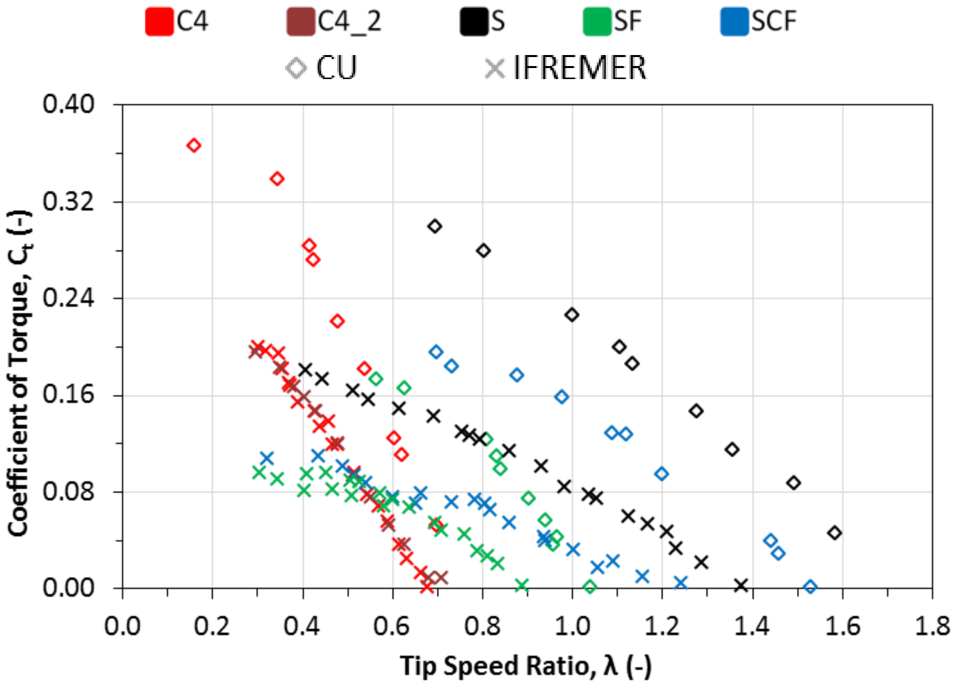

**Note: $C_p$max/λ operating point is highlighted in bold and by a larger symbol for each configuration**

**$U_\infty$=0.77 m/s for CU testing and $U_\infty$=0.75 m/s for IFREMER testing**

**Figure 94 Performance results ($C_t$ vs. λ) for CU vs. IFREMER**

The results from the SF testing in Figure 92 and Figure 94 do not display the distinct separate two regions that were present during the only other Savonius with flaps dynamic testing found in the literature by (Reupke and Probert, 1991). The only similarity between the results from this study and those by (Reupke and Probert, 1991) are the maximum efficiency $C_p$, achieved by the SF achieved at IFREMER (0.046) is comparable to 0.04 in the literature. Although the corresponding λ's are not similar, $C_p$max for IFREMER occurs at a higher λ=0.528 compared to λ=0.25 in the literature.

From Figure 95 it can be seen that the results from CU and IFREMER for the peak operating points for the various flow conditions do not coincide with the average point calculated from a literature review, see Section 8.3, or the bounds of the standard deviation. The $C_p$max/λ operating points for the CU testing occur at both a higher $C_p$ and higher λ than the literature whereas for the IFREMER testing the $C_p$max/λ operating point occurs at both a lower $C_p$ and lower λ.

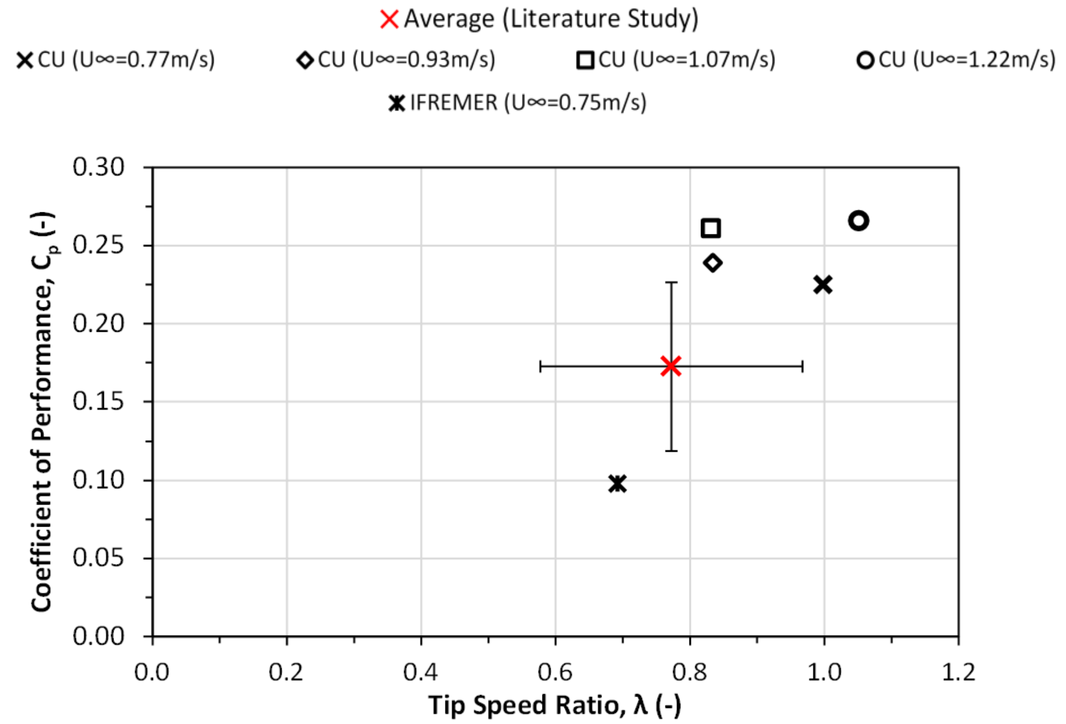

**Note: Literature used to calculate the average found in Figure 50 and Table 12.**

**Figure 95 Comparing physical testing results of the conventional Savonius to literature**

Due to logistics in transporting the laboratory equipment to IFREMER the shaft had to be made in 2 parts and was therefore not perfectly straight once re-connected. This was an issue when plotting torque and Power vs. θ for the dynamic testing since the imperfection in the shaft (due to a small bend) is captured by the load cell and highlighted during torque data capture. However since the encoder sits on top of the shaft, it does not display the shaft's imperfection. The difference in ω during a revolution for both the 1 stage C4 and 2-stage C4 (C4_2) can be seen in Figure 96. Through offsetting the 2 stages by $45^o$ the large fluctuation in ω during a cycle exhibited by C4 has been reduced to an almost consistent value for C4_2, a result consistent with studies of a multiple staged Savonius (see Section 8.3.2). In conjunction with the results from Figure 92, i.e. identical $C_p$-λ curves for both the C4 and C4_2, this results in the C4_2 producing a steadier power output with no loss in performance compared to that of the single stage C4.

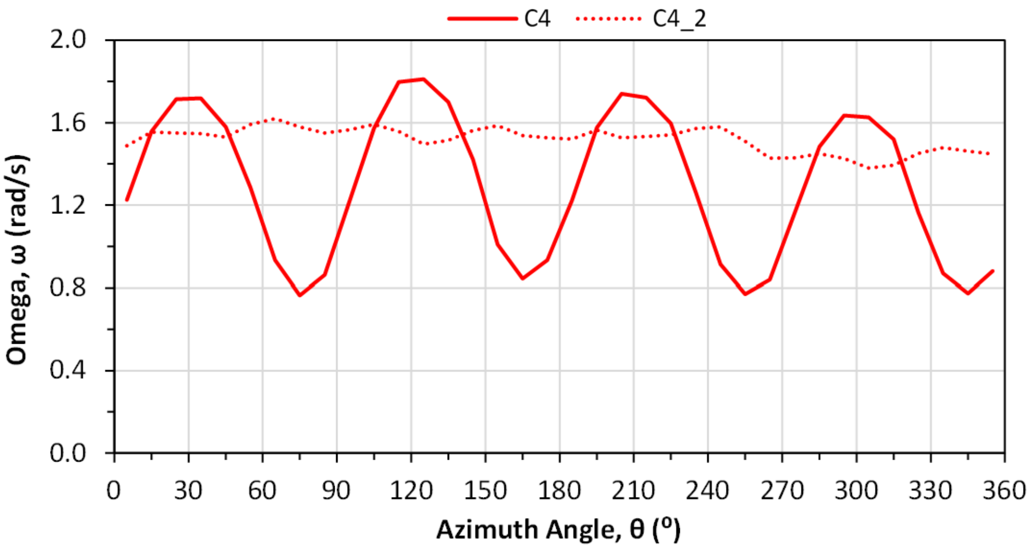

**Figure 96 Omega vs.θ comparison for 1 stage vs. 2 stage C4**

Figure 97 shows the starting torque ($C_t$ vs. θ) for C4, S and SF. Each turbine has a colour indicator, whilst the results from CU and IFREMER are indicated by a complete line and broken line respectively. As seen in Figure 97 the results from IFREMER for the starting torque behaviour of both C4 and Savonius configurations are of lower magnitude than that recorded in CU. The IFREMER results show a similar distribution to that of the CU results for the C4 and SF configurations but have been shifted downwards. However the distribution for S is different for the IFREMER results compared to CU.

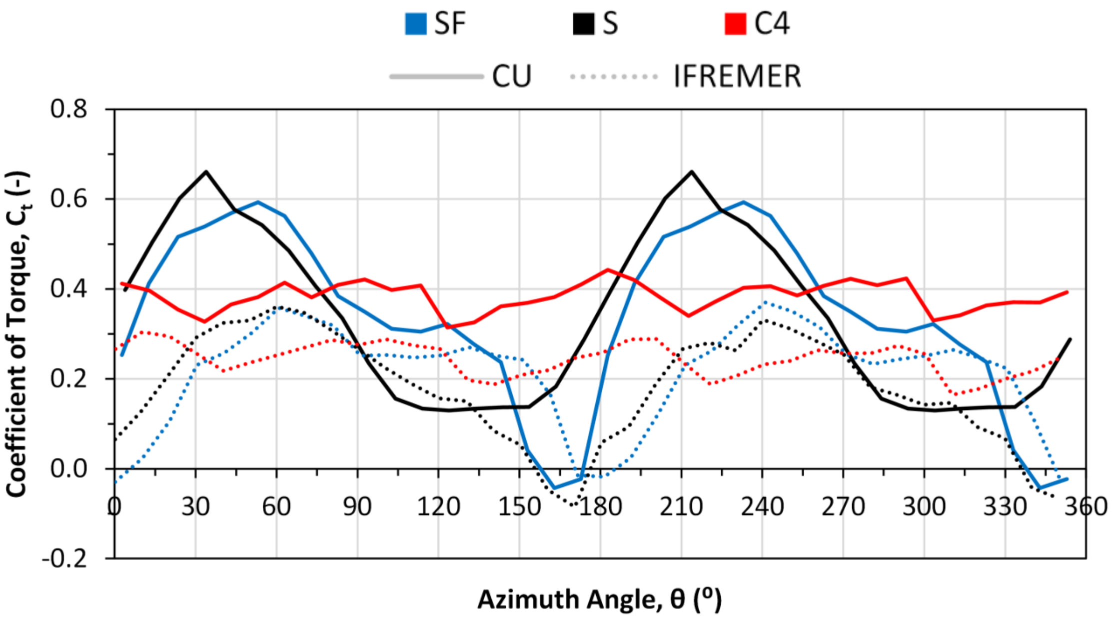

**Figure 97 Starting torque performance data for CU vs. IFREMER**

Figure 97 shows that the Savonius generates negative torque for $160^o \leq \theta \leq 170^o$ and $340^o \leq \theta \leq 350^o$ during IFREMER testing but does not generate any negative $C_t$ during CU testing. C4 is the only configuration to display positive $C_t$ throughout the cycle and is therefore the sole configuration to be considered self-starting. In both CU and IFREMER testing, S generates greater $C_t$ than SF for $0^o \leq \theta \leq 45^o$, for CU testing SF generates greater $C_t$ than S for $45^o \leq \theta \leq 150^o$ yet this is extended to $45^o \leq \theta \leq 180^o$ during IFREMER testing. This result is expected since the flaps are open in the returning bucket for SF during $45^o \leq \theta \leq 180°$ and therefore generate less negative $C_t$ in the returning bucket compared to S.

**Table 27 Savonius starting torque results from physical testing and literature**

| Study | Maximum | | Minimum | |
|---|---|---|---|---|
| | $C_t$ (-) | θ (°) | $C_t$ (-) | θ (°) |
| **CU** | **0.65** | **35** | **0.15** | **120-155** |
| **IFREMER** | **0.35** | **60** | **-0.10** | **170** |
| Kyozuka, (2008) | 0.7 | 30 | 0.2 | 120 |
| Hayashi et al., (2005) | 0.40 | 45 | -0.10 | 165 |
| Fujisawa and Gotoh, (1994) | 0.33 | 30 | -0.05 | 160 |
| Irabu and Roy, (2011) | 1.10 | 90 | 0.20 | 160 |
| Kamoji et al., (2009a) | 0.36 | 25 | -0.13 | 165 |

**Note: Values from literature are approximations. Obtained from reading values off figures**

It can be seen from Table 27 that for the CU study $C_{tmax}$ is higher than all the studies besides Irabu and Roy, (2011) and similar to the results by Kyozuka, (2008) whilst the $C_{tmin}$ is of similar magnitude to that measured by Kyozuka, (2008) and Irabu and Roy, (2011) but occurs at smaller values of θ. Similarly it can be seen that the data from IFREMER shares similar magnitudes for $C_{tmax}$ to that of Fujisawa and Gotoh, (1994); Hayashi et al., (2005) and Kamoji et al., (2009a) but occurs at $\theta=60^o$ which is larger than that of the literature. For $C_{tmin}$ the IFREMER data share's close resemblance for both magnitude and θ to Fujisawa and Gotoh, (1994); Hayashi et al., (2005) and Kamoji et al., (2009a). Besides Kyozuka, (2008) all of the literature in Table 27 are wind studies and are all conducted in open wind tunnel test sections resulting in minimum blockage, this explains as to why the IFREMER results (minimum blockage) as opposed to the CU results share similarities with 3 out of the 4 studies. A reason for the increased values of $C_t$ found by Irabu and Roy, (2011) could be since the turbine is orientated as a transverse horizontal axis turbine (see Section 4.2.3) and it's close proximity to the bottom surface leading to augmented wind speeds and hence increased $C_t$ values. Kyozuka, (2008) gave no details of the blockage factor but from the similarities shown to the results of CU a significant blockage factor is assumed.

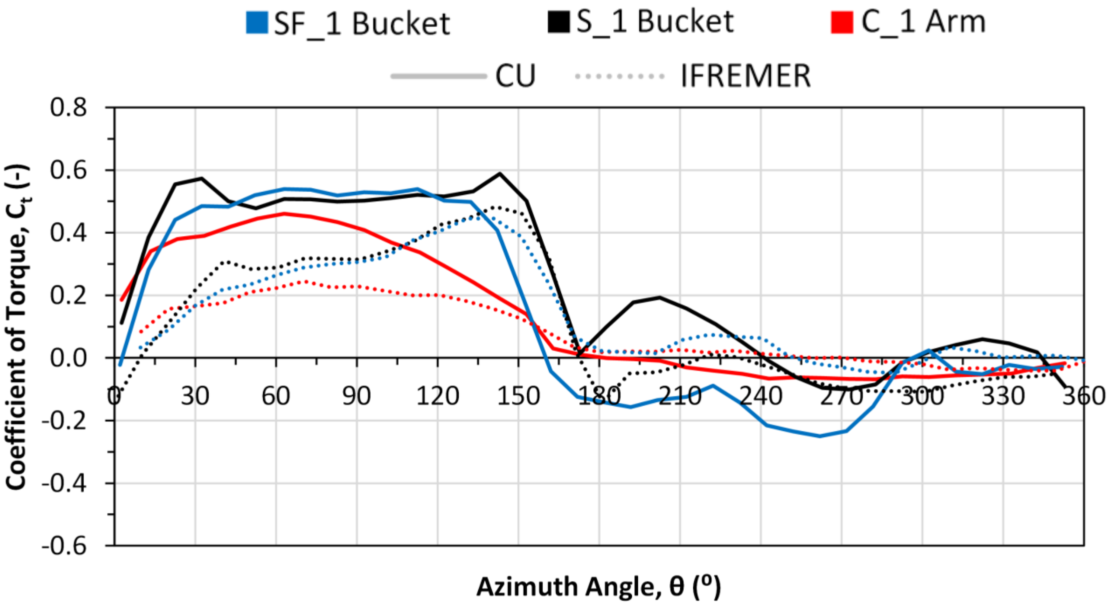

**Figure 98 Starting torque performance data for CU vs. IFREMER for 1 blade configurations**

Figure 98 shows the starting torque ($C_t$ vs. θ) for a single flap/bucket for C, S and SF. Each turbine has a colour indicator whilst the results from CU and IFREMER are indicated by a complete line and broken line respectively. Figure 98 shows that the results from IFREMER for the starting torque behaviour of both C4 and Savonius configurations are of lower magnitude than that recorded in CU. Similar to the CU results, S still maintains the highest $C_t$ of all configurations, $C_t$ =0.5 at $\theta=140^o$. For $0^o \leq \theta \leq 180^o$ C4 maintains a similar distribution for the IFREMER results as the CU results but at a lower magnitude. However S and SF do not have the same distribution, unlike the CU results the $C_t$ for the IFREMER results does not rise, plateau then decrease for S and SF for $0^o \leq \theta \leq 180^o$, conversely the $C_t$ rises gradually from $0^o \leq \theta \leq 140^o$, peaks, then decreases sharply to $C_t=0$ at $\theta=180^o$. The biggest difference between the IFREMER and CU results occurs for $180^o \leq \theta \leq 360^o$. During CU testing S achieves positive amounts of $C_t$ for $180^o \leq \theta \leq 360^o$ however this is not present for the IFREMER testing, S generates only negative $C_t$. On the other hand SF generates less negative $C_t$ for IFREMER testing compared to CU whilst also generating positive $C_t$ for $200^o \leq \theta \leq 250^o$ and $300^o \leq \theta \leq 330^o$, which is not present during testing at CU. C4 continues to generate a small amount of negative $C_t$ (<0.05) for $180^o \leq \theta \leq 360^o$ as expected.

The eradication of the positive $C_t$ and therefore the lift force experienced by S for $180^o \leq \theta \leq 360^o$ in Figure 98 during IFREMER testing compared to CU could be used to explain the reduction in $C_t$ at $C_p$max/λ conditions seen in Figure 94 and the reduction in starting torque (including negative $C_t$) seen in Figure 97 for IFREMER results compared to CU.

### 10.2.3 Analysis of blockage effect correction factors

Figure 99 shows both the Alexander and Pope & Harper blockage corrections applied to the CU results for both (a) C4 and (b) Savonius configurations; no blockage corrections were required for the IFREMER results (as discussed in Section 9.5).

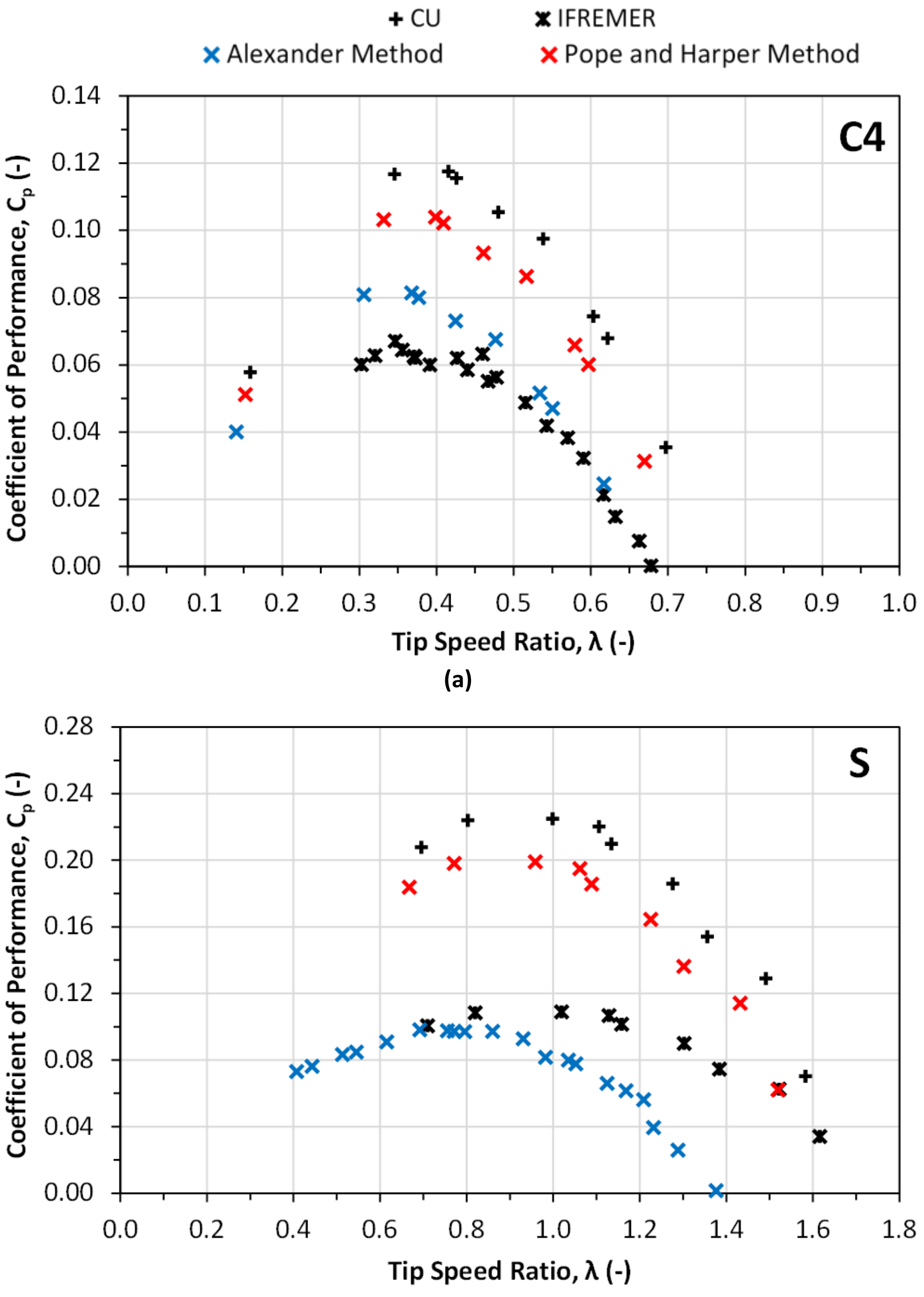

(a)

(b)

**Note: $U_\infty$=0.77 m/s for CU testing and $U_\infty$=0.75 m/s for IFREMER testing**

**Figure 99 Comparison of blockage corrections for (a)C4 (b)Savonius**

Figure 99a shows that both methods shift the $C_p$-λ downwards, reducing both the $C_p$ and λ values. The original $C_p$max/λ for C4 is reduced from 0.117/0.415 to 0.104/0.398 for the Pope and Harper method and further reduced to 0.081/0.367 for the Alexander method; a reduction in $C_p$max of 11% and 31% respectively. Comparing both methods the Alexander method has the closest resemblance to the unblocked case, i.e. the

IFREMER results ($C_p$max/λ=0.067/0.346) but still over predicts performance by 17%. Figure 99b shows that both methods shift the $C_p$-λ downwards, reducing both the $C_p$ and λ values for S. The original $C_p$max/λ for S is reduced from 0.225/0.999 to 0.199/0.959 for the Pope and Harper method and further reduced to 0.109/1.019 for the Alexander method; a reduction in $C_p$max of 12% and 52% respectively. Comparing both methods the Alexander method (0.109) shows the greatest similarity to the $C_p$max value of the unblocked IFREMER results (0.098), only 11% greater, however the Cp-λ curve lies at a lower λ range for the IFREMER results (i.e. shifted to the left). In conclusion it is the Alexander method that provides the most accurate results when altering the results of CU to account for the blockage effects with the aim of reproducing the results from IFREMER (whereby the blockage is minimal).

The blockage corrections applied in this study are constant values and therefore do not account for the change in angular velocity (and hence, nor λ) during a $C_p$-λ curve. As the λ of a turbine increases it is expected that the degree of blockage will increase up to a limiting value when λ reaches a point whereby the rotating turbine forms a solid wall. Such a hypothesis can be proven using the blockage correction provided by A.S. Bahaj et al., (2007b) however this entails measuring the flow speed at discrete points surrounding the turbine during performance testing at various λ. Chen and Liou, (2011) conducted such a study and discovered that BF increased with increasing λ until for λ>6 the BF remained constant.

# 11 Numerical Modelling

**This chapter contains descriptions of Ansys CFX-the CFD software used for the numerical modelling. Two turbulence models were used for the simulations, k-ε and SST model, which resolved the boundary layers by use of a wall function or direct resolution; providing the required mesh density was used. CarBine was simulated through defining the mesh motion of subdomains within a rotating domain whereas the Savonius could be simulated using a transient rotor stator (TRS) option. Steady-state simulations were used for starting torque analysis whereas transient unsteady simulations of the rotating turbine domain were used to produce $C_p$ vs. $\lambda$ curves. Simulations were predominantly 2D with a selection of 3D simulations. The performance of both CarBine and Savonius were simulated using the geometry of CU and a large domain geometry whereby no blockage effect was present. A Verification study was carried out for: Spatial discretization, large domain dimensions and iterative convergence for transient simulations.**

---

Computational fluid dynamics (CFD) modelling is a computer based tool and is used by researchers and developers of tidal stream turbines to both predict and optimise the performance of a tidal turbine. CFD modelling is able to simulate the behaviour of fluid flow, heat transfer and other physical processes through solving the equations of flow, known as the Navier-Stokes equations, for a region of interest surrounded by specified boundary conditions (Ansys, Inc., 2012). Conceived in the nineteenth century and with no known analytical solution, the Navier-Stokes equations can be discretised and solved numerically; the method for which varies between different CFD models. Studies on tidal turbines such as Gretton et al., (2009); Hameed and Shahid, (2012); Howell et al., (2010); Mason-Jones et al., (2012); McTavish et al., (2012); Raciti Castelli et al., (2011) and Yang and Lawn, (2011) have used CFD modelling for:

- Design enhancement of parameters such as blade shape, optimum angle of attack, number of blades etc.;
- Modelling the behaviour of a tidal turbine under conditions not achievable in a laboratory setting, such as full scale modelling, behaviour under higher flow speeds, site specific testing, minimal blockage etc.; and

- Conducting full scale array studies.

Compared to physical testing, CFD modelling can save on time and cost since design alterations can be completed quicker and cheaper than building new physical models (Slagter, 2011). However the simulation run times of CFD models can be considerably longer than that of physical data collection. Regardless of the savings CFD analysis provides, albeit time and or cost, CFD models must be validated with “real data” from physical models at some stage of the analysis. For example, in order to conduct full scale tidal turbine studies using CFD (since full scale physical data is typically unavailable), a scaled turbine with identical dimensions to a physical model is analysed and validated against the results of the physical model from laboratory studies/ field testing. If adequate validation is achieved the CFD model can justifiably be enlarged to full scale with confidence.

## 11.1 Ansys CFX

This section describes how the commercial CFD software package, Ansys CFX (versions 12.0-14.0) was used in the development of CarBine, to satisfy the requirements stated in Section 7.4. There was a multitude of CFD software available to choose from but Ansys CFX was chosen based upon its known ability to model turbo machinery and the vast support structure available, including official Ansys CFX documentation (Ansys, Inc., 2012, 2009a, 2009b, 2009c, 2004a), and other tidal turbine studies that utilised Ansys CFX (Gretton et al., 2009; Hameed and Shahid, 2012; Jo et al., 2012; Untaroiu et al., 2011; Vahdati et al., 2011).

### 11.1.1 Theory

Only a brief outline of the theory behind Ansys CFX, herein described as CFX, is included in this section, since a complete description (including all equations) can be found in Ansys, Inc., (2012, 2009a). CFX discretises the flow domain using the finite volume technique in order to solve the partial differential unsteady Navier Stokes equations in their conservative form and other related flow equations, such as the conservation of mass and momentum. The finite volume technique discretises the entire domain into smaller control volumes, namely elements.

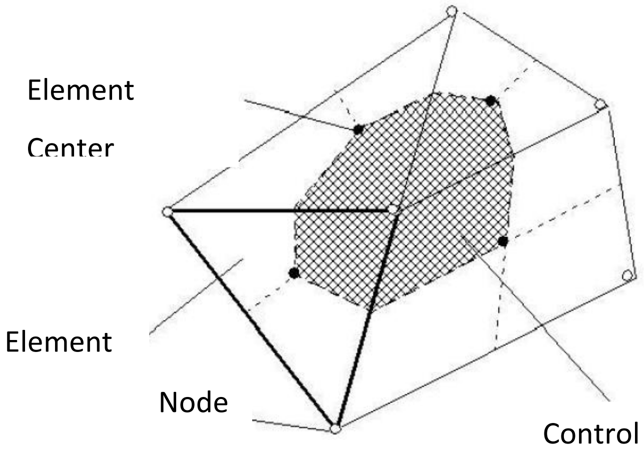

**Figure 100 CFX control volume, element and nodes (Ansys, Inc., 2009a)**

The flow equations are then discretised and solved iteratively for each element whilst the solution variables and fluid properties are stored at the nodes, with a control volume surrounding each mesh node as seen in Figure 100. Since the equations are solved uniquely for each control volume, encompassing all of the control volumes provides a full view of the fluid flow and variables throughout the domain.

### 11.1.2 Turbulence models

Although the Navier-Stokes equations are capable of describing both laminar and turbulent flows (as described in Section 5.2), for realistic Reynolds numbers the length and time scales required are too small to enable a direct numerical solution due to the limits of current computational power. As a result turbulence models have been developed that account for turbulence but do not require the prohibitively small element sizing and time scales for direct numerical solution. Turbulence models modify the unsteady Navier-stokes equations through introducing an averaged and fluctuating component of turbulence (seen in Equation (15)) to produce the Reynolds Averaged Navier-Stokes (RANS) equations. The averaging procedure does however introduce unknowns containing products of the fluctuating quantities, these terms are labelled “turbulent” or “Reynolds” stresses and are difficult to determine directly. To achieve “closure” (whereby there are sufficient equations for all of the unknowns) the Reynolds stresses need to be related to the known mean flow variables and therefore modelled by additional equations. The difference between the various turbulence models available are the different equations used for closure (Ansys, Inc., 2009a).

Turbulence models using the RANS technique are described as statistical methods, whilst there are other methods such as Large Eddy Simulation (LES), used in studies such as Li et al., (2013), which directly resolve large eddies but model eddies smaller than the mesh are both unsteady and computationally demanding (Eggenspieler, 2012), as a result these will not be discussed. Obtaining closure of the RANS models can be done by either using Eddy Viscosity Models or Reynolds-Stress models (RSM). Eddy Viscosity models were chosen for this study since RSMs are more difficult to converge and more computationally expensive compared to Eddy Viscosity models (Eggenspieler, 2012).

Since there is not a single, practical turbulence model that can reliably predict all turbulent flows with sufficient accuracy, two turbulence models are going to be considered for this study, the k-ε and the SST model. The k-ε and SST models use different approaches to solving the boundary layer flow. The k-ε model utilises a scalable wall function to solve the equations within the boundary layer whilst the SST model can fully resolve the boundary layer (based on an appropriate mesh). Both models are classed as eddy-viscosity models which assumes that turbulence consists of small eddies continuously forming and dissipating whilst Reynolds stresses are proportional to the mean velocity gradients (Ansys, Inc., 2009a). Further details of the turbulence models and all equations can be found in Ansys, Inc., (2009a) and Wilcox, (1994).

#### *11.1.2.1 Shear Stress Transport (SST)*

Recommended by Ansys for simulating separated flows and the most commonly used in aerodynamics (Eggenspieler, 2012), the SST model is designed to overcome the issues that arise from using the k-ε model, the primary difference of the SST model is its use of a k-ω model for near wall treatment (viscous/shear dominated flow) and the use of the k-ε model for the bulk flow (i.e. free shear flows). Both models are interlinked through the use of a blending function, ensuring a smooth transition between the two. The SST model was designed to overcome the deficiencies experienced with k-ω models, therefore SST is recommended over k-ω. In support of its effectiveness, the SST model of (Menter, 1994) was rated as the most accurate model for aerodynamic applications at a NASA Technical Memorandum (Bardina et al., 1997).

The STT model requires a fine mesh with a non-dimensional wall distance (see Section11.1.3.1), $y^+$<2 and CFX recommends that a minimum of 10 nodes be used in order to accurately solve the flow in the boundary layer. Since this wall distance is not always feasible, an automatic wall treatment function has been incorporated which shifts from low Reynolds number formulation to a wall function formulation. Applying the wall function whilst using the SST model would produce results similar to the of the k-ε model.

### *11.1.2.2 k-ε*

The most widely used RANS turbulence model (Eggenspieler, 2012), the k-ε model is a two equation turbulence model and offers a compromise between computational demand and numerical accuracy (Ansys, Inc., 2009a). The k-ε model is commonly used for predictions of turbulent flow due to its robustness, economy and reasonable accuracy for a wide range of flows (Ansys, Inc., 2004b). However issues that arise with the use of the k-ε model include:

- Solving for rotating fluids;
- Flows over curved surfaces;
- Performs poorly when faced with non-equilibrium boundary layers;
- Predicts onset of separation too late;
- Under-predicts the amount of separation (Ansys, Inc., 2009a, 2004b; Eggenspieler, 2012).

Boundary layer separation is a key parameter with regards to a turbine's overall performance and under predicting the amount of separation can lead to overly optimistic performance values, further discussed in Section 4.1.1. The k-ε model uses a scalable wall function (see Section 11.1.3.2) to model the flow in the viscous sub-layer, it therefore does not require a high resolution mesh adjacent to a wall; considerably reducing the simulation time. Compared to the SST model that requires $y^+<2$, the k-ε model requires $11.06<y^+\leq300$.

### 11.1.3 Near Wall modelling

#### *11.1.3.1 $y^+$ – Non-dimensional wall distance*

$y^+$ is a non-dimensional parameter used to measure the height of the boundary layer when solving the flow in the near wall region, i.e. the boundary layer for a no slip wall. $y^+$ is the normal distance from the wall to the nearest node (i.e. a mesh dependant parameter) and is calculated using

$$y^+ = \frac{yU_\tau}{\nu} \tag{52}$$

$$U_\tau = \sqrt{\frac{\tau_w}{\rho}} \tag{53}$$

where $U_\tau$ (m/s) is the near wall velocity, $y$ (m) the normal distance from the wall and $\tau_w$ (N/m$^2$) the wall shear stress (defined by the normal velocity gradient at the wall). If the $y^+$ value lies within the laminar sub layer of the boundary layer then depending on the turbulence model in question the scalable wall functions (see Section 11.1.3.2) are either applied (k-ε) or not applied (SST), however if $y^+$ lies in the turbulent region of the boundary layer, i.e. outside the laminar sub layer then scalable wall functions are applied regardless of the turbulence model.

#### *11.1.3.2 Scalable Wall functions*

If accurately resolving the boundary layer is unimportant or unfeasible (due to mesh demands) then using an appropriate turbulence model, such as k-ε, a scalable wall function can be applied to model the near wall region. The wall functions cover the laminar sub layer, effectively linking the wall to the turbulent boundary layer. The primary benefit is the reduction in simulation time since wall functions do not required a high mesh resolution in the laminar sub layer whereby resolving the boundary layer requires a fine mesh in the near wall region to achieve a $y^+<2$ (for SST). Although a study by Maître et al., (2013) on various $y^+$ values using the SST model on an aerofoil concluded that $y^+<1.57$ before results began to diverge.

Care should be taken to ensure the correct application of the wall function to ensure it is appropriate, since it does possess limitations. Wall functions operate through applying empirical log law formulae to link the tangential wall velocity to the wall shear stress in the near wall viscosity dominated region; providing mean values for both the flow and the turbulence equations and can therefore be less accurate than directly solving the boundary layer. Irrelevant of the density of the mesh in the near wall region, scalable wall functions ensure that the $y^+$ value is limited to

$$y^+ = \max(y^+, 11.06) \tag{54}$$

The transitional point between the laminar sub layer and the turbulent region of the boundary layer is in the blending region and is assumed to be at $y^+$=11.06, as seen in Figure 101 . This ensures that whilst using a scalable wall function all mesh points are located in the fully turbulent region of the boundary layer.

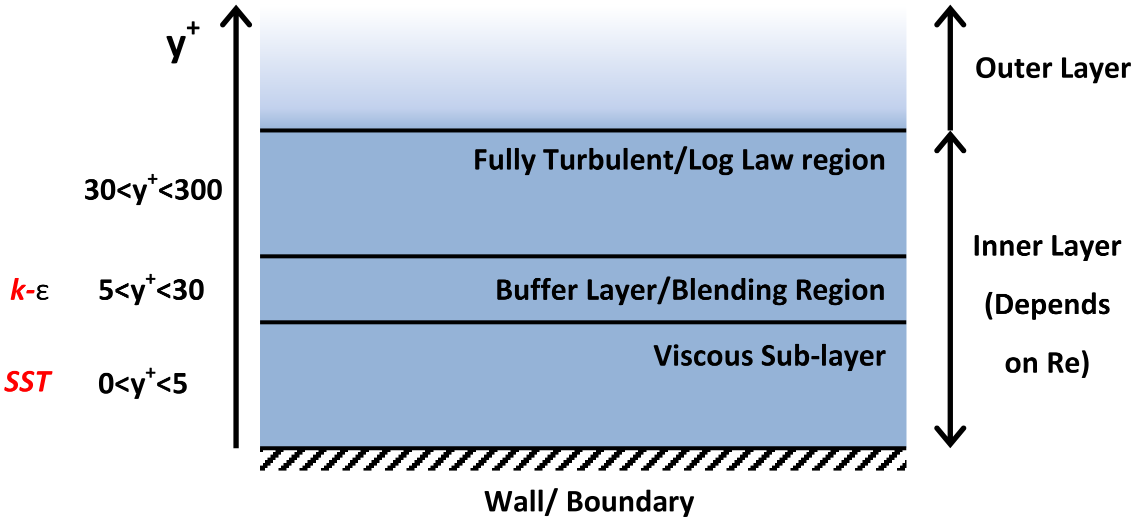

**Figure 101 Near-wall treatment and $y^+$**

## 11.2 CFX Process

Figure 102 illustrates the 5 primary steps for progression of a CFX model from design to solution; all of which are accessed and housed within the Ansys Workbench.

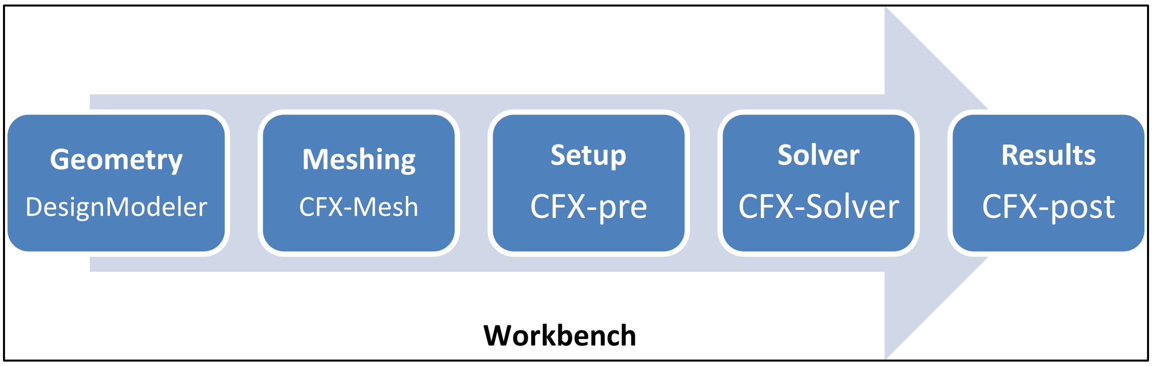

**Figure 102 Five stages of a CFX model**

### 11.2.1 Geometry

For this study two geometries were created, the first based on the CU flume dimensions and the second based on a large unblocked flume. The large flume describes a geometry whereby minimal solid blockage (see Section 9.5) i.e. no wall effects are present, Section 11.2.7.2 includes the details. The different regions of both geometries are drawn and defined using DesignModeler-a design application within Ansys Workbench. Both geometries were divided into two domains: near and far. The near domain is circular, positioned at x,y=(0,0) and contains the turbine geometry whilst the far domain contains the remainder of the model and the bulk of the flow, including inlet, outlet and walls. The far domain is divided into separate bodies for efficient meshing purposes (see section below) but are all combined to form a single far domain part. The near domain must be cylindrical in order to rotate using the multiple frames of reference (MFR) function. A Boolean operation is used for the near domain to subtract the blade volumes from the fluid body.

This study primarily comprised of a 2D analysis but it also includes 3D. The 2D plane is located at mid height of the turbine z=0.25 m, along the x-y plane. For the 3D Savonius geometry the central shaft extends for the height of the turbine. 2D geometries within CFX studies are often described as 2.5D due to their singular element thickness. 2D analysis was predominantly used since its reduced element count compared to 3D results in an efficient computational demand. Since CarBine is at the design optimisation stage it is vital that the CFX simulations are as efficient as possible to enable comparisons between multiple designs and thus design optimisation. In order to use the SST turbulence model a high resolution mesh is required to maintain a $y^+<2$

for the turbine blades, as a result an SST solution for a 3D analysis was not pursued due to the high computational demand, with Abraham et al., (2012) stating that each data point of a 3D unsteady simulation of a Savonius type turbine with 23 x $10^6$ elements took 45 days to complete. Therefore in 2D analysis, both SST and k-ε models are used but in 3D it is solely the k-ε model.

### 11.2.2 Mesh

In this step the mesh is applied to the geometry using CFX-meshing. Ansys, Inc., (2009b, 2004a) provide guidance on creating a mesh. CFX-meshing can be either structured (hexahedra shaped elements) or unstructured (tetrahedral shaped elements). A structured mesh is preferred to an unstructured mesh where possible since it has fewer elements, aids convergence and reduces the likelihood of numerical diffusion compared to an unstructured mesh. However a structured mesh should be roughly aligned to the flow and cannot be used to mesh complicated shapes, since it can produce highly skewed elements that reduce the mesh quality.

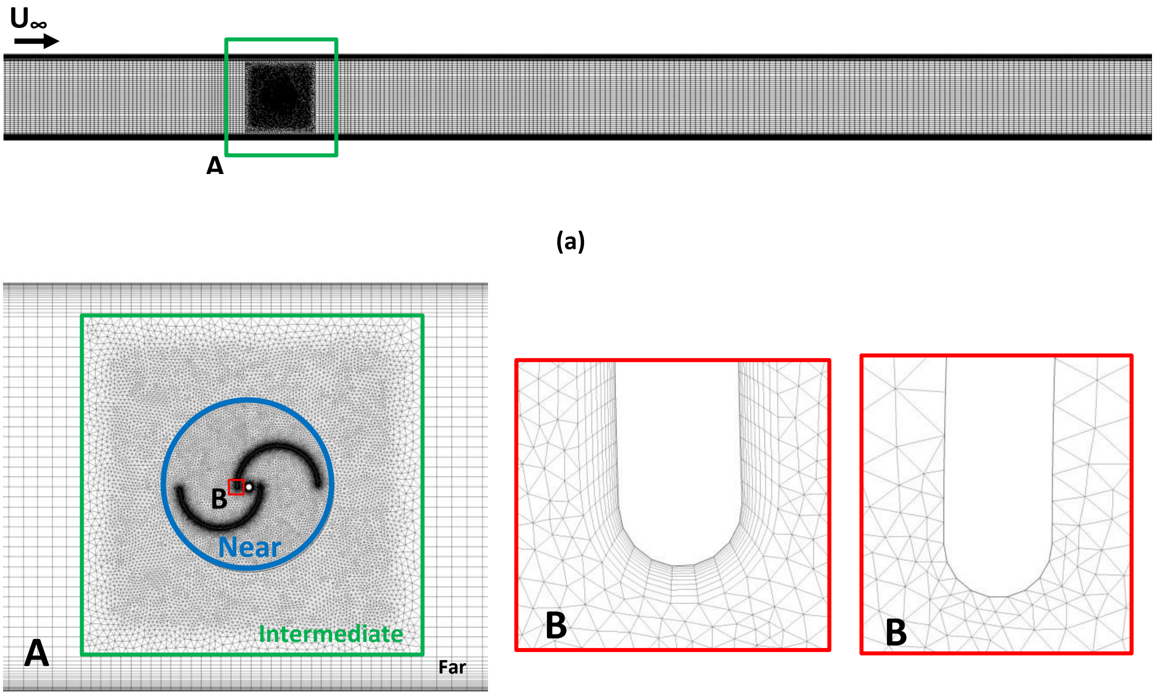

(a)

(b) (c) (d)

**Figure 103 Mesh for CU flume domain for the Savonius geometry (a) complete domain (b) Near domain and Intermediate zone (c) SST blade mesh (d) k-ε blade mesh**

For both geometries (CU flume and large domain) in this study and for both 2D and 3D a mix of both unstructured and structured zones were used, as illustrated in Figure 103. An intermediate zone, seen in Figure 103b was included between the structured and unstructured zones, to create a smooth transition between the two, since abrupt changes in element types should be avoided in critical areas (Ansys, Inc., 2009c).

To produce an efficient mesh (with regards to the element count) the mesh resolution was linked to the regions of highest interest. Since this study is analysing a turbine's performance the near domain was the main region of interest and therefore had the highest mesh resolution. Incorporating the same mesh resolution from the near domain to the far domain would needlessly increase the simulation time; however when moving away from regions of interest with high mesh density it is important to design a mesh with smooth transition from a high to a lower resolution. Sharp transitions can lead to a low quality mesh with elements exceeding the recommended mesh metrics limits; therefore a mesh with a smooth transition was required. As seen in Figure 105 and Table 28 the far domain was divided into separate parts to facilitate an efficient mesh. The aim is that when moving upstream and downstream of the near domain the mesh resolution decreased gradually. For each different turbine geometry modelled (CarBine or Savonius) the far domain mesh remains identical. However for the near domain mesh, the mesh sizing remains identical between models but the mesh differs depending on the turbine geometry (size, number of blades etc.) as seen in Figure 103b and Figure 104.

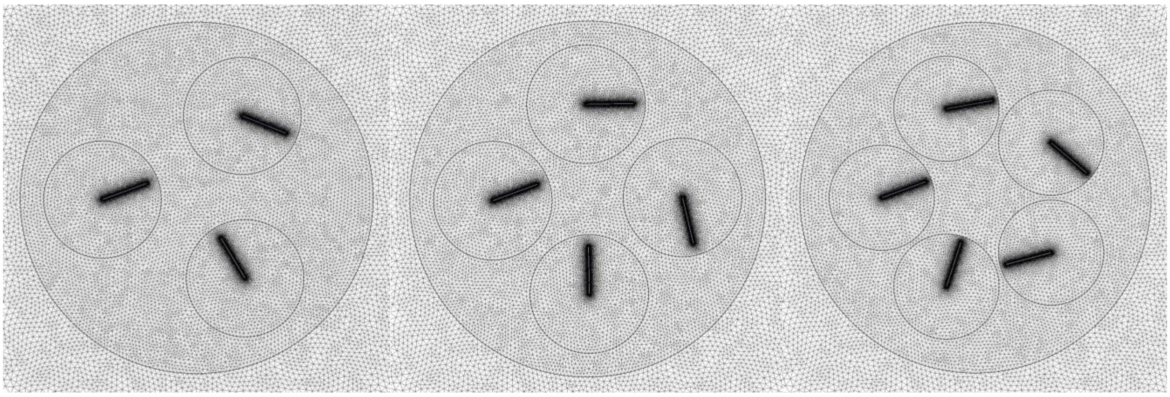

**(a)** **(b)** **(c)**

**Figure 104 Near domain mesh for CarBine (a)C3 (b)C4 and (c)C5**

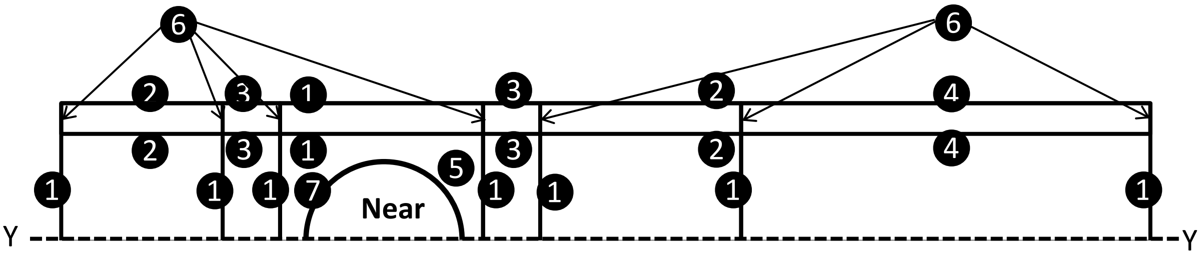

Figure 105 Breakdown of mesh sizing (cross-section along flume centreline)

Table 28 Mesh sizings for Figure 105

| # | Type | Sizing [m] | # | Type | Sizing [m] |
|---|---|---|---|---|---|
| **1** | Edge | 0.030 | **5** | Face | 0.010 |
| **2** | Edge | 0.060 | **6** | Edge | 0.003 |
| **3** | Edge | 0.045 | **7** | Edge | |
| **4** | Edge | 0.075 | | | |

Although CFX-meshing produces an automatic mesh, controls were applied to tailor the mesh. The controls used included body, face and edge sizing, in addition to inflation on the geometry of the blades. To maintain a structured grid in the far domain, edge sizing was used along all virtual edges, as seen in Figure 105. Inflation was used on the turbine blades for the SST model mesh to obtain a $y^+<2$. The inflation control is used to mesh the boundary layer of a wall through applying a thin layer of prismatic elements. The thickness of the first element depends upon the desired $y^+$ value. For the SST model a criteria of $y^+<2$ was used, based on Section 11.1.3.1. Since the k-ε model does not resolve the viscous sub layer of the boundary layer and requires a $11.06 \leq y^+ \leq 300$, inflation was not required. The desired $y^+$ values along the turbine blades were achieved through trial and error. Initial estimates of the near wall distance for a desired $y^+$ were calculated using equations such as Equations (52) and (53), the $y^+$ was then monitored during trial simulations and if deemed too high (in the case of SST) or too low (in the case of k-ε) then it was altered. Both the average and the maximum y+ along the blade geometries were monitored, since from Equation (52) $y^+$ is a function of the Reynold's number and therefore changes along the blade length. The blade mesh sizing used for the SST turbulence model were inflation along the blade edges with an initial size of 2.38x10$^{-5}$ m, a growth ratio of 1.2 and a minimum number of elements of 10 and can be seen in Figure 103c. In addition to inflation, a fine edge sizing of 5.0x10$^{-5}$ m was required in order to obtain the recommended aspect ratio for inflated edges. The required blade mesh sizing for the k-ε turbulence model to maintain the recommended y$^+$ values was sufficient from the body sizing of the near domain, 7.5x10$^{-3}$ m, and can be seen in Figure 103d. For the 2D CU flume domain, the far field had 31063 elements for both the k-ε and SST model, whilst using the 2D Savonius geometry in the CU flume domain as an example, the SST model had 129,313 elements in the near domain compared to 11491 elements for the k-ε model; therefore the k-ε model had only 11% of the element count of the SST model. The mesh for the 3D model was extrapolated from the 2D model using identical sizing, the wireframe of the 3D geometry for the Savonius and the location of the 2D plane can be seen in Figure 106.

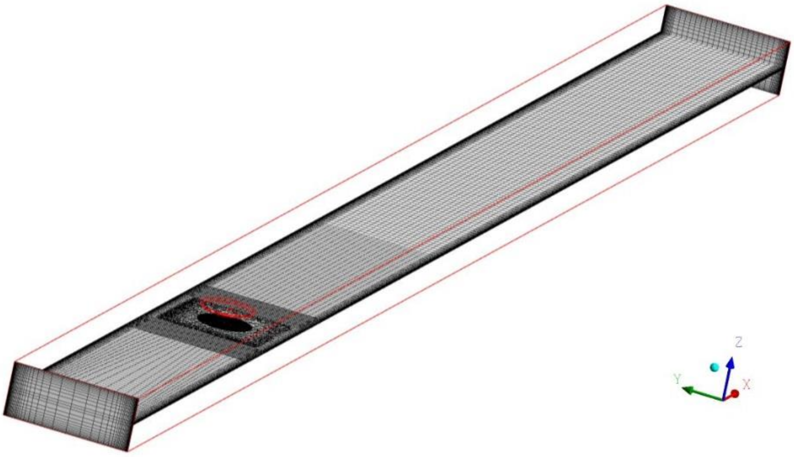

**Figure 106 3D wireframe of CU geometry and location of 2D plane, z=0.25 m along x-y plane**

For both the SST and k-ε models, to maintain a structured grid near the walls in the far domain a bias edge (2D)/face (3D) was used along the flume walls but designed to a y$^+$>11.06 (seen in Figure 103b), since resolving the boundary layer of the flume walls for the SST model was deemed unnecessary, therefore the automatic wall function was used. For all interfaces such as the interface between the near and far domain (Ansys, Inc., 2009a) recommends similar element length scales either side of the interface. This was achieved through applying equal edge (2D)/ face (3D) sizing for the mesh both sides of the interface, as seen in Figure 103b and Figure 104.

Since simulation time is directly proportional to the number of elements in the mesh, it was therefore vital that a mesh convergence study was carried out, seen in section 11.2.7.1. A mesh convergence study achieves a balance between the number of elements and simulation time through comparing the results of numerous simulations with varying degrees of mesh densities. The chosen mesh will achieve similar results to that of the densest mesh but with greatly reduced simulation time. Conducting a mesh convergence study reduces the spatial discretization errors, which (CFD Online, 2013) describes as one of the key sources of simulations errors.

ANSYS meshing provides mesh metrics to quantify the mesh quality. Throughout meshing the mesh metrics adhered to were: Aspect ratio and skewness of the elements. Aspect ratio is the ratio of the shortest side to the longest side of an element. For a triangle or a square the perfect aspect ratio is equal to 1. Ansys recommends an aspect ratio <40 for non-inflated layers and <50 for inflated layers. Skewness refers to the deviation from an equilateral volume, the metric ranges from 0 (good) to 1 (bad). Ansys recommends a skewness value of <0.95. During meshing if the recommended limits for the mesh metrics were exceeded, Ansys provides an option to highlight the worst elements through selecting “show worse elements”. Subsequently the mesh was refined in the areas of concern until the recommended mesh metric limits were satisfied.

### 11.2.3 Set-up

Referred to as CFX-Pre in the Ansys Workbench, it is where the physics and parameters of the simulation are defined. The parameters of the boundary conditions for all models can be seen in Table 29. Since the CFX models will be validated against data from the physical testing at CU, an identical flow condition to that used for testing at CU was applied to the CFX models. The chosen flow condition, as seen in Table 29 corresponds to the flow condition at a pump power of 25% and was inputted to CFX as a homogenous (plug) flow. A plug flow condition was used since the flow speed within the turbine cross-section during physical testing is relatively uniform, see Figure 72 and

Figure 73 whilst since the CFX study is an initial study, using a plug flow simplifies the set-up. Further details on the derivation of the flow condition can be found in Section 10.1.

**Table 29 Boundary conditions for all CFX models**

| Boundary Condition | Scenario | Geometry | | |
|---|---|---|---|---|
| | | Flume | | Large |
| | | 2D | 3D | 2D |
| Inlet | U (m/s) | 0.77 | 0.77 | 0.77 |
| | V (m/s) | 0 | 0 | 0 |
| | W (m/s) | 0 | 0 | 0 |
| | I (%) | 10 | 10 | 10 |
| Outlet | outlet/opening | outlet | outlet | outlet |
| Lateral Walls | free/no-slip | no-slip | no-slip | free-slip |
| Top Surface (z=0m) | wall | symmetry | free-slip | symmetry |
| Bottom surface (z=max) | wall | symmetry | no-slip | symmetry |

Both steady state and transient simulations were conducted during this study. A steady-state analysis is whereby the turbine characteristics do not change with time, therefore no real time flow information is required; this method was used to predict the static performance of the turbines. A steady state simulation has no concept of elapsed time since CFX applies a “false timestep” to under-relax the equations as they iterate towards the final solution (Ansys, Inc., 2009a). Steady state analysis was used to analyse the starting torque behaviour of both CarBine and the Savonius and the behaviour of solitary arms/buckets. The $C_t$ for starting torque will be analysed at $10^{o}$ intervals (identical to the physical testing, see Section 9.4.3.2) for 2D simulations and at every $20^{o}$ for the 3D simulations.

A transient analysis, whereby real time flow information is required was used for obtaining $C_p$-$\lambda$ curves, whereby the timestep (s) and simulation time (s) must be defined. The timestep is the frequency at which the governing equations are solved and is determined through a timestep independency study, seen in Section 11.2.7.3. The simulation time is determined once convergence of a solution is obtained, for a rotating turbine this is achieved once monitored parameters are repeated for subsequent revolutions. Similar to the mesh convergence study (see Section 11.2.7.1), a balance is required between a lower timestep with increased accuracy and computational demand. For the rotating simulations the timestep was proportional to a fixed rotated angle, e.g. a timestep every $2^o$, as seen in Figure 114. Ansys, Inc., (2009c) recommends a timestep in the region of 0.1/ω to 1.0/ω for turbomachinery. Conducting a timestep study reduces the temporal discretization errors, which CFD Online, (2013) describes as one of the key sources of simulations errors.

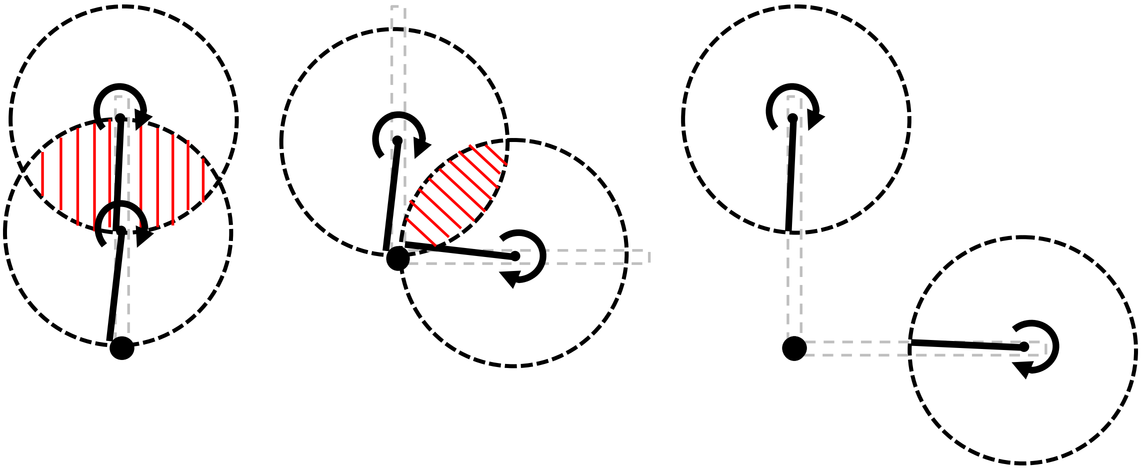
(a) (b) (c)

Figure 107 MRFs of CarBine (a) Inner and outer flaps (b) inner only (c) outer only

For obtaining a $C_p$-λ curve the near domain must be rotated, for this CFX provides the transient rotor stator (TRS) option. The TRS option uses an angular velocity (ω) value as an input, for this study the angular velocity is calculated using the expressions in Table 31; resulting in a uniform value for the angular velocity during a revolution. Since the Savonius turbine is a rigid body the entire near domain can simply be modelled as a TRS: CarBine however cannot. The two degrees of rotational freedom present in the CarBine design i.e. the flaps rotating about their local z axes and the arms rotating about the global Z axis (seen in Figure 40) results in CarBine being difficult to model precisely. Rigid body turbines, such as a Savonius with the single degree of rotational freedom, are easy to simulate and can be done through using a single multiple frame of reference (MFR). However the two flaps per arm CarBine design cannot be simulated using several MFR since MFR cannot overlap, as seen in Figure 107. Therefore the only CarBine configurations that can be simulated are those with only the outer flap on each arm; since modelling only the inner flaps will result in the MFR from other arms overlapping. The solution was to use subdomains within the near domain, as seen in Figure 108. The subsequent geometry and mesh for the 3, 4 and 5 arm CarBine can be seen in Figure 104. The subdomains would rotate at the angular velocity of the near domain ω but would also rotate about their local axes $\omega_\alpha$ using the mesh motion specified by the CEL expressions in Table 30. The CEL expressions ensure that the CarBine flaps remain in a closed position i.e. flaps pointing towards the central axis of the turbine whilst in the generating phase, but open to align with the flow in the non-generating phase.

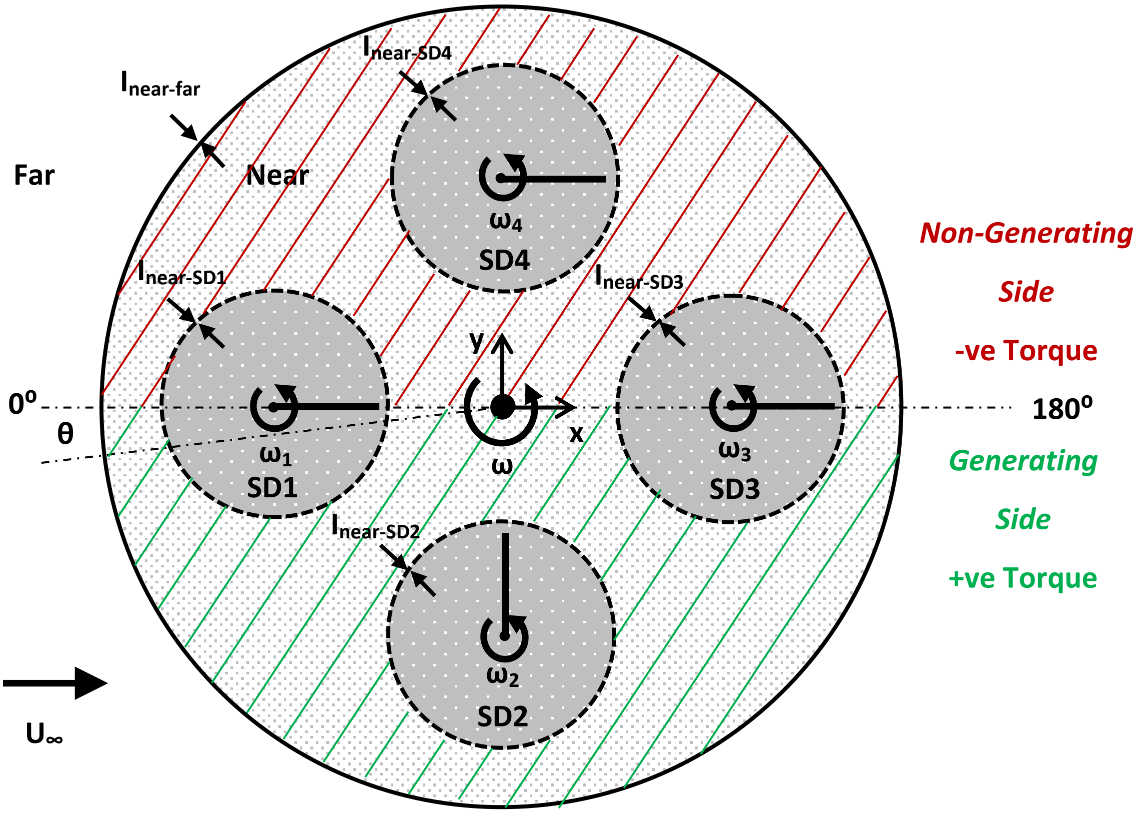

**Notes:**

**SD – Sub-domain; $I_{near-far}$ –Interface between the near and far domain; ω-global angular velocity; $\omega_1$ – local sub domain angular velocity**

Figure 108 CFX Composition of near domain for 4 arm CarBine

Using SD1 from Figure 108 as an example, the following CEL expressions in Table 30 describe the motion of SD1; the expressions are repeated for subsequent subdomains. The motions of the subdomains are described using the specified location option in CFX. The TRS option cannot be used for the subdomain motion since the TRS requires a fixed position for the axis of rotation, i.e. the local z axis; as a result the specified location for mesh motion was used.  The chosen mesh motion option in CFX was the specified location.  Specified location permits the user to dictate the mesh motion of the subdomain using Cartesian coordinates x, y and z relative to the starting position of the mesh.  For the CarBine simulation the calculated Cartesian coordinates for the motion of the subdomain at each timestep are defined using: F1xNew, F1yNew and F1zNew (highlighted in Table 30).

**Table 30 CFX Expressions for CarBine flaps**

| Parameter | CEL Expression | |
|---|---|---|
| F1Angle | 180[deg] | (55) |
| F1x0 | $Radius * \cos(F1Angle)$ | (56) |
| **F1xNew** | $\boldsymbol{\left((x - F1x0) - Total\ Mesh\ displacement\ X\right) * \cos(FlapAngleF1) + \left((y - F1y0) - Total\ Mesh\ Displacement\ Y\right) * \sin(FlapAngleF1) + F1x0}$ | (57) |
| F1y0 | $Radius * \sin(F1Angle)$ | (58) |
| **F1yNew** | $\boldsymbol{-\left((x - F1x0) - Total\ Mesh\ displacement\ X\right) * \sin(FlapAngleF1) + \left((y - F1y0) - Total\ Mesh\ Displacement\ Y\right) * \cos(FlapAngleF1) + F1y0}$ | (59) |
| F1z0 | 0[m] | (60) |
| **F1zNew** | $\boldsymbol{\left((z - F1z0) - Total\ Mesh\ Displacement\ Z\right) + F1z0}$ | (61) |
| FlapAngleF1 | $FAngles(NearAngle)$ | (62) |

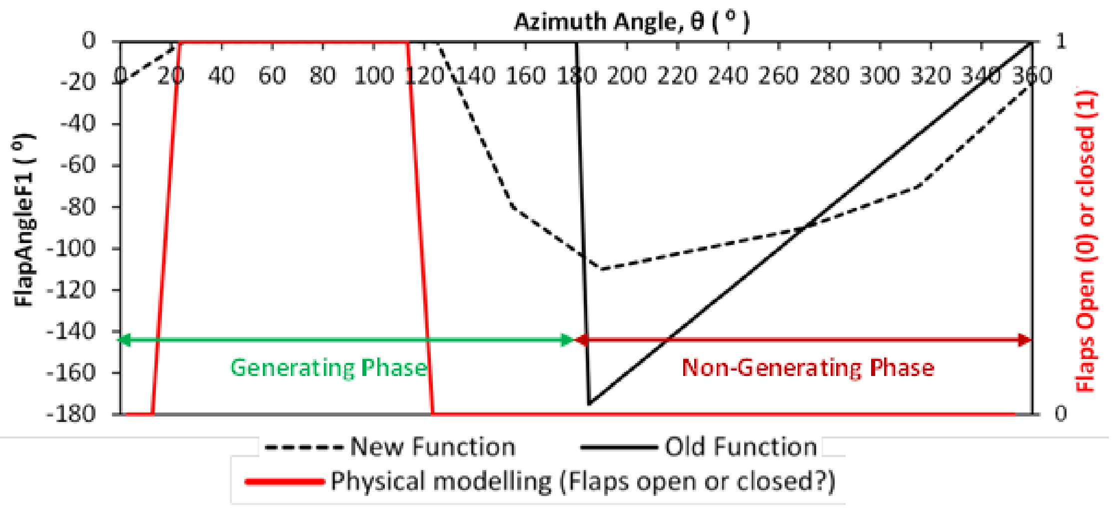

**Figure 109 CFX User function for CarBine flap angle**

FAngles is defined in CFX as a user function. The user function works through taking an input argument, in this case “NearAngle”, and outputting a value based on a reference table. The reference table indicates that based on the NearAngle (i.e. the global rotated angle) whether the flap for the subdomain in question should be open or closed. Initially the function was based on the flaps being closed for $0^{o} \leq \theta \leq 180^{o}$ and open for $180^{o} < \theta < 360^{o}$, but during trials it was discovered that the transition between closed and open flap, i.e. from $180^{o}$ to $181^{o}$ was too sudden. This caused a severe spike in both the residuals and the monitored data points, including torque on other flaps, and temporarily caused numerical diffusion. Subsequently a new user function was defined whereby the flaps open gradually, resulting in flaps being closed for $20^{o} \leq \theta \leq 130^{o}$, opening during $130^{o} \leq \theta \leq 190^{o}$ and finally closing during $320^{o} \leq \theta \leq 360^{o}$. This new function was based upon observations of the flap behaviour during physical static testing of CarBine, the results of which can also be seen in Figure 109. In Figure 109, for the functions, a FlapAngle of $0^{o}$ indicates a closed flap, whilst a FlapAngle of $180^{o}$ indicates an open flap (parallel with the flow). Although the results of the flap behaviour for physical testing in Figure 109 show the flaps were either open or closed, in reality, similar to that of the new function, the flaps would gradually begin to close from $180^{o} < \theta < 360^{o}$. Although from observations, the opening process was more sudden than that prescribed in the new function.

#### ***11.2.3.1 CEL***

CFX Expression Language (CEL) is “an interpreted, declarative language that has been developed to enable CFX users to enhance their simulations without recourse to writing and linking separate external Fortran routines” (Ansys, Inc., 2009c, p. 133). For this study CEL was used to calculate parameters based on other variables and to specify parameters to monitor as seen in Table 31 and Table 32.

**Table 31 CEL expressions for CFX simulation parameters**

| Parameter | Acronym | CEL Expression | |
|---|---|---|---|
| Time step | Tstep | $tTotal/((360/DegreesTstep) * NoRevolutions)$ | (63) |
| Total Simulation Time | tTotal | $((2 * pi[rad])/Omega) * NoRevolutions$ | (64) |
| Rotated angle per time step | DegreesTstep$^{a}$ | $if(NearAngle < 13 * pi[rad]), 10,2)$ | (65) |
| Total rotated angle | NearAngle | $Omega * t$ | (66) |
| Current simulation time | t | CFX VARIABLE | |
| Angular Velocity | Omega | $(TSR * U)/Radius$ | (67) |
| Freestream flow speed | U | 0.77 [ms^-1] | |
| Turbine Radius | Radius | 0.2[m] | |
| Tip Speed Ratio | TSR | USER DEFINED | |
| Number of Revolutions | NoRevolutions$^{b}$ | 8 | |

**Note: $^{a,b}$ study relating to these definitions can be found in Section 11.2.7.3**

**Table 32 Monitor points for CFX simulations**

| Monitor Point | CEL Expression | |
|---|---|---|
| Torque on Blade 1 in the z axis$^{a}$ | $torque\_z()@Blade1$ | (68) |
| Average y+ on Blade 1$^{a}$ | $areaAve(yplus)@Blade1$ | (69) |
| Maximum y+ on Blade 1$^{a}$ | $maxVal(yplus)@Blade1$ | (70) |
| Total Rotated Angle | See Table 31 | |

**Note: Monitor points are repeated for each blade being modelled e.g. for a Savonius there are two sets, whereas for the four arm CarBine there are 4 sets.**

#### *11.2.3.2 Domain Interfaces*

Since the geometries consists of two domains, the near and far, an interface was required linking both. The rotating behaviour of the near domain meant a general grid interface (GGI) was used. This interface ensures the fluxes are conserved across the interface and is used when the elements either side do not directly align (Ansys, Inc., 2009d). For the Savonius turbine only one interface was required, thus being for the near-far domain interface. However for the CarBine simulations in addition to the near-far domain interface, an interface is also required between each subdomain and the near domain as illustrated in Figure 108.

### 11.2.4 Solver

The CFX solver provides a solution to the problem through:

- Integrating the partial differential RANS equations over the control volumes, which is the equivalent of applying a basic conservation law (such as mass or momentum) to each of the control volumes;
- The integral equations are then converted to algebraic equations through applying approximations to the terms in the integral equations;
- finally the algebraic equations are solved iteratively, due to non-linearity (Ansys, Inc., 2009a).

A solution is said to converge as it approaches the exact solution with the difference termed the residual. CFX provides recommendations for the average RMS residual levels and suggest $1x10^{-6}$, for tight convergence which is more than sufficient for most engineering applications (Ansys, Inc., 2010) this was adhered to throughout the CFX modelling for both steady state and transient simulations. As recommended in (Roache et al., 1986) all solutions were obtained using the second order accurate backward Euler scheme. Steady state solutions, unlike transient, are considered solved when the RMS residuals reach their target. However for the transient simulations, each timestep had a maximum of 10 loops (i.e. the number of iterations per timestep) to achieve the residual level. For the steady state solution attention was also paid to the monitored data points to ensure that these reached a converged value prior to the end of the simulation. To avoid round-off errors double precision was used for all simulations. Finally once a solution is achieved a results file is created and passed onto the post processing stage

### 11.2.5 Results

It is in CFX-Post in ANSYS Workbench that the results of the simulation can be visualised using various methods such as contour plots and flow streamlines. However during this study all relevant data was exported from the solver through specifically monitoring the required parameters, namely the torque on the blades, the $y^+$ values along the blades and the rotated angle as seen in Table 32. This both reduced the simulation time since irrelevant data was not saved at each timestep and allowed real time monitoring of the values of the parameters, this was particularly useful when deciding if convergence had been achieved during steady state simulations.

### 11.2.6 Application to study

Based on its capabilities, the following scenarios were simulated using CFX:

**Table 33 Simulated scenarios using CFX**

| Turbine | Configuration | ω? | Geometry | | |
|---|---|---|---|---|---|
| | | | Flume | | Large |
| | | | 2D | 3D | 2D |
| **CarBine** | 3 Arm[1] | ✓ | ✓ | | |
| | 4 Arm[1] | ✓ | ✓ | ✓ | ✓ |
| | 5 Arm[1] | ✓ | ✓ | | |
| | Single Arm[2] | | ✓ | ✓ | ✓ |
| **Savonius** | 2 Buckets | ✓ | ✓ | | ✓ |
| | 2 Buckets | | ✓ | | ✓ |
| | 2 Bucket & disks | ✓ | | ✓ | |
| | 1 Bucket | | ✓ | ✓ | ✓ |

**Notes:**

**[1] Each arm comprising of an outer flap only, see Section11.2.1**

**[2] Comprising of both an inner and outer flap**

### 11.2.7 Verification

The importance of verifying a numerical model is highlighted by (Gretton et al., 2009) who state that a study should be conducted on the following numerical parameters:

- Spatial discretization;
- Distance to far-field boundary;
- Iterative convergence.

#### *11.2.7.1 Spatial Discretization*

The spatial discretization study, also described as a mesh convergence study, was conducted on a single CarBine flap for a steady state 2D analysis using the k-ε turbulence model. The k-ε model was chosen over the SST model for this study to reduce the simulation time. The torque was analysed on the flap every $10^{o}$ from $0^{o} \leq \theta \leq 180^{o}$ and averaged for various meshes. As seen in Table 34 the recommended minimum grid refinement of 1.3 by Celik et al., (2008) has been exceeded. Since the geometry is divided into 2 domains, near and far, the mesh convergence was analysed as a complete geometry and individually for the near and far domains. The meshes are identified via a case number, e.g. 1.2, the first digit refers to the near mesh used whilst the second digit refers to the far mesh. Three different near mesh resolutions and 4 different far mesh resolutions were used in total. As seen from Table 34 and Figure 110 there was little variation (<1%) in torque for all meshes when compared to the finest mesh, case 1.1. As expected the simulation decreased with decreasing element count. Case 1.3 was used as the mesh sizing for all 2D simulations since it achieved the closest match to that of Case 1.1.

**Table 34 Mesh details for mesh convergence study**

| **Case Number** | **Element Count** | | | **Grid Refinement Factor (Case Number/Case 3.4)** | **$C_t$** | | **Time ratio compared to Case 1.1** |
|---|---|---|---|---|---|---|---|
| | ***Near*** | ***Far*** | ***Total*** | | ***Average (Nm)*** | ***Ratio compared to Case 1.1*** | |
| **1.1** | 43682 | 122549 | 166231 | 3.45 | 0.918 | 1.000 | 1.00 |
| **1.2** | 43682 | 49709 | 93391 | 1.94 | 0.924 | 1.006 | 0.55 |
| **1.3** | 43682 | 31065 | 74747 | 1.55 | 0.920 | 1.002 | 0.44 |
| **2.3** | 36873 | 31065 | 67938 | 1.41 | 0.914 | 0.995 | 0.40 |
| **1.4** | 43682 | 22301 | 65983 | 1.37 | 0.926 | 1.009 | 0.40 |
| **2.4** | 36873 | 22301 | 59174 | 1.23 | 0.967 | 1.014 | 0.32 |
| **3.3** | 25891 | 31065 | 56956 | 1.18 | 0.930 | 1.054 | 0.36 |
| **3.4** | 25885 | 22301 | 48186 | 1.00 | 0.931 | 1.013 | 0.30 |

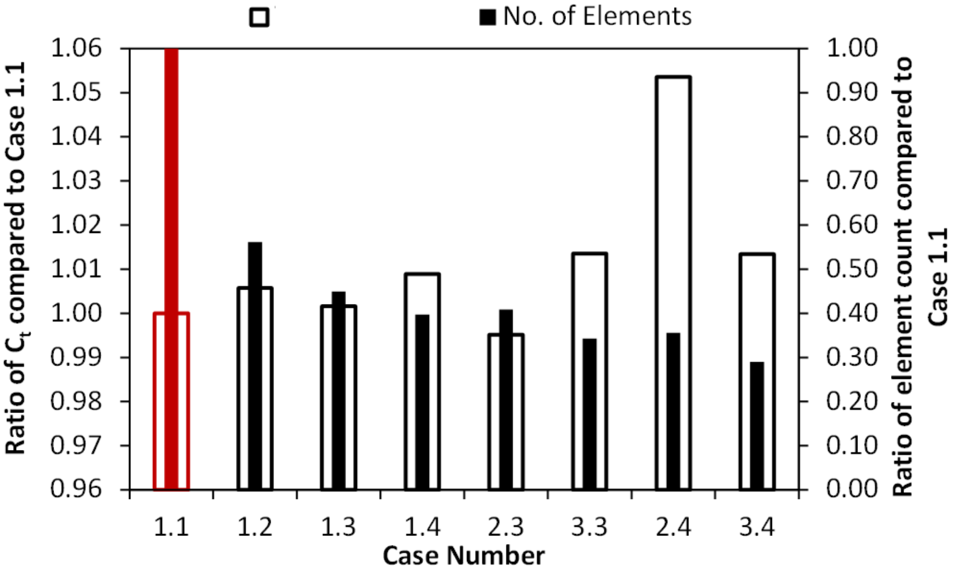

Figure 110 Mesh convergence study, $C_t$ and no. of elements vs. Case number (from Table 34)

### 11.2.7.2 *Large domain dimensions study*

The purpose of the large domain dimensions study is to compare the performance of tidal turbines in a domain whereby minimal horizontal blockage is present (vertical blockage is not an issue for the 2D study) with that of flume conditions, further details in Section 9.5. In order to determine the dimensions of the large domain a large domain convergence study was conducted, whose primary aim was to increase the width of the domain until the monitored points converged.

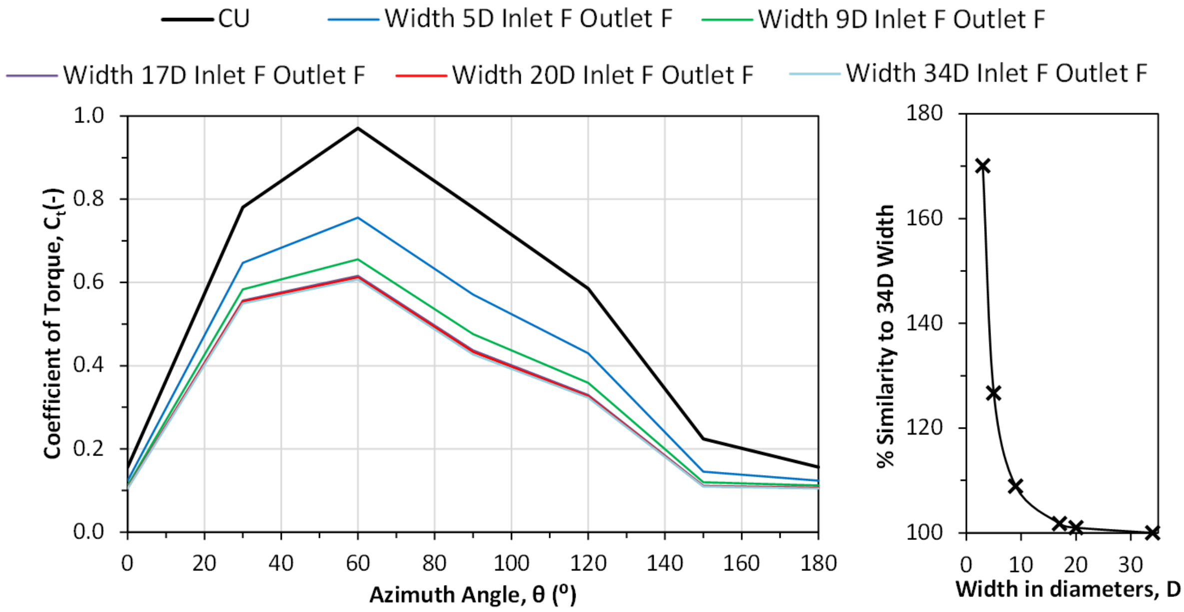

Figure 111 CFX Mesh Convergence Study – Width analysis

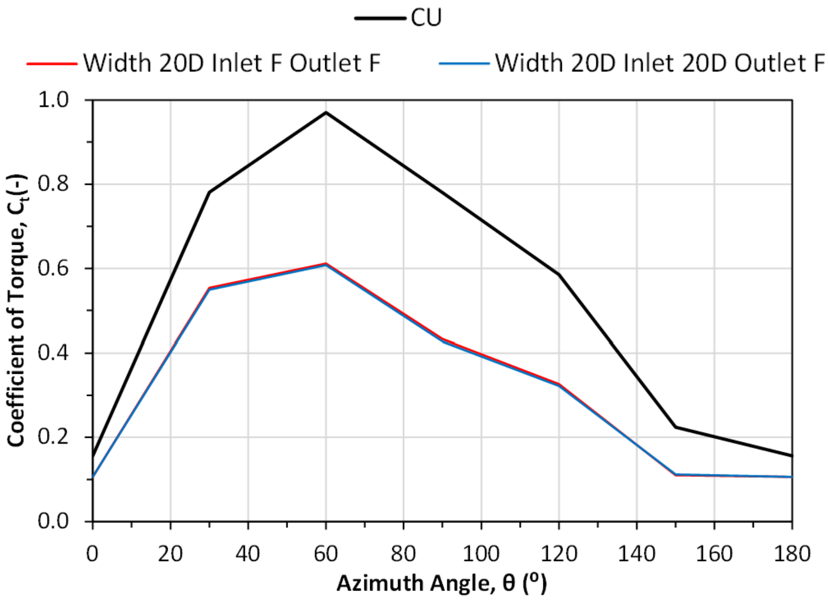

Figure 112 CFX Mesh Convergence Study – Inlet analysis

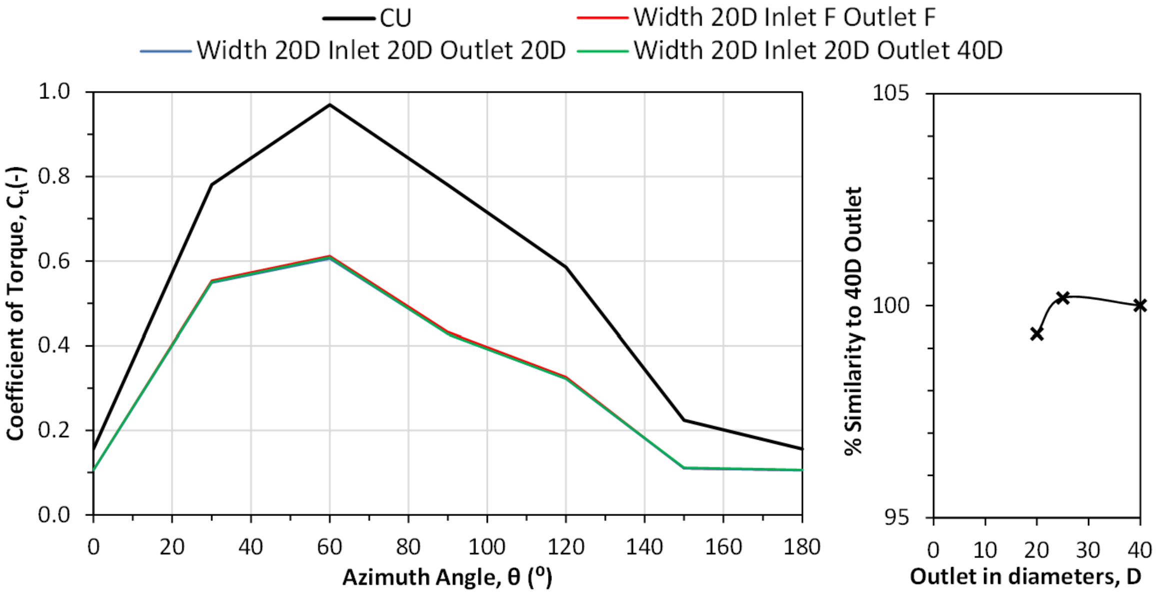

Figure 113 CFX Mesh Convergence Study – Outlet analysis

Figure 111 shows convergence for the width dimension is achieved at 20D and it is clear from Figures Figure 112 and Figure 113 that extending both the inlet and outlet distances had minimal difference on the results (<1%). Therefore the dimensions used for the large domain are width: 20D, Inlet and Outlet: CU flume dimensions.

### 11.2.7.3 *Iterative convergence for transient simulations*

This section describes the study designed to find the timestep and total simulation time required in order to obtain converged results for the $C_p$-λ curves. This study obtained a solution for a rotating Savonius turbine. Rather than analysing physical timesteps the timesteps were calculated as a proportion of the rotated angle of the near domain. Additionally, rather than analysing the physical total simulation time the time was made proportional to the number of revolutions.

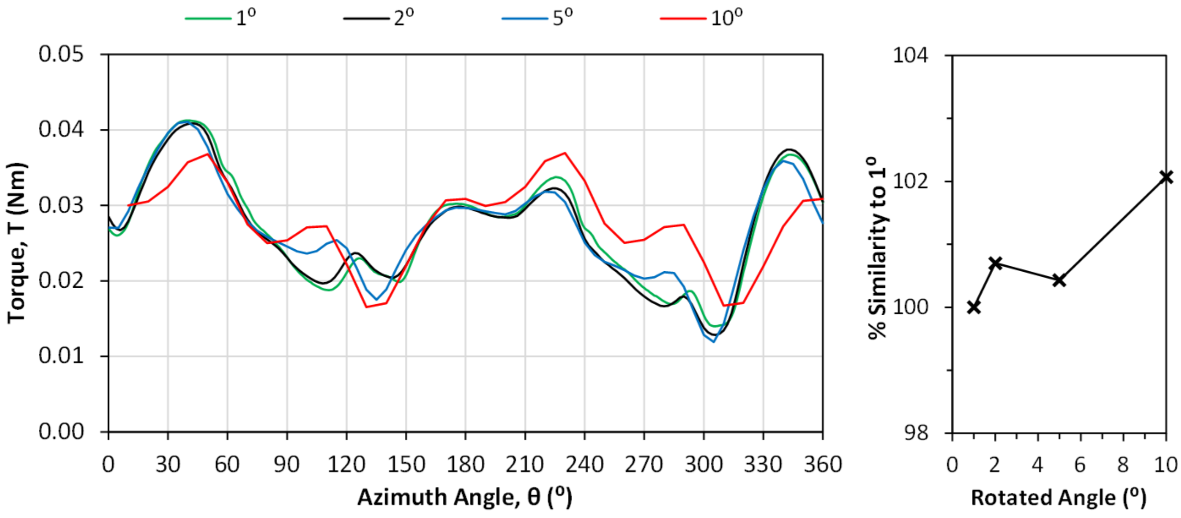

**Figure 114 Study of rotated angle per timestep**

Figure 114 shows the rotated angle per timestep and the percentage similarity of the torque for the rotated angles compared to the smallest angle, 1°. A rotated angle of 10° is only 2% different to the average torque of the 1°, however visually it is clear that the torque is considerably different. It is clear from Figure 114 that the average torque converges as the timestep approaches 1°. Since the 2° rotated angle is within 1% of the 1° rotated angle and based upon visual inspection it closely matches the torque of the 1° rotated angle; 2° was therefore chosen as the angle to be rotated every timestep.

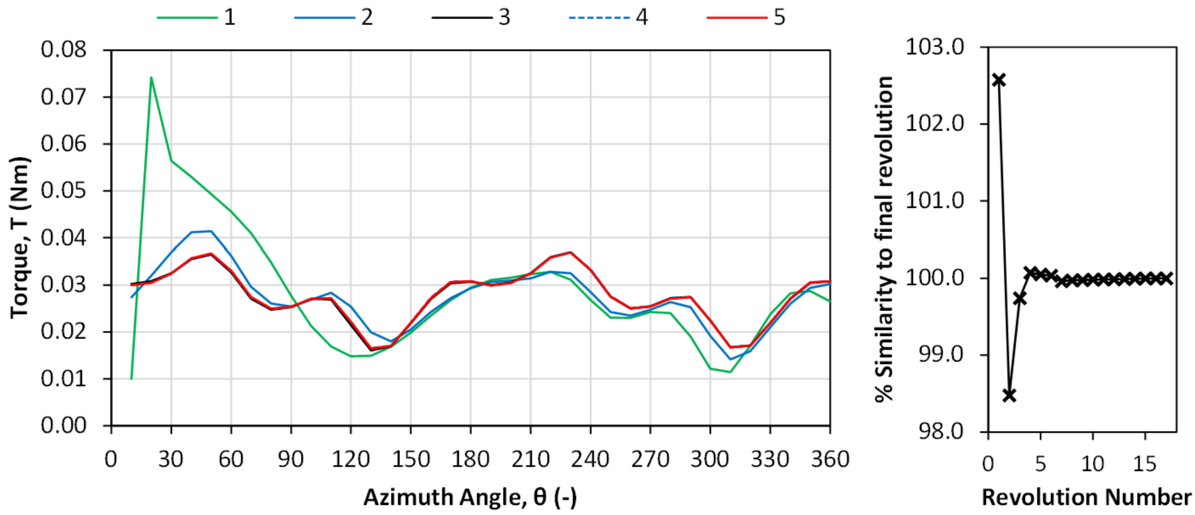

**Figure 115 Study of number of revolutions**

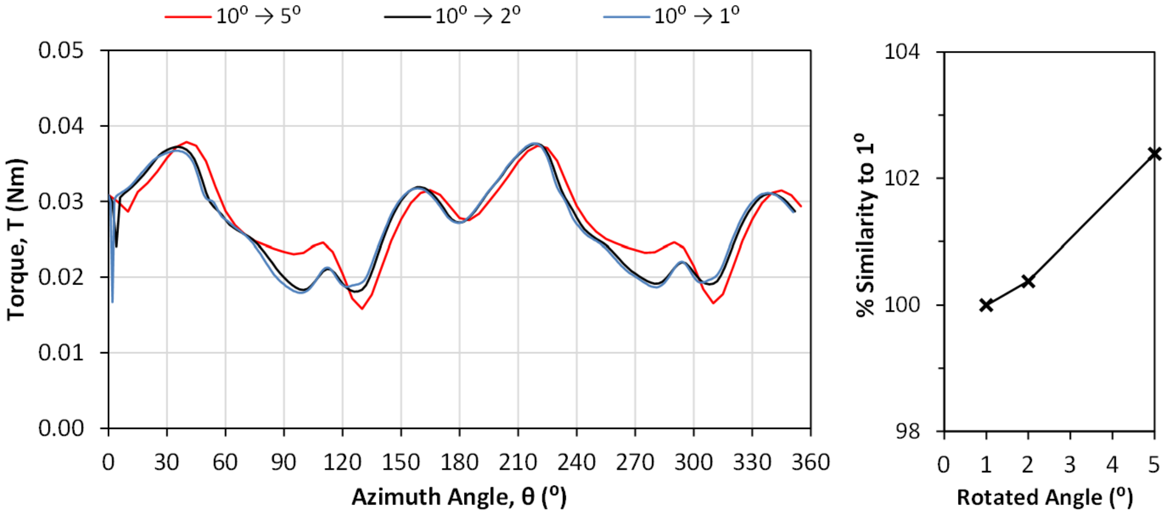

**Figure 116 Study of the change in rotated angle for 5th revolution**

For the total simulation time, the near domain was rotated until the torque was deemed to have converged. From Figure 115 it can be seen that from the fourth revolution onwards there is minimal variation in the average torque of a revolution. In order to reduce the total simulation time a 10° rotated angle was used for the first four revolutions and for the fifth revolution the rotated angle was reduced to 2°, this was also done for angles of 1° and 5° and can be seen in Figure 116. However as seen in Figure 116 there is a spike in the data at the start of the fifth revolution as the rotated angle changes from 10° to 2°. In order to avoid this spike, the rotated angle for future simulations will change halfway through the fourth revolution.

# 12 Numerical Modelling-Results & Discussion

**This chapter contains the simulation results for the numerical modelling using Ansys CFX and is divided into the results from simulations of CarBine and the Savonius. Simulations of CarBine revealed that C5 achieved the greatest $C_p$max (0.104 (SST), 0.109 (k-ε)) followed by C4 (0.146, 0.154) and C3 (0.135, 0.155), with each simulation over predicting the performance values compared to physical model results. For all CarBine simulations the results showed similar distribution but at a greater offset to those of the physical testing with $C_p$max occurring at a similar λ=0.4. For unsteady simulations of the Savonius the 3D results show greatest similarity to the physical testing results, with only a 20% over prediction in $C_p$max. For both CarBine and Savonius simulations it is the steady state simulations of the starting torque which produced the best validation to physical testing results. For all simulations the k-ε model predicts greater performance than the SST model, whilst 3D simulations provide closer validation to physical testing results than 2D simulations.**

For data analysis, Equations (3)-(7) were used where torque, T was averaged over a revolution. Table 29 details the flow conditions used for the simulations, thus being a plug flow of $U_\infty$=0.77 m/s and turbulence intensity, I=10%. Simulations are 2D unless stated otherwise. For 2D simulations both the k-ε and SST turbulence models are employed but for 3D analysis it is solely the k-ε turbulence model. Two different geometries are used in the numerical model study, thus being the CU geometry (see Table 15) and the large domain geometry (see Section 11.2.7.2). Within this chapter the numerical modelling results are compared to the physical testing results wherever available. Particular attention is paid to the C4 configuration since C4 achieved the greatest $C_p$max of the CarBine configurations during physical testing.

## 12.1 CarBine Results

### 12.1.1 Transient analysis of $C_p$ vs. λ for all configurations

Figure 117 shows the performance results of 2D transient unsteady simulations of various CarBine configurations. Each Carbine configuration has a colour indicator whilst both the k-ε and SST turbulence model have different symbols, in addition the physical testing results for each CarBine configuration are indicated by a different symbol. It is important to note that the physical testing results are for configurations with both an inner and outer flap for each arm whereas the simulations only possess an outer flap for each arm. Besides for C4 whereby physical testing results are available for an outer flap only, further discussed below in Figure 118. The reasons for why configurations with both an inner and outer flap could not be simulated can be found in Section 11.2.3.

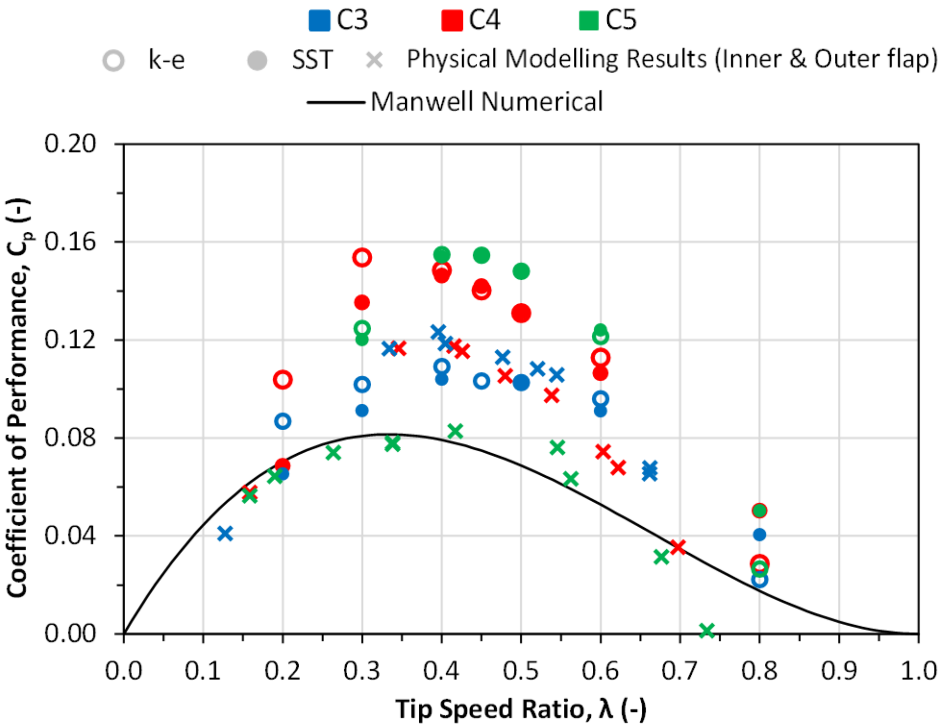

**Figure 117 $C_p$ vs. λ comparison of CFX vs. physical testing results for CarBine**

**Table 35 Summary of $C_p$max/λ for CFX vs. physical testing results from Figure 117**

| CarBine | SST | | k-ε | | Physical testing | |
|---|---|---|---|---|---|---|
| | $C_p$ | λ | $C_p$ | λ | $C_p$ | λ |
| C3 | 0.104 | 0.400 | 0.109 | 0.400 | 0.123 | 0.395 |
| C4 | 0.146 | 0.400 | 0.154 | 0.400 | 0.117 | 0.415 |
| C5 | 0.135 | 0.450 | 0.155 | 0.400 | 0.083 | 0.417 |

In Figure 117 it can be seen that CFX predicts that the highest performing configuration is the C5 configuration, followed by C4 and finally C3. This is the opposite outcome to the physical testing results. From Table 35 it can be seen that the optimum operating conditions for both the simulations and physical testing results occur at an identical λ=0.4. However the simulations for both C4 and C5 over predict the $C_p$max value for both turbulence models whereas for C3 the results from the turbulence models are comparable to that of the physical testing results. Although as seen in the physical testing results in Figure 79 for C4, the $C_p$max of C4O (outer flap only) is 39% lower compared to C4 (inner and outer flap). As a result, although the results from the simulation of C3 are comparable to the physical testing results, for physical results of an outer flap only the difference between simulation and physical results would be much greater. Despite the over prediction of the simulations, each of the simulations predicts a very similar distribution to the physical testing results which is a distribution similar to the Manwell curve but offset at higher $C_p$ values. Comparing both turbulence models it can be seen that although both the k-ε and SST models have similar results for λ=0.4-0.5 for the lower and higher values of λ the k-ε model predicts higher $C_p$ values than the SST model.

### 12.1.2 Transient analysis of $C_p$ vs. λ for C4 and C40

Using Figure 118, which has isolated the performance of C4 (the highest performing CarBine configuration from physical testing) from Figure 117, the results from the simulations of C4 can be directly compared to the physical model results of C4O. The results of both turbulence models predict $C_p$max values of around 100% greater than that of the physical testing results although the distribution of the data is very similar with $C_p$max occurring at an identical value of λ=0.4 for the SST model and C4O physical model whereas it occurs at λ=0.3 for the k-ε model. The performance results from the large domain, simulated using the k-ε model, lie perfectly on the curve of the C4 physical testing results although $C_p$max occurs at λ=0.3. Compared to the k-ε simulation of the CU domain, the predicted large domain $C_p$max is 20% less which is an expected result based on the minimal blockage present in the large domain. This result is also seen in the physical testing between CU and IFREMER, see Section 10.2.2.

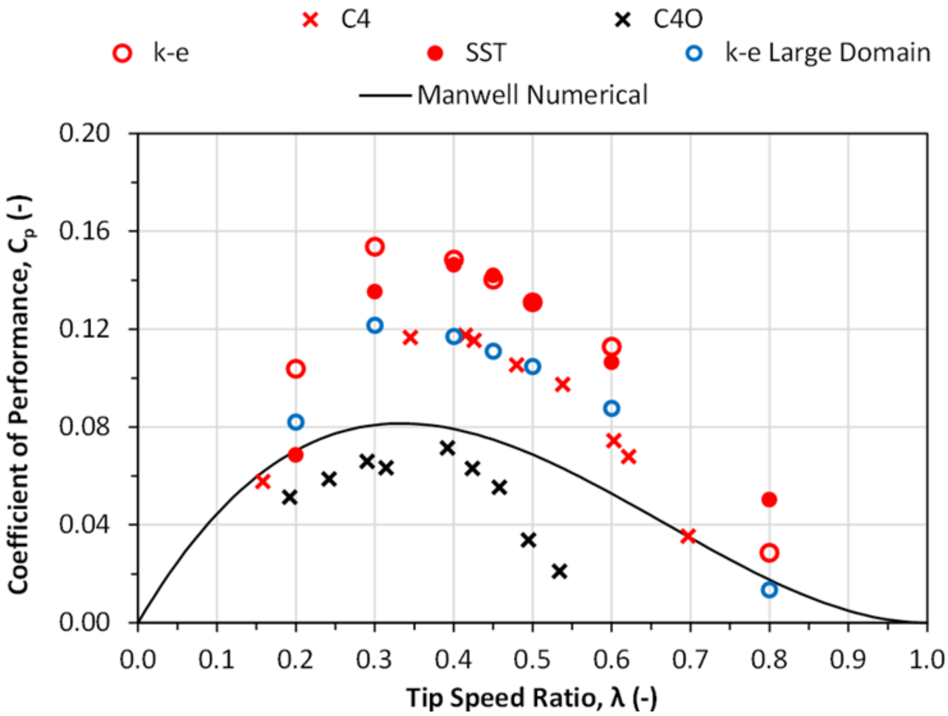

**Figure 118 $C_p$ vs. λ comparison of CFX vs. physical testing results for C4**

### 12.1.3 Transient analysis of $C_p$ vs. θ for C40

Figure 119 shows the $C_t$ vs. θ for the CarBine C4O configuration for the 2D unsteady dynamic simulations for both the k-ε and SST turbulence models and the results from the physical testing for λ=0.4 (optimum operating condition). The accompanying $C_p$-λ curves for the simulations and physical models can be seen in Figure 118 and Figure 79 respectively. Both turbulence models exhibit the $90^o$ phase repeating pattern shown in the results of the physical model. The k-ε model predicts greater performance than that of the SST model for the first $15^o$-$40^o$ of each phase which is reflected by the greater predicted $C_p$ value in Figure 118. The 2D simulations show large variance in $C_t$ over a $90^o$ phase which is contrary to the physical model which shows little variance. Rather than the flat crested peaks in $C_t$ for the physical model the simulations show 3 peaks for each $90^o$ phase. Ignoring the 3D effects that are not accounted for during 2D simulations (discussed later in this section) the largest difference between the physical model and results from the numerical models are that the turbines in the numerical models are driven i.e. rotate at a constant specified ω, whereas the physical models rotate based on the hydrodynamic forces on the turbine blades, resulting in an unsteady ω.

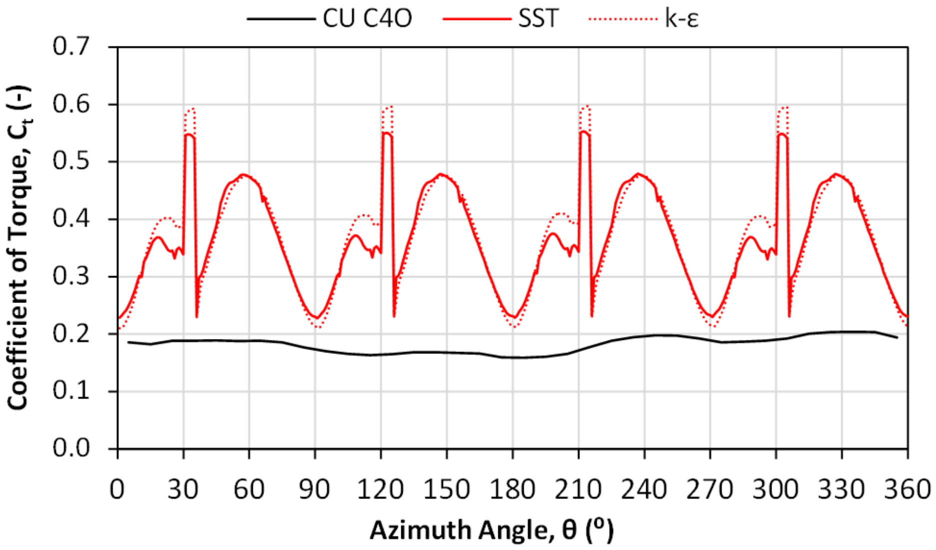

**Figure 119 $C_t$ vs. θ for CFX vs. physical testing results for λ=0.4**

### 12.1.4 Steady state analysis of a single arm

Figure 120 shows the starting $C_t$ for steady state 2D and 3D simulations for both CU and large domain geometry of a 1 arm (inner and outer flap) CarBine. For the CU geometry the SST model under-predicts $C_t$ for $0^o \le \theta \le 40^o$ whilst they over-predict $C_t$ for $50^o \le \theta \le 150^o$. The 3D simulations of the CU geometry under-predict $C_t$ for $0^o \le \theta \le 120^o$ and over-predict $C_t$ for $120^o \le \theta \le 140^o$. The 3D geometry without the disks has a higher $C_t$ value, typically around 0.075 greater from $0^o \le \theta \le 160^o$, than the 3D geometry with disks. This is an expected result since both the top and bottom disks provide additional unwanted skin friction drag to the turbine which reduces the overall generated torque. For the 2D simulations of the large domain, compared to the IFREMER data both the k-ε and SST models over-predict $C_t$ for $0^o \le \theta \le 180^o$. The angle of maximum $C_t$ is predicted to be at $\theta=80^o$ for both 2D (k-ε and SST) and the 3D simulations of the CU geometry whereby for the physical model it is at $\theta=65^o$. The angle of maximum $C_t$ is predicted to be at $\theta=70^o$ for both 2D (k-ε and SST) simulations of the large domain which coincides with the position of maximum $C_t$ for the results from the IFREMER physical model.

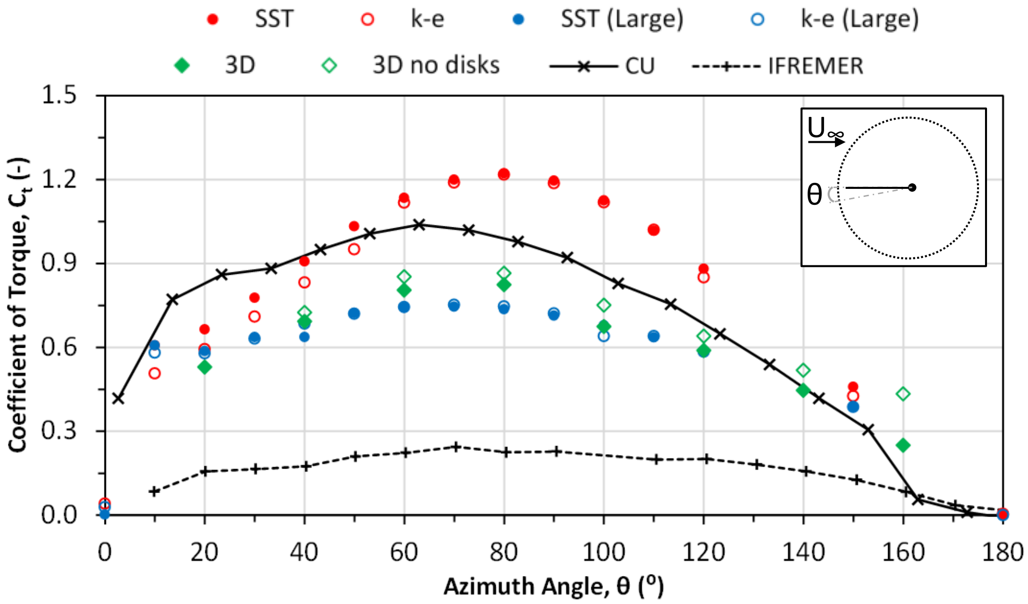

Figure 120 CFX vs. Laboratory results for static state 1 arm CarBine

### 12.1.5 Steady state analysis of C4

Figure 121 shows the steady state analysis of the starting $C_t$ for C4 modelled for one phase ($90^o$) using only the arms in the positive generating side, i.e. ignoring the open flaps. The SST and k-ε model predict a negative $C_t$ for $0^o \leq \theta \leq 10^o$ whereas in this region the physical model produces positive results with $\theta=3.5^o$ being the peak $C_t$ for $0^o \leq \theta \leq 90^o$. The peak $C_t$ =0.94 at $\theta=30^o$ for the SST model whereas the peak $C_t$ =0.73 at $\theta=80^o$ for the k-ε model. Despite the large differences in $C_t$ for the SST model compared to the physical model for $0^o \leq \theta \leq 10^o$ for $20^o \leq \theta \leq 80^o$ the SST model shows good agreement to the distribution of the physical model (besides the spike at $\theta=30^o$) where it over-predicts $C_t$ by around 50%. For $0^o \leq \theta \leq 50^o$ the k-ε model is less similar to the physical model than the SST model, but for $60^o \leq \theta \leq 80^o$ the k-ε model does show a similar distribution to that of the physical model. The magnitude of the over-prediction of the simulations could be reduced with the inclusion of the open flaps, which would be subjected to skin friction drag subsequently introducing additional negative $C_t$ to reduce the over-prediction. The 2 arm geometry used for the simulations lie flush against the turbine shaft and can therefore trap fluid. For the physical model the flaps do not create a perfect joint at the centre and there is space for fluid to escape. Trapping the fluid within the corner between both arms is likely to lead to stagnation points and therefore a higher pressure differential either side of the arms leading to a larger induced torque, this could also explain the over-prediction of the simulation results.

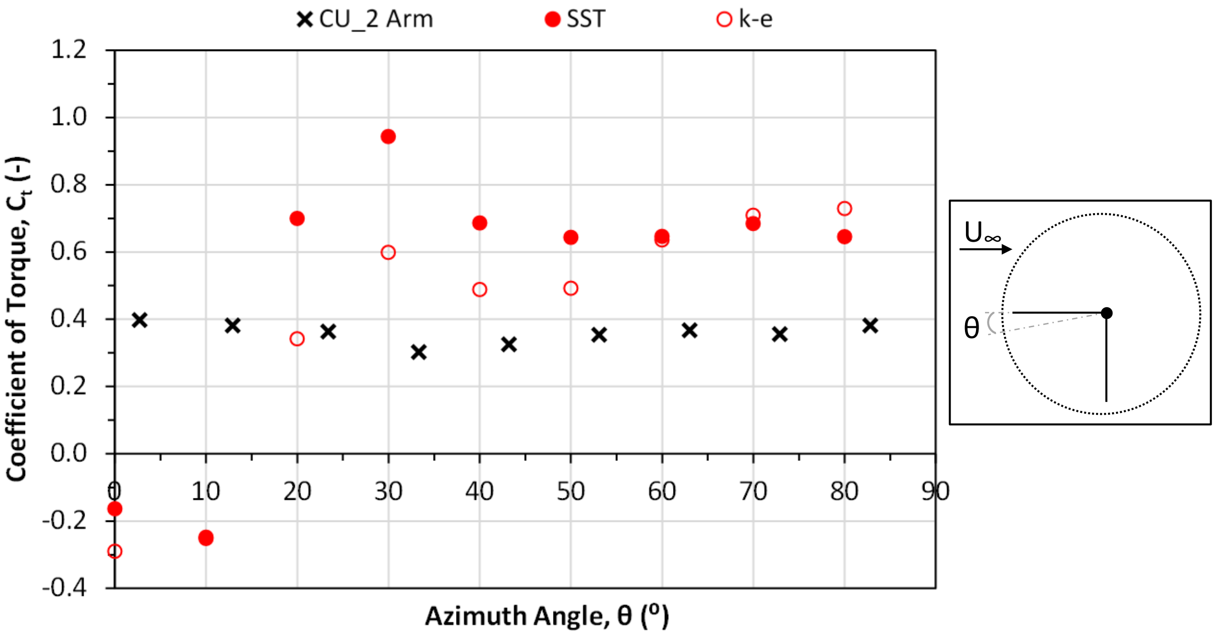

**Figure 121 Starting torque for C4 (2 Arms), CFX vs. Physical Model**

## 12.2 Savonius Results

### 12.2.1 Transient analysis

Figure 122 shows the $C_p$-λ curves for transient unsteady 2D and 3D CFX simulations of the conventional Savonius and compared to the results of the physical models from CU and IFREMER. Figure 122 shows that similar to the physical testing results the simulation results show a decrease in the $C_p$max value for the large domain geometry compared to the CU geometry. For both the k-ε and SST turbulence models the simulations of the large geometry and CU both show that $C_p$max occurs at λ=1.0, similar to that of the CU physical testing results, as seen in Table 36. The large geometry simulations do not show the decrease in λ range that the physical testing results show for IFREMER compared to CU. For the 2D simulations, for both CU and large domain geometry scenarios the results are exaggerated compared to the physical testing results. For both the large geometry and CU simulations, the k-ε turbulence model shows larger over prediction of the performance than the SST model. For CU simulations the 3D results show the closest resemblance to the physical testing results; as seen in Table 36 the $C_p$max/λ=0.274/1.000 which is a 20% over prediction compared to the physical testing results ($C_pmax/\lambda$=0.225/0.999). However the distribution of the 3D data does resemble that of the physical testing results. For $\lambda$=1.2 the 3D result lies on the curve of the physical testing results.

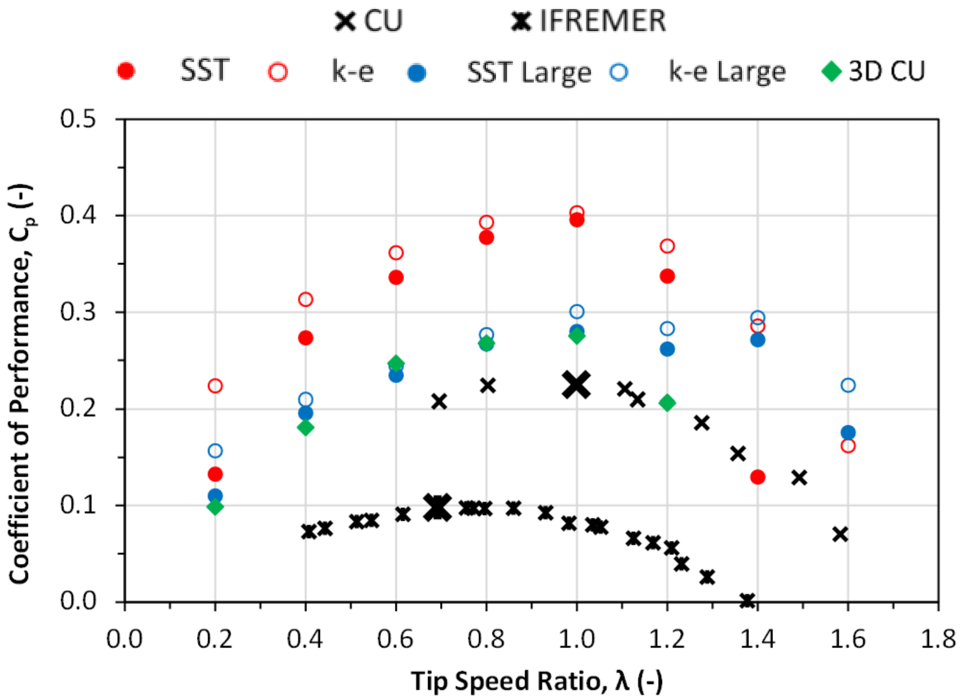

**Figure 122 $C_p$ vs. λ results for CFX vs. Laboratory results for the Savonius**

**Table 36 Summary of $C_pmax/\lambda$ values for both physical and numerical modelling of conventional Savonius**

| Geometry | Physical | Numerical | | |
|---|---|---|---|---|
| | | 2D | | 3D |
| | | k-ε | SST | k-ε |
| **CU** | 0.225/0.999 | 0.403/1.000 | 0.396/1.000 | 0.274/1.000 |
| **LARGE/ IFREMER** | 0.098/0.692 | 0.300/1.000 | 0.280/1.000 | - |

Figure 123 shows the $C_t$ vs. θ for $C_pmax/\lambda$ operating conditions for the simulations from Figure 122, with $C_pmax$ occurring at $\lambda$=1.0 for each simulation. Figure 123a shows that each simulation shows a similar distribution with $C_tmax$ occurring at $0^o \leq \theta \leq 30^o$ and $C_tmin$ occurring for $90^o \leq \theta \leq 120^o$. Both $C_tmax$ and $C_tmin$ occur at around $10^o$ later for the 3D simulation compared to that of the 2D simulations. The greatest difference between the turbulence models occurs at the lower $C_t$ values for $75^o \leq \theta \leq 130^o$ whereby the SST model predicts a lower $C_t$ than the k-ε model. Figure 123b shows that for a single bucket of the Savonius in the advancing stage a positive $C_t$ is generated for

$0^o \leq \theta \leq 140^o$ for each of the simulations Similarly in the returning phase a positive $C_t$ is generated for $300\text{-}320^o \leq \theta \leq 360^o$ for each of the simulations with the large domain simulations generating the lowest $C_t$ as expected. The positive $C_t$ in the returning phase can only be attributed to the generation of lift force, since the bucket is moving into the freestream flow it cannot be generating drag force. Unlike in the advancing stage the large domain simulations generate the greatest positive $C_t$ in the returning phase with the 3D simulation generating the least.

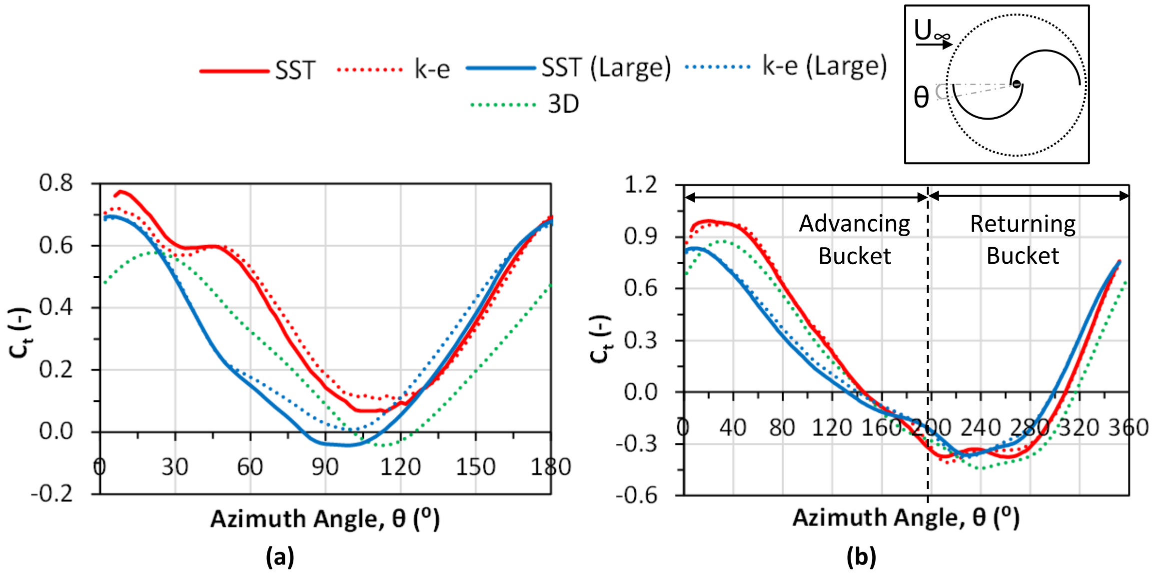

**Figure 123 $C_t$ vs. θ at optimum operating conditions (a)2 buckets (b)1 bucket**

### 12.2.2 Steady state analysis of a single bucket

Figure 124 shows the starting torque results for steady state simulations of a 1 bucket Savonius tested at CU and compared to 2D and 3D CFX simulations. For $0^o \leq \theta \leq 60^o$ the SST model under-predicts $C_t$, for $60^o \leq \theta \leq 120^o$ it shows close resemblance to the physical testing but then under-predicts $C_t$ for $120^o \leq \theta \leq 180^o$. For $180^o \leq \theta \leq 360^o$ the SST model does not predict any positive $C_t$ as measured by the physical models. Similar to the SST model, the results for the k-ε model shows close resemblance to the physical model for $60^o \leq \theta \leq 120^o$ but for $0^o \leq \theta \leq 60^o$ and $60^o \leq \theta \leq 120^o$ the k-ε model, although over-predicting, bears the closest resemblance to the distribution of the physical model. The k-ε model predicts the spike in $C_t$ in the physical model at both $\theta=20^o$, $160^o$ unlike the SST model. The SST and k-ε models are also considerably different for $180^o \leq \theta \leq 360^o$. Unlike the SST model which predicts $C_t \leq 0$, the k-ε model predicts a considerable amount of positive $C_t$ (up to $C_t=0.35$) for $180^o \leq \theta \leq 360^o$. Although over-predicted, the distribution of the positive $C_t$ for the k-ε model during $180^o \leq \theta \leq 360^o$ follows a similar distribution to that of the SST and physical model. Of all the simulations the 3D results bear the closest resemblance to that of the physical models for all values of θ besides at $\theta=40^o$, $140^o$, at these angles the 3D results over-predict $C_t$. Similar to the 2D k-ε results, the 3D results do predict positive $C_t$ values for $180^o \leq \theta \leq 360^o$ and at a similar distribution and magnitude to that of the physical model. The positive $C_t$ exhibited by the k-ε model during $180^o \leq \theta \leq 360$ but not by the SST model for 2D simulations implies the presence of lift force and is visualised using Figure 125 for $\theta=200^o$. At this angle the k-ε model predicts $C_t=0.330$ whilst the SST model predicts $C_t=0.006$. As discussed in detail in Section 4.1, lift force is generated by attached flow over a surface. Such an attached flow is highlighted in Figure 125 for the k-ε model but is absent for the SST model, which explains as to why the k-ε model predicts significantly higher $C_t$ value than the SST model at $\theta=200^o$.

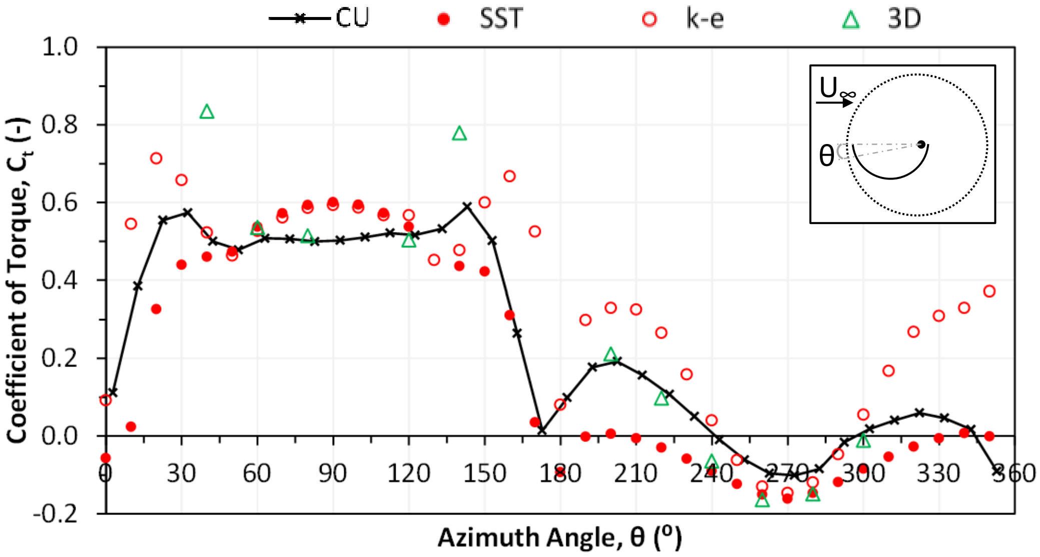

**Figure 124 Starting torque results for 1 Bucket Savonius; CFX vs. physical testing at CU**

For the steady state analysis of the static torque in Figure 124 there are values of θ whereby a solution could not be obtained for the 3D simulations, namely $20^o$, $100^o$, $160^o$, $320^o$ and $340^o$. At these angles the residuals displayed a "bouncy" behaviour synonymous with a diverging transient solution meaning the target residuals were not reached, as seen in Figure 126. The protocols for obtaining a converged solution (CFD Online, 2013) were adhered to but to no avail, leading to the flow at these angles being classed as transient and therefore a steady state solution was unobtainable.

Further manipulation of the mesh for each individual angle could have led to converged solutions since altering mesh sizing downstream of the flow such as creating a coarser mesh to ensure small shedding features are not captured (which could be the source of the transient behaviour) could result in a converged solution. However for consistency across all results the meshes were not altered.

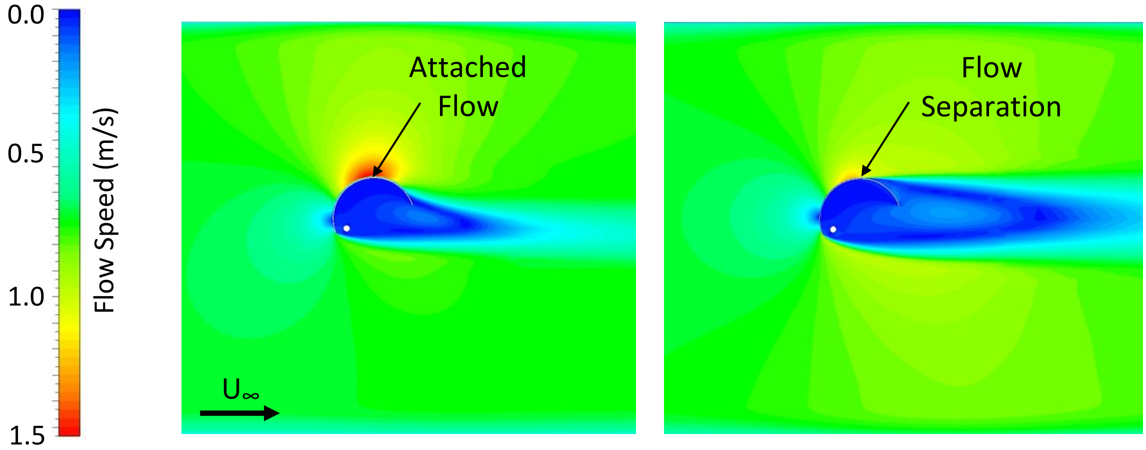

(a) (b)

**Figure 125 Velocity contours for steady state 1 bucket Savonius for 2D simulations at θ=200$^0$ (a) k-ε model (b) SST model**

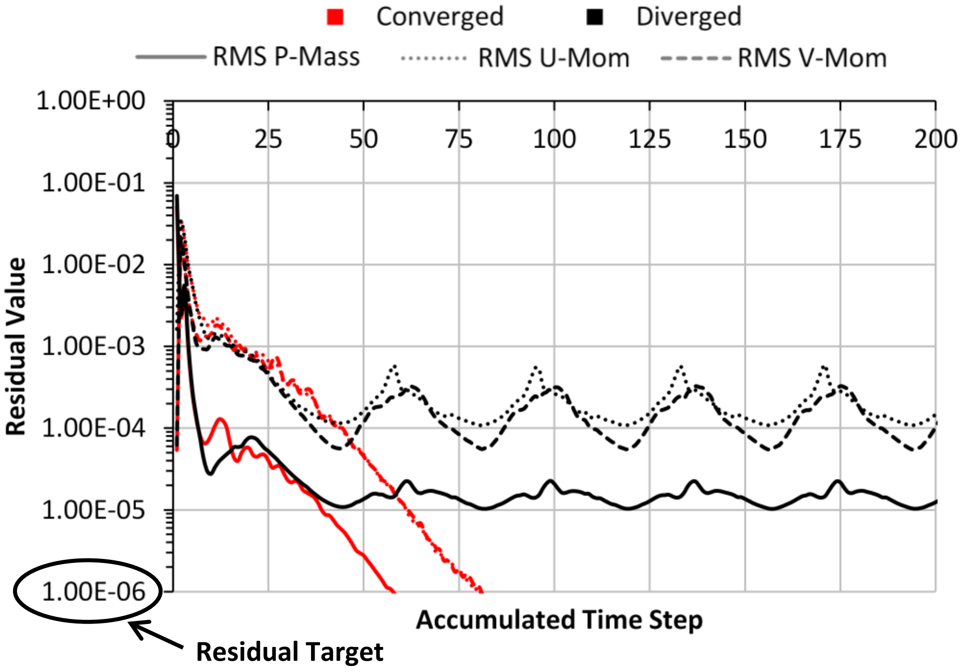

**Figure 126 Example of steady state simulations for converged and diverged solutions**

Figure 127 shows the starting torque results for steady state 2D simulations of a 1 bucket Savonius tested at IFREMER and compared to simulations of the large domain.

It can be seen that the SST model provides the most accurate prediction of the starting torque for the entire range of θ compared to the results from IFREMER. The biggest difference between the SST model and the physical results occurs at $120^o \leq \theta \leq 150^o$, whereby the SST model under-predicts the $C_t$ whereas there is a spike in $C_t$ for the physical results. For $0^o \leq \theta \leq 180^o$ both the k-ε and SST model predict a symmetrical distribution of $C_t$ however as already mentioned the physical results are not symmetrical with $C_t$max occurring at a spike in the data for $120^o \leq \theta \leq 150^o$. For $180^o \leq \theta \leq 360^o$ the k-ε model hugely over-predicts $C_t$, with the model predicting positive $C_t$ values equal to those found in the $0^o \leq \theta \leq 180^o$ range. The SST model however predicts $C_t$ values close to 0, similar to the physical results. Both models do predict a similar sinusoidal distribution for $180^o \leq \theta \leq 360^o$ but the k-ε model over predicts the magnitude of $C_t$.

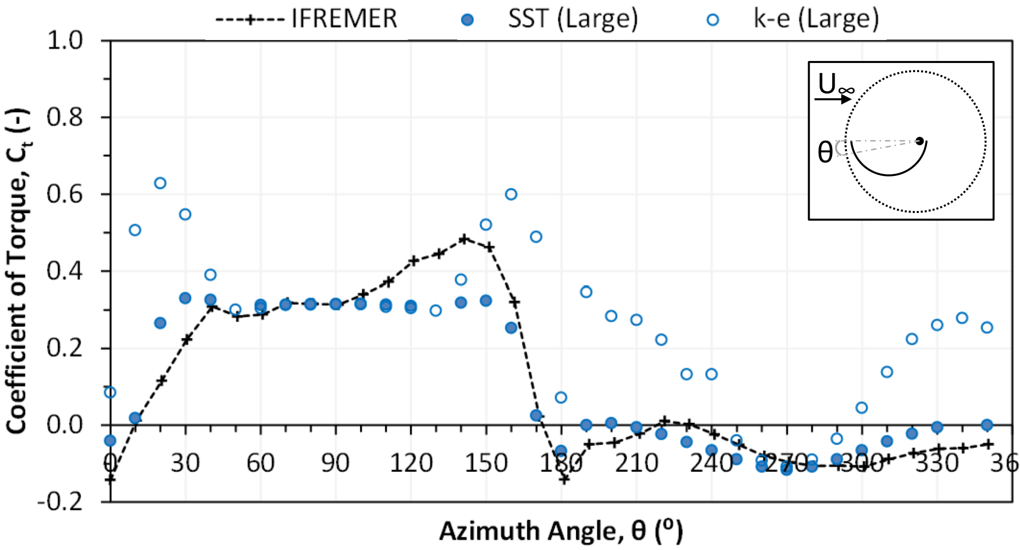

**Figure 127 Starting torque results for 1 Bucket Savonius; CFX vs. physical testing for large domain and IFREMER**

### 12.2.3 Steady state analysis of a twin bucket

Figure 128 shows the starting torque results from steady state 2D simulations of the 2 bucket Savonius. For the CU simulations the SST model shows the closest resemblance to the physical model for $0^o \leq \theta \leq 70^o$; similarly for the large domain study when comparing to the IFREMER physical model results. For $70^o \leq \theta \leq 130^o$ both CU and the large domain simulations display similar results for both turbulence models. For $140^o \leq \theta \leq 170^o$ the results from the turbulence models differ for both the CU and the large domain geometry. The k-ε model predicts higher $C_t$ values than the SST model for both the CU and large domain geometry. For the CU geometry $C_t$max is predicted at $30^o$ for the k-ε model and at $60^o$ for the SST model. For the large domain geometry $C_t$max is predicted at $30^o$ for the k-ε model and at $50^o$ for the SST model. The SST model predicts negative $C_t$ for $\theta=150^o$, $160^o$ for both geometries whereas the k-εmodel does not predict negative $C_t$ for either geometry. For both geometries the k-ε model over predicts $C_t$ for the entire range of θ, whereas the SST model over predicts $C_t$ for $0^o\leq\theta\leq150^o$ for the large domain compared to the IFREMER physical model and for $60^o\leq\theta\leq150^o$ for the CU geometry compared to the physical model. For the CU geometry the SST model under predicts $C_t$ for $0^o\leq\theta\leq40^o$.

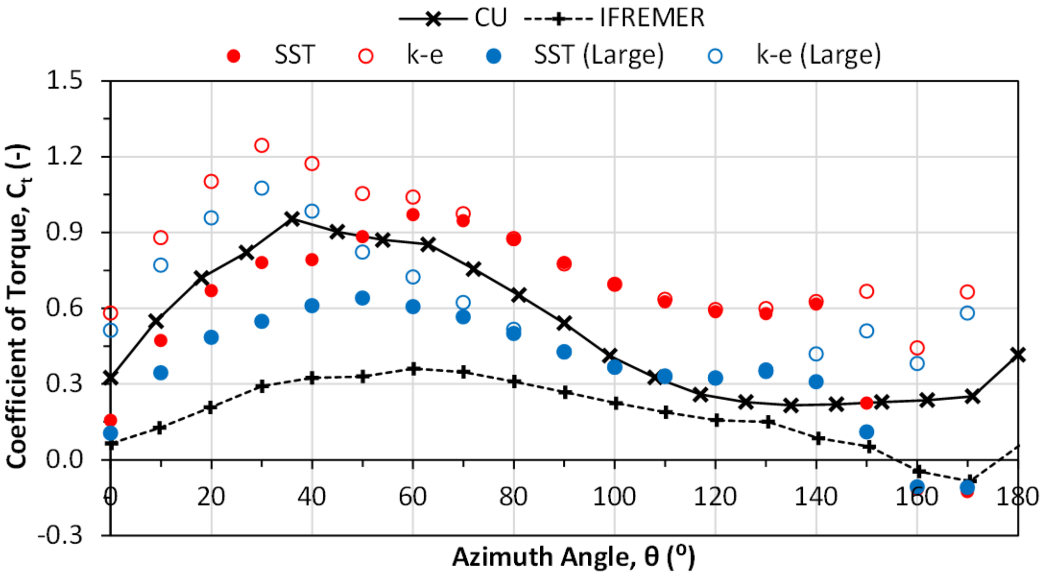

**Figure 128 Starting torque results for CFX vs. physical testing for the Savonius**

The results in Figure 129 are for the $C_t$ of 1 bucket (B1) from the steady state solution of the starting $C_t$ of the Savonius from Figure 128. There are no physical model results available for comparison since the physical model set-up was unable to measure the torque of individual blades within a multi-blade configuration. For $0^o\leq\theta\leq180^o$ the largest difference between the CU and large domain simulations occurs for $40^o\leq\theta\leq160^o$ whereby the $C_t$ for the CU simulations forms a symmetrical crest with $C_t$max≈0.9 (for both turbulence models) for $\theta=90^o$, whereby for the large domain simulations rather than a crest the $C_t$ plateaus for $40^o\leq\theta\leq160^o$ with $C_t$max for both turbulence models occurring at $\theta=30^o$.

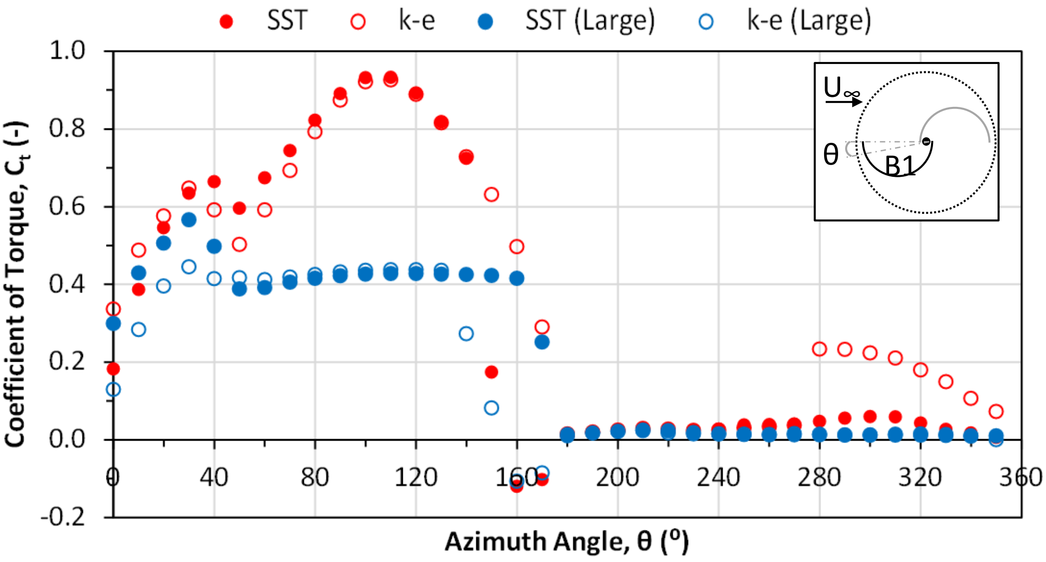

**Figure 129 Starting torque results from CFX for B1 of the Savonius**

The main region of interest in Figure 129 is $180^o \leq \theta \leq 360^o$, which is to be compared to the same region in Figure 124 and Figure 127. For the CU geometry, Figure 124 predicts positive $C_t$ for the k-ε model, 3D model and physical model for $\theta=180^o$-$240^o$ and $\theta=330^o$-$345^o$ whereas in Figure 127 positive $C_t$ is only predicted by the k-ε model for similar angles. Any positive $C_t$ present for $180^o \leq \theta \leq 360^o$ for a single bucket can only be attributed to lift force since the bucket is moving against the flow, meaning any drag force would be negative. It is the magnitude of the lift force in $180^o \leq \theta \leq 360^o$ which is responsible for the Savonius reaching $\lambda \geq 1.0$. Using (6) it is the increase in λ, hence ω (see (7)), that enables the Savonius to achieve greater $C_p$ values (see Figure 87a) than that of the CarBine configurations.

### 12.2.4 Discussion

Comparing the physical model results for this region, using both Figure 124 and Figure 127, it can be seen that positive $C_t$ is only present for results from CU. However this is only for a single bucket and therefore the interaction between two buckets for a complete Savonius to show if lift force is still present can be seen in Figure 129 whereby similar to the physical model studies of a 1 bucket Savonius, larger lift force is predicted by both the SST and k-ε model for the CU geometry compared to the large domain geometry. However this is only a starting torque analysis and it therefore cannot be concluded that this behaviour is reflected during dynamic performance. From analysing Figure 123b which is the $C_t$ for an individual Savonius bucket within a 2 bucket rotating study it can be seen that lift force is also predicted for $180^o \leq \theta \leq 360^o$ for all simulations (both turbulence models and both 2D and 3D) and similar to Figure 129 this occurs for $300^o \leq \theta \leq 360^o$. However there are restrictions to the validity of the unsteady simulations of the dynamic performance, mainly due to the Savonius rotating at a fixed, defined ω. Therefore the turbine is being driven and is not rotating due to hydrodynamic interactions. As seen from the physical model results Figure 86 ω is not constant but adheres to the form of a sine wave and therefore the $C_t$ for a Savonius driven by the hydrodynamic forces is expected to be markedly different to that of the $C_t$ of a driven Savonius as seen in this study.

Throughout the numerical modelling results when 2D and 3D results are available the 2D results predict greater performance, as seen by Yang and Lawn, (2013) for simulation of the Hunter VATT. A 2D simulation effectively assumes an infinite aspect ratio and therefore does not account for 3D geometries such as the top and bottom disks, which are present in the physical testing, although Howell et al., (2010) concluded that the inclusion of arms for a 3D simulation of a Darrieus style turbine resulted in minimal difference to performance results. But as discussed in Section 8.3.6, end disks are an important aspect of the design for the Savonius since they produce an increase in the performance ($C_p$). The common census as to the over-prediction of 2D models compared to 3D models is due to vortices at the top and bottom of the turbine being present in the 3D and not the 2D studies, leading to an over-estimation of performance ($C_p$) in the 2D results (Howell et al., 2010). Yang and Lawn, (2013) compared 2D and 3D CFD results for a VATT and concluded that the difference between both sets of results is largely accounted for by the aspect ratio, as the aspect ratio of the turbine increases the results of the 2D and 3D studies become more uniform. This can be accounted for by the fact that the proportional effect of the negative impact of tip vortices is reduced with increasing aspect ratio.

Comparing the 2 turbulence models, SST and k-ε, for all simulations it can be seen that k-ε predicts greater performance values than that of the SST model; an observation shared by (Altan and Atılgan, 2008). The over prediction in performance of the k-ε simulations (compared to SST) can be accounted for by the disadvantages of the k-ε model stated in Section 11.1.2.2, mainly that the k-ε model under predicts the amount of separation (Ansys, Inc., 2010). Under predicting separation results in attached flow which can generate lift force as opposed to drag force when separation occurs, as seen in Figure 125b which in turn produces enhanced performance results. The difference between both turbulence models is more prominent for simulations of the Savonius in Figure 122 compared to the simulations of the CarBine configurations in Figure 117. This can be attributed to the curved surface of the Savonius at particular angles for $300^{o} \leq \theta \leq 360^{o}$ acting as a hydrofoil, creating a pressure differential between the fast moving fluid over the convex surface of the bucket compared to the slow moving/stagnant flow along the concave surface of the bucket. In conjunction with the delayed prediction of separation of the k-ε model this leads to exaggerated performance values.

All 3D simulations predict a greater performance compared to the results from physical testing. Using Figure 122 as an example, the predicted $C_p$max value for the 3D simulation is 20% greater than that of the physical testing results. This over prediction could be due to the combination of a lack of modelling of the free surface and modelling using a homogenous (plug) inflow during simulations rather than a non-homogenous inflow. Bahaj et al., (2007b) and Sun et al., (2008) investigated the effects of the free surface and concluded that a shallow immersion will prevent full wake expansion since the free surface causes a reflection plane resulting in a reduction in performance ($C_p$). In the near vicinity of the turbine such an effect causes a reduction in the pressure differential across the turbine. The free surface effects and hence reduction in flow depth immediately downstream of a turbine in an enclosed channel was not accounted for during simulations for this study. Therefore modelling the free surface should result in decreased performance predictions. In the case of a drag driven turbine this will reduce the pressure drag and thus have a negative impact on performance. Maganga et al., (2010) compared the results from a numerical study of homogenous inflow vs. non-homogenous inflow and concluded that for a non-homogenous inflow, i.e. incorporating a shear profile (see Section 5.1) the results show a reduction in performance of around 10%. A similar reduction in power was observed by Croft et al., (2010).

# 13 Conclusions

The aims of the thesis highlighted in the introduction are provided in grey with the accompanying conclusion for each in black. The overall aim of the thesis was to further the understanding of CarBine- a novel vertical axis tidal turbine and to progress through stage two of the staged development framework (University of Southampton, 2008) for a tidal stream turbine; this was achieved through a combination of physical and numerical modelling.

- **To quantify the performance of CarBine, a novel vertical axis tidal stream turbine, via physical testing**

CarBine was successfully constructed as a kit-style turbine. The benefit of a kit-style turbine was the ability to interchange both the phase angle of CarBine and number of flaps per arm without the need to construct an entirely new prototype. Prior to this study only a fixed 3 arm, 2 flap (per arm) CarBine had been tested. A bespoke mechanical disk brake power take-off system was manufactured to load CarBine during testing. This new test rig was designed to synchronise the data capture of both the torque (using a load cell) and angular velocity (using a rotary encoder) of the turbine with respect to its rotated angle; thus enabling both time averaged performance values to be obtained along with a detailed study of the turbine's performance throughout a rotation. Initially there were issues with the load applicator of the PTO, with CarBine unable to exceed the applied friction after applying minimal load. The issue was resolved by swapping the brake pad material from cork to the smoother PTFE. Using PTFE enabled a range of loads to be applied resulting in performance capture of a wider range of $\lambda$ and hence the $C_p$max value. The synchronisation of the torque and angular velocity data capture proved important in comparing various CarBine configurations but the manual input of the PTO required care to be taken when varying the load to ensure the turbine reached steady conditions prior to data capture. The system also benefited from near real-time data analysis to ensure the peak of the Cp-$\lambda$ curve had been captured.

CarBine was tested for a variety of phase angles (60°, 72°, 90° & 120°) at a range of freestream flow speeds in the hydraulic flume at CU to obtain $C_p$ vs $\lambda$ and T & $\omega$ vs. $\theta$

data. The greatest performance of CarBine was achieved by the C4 configuration (90° phase angle) with $C_p$max/$\lambda$=0.132/0.441 achieved at a flow speed of 1.22 m/s. In addition, from static testing C4 generated positive torque at all angles and is therefore deemed to be self-starting. Once design optimisation was undertaken at CU a research proposal was accepted by MARINET to facilitate testing at IFREMER. From a literature review the blockage factor at CU was known to exceed recommended levels and therefore the data required correction factors. The blocked environment was not an issue during design optimisation but posed an issue if the performance results of CarBine were to be compared to other turbines tested in an unblocked environment. The larger flume cross-section at IFREMER revealed the extent of the blockage effect at CU with the performance of C4 reducing by 43% to $C_p$max /$\lambda$=0.067/0.346 for similar freestream flow speeds. Although the literature guides towards the use of blockage factors, these are generic, and as discovered in this study, these can lead to varied results; highlighting the need for testing at IFREMER for increased confidence in the performance results. A two-staged C4 (offset at 45°) was tested at IFREMER that successfully replicated the $C_p$max of a single-staged C4 but ironed out the power fluctuations during a cycle; a desirable attribute for electricity generation for the end user. To the author’s knowledge there was no literature on the optimisation of performance characteristics of a drag driven turbine similar to that of CarBine prior to this study.

- **Create a framework for numerical modelling of CarBine to support design optimisation**

A commercial CFD software package, namely Ansys CFX, was chosen for the numerical modelling. Ansys CFX was chosen based upon its known ability to model turbo machinery and the vast support structure available, from both developers and of case studies relating to tidal stream turbine application in the literature.

The aim was to simulate the dynamic performance of CarBine as close to the conditions experienced during physical testing at CU; enabling the physical testing results to be used as validation data for CFX. The two degrees of motion of CarBine were successfully modelled within CFX using a rotating domain (transient rotor-stator) with embedded rotating subdomains. Unfortunately this technique could only simulate CarBine with one outer flap since the subdomains cannot overlap. This limited the use of CFX for optimisation purposes since physical testing results show that performance is greater with the inclusion of both an inner and outer flap. The rotation of the subdomain followed a user-inputted function. This function, dictating when flaps were open/closed, was constructed from observations during physical testing of a steady state single arm CarBine. The validity of a universal function for a variety of CarBine configurations is questionable, since the opening and closing angles of flaps will be affected by adjacent arms the position of which vary with different configurations.

Two different turbulence models were chosen for the simulations, k-ε and SST, for their different approaches to solving the near-wall boundary. Simulations were predominantly 2D, due to computational and time restraints, with a selection of 3D simulations. Limitations of the 3D simulations included the absence of a free surface model and the inability to simulate using the SST turbulence model (due to computational restraints). Prior to any comparisons to physical testing results, the numerical modelling was subjected to verification studies.

Comparing the results of the 2D transient simulations of CarBine for C3, C4, and C5 with physical testing results at CU show that the numerical results over predict performance but show a similar distribution to that of the physical model results. Despite this the numerical results do mirror the optimisation of the physical testing with C4 achieving the highest $C_p$ of all the configurations. Physical test results were collected for C4 with an outer flap only (C4O) and compared to the C4 simulations, the simulation over-predicted $C_p$max by a factor of two but predicted $C_p$max at $\lambda=0.4$ which is identical to the physical model. Transient simulations of CarBine configurations in a large domain (i.e. the absence of blockage effects) highlighted the reduction in performance ($C_p$) compared to that in the highly blocked CU domain. Steady state simulations were obtained for a single arm of CarBine and for a 2 arm with $90^o$ phase angle (C4) for the geometry of both CU and a large domain. Results were used to prove the self-starting ability of the C4 configuration. 3D results show the closest resemblance to those of the physical testing, although 3D results under-predict the generated torque in the steady state simulations.

Comparing turbulence models, the SST model showed the closest validation to the physical results however the SST model required a high density near wall mesh resulting in an 89% greater number of elements compared to the k-ε model mesh (for C4) and therefore a considerably greater simulation time.

The greatest discrepancy between the numerical modelling and the physical testing of CarBine was that during numerical modelling the turbines are driven, i.e. rotate at a constant specified ω, whereas the physical models rotate as a result of the hydrodynamic forces on the turbine blades, resulting in an unsteady ω. This discrepancy brings caution to analysing the torque/ power history of simulated blades.

This study proves the ability of Ansys CFX to dynamically simulate the 2-degrees of freedom of CarBine and is a step forward in the turbine's development.

- **Analyse the competitiveness of CarBine through comparing its performance to rival technologies**

Although a small range of rival technologies were highlighted, the Savonius was chosen as Carbine's nearest competitor since it is regarded as the most developed drag-type turbine; this is reflected in the volume of literature available on the Savonius. Despite this the majority of literature analyses the performance of the Savonius in wind. For this reason, a physical model of an optimally configured Savonius (based on the result of a literature review) of identical size to CarBine and at identical test conditions was analysed.

Physical testing of the Savonius revealed its superior performance to that of CarBine's optimum configuration, C4, exceeding CarBine's $C_p$ by 101% at CU ($C_p$max/λ=0.266/1.051). The increased performance of the Savonius is attributed to its higher angular velocity ($C_p$max at λ=1.0), over twice that of CarBine ($C_p$max at λ=0.4); since CarBine generates greater torque than the Savonius. The inferior performance of CarBine lead to the design of a Savonius with flaps; whose aim was to improve the performance of the Savonius through incorporating flaps, similar to CarBine, to reduce the negative drag force on the returning bucket. However the performance of the Savonius with flaps proved inferior to the Savonius and marginally better than CarBine. It is hypothesised that the inferior performance of the Savonius with flaps is due to the loss of lift force for $180^o \leq \theta \leq 360^o$ as a result of the flaps. Although the Savonius achieved greater $C_p$max values than C4, C4 did exhibit greater starting torque behaviour than S, displaying both greater average $C_t$ and lower fluctuation in $C_t$ over a revolution.

The Savonius was simulated using both a steady state and transient analysis for both 2D and 3D simulations. A steady state analysis was used to simulate the starting torque ($C_t$ vs. $\theta$) whilst an unsteady transient analysis was used to simulate the dynamic performance ($C_p$, $C_t$ vs. $\lambda$). 3D simulations showed very close agreement with the physical model whilst the 2D simulations over predicted performance. Closer agreement to physical model results was achieved for starting torque comparisons compared to the dynamic performance. For 3D simulations the $C_p$max was predicted to within 20% of the physical model.

Similar to the physical testing results, the results from the large domain simulations showed a decrease in performance compared to the simulations from CU. Overall the CU simulations showed greater validation to the physical testing results than those from the large domain when compared to the IFREMER results. The numerical simulations were used to show that the lift force generated by the Savonius during dynamic testing is present in CU for a high blockage environment but is absent when tested in a large domain, where there is no blockage effect present. Such a conclusion could not be drawn from the physical testing results since only the net torque can be measured during testing whereas for the numerical modelling the torque for the individual blades could be monitored.

# 14 Future Work

The staged development framework (University of Southampton, 2008) for tidal stream turbines states that a $C_p$>0.3 should be reached to enable progression through stage two, to ensure economically feasible energy extraction. This was not achieved for CarBine, with $C_p$max=0.132. As a result further work must be conducted on CarBine to refine the design and establish a greater $C_p$max. Improving the performance of CarBine is likely to be based around:

- Researching the opening and closing procedure of the flaps

  During physical testing it was seen that the flaps open with an abrupt swinging motion whilst the flaps don't close until around θ=20°. It is hypothesised that restricting the angle at which a flap opens to may result in flaps closing closer to θ=0° and thus generate torque for 0°≤θ≤20° unlike previously, which could potentially lead to a greater $C_p$max value. To achieve this during physical testing, stoppers could be placed to restrict the opening angle of the flaps whilst it would also be beneficial to analyse the exact angular position of the flaps during a rotation. During this study it was only possible to measure the angular position of the entire turbine. In order to do this an encoder could be attached to the shaft of both the inner and outer flap of a single arm of CarBine that would measure the angular position of the flaps during a revolution but would also enable the calculation of the angular velocity of the flaps at both the closing and opening procedure; which could be used as the parameter to minimise during this testing of fixing the maximum opening angle of the flaps.

- Flap Supports

  During this study the flaps were sandwiched between two disks. Disks were used solely as a method to enable quick configuration changes, i.e. position of flaps. A study is required to determine the optimum support for the flaps with the likelihood of the design being either arms or disks. Aerodynamically designed arms would produce very little negative drag and considerably less frictional drag than the current disks, however the disks may act as a small shrouding device, funnelling the flow to the flaps of CarBine. This would require either physical or numerical modelling to provide a solution.

Although CarBine has a low $C_p$max value, the initial two turbine array study provides encouragement for further study into the potential dense array spacing of CarBine. In order to visualise the potential denser array spacing of CarBine a detailed wake study of CarBine would need to be conducted. Quantifying the 3D wake of CarBine using an ADV would be time consuming and only produce a time-averaged picture of the wake. However an evolution of the preliminary PIV study (found in Appendix B), incorporating high intensity lasers and high frequency cameras would be both time efficient and produce both instantaneous and time averaged profiles of the wake. Additionally to add further credibility to the two turbine array study and any further dense array studies, it would be vital for physical testing to be conducted in a facility with minimal blockage, such as IFREMER.

Future work regarding numerical modelling would be focused on incorporating the geometries of both an inner and outer flap for each arm of CarBine. Such is the complexity of CarBine and the inability to use two subdomains per arm (see Figure 107) the solution will require mesh deformation. Mesh deformation is a more unstable approach to mesh motion since the mesh becomes dynamic during a simulation and is therefore prone to errors such as the presence of highly skewed elements of negative volume errors. In conjunction with mesh deformation, to mimic the exact unsteady behaviour of Carbine would require a one way fluid interaction simulation whereby the rotation of the flaps is calculated based on the torque generated from the hydrodynamic interactions of the fluid and the flaps. Such a study for a Savonius has been conducted by D'Alessandro et al., (2010).

Irrespective of its current low $C_p$max value, to progress CarBine along the staged development framework requires testing at an intermediate scale. Work is currently being carried out to create a larger scaled CarBine for river testing in Georgia, USA. Since site characterisation has already been completed (Bomminayuni et al., 2012), testing would focus solely on the performance of CarBine in a natural environment, subjected to shear flows, sediment etc.

# References

ABPmer, 2008. Atlas of UK Marine Renewable Energy Resources [WWW Document]. URL http://www.renewables-atlas.info/ (accessed 8.30.13).

Abraham, J.P., Plourde, B.D., Mowry, G.S., Minkowycz, W.J., Sparrow, E.M., 2012. Summary of Savonius wind turbine development and future applications for small-scale power generation. J. Renew. Sustain. Energy 4, 042703. doi:10.1063/1.4747822

Ahmadian, R., Falconer, R.A., 2012. Assessment of array shape of tidal stream turbines on hydro-environmental impacts and power output. Renew. Energy 44, 318–327. doi:10.1016/j.renene.2012.01.106

Akwa, J.V., 2010. Savonius wind turbine aerodynamics analysis using computational fluid dynamics (MSc Thesis). Federal University of Rio Grande do Sul, Porto Alegre, Brazil.

Akwa, J.V., Vielmo, H.A., Petry, A.P., 2012. A review on the performance of Savonius wind turbines. Renew. Sustain. Energy Rev. 16, 3054–3064. doi:10.1016/j.rser.2012.02.056

Alderney Renewable Energy, 2013. Tidal Development Programme [WWW Document]. URL http://www.are.gb.com/projects/tidal/ (accessed 8.30.13).

Aldoss, T.K., Najjar, Y.S.H., 1985. Further development of the swinging-blade Savonius rotor. Wind Eng. 9, 165–170.

Aldoss, T.K., Obeidat, K.M., 1987. Performance analysis of two Savonius rotors running side by side using the discrete vortex method. Wind Eng 11, 265–276.

Alexander, A.J., Holownia, B.P., 1978. Wind tunnel tests on a Savonius rotor. J. Wind Eng. Ind. Aerodyn. 3, 343–351.

Alstom, 2013. Harnessing tidal energy to fuel a sustainable future [WWW Document]. URL http://www.tidalgeneration.co.uk/ (accessed 9.17.13).

Altan, B.D., Atılgan, M., 2008. An experimental and numerical study on the improvement of the performance of Savonius wind rotor. Energy Convers. Manag. 49, 3425–3432. doi:10.1016/j.enconman.2008.08.021

Altan, B.D., Atılgan, M., 2010. The use of a curtain design to increase the performance level of a Savonius wind rotors. Renew. Energy 35, 821–829. doi:10.1016/j.renene.2009.08.025

Ansys, Inc., 2004a. ANSYS CFX Mesh Tutorials.

Ansys, Inc., 2004b. Innovative Turbulence Modeling: SST Model in ANSYS CFX-Technical Brief.

Ansys, Inc., 2009a. ANSYS CFX Solver Theory Guide.

Ansys, Inc., 2009b. ANSYS CFX Mesh.

Ansys, Inc., 2009c. ANSYS CFX Reference Guide.

Ansys, Inc., 2009d. Introduction to CFX-Interfaces, Sources and Additional Variables.

Ansys, Inc., 2010. ANSYS CFX Solver Modelling.

Ansys, Inc., 2012. ANSYS CFX Introduction.

Antheaume, S., Maître, T., Achard, J.-L., 2008. Hydraulic Darrieus turbines efficiency for free fluid flow conditions versus power farms conditions. Renew. Energy 33, 2186–2198. doi:10.1016/j.renene.2007.12.022

Argyriadis, K., 2008. Guidelines for the Certification of Ocean Energy Converters as well as International Standards.

Armstrong, S., Fiedler, A., Tullis, S., 2012. Flow separation on a high Reynolds number, high solidity vertical axis wind turbine with straight and canted blades and canted blades with fences. Renew. Energy 41, 13–22. doi:10.1016/j.renene.2011.09.002

Atlantis Resources Corporation, 2013. Development Process [WWW Document]. URL http://www.atlantisresourcescorporation.com/development-process.html (accessed 8.30.13).

Atlantis Resources Ltd, 2013a. Project-San Remo, Australia [WWW Document]. URL http://atlantisresourcesltd.com/projects/test-sites/san-remo-australia.html (accessed 11.17.13).

Atlantis Resources Ltd, 2013b. News [WWW Document]. URL http://atlantisresourcesltd.com/medianews/news.html (accessed 11.17.13).

Aviation Enterprises Ltd., 2013. Composite Tidal and Wind Turbine Blades [WWW Document]. URL http://www.aviationenterprises.co.uk/P6%20Renewables.html (accessed 8.30.13).

AWATEA, 2008. Environmental Impacts of Marine Energy Converters. Energy Efficiency and Conservation Authority, Auckland.

AzeoTech Inc., 2009. DAQFactory - LabJack Application Guide.

Babu, K.S., Raju, N.V.S., Reddy, M.S., Rao, D.N., 2006. The material selection for typial wind turbine blades using a MADM approach & analysis of blades, in: The 18th International Conference on Multiple Criteria Decision Making. Presented at the International Conference on Multiple Criteria Decision Making, Chania, Greece.

Bahaj, A.S., 2011. Generating electricity from the oceans. Renew. Sustain. Energy Rev. 15, 3399–3416. doi:10.1016/j.rser.2011.04.032

Bahaj, A.S., Batten, W.M.J., McCann, G., 2007a. Experimental verifications of numerical predictions for the hydrodynamic performance of horizontal axis marine current turbines. Renew. Energy 32, 2479–2490. doi:10.1016/j.renene.2007.10.001

Bahaj, A.S., Molland, A.F., Chaplin, J.R., Batten, W.M.J., 2007b. Power and thrust measurements of marine current turbines under various hydrodynamic flow conditions in a cavitation tunnel and a towing tank. Renew. Energy 32, 407–426. doi:10.1016/j.renene.2006.01.012

Bahaj, A.S., Myers, L., 2004. Analytical estimates of the energy yield potential from the Alderney Race (Channel Islands) using marine current energy converters. Renew. Energy 29, 1931–1945. doi:10.1016/j.renene.2004.02.013

Bahaj, A.S., Myers, L.E., Thompson, G., 2007. Characterising the wake of horizontal axis marine current turbines.

Bahaj, A.S., Rawlinson-Smith, R.I., Thomson, M., Myers, L.E., 2011. The Effect of Boundary Proximity Upon the Wake Structure of Horizontal Axis Marine Current Turbines. J. Offshore Mech. Arct. Eng. 134, 021104–021104. doi:10.1115/1.4004523

Bardina, J.E., Huang, P.G., Coakley, T.J., 1997. Turbulence Modeling Validation, Testing, and Development. NASA TM-110446.

Batten, W.M.J., Bahaj, A.S., Molland, A.F., Chaplin, J.R., 2006. Hydrodynamics of marine current turbines. Renew. Energy 31, 249–256. doi:10.1016/j.renene.2005.08.020

Batten, W.M.J., Bahaj, A.S., Molland, A.F., Chaplin, J.R., 2008. The prediction of the hydrodynamic performance of marine current turbines. Renew. Energy 33, 1085–1096. doi:10.1016/j.renene.2007.05.043

BBC, 2013a. Case for Severn barrage “unproven”. BBC.

BBC, 2013b. “No case for £25bn Severn Barrage”. BBC.

BBC, 2013c. Three rescued as yacht hits turbine. BBC.

BBC, 2013d. Marine energy risk to salmon studied. BBC.

BBC, 2013e. Huge tidal energy project approved. BBC.

BBC, 2013f. “Unprecedented activity” at pier. BBC.

Bergey, K.H., 1979. The Lanchester-Betz limit. J. Energy 3, 382–384.

Betz, A., 1920. Das Maximum der theoretisch möglichen Ausnutzung des Windes durch Windmotoren. Z. Für Gesamte Turbinenwesen 26, 307–309.

Bhutta, M.M.A., Hayat, N., Farooq, A.U., Ali, Z., Jamil, S.R., Hussain, Z., 2012. Vertical axis wind turbine – A review of various configurations and design techniques. Renew. Sustain. Energy Rev. 16, 1926–1939. doi:10.1016/j.rser.2011.12.004

Bibeau, E.L., Kassam, S., Woods, J., Molinski, M., Bear, C., 2009. Operating a 5-kw grid-connected hydrokinetic turbine in a river in cold climates 35, 67–69.

Binnie Black & Veatch, 2001. The Commercial Prospects for Tidal Stream Power (No. ETSU T/06/00209/REP). Department of Trade and Industry.

Black & Veatch Consulting Ltd, 2005. PHASE II UK Tidal Stream Energy Resource Assessment (No. 107799/D/2200/03). Carbon Trust, London.

Bloomberg, 2013. Putin Pipeline to Send 25% of Russia’s Oil Exports East - Bloomberg [WWW Document]. URL http://www.bloomberg.com/news/2013-03-07/putin-pipeline-to-send-25-of-russia-s-oil-exports-east.html (accessed 8.29.13).

Blue Energy Canda Inc., 2013. Blue Energy [WWW Document]. URL http://www.bluenergy.com/index.html (accessed 9.17.13).

Blunden, L.S., Bahaj, A.S., 2006. Initial evaluation of tidal stream energy resources at Portland Bill, UK. Renew. Energy 31, 121–132. doi:10.1016/j.renene.2005.08.016

Blunden, L.S., Bahaj, A.S., 2007. Tidal energy resource assessment for tidal stream generators. Proc. Inst. Mech. Eng. Part J. Power Energy 221, 137–146. doi:10.1243/09576509JPE332

Boat Painting Guide, 1997.

Bomminayuni, S., Bruder, B., Stoesser, T., Haas, K., 2012. Assessment of hydrokinetic energy near Rose Dhu Island, Georgia. J. Renew. Sustain. Energy 4, 063107–063107–16. doi:doi:10.1063/1.4766884

Boslet, M., 2010. A Big Setback for Tidal Power [WWW Document]. URL http://www.greentechmedia.com/articles/read/a-big-setback-for-tidal-power (accessed 8.30.13).

BP, 2014a. Natural gas production | About BP | BP Global [WWW Document]. BP. URL http://www.bp.com/en/global/corporate/about-bp/energy-economics/statistical-review-of-world-energy-2013/review-by-energy-type/natural-gas/natural-gas-production.html (accessed 3.25.14).

BP, 2014b. Oil production | About BP | BP Global [WWW Document]. BP. URL http://www.bp.com/en/global/corporate/about-bp/energy-economics/statistical-review-of-world-energy-2013/review-by-energy-type/oil/oil-production.html (accessed 3.25.14).

British Standard, 2012. Maritime Works-Code of practice for geotechnical design (No. BS 6349). British Standards Institute, London.

Bryden, I., Melville, G.T., 2004. Choosing and evaluating sites for tidal current development. Proc. Inst. Mech. Eng. Part J. Power Energy 218, 567–577. doi:10.1243/0957650042584375

Bryden, I., Norris, J., 2007. European Marine Energy Centre: facilities and resources. Proc. ICE - Energy 160, 51–58. doi:10.1680/ener.2007.160.2.51

bsi, 2014. Standard in development: PD IEC/TS 62600-201 ED 1.0 [WWW Document]. Bsi Stand. Dev. URL http://standardsdevelopment.bsigroup.com/Home/Project/201201965 (accessed 3.25.14).

Business Green, 2013. Swansea tidal lagoon powers forward with engineering giants [WWW Document]. URL http://www.businessgreen.com/bg/news/2278685/swansea-tidal-lagoon-powers-forward-with-engineering-giants (accessed 8.29.13).

Carbon Trust, 2010. Renewable energy sources.

Carbon Trust, 2011. Accelerating marine energy. DECC, London.

Celik, I.B., Ghia, U., Roache, P.J., 2008. Procedure for estimation and reporting of uncertainty due to discretization in CFD applications. J. Fluids Eng. 130.

CFD Online, 2013. Best practice guidelines for turbomachinery CFD [WWW Document]. URL http://www.cfd-online.com/Wiki/Best_practice_guidelines_for_turbomachinery_CFD (accessed 11.27.13).

Chadwick, A.J., Morfett, J.C., Borthwick, M., 2004. Hydraulics in civil and environmental engineering. Spon Press, London.

Challans, P., 2009. Analysis and Modelling of a Tidal Stream Turbine (MSc Thesis). Cardiff University, Cardiff.

Chen, T.Y., Liou, L.R., 2011. Blockage corrections in wind tunnel tests of small horizontal-axis wind turbines. Exp. Therm. Fluid Sci. 35, 565–569. doi:10.1016/j.expthermflusci.2010.12.005

Chrysafis, N., 2008. Feasibility Study of New Turbine Concept (MSc Thesis). Cardiff University, Cardiff.

Clarke, J.A., Connor, G., Grant, A.D., Johnstone, C.M., 2006. Regulating the output characteristics of tidal current power stations to facilitate better base load matching over the lunar cycle. Renew. Energy 31, 173–180. doi:10.1016/j.renene.2005.08.024

Clean Current, 2007. Turbine Removal [WWW Document]. Renew. Energy Race Rocks. URL http://racerocks.ca/energy/tidalremove/gfsept1711topside.jpg (accessed 3.24.14).

Clifford, N.J., French, J.R., Hardisty, J., 1993. Turbulence: perspectives on flow and sediment transport. Wiley, Chichester; New York.

Couch, S.J., Bryden, I., 2006. Tidal current energy extraction: Hydrodynamic resource characteristics. Proc. Inst. Mech. Eng. Part M J. Eng. Marit. Environ. 220, 185–194. doi:10.1243/14750902JEME50

Cox, T., 2013. Tidal power project headed for next stage [WWW Document]. Bang. Dly. News. URL http://bangordailynews.com/2013/08/13/news/down-east/tidal-power-project-headed-for-next-stage/ (accessed 9.20.13).

Croft, N., Lin, B., Williams, A., Mason-Jones, A., Fidler, R., Loman, J., Wooldridge, C., Thomas, S., Cook, A., Gallie, R., O'Doherty, T., Willis, M., O'Doherty, D., Gao, G., Ahmadian, R., Muhasilovic, M., Masters, I., Horsfall, I., Cross, M., Falconer, R., Fryett, I., Evans, P., 2010. Tidal turbine deployment in the Bristol Channel: a case study. Proc. ICE - Energy 163, 93–105. doi:10.1680/ener.2010.163.3.93

D'Alessandro, V., Montelpare, S., Ricci, R., Secchiaroli, A., 2010. Unsteady Aerodynamics of a Savonius wind rotor: a new computational approach for the simulation of energy performance. Energy 35, 3349–3363. doi:10.1016/j.energy.2010.04.021

Dadswell, M.J., Rulifson, R.A., 1994. Macrotidal estuaries: a region of collision between migratory marine animals and tidal power development. Biol. J. Linn. Soc. 51, 93–113. doi:10.1111/j.1095-8312.1994.tb00947.x

Darrieus, G.J.M., 1931. Turbine having its rotating shaft transverse to the flow current. 1835018.

Davies, C.M., 2012. Certification schemes for wave and tidal stream renewable energy installations (No. 155559). TATA Steel, Rotherham, UK.

Davies, P., 2009. Guidelines for design basis of marine energy conversion systems: marine renewable energy guides. European Marine Energy Centre, Orkney.

Davies, P., Germain, G., Gaurier, B., Boisseau, A., Perreux, D., 2013. Evaluation of the durability of composite tidal turbine blades. Philos. Transact. A Math. Phys. Eng. Sci. 371, 20120187. doi:10.1098/rsta.2012.0187

Davis, N., VanBlaricom, G.R., Dayton, P.K., 1982. Man-made structures on marine sediments: Effects on adjacent benthic communities. Mar. Biol. 70, 295–303. doi:10.1007/BF00396848

De Vries, E., 2012. Close up - the E126, still the world's biggest turbine [WWW Document]. Wind Power Mon. URL http://www.windpowermonthly.com/article/1138562/close---e126-worlds-biggest-turbine (accessed 8.30.13).

DECC, 2012a. UK Renewable Energy Roadmap Update 2012.

DECC, 2012b. UK Energy in Brief 2012.

DECC, 2012c. DECC Digital Strategy.

DECC, 2012d. Digest of UK Energy Statistics.

DECC, 2013a. The Offshore Wind Programme Board annual report.

DECC, 2013b. UK Energy in Brief 2013.

DECC, 2013c. Reducing the UK's greenhouse gas emissions by 80% by 2050 [WWW Document]. URL https://www.gov.uk/government/policies/reducing-the-uk-s-greenhouse-gas-emissions-by-80-by-2050 (accessed 8.29.13).

DECC, 2013d. Renewables Obligation Banding Review for the period 1 April 2013 to 31 March 2017. UK Government, London.

DECC, 2013e. Wave and tidal energy: part of the UK's energy mix [WWW Document]. URL https://www.gov.uk/wave-and-tidal-energy-part-of-the-uks-energy-mix#tidal-range-potential (accessed 8.29.13).

Deng, Z., Carlson, T., Dauble, D., Ploskey, G., 2011. Fish Passage Assessment of an Advanced Hydropower Turbine and Conventional Turbine Using Blade-Strike Modeling. J. Artic. 4.

Det Norske Veritas, 2007. Design of Offshore Wind Turbine Structures (No. DNV-OS-J101), Offshore Standard. Norway.

Dobrev, I., Massouh, F., 2011. CFD and PIV investigation of unsteady flow through Savonius wind turbine. Energy Procedia 6, 711–720. doi:10.1016/j.egypro.2011.05.081

Dobrev, I., Massouh, F., 2012. Exploring the Flow around a Savonius Wind Turbine, in: 16th International Symposium on Applications of Laser Techniques to Fluid Mechanics. Presented at the International Symposium on Applications of Laser Techniques to Fluid Mechanics, Lisbon, Portugal.

Douglas, C.A., Harrison, G.P., Chick, J.P., 2008. Life cycle assessment of the Seagen marine current turbine. Proc. Inst. Mech. Eng. Part M J. Eng. Marit. Environ. 222, 1–12. doi:10.1243/14750902JEME94

Drilling Contractor, 2012. Upgrades extend drilling capabilities of Beryl platform rigs [WWW Document]. Drill. Contract. URL http://www.drillingcontractor.org/upgrades-extend-drilling-capabilities-of-beryl-platform-rigs-18383 (accessed 8.30.13).

DTI, 1993. Tidal Stream Energy Review (No. ETSU T/05/00155/REP). Department of Trade and Industry.

Efird, K.D., 1977. Effect of Fluid Dynamics on the Corrosion of Copper-Base Alloys in Sea Water. Corrosion 33, 3–8. doi:10.5006/0010-9312-33.1.3

Eggenspieler, G., 2012. ANSYS Turbulence Modeling.

Elphick, P., 2008. Open Hydro successfully deploys subsea tidal turbine [WWW Document]. URL http://www.openhydro.com/news/OpenHydroPR-100908.pdf (accessed 8.30.13).

EMEC, 2013a. Standards [WWW Document]. URL http://www.emec.org.uk/standards/ (accessed 8.30.13).

EMEC, 2013b. Tidal Devices [WWW Document]. URL http://www.emec.org.uk/marine-energy/tidal-devices/ (accessed 8.30.13).

EMEC, 2013c. EMEC: European Marine Energy Centre [WWW Document]. URL http://www.emec.org.uk/ (accessed 8.30.13).

EMEC, 2013d. Blog: Unprecedented tidal energy activity at Hatston Pier : EMEC: European Marine Energy Centre [WWW Document]. URL http://www.emec.org.uk/blog-unprecedented-tidal-energy-activity-at-hatston-pier/ (accessed 8.30.13).

EMEC, 2013e. Tidal test site : EMEC: European Marine Energy Centre [WWW Document]. URL http://www.emec.org.uk/facilities/tidal-test-site/ (accessed 8.30.13).

Encyclopedia Britannica, 2013. photic zone (oceanography) [WWW Document]. URL http://www.britannica.com/EBchecked/topic/457662/photic-zone (accessed 8.30.13).

Energy for Students, 2012. Bad Weather Strands Broken Turbine [WWW Document]. URL http://energyforstudents.ca/bad_weather_strands_broken_turbine_in_nb (accessed 8.30.13).

EquiMar, 2010a. Deliverable 3.3: Assessment of current practice for tank testing of small marine energy devices.

EquiMar, 2010b. Deliverable 3.4: Best practice for tank testing of small marine energy devices.

European Commission, 1996. The exploitation of tidal and marine currents. Wave energy. Project results (No. EUR 16683 EN). Commission of the European Communities. Directorate-General for Science, Research and Development.

European Parliament, 2009. EC 2009/28/EC.

Falcão, A.F. de O., 2010. Wave energy utilization: A review of the technologies. Renew. Sustain. Energy Rev. 14, 899–918. doi:10.1016/j.rser.2009.11.003

Flumill AS, 2013. Home [WWW Document]. URL http://www.flumill.com/ (accessed 8.30.13).

Fraenkel, 2011. Underwater windmills, Harnessing the World’s marine currents. INGENIA.

Frid, C., Andonegi, E., Depestele, J., Judd, A., Rihan, D., Rogers, S.I., Kenchington, E., 2012. The environmental interactions of tidal and wave energy generation devices. Environ. Impact Assess. Rev. 32, 133–139. doi:10.1016/j.eiar.2011.06.002

Fujisawa, N., 1992. On the torque mechanism of Savonius rotors. J. Wind Eng. Ind. Aerodyn. 40, 277–292. doi:10.1016/0167-6105(92)90380-S

Fujisawa, N., Gotoh, F., 1994. Experimental Study on the Aerodynamic Performance of a Savonius Rotor. J. Sol. Energy Eng. 116, 148–152. doi:10.1115/1.2930074

Fullick, A., Fullick, P., 2000. Chemistry. Heinemann Educational.

Gan, K.K., 2004. Lecture 4 Propagation of errors.

Garrett, C., Cummins, P., 2007. The efficiency of a turbine in a tidal channel. J. Fluid Mech. 588, 243–251. doi:10.1017/S0022112007007781

Gaurier, B., Davies, P., Deuff, A., Germain, G., 2013. Flume tank characterization of marine current turbine blade behaviour under current and wave loading. Renew. Energy 59, 1–12. doi:10.1016/j.renene.2013.02.026

Germain, G., 2008. Marine current energy converter tank testing practices, in: 2nd International Conference on Ocean Energy (ICOE 2008), 15th–17th October 2008, Brest, France.

Gilbert, P.T., 1978. Corrosion Resisting Properties of 90/10 Copper–Nickel–Iron Alloy with Particular Reference to Offshore Oil and Gas Applications. Br. Corros. J. 14, 20–25. doi:10.1179/000705979798276059

Giles, J., Myers, L., Bahaj, A., Shelmerdine, B., 2011. The downstream wake response of marine current energy converters operating in shallow tidal flows, in: Proceedings of the World Renewable Energy Congress. Presented at the World Renewable Energy Congress, Linköping University, Linköping, Sweden, pp. 2270–2277.

GL Renewables Certification, 2013. List of Certifications (Marine Renewables).

Golecha, K., Eldho, T.I., Prabhu, S.V., 2011. Influence of the deflector plate on the performance of modified Savonius water turbine. Appl. Energy 88, 3207–3217. doi:10.1016/j.apenergy.2011.03.025

Golecha, K., Eldho, T.I., Prabhu, S.V., 2012. Study on the Interaction between Two Hydrokinetic Savonius Turbines. Int. J. Rotating Mach. 2012. doi:10.1155/2012/581658

Gooch, S., Thomson, J., Polagye, B., Meggitt, D., 2009. Site characterization for tidal power, in: OCEANS 2009, MTS/IEEE Biloxi - Marine Technology for Our Future: Global and Local Challenges. Presented at the OCEANS 2009, MTS/IEEE Biloxi - Marine Technology for Our Future: Global and Local Challenges, pp. 1–10.

Gorlov, A.M., 1995. The helical turbine: A new idea for low-head hydro. Hydro Rev. 14.

Gregory, G., Bahaj, A.., Roberts, P., Huxley-Reynard, C., 2007. Facilities for marine current energy converter characterization, in: 7th European Wave and Tidal Energy Conference (EWTEC). Presented at the European Wave and Tidal Energy Conference, Porto, Portugal.

Gretton, G., 2009. The hydrodynamic analysis of a vertical axis tidal current turbine (Doctor of Philosophy). The University of Edinburgh, Edinburgh.

Gretton, G., Bruce, T., Ingram, D., 2009. Hydrodynamic modelling of a vertical axis tidal current turbine using CFD, in: Proceedings of the 8th European Wave and Tidal Energy Conference (EWTEC). Presented at the European Wave and Tidal Energy Conference, Upssala, Sweden, pp. 468–476.

Hafren Power, 2013a. The Severn Barrage [WWW Document]. URL http://www.hafrenpower.com/severn-barrage/ (accessed 8.29.13).

Hafren Power, 2013b. About Us [WWW Document]. URL http://www.hafrenpower.com/about-us/index.html (accessed 8.29.13).

Hagerman, G., Polagye, B., Bedard, R., Previsic, M., 2006. Methodology for estimating tidal current energy resources and power production by tidal in-stream energy conversion (TISEC) devices. EPRI North Am. Tidal Stream Power Feasibility Demonstr. Proj.

Hameed, M.S., Shahid, F., 2012. Evaluation of Aerodynamic Forces over a Vertical Axis Wind Turbine Blade through CFD analysis. J Appl Mech Eng 2, 2.

Han, S.-H., Park, J.-S., Lee, K.-S., Park, W.-S., Yi, J.-H., 2013. Evaluation of vertical axis turbine characteristics for tidal current power plant based on in situ experiment. Ocean Eng. 65, 83–89. doi:10.1016/j.oceaneng.2013.03.005

Harries, T., Brammer, J., Bockelmann-Evans, B.N., Kwan, A.S.K., 2013. Quantification and visualisation of blockage effects for a savonius type turbine using particle image velocimetry, in: 35th IAHR World Congress. Presented at the IAHR World Congress, Chengdu, China.

Harvey, C., Loder, A., 2013. Fracking Boom Pushes U.S. Oil Output to 25-Year High [WWW Document]. Bloomberg. URL http://www.bloomberg.com/news/2013-12-11/fracking-boom-pushes-u-s-oil-output-to-25-year-high.html (accessed 3.25.14).

Hayashi, T., Li, Y., Hara, Y., 2005. Wind tunnel tests on a different phase three-stage Savonius rotor. JSME Int. J. Ser. B 48, 9–16.

Health & Safety Executive, 2002. Corrosion Protection (Offshore Technology Report No. 2001/011).

Henriksen, O.D., Teilmann, J., Carstensen, J., 2003. Effects of the Nysted Offshore Wind Farm construction on harbour porpoises. 2002 Annu. Status Rep. Acoust. TPOD Monit. Programme Minist. Environ.

Houghton, E.L., Carpenter, P.W., 2003. Aerodynamics for engineering students. Butterworth-Heinemann, Oxford; Boston.

House of Commons, 2013. A Severn Barrage?: Government Response to the Committee’s Second Report of Session 2013-14 (No. HC 622). London.

Howell, R., Qin, N., Edwards, J., Durrani, N., 2010. Wind tunnel and numerical study of a small vertical axis wind turbine. Renew. Energy 35, 412–422. doi:10.1016/j.renene.2009.07.025

Hydrovolts, 2012. New Clean Technology [WWW Document]. URL http://hydrovolts.com/ (accessed 9.17.13).

InflationData.com, 2013. Historical Oil Prices: InflationData.com [WWW Document]. URL http://inflationdata.com/Inflation/Inflation_Rate/Historical_Oil_Prices_Table.asp (accessed 11.13.13).

Ingram, D.M., Smith, G., Bittencourt-Ferreira, C., Smith, H., 2011. Protocols for the equitable assessment of marine energy converters. Institute for Energy Systems, School of Engineering, University of Edinburgh, Edinburgh.

Innovation, 2012. Nova Innovation welcomes Scottish Government renewables fund [WWW Document]. URL http://www.novainnovation.co.uk/index.php/media-menu (accessed 8.30.13).

Inquirer Business, 2013. New York oil soars after Canadian pipelines shut | Inquirer Business [WWW Document]. URL http://business.inquirer.net/128849/new-york-oil-soars-after-canadian-pipelines-shut (accessed 8.29.13).

International Energy Agency, 2005. IEA - September:- Resources to Reserves - Oil and Gas Technologies for the Energy Markets of the Future [WWW Document]. URL http://www.iea.org/newsroomandevents/pressreleases/2005/september/name,20168,en.html (accessed 8.29.13).

International Energy Agency, 2013. Key World Energy Statistics.

International Marine, 2013a. Antifoulings - Introduction [WWW Document]. URL http://www.international-marine.com/antifoulings/introduction.aspx?referrer=AntifoulingsLanding (accessed 8.30.13).

International Marine, 2013b. Foul Release Coatings [WWW Document]. URL http://www.international-marine.com/foulrelease/foul-release-home.aspx (accessed 8.30.13).

Irabu, K., Roy, J.N., 2011. Study of direct force measurement and characteristics on blades of Savonius rotor at static state. Exp. Therm. Fluid Sci. 35, 653–659. doi:10.1016/j.expthermflusci.2010.12.015

IT Power, 2013. Seaflow – 300kW Marine Current Turbine Tidal Energy Pilot Project, UK [WWW Document]. URL http://www.itpower.co.uk/our-projects/tidal-energy/seaflow-300kw-marine-current-turbine-tidal-energy-pilot-project-uk/ (accessed 8.30.13).

ITTC, 2008. Guide to the Expression of Uncertainty in Experimental Hydrodynamics (No. 7.5-02-01-01), ITTC-Recommended Procedures and Guidelines.

Jo, C.H., Yim, J.Y., Lee, K.H., Rho, Y.H., 2012. Performance of horizontal axis tidal current turbine by blade configuration. Renew. Energy 42, 195–206. doi:10.1016/j.renene.2011.08.017

Kamoji, M.A., Kedare, S.B., Prabhu, S.V., 2009a. Performance tests on helical Savonius rotors. Renew. Energy 34, 521–529. doi:10.1016/j.renene.2008.06.002

Kamoji, M.A., Kedare, S.B., Prabhu, S.V., 2009b. Experimental investigations on single stage modified Savonius rotor. Appl. Energy 86, 1064–1073. doi:10.1016/j.apenergy.2008.09.019

Khan, M.J., Bhuyan, G., Iqbal, M.T., Quaicoe, J.E., 2009. Hydrokinetic energy conversion systems and assessment of horizontal and vertical axis turbines for river and tidal applications: A technology status review. Appl. Energy 86, 1823–1835. doi:10.1016/j.apenergy.2009.02.017

Khan, M.N.I., Iqbal, M.T., Hinchey, M., 2008. Submerged water current turbines, in: OCEANS 2008. Presented at the OCEANS 2008, pp. 1–6. doi:10.1109/OCEANS.2008.5151891

Kiho, S., Shiono, M., Suzuki, K., 1996. The power generation from tidal currents by darrieus turbine. Renew. Energy 9, 1242–1245. doi:10.1016/0960-1481(96)88501-6

King, J., Tryfonas, T., 2009. Tidal stream power technology - state of the art, in: OCEANS 2009 - EUROPE. Presented at the OCEANS 2009 - EUROPE, pp. 1–8. doi:10.1109/OCEANSE.2009.5278329

Kumbernuss, J., Chen, J., Yang, H.X., Lu, L., 2012. Investigation into the relationship of the overlap ratio and shift angle of double stage three bladed vertical axis wind turbine (VAWT). J. Wind Eng. Ind. Aerodyn. 107–108, 57–75. doi:10.1016/j.jweia.2012.03.021

Kyozuka, Y., 2008. An Experimental Study on the Darrieus-Savonius Turbine for the Tidal Current Power Generation. J. Fluid Sci. Technol. 3, 439–449. doi:10.1299/jfst.3.439

Lago, L.I., Ponta, F.L., Chen, L., 2010. Advances and trends in hydrokinetic turbine systems. Energy Sustain. Dev. 14, 287–296. doi:10.1016/j.esd.2010.09.004

Lanchester, F.W., 1915. A contribution to the theory of propulsion and the screw propeller. Trans. Institu Tion Nav. Archit. 57, 98–116.

Lang, K., 2010. Spring and neap tides [WWW Document]. NASAs Cosm. URL http://ase.tufts.edu/cosmos/view_picture.asp?id=381 (accessed 8.29.13).

Langlois, T.J., Anderson, M.J., Babcock, R.C., 2005. REEF-ASSOCIATED PREDATORS INFLUENCE ADJACENT SOFT-SEDIMENT COMMUNITIES. Ecology 86, 1508–1519. doi:10.1890/04-0234

Legrand, C., 2009. Assessment of tidal energy resource: marine renewable energy guides. European Marine Energy Centre, Orkney.

Li, C., Zhu, S., Xu, Y., Xiao, Y., 2013. 2.5D large eddy simulation of vertical axis wind turbine in consideration of high angle of attack flow. Renew. Energy 51, 317–330. doi:10.1016/j.renene.2012.09.011

Li, Y., Barbara, J.L., Sander, M.C., 2007. Modeling tidal turbine farm with vertical axis tidal current turbines, in: IEEE International Conference on Systems, Man and Cybernetics, 2007. ISIC. Presented at the IEEE International Conference on Systems, Man and Cybernetics, 2007. ISIC, pp. 697–702. doi:10.1109/ICSMC.2007.4413776

Li, Y., Calisal, S.M., 2010. Three-dimensional effects and arm effects on modeling a vertical axis tidal current turbine. Renew. Energy 35, 2325–2334. doi:10.1016/j.renene.2010.03.002

Li, Y., Calışal, S.M., 2010. Modeling of twin-turbine systems with vertical axis tidal current turbines: Part I—Power output. Ocean Eng. 37, 627–637. doi:10.1016/j.oceaneng.2010.01.006

Lohse, D.P., Gaddam, R.N., Raimondi, P.T., 2008. Predicted Effects of Wave Energy Conversion on Communities in the Nearshore Environment, in: DEVELOPING WAVE ENERGY IN COASTAL CALIFORNIA: POTENTIAL SOCIO-ECONOMIC AND ENVIRONMENTAL EFFECTS. California Energy Commission (Public Interest Energy Research Program), California, USA.

Long Finance, 2013. Boosting Renewables-Alderney's Tidal Energy Project [WWW Document]. URL http://www.longfinance.net/la-news/srib-blog/336-susans-next-blog64.html (accessed 8.30.13).

Lynch. K. P., 2011. Fluere for Particle Image Velocimetry-User Manual.

MacKay, D.J.C., 2009. Sustainable Energy: Without the Hot Air. Uit Cambridge Limited.

Maganga, F., Germain, G., King, J., Pinon, G., Rivoalen, E., 2009. Experimental study to determine flow characteristic effects on marine current turbine behaviour. Presented at the EWTEC 2009, Uppsala.

Maganga, F., Germain, G., King, J., Pinon, G., Rivoalen, E., 2010. Experimental characterisation of flow effects on marine current turbine behaviour and on its wake properties. IET Renew. Power Gener. 4, 498–509. doi:10.1049/iet-rpg.2009.0205

Maine Sunday Telegram, 2012. Maine tidal turbine goes online, first in North America [WWW Document]. URL http://www.pressherald.com/news/ORPC-turbine-off-Eastport-is-the-first-to-do-so-in-North-America.html (accessed 8.30.13).

Maine Technology Institute, 2013. Innovators in the News - Ocean Renewable Power Company's (ORPC) TidGen device first commercial, grid-connected, hydrokinetic tidal energy project in North America [WWW Document]. URL http://www.mainetechnology.org/news-events/innovators-in-the-news/post/ocean-renewable-power-company-s-orpc-tidgen-device-first-commercial-grid-connected-hydrokinetic-tidal-energy-project-in-north-america (accessed 8.30.13).

Maître, T., Amet, E., Pellone, C., 2013. Modeling of the flow in a Darrieus water turbine: Wall grid refinement analysis and comparison with experiments. Renew. Energy 51, 497–512. doi:10.1016/j.renene.2012.09.030

Mankins, J.C., 1995. Technology readiness levels.

Manwell, J.F., McGowan, J.G., Rogers, A.L., 2009. Aerodynamics of Wind Turbines, in: Wind Energy Explained. John Wiley & Sons, Ltd, pp. 91–155.

Marine Current Turbines Ltd., 2013a. Sea Generation [WWW Document]. URL http://www.seageneration.co.uk/ (accessed 9.17.13).

Marine Current Turbines Ltd., 2013b. Testing [WWW Document]. URL http://www.marineturbines.com/SeaGen-Technology/Testing (accessed 8.30.13).

Marine Scotland, The Scottish Government, AECOM, METOC, 2012. Part 2: Regional Locational Guidance for Marine Energy. The Scottish Government, Aberdeen, Scotland.

MARINET, 2013a. Test-stages Protocol [WWW Document]. URL http://www.fp7-marinet.eu/about_test-stages-protocol.html (accessed 9.17.13).

MARINET, 2013b. About [WWW Document]. URL http://www.fp7-marinet.eu/about_summary.html (accessed 9.17.13).

Marsh, G., 2009. Wave and tidal power – an emerging new market for composites [WWW Document]. Reinf. Plast. URL http://www.renewableenergyfocus.com/view/1710/wave-and-tidal-power-an-emerging-new-market-for-composites/ (accessed 8.30.13).

Maskell, E.C., 1963. A theory of the blockage effects on bluff bodies and stalled wings in a closed wind tunnel. DTIC Document.

Mason-Jones, A., O'Doherty, D.M., Morris, C.E., O'Doherty, T., Byrne, C.B., Prickett, P.W., Grosvenor, R.I., Owen, I., Tedds, S., Poole, R.J., 2012. Non-dimensional scaling of tidal stream turbines. Energy 44, 820–829. doi:10.1016/j.energy.2012.05.010

McAdam, R.A., Houlsby, G.T., Oldfield, M.L.G., 2013a. Experimental measurements of the hydrodynamic performance and structural loading of the transverse horizontal axis water turbine: Part 2. Renew. Energy 59, 141–149. doi:10.1016/j.renene.2013.03.015

McAdam, R.A., Houlsby, G.T., Oldfield, M.L.G., 2013b. Experimental measurements of the hydrodynamic performance and structural loading of the Transverse Horizontal Axis Water Turbine: Part 1. Renew. Energy 59, 105–114. doi:10.1016/j.renene.2013.03.016

McAdam, R.A., Houlsby, G.T., Oldfield, M.L.G., 2013c. Experimental measurements of the hydrodynamic performance and structural loading of the Transverse Horizontal Axis Water Turbine: Part 3. Renew. Energy 59, 82–91. doi:10.1016/j.renene.2013.03.012

McAdam, R.A., Houlsby, G.T., Oldfield, M.L.G., McCulloch, M.D., 2010. Experimental testing of the transverse horizontal axis water turbine. IET Renew. Power Gener. 4, 510–518. doi:10.1049/iet-rpg.2009.0194

McCann, G., Thomson, M., Hitchcock, S., 2008. Implications of Site-Specific Conditions on the Prediction of Loading and Power Performance of a Tidal Stream Device, in: 2nd International Conference on Ocean Energy (ICOE 2008). Presented at the International Conference on Ocean Energy, Brest, France.

McCann, G.N., 2007. Tidal current turbine performance and loading sensitivity to waves and turbulence – a parametric study, in: 7th European Wave and Tidal Energy Conference. Presented at the European Wave and Tidal Energy Conference, Porto, Portugal.

McEwen, L., Evans, R., Meunier, M., 2012. Cost-Effective Tidal Turbine Blades, in: 4th International Conference on Ocean Energy. Presented at the International Conference on Ocean Energy, Dublin, Ireland.

McLindon, A., Gray, P., 2008. OpenHydro Becomes First Tidal Energy Company to Generate Electricity onto the UK National Grid.

McTavish, S., Feszty, D., Sankar, T., 2012. Steady and rotating computational fluid dynamics simulations of a novel vertical axis wind turbine for small-scale power generation. Renew. Energy 41, 171–179. doi:10.1016/j.renene.2011.10.018

MEM, 2012. Marine Energy - Global Technology Review 2012.

Menet, J.L., 2002. Local production of electricity with a small Savonius rotor, in: Proceedings from Global Wind Power Conference. Presented at the Global Wind Power Conference, Paris, France.

Menet, J.-L., Bourabaa, N., 2004. Increase in the Savonius rotors efficiency via a parametric investigation, in: Proceedings of the European Wind Energy Conference. Presented at the European Wind Energy Conference, London, UK.

Menter, F.R., 1994. Two-Equation Eddy-Viscosity Turbulence Models for Engineering Applications. Am. Inst. Aeronaut. Astronaut. 32, 1598–1605.

MEPS (International) Ltd, 2014. Stainless Steel Prices [WWW Document]. URL http://www.meps.co.uk/Stainless%20Prices.htm (accessed 8.21.14).

Milne, I.A., Day, A.H., Sharma, R.N., Flay, R.G.J., Bickerton, S., 2011. Tidal Turbine Blade Load Experiments for Oscillatory Motion, in: 9th European Wave and Tidal Energy Conference. Presented at the European Wave and Tidal Energy Conference, Southampton, UK.

Milne, I.A., Sharma, R.N., Flay, R.G.J., Bickerton, S., 2010. A preliminary analysis of the effect of the onset flow structure on tidal turbine blade loads, in: OCEANS 2010 IEEE - Sydney. Presented at the OCEANS 2010 IEEE - Sydney, pp. 1–8. doi:10.1109/OCEANSSYD.2010.5603550

Minesto Ltd, 2013. News [WWW Document]. URL http://minesto.com/news/ (accessed 8.30.13).

Mishnaevsky Jr, L., 2012. Composite materials for wind energy applications: micromechanical modeling and future directions. Comput. Mech. 50, 195–207. doi:10.1007/s00466-012-0727-5

MODEC, 2013. SKWID.

Moffat, R.J., 1988. Describing the uncertainties in experimental results. Exp. Therm. Fluid Sci. 1, 3–17. doi:10.1016/0894-1777(88)90043-X

Mohamed, M.H., Janiga, G., Pap, E., Thévenin, D., 2011. Optimal blade shape of a modified Savonius turbine using an obstacle shielding the returning blade. Energy Convers. Manag. 52, 236–242. doi:10.1016/j.enconman.2010.06.070

Mohan, M., 2008. THE ROYAL INSTITUTION OF NAVAL ARCHITECTS THE ADVANTAGES OF COMPOSITE MATERIAL IN MARINE RENEWABLE ENERGY STRUCTURES, in: RINA Marine Renewable Energy Conference. Presented at the RINA Marine Renewable Energy Conference.

Mycek, P., Gaurier, B., Germain, G., Lothodé, C., Pinon, G., Rivoalen, É., 2013. Numerical and experimental characterisation of interactions between two marine current turbines. Rev. Paralia 6, 2.1–2.12. doi:10.5150/revue-paralia.2013.002

Myers, L., Bahaj, A.S., 2005. Simulated electrical power potential harnessed by marine current turbine arrays in the Alderney Race. Renew. Energy 30, 1713–1731. doi:10.1016/j.renene.2005.02.008

Myers, L., Bahaj, A.S., 2009. Near wake properties of horizontal axis marine current turbines, in: Proceedings of the 8th European Wave and Tidal Energy Conference. pp. 558–565.

Myers, L.E., Bahaj, A.S., Germain, G., 2008. Flow boundary interaction effects for marine current energy conversion devices, in: 10th World Renewable Energy Congress. Presented at the World Renewable Energy Congress, Glasgow, Scotland.

Nakajima, M., Iio, S., Ikeda, T., 2008. Performance of Savonius rotor for environmentally friendly hydraulic turbine. J. Fluid Sci. Technol. 3, 420–429.

NASA, 2013. Shape Effects on Drag [WWW Document]. URL http://www.grc.nasa.gov/WWW/k-12/airplane/shaped.html (accessed 11.26.13).

Natural Environment Research Council, 2013. An environmental knowledge exchange hub for the marine renewable energy sector [WWW Document]. URL https://ke.services.nerc.ac.uk/Marine/Pages/Home.aspx (accessed 8.30.13).

Neill, S.P., Litt, E.J., Couch, S.J., Davies, A.G., 2009. The impact of tidal stream turbines on large-scale sediment dynamics. Renew. Energy 34, 2803–2812. doi:10.1016/j.renene.2009.06.015

Nielsen, K., 2010. Development of Recommended Practices for Testing and Evaluating Ocean Energy Systems (No. T02-0.0). Ocean Energy Systems, International Energy Agency.

Nielsen, K., Meyer, N.I., 1997. Danish Wave Energy Program.

Nishino, T., Willden, R.H.J., 2012. Effects of 3-D channel blockage and turbulent wake mixing on the limit of power extraction by tidal turbines. Int. J. Heat Fluid Flow 37, 123–135. doi:10.1016/j.ijheatfluidflow.2012.05.002

NOAA, 2013. Our Restless Tides, Explanation of Astronomical Factors, Tides and Tidal Currents [WWW Document]. Tides Curr. URL http://co-ops.nos.noaa.gov/restles3.html (accessed 8.29.13).

Norris, J.V., Droniou, E., 2007. Update on EMEC activities, resource description, and characterisation of wave-induced velocities in a tidal flow. Proc. 7th EWTEC 11–13.

NORSOK standard, 1997. Surface preparation and protective coating (No. M-501). Norwegian Technology Standards Institution.

Nortek AS, 2002. Weak spots [WWW Document]. URL http://www.nortek-as.com/en/knowledge-center/forum/velocimeters/30180961 (accessed 11.27.13).

Nortek AS, 2009. Vectrino Velocimeter-User Guide.

Nova Scotia Power, 2013. Annapolis Tidal Station [WWW Document]. URL http://www.nspower.ca/en/home/aboutnspower/makingelectricity/renewable/annapolis.aspx (accessed 8.29.13).

NREL, 2012. Biomass Energy Basics [WWW Document]. Natl. Renew. Energy Lab. NREL U Dep. Energy. URL http://www.nrel.gov/learning/re_biomass.html (accessed 11.27.13).

O’Doherty, T., Mason-Jones, A., O’Doherty, D.M., Byrne, C.B., Owen, I., Wang, Y., 2009. Experimental and computational analysis of a model horizontal axis tidal turbine, in: 8th European Wave and Tidal Energy Conference (EWTEC). Presented at the European Wave and Tidal Energy Conference (EWTEC), Uppsala, Sweden.

OECD Marine Fouling Catalogue, 1965.

Ofgem, 2013. Feed-in-Tariff (FIT) scheme [WWW Document]. URL https://www.ofgem.gov.uk/environmental-programmes/feed-tariff-fit-scheme (accessed 11.13.13).

On-line ROC Auction Service, 2013. eRoc on-line auctions [WWW Document]. URL http://www.eroc.co.uk/ (accessed 8.29.13).

OpenHydro, 2013. Images [WWW Document]. URL http://www.openhydro.com/images.html (accessed 8.30.13).

Orme, J.A.C., Masters, I., Griffiths, R.T., 2001. Investigation of the effect of biofouling on the efficiency of marine current turbines, in: Marine Renewable Energy Conference 2001. Newcastle, pp. 91–99.

Orme, J.A.C., Masters, I., Mima, C., 2006. Analysis and comparison of support structure concepts for tidal stream turbines, in: Proceedings of World Maritime Technology Conference.

ORPC, 2013. Ocean Renewable Power Company (ORPC) [WWW Document]. URL http://www.orpc.co/default.aspx (accessed 8.30.13).

Owen, A., Bryden, I.G., 2005. Prototype Support Structure for Seabed Mounted Tidal Current Turbines. Proc. Inst. Mech. Eng. Part M J. Eng. Marit. Environ. 219, 173–183. doi:10.1243/14750902JEME28

Pankhurst, R.C., Holder, D.W., 1952. Wind-tunnel technique: an account of experimental methods in low-and high-speed wind tunnels. Pitman.

Pelamis Wave Power Ltd., 2013a. Image library [WWW Document]. URL http://www.pelamiswave.com/image-library (accessed 8.29.13).

Pelamis Wave Power Ltd., 2013b. Technology [WWW Document]. URL http://www.pelamiswave.com/pelamis-technology (accessed 8.29.13).

Pelamis Wave Power Ltd., 2013c. About Us [WWW Document]. URL http://www.pelamiswave.com/about-us (accessed 8.29.13).

Pelamis Wave Power Ltd., 2013d. Agucadoura [WWW Document]. URL http://www.pelamiswave.com/our-projects/project/6/CEO-at-Agucadoura (accessed 8.29.13).

Pelamis Wave Power Ltd., 2013e. news [WWW Document]. URL http://www.pelamiswave.com/news/news/134/ScottishPower-Renewables-Pelamis-P2-Machine-Celebrates-One-Year-of-Accelerated-Real-Sea-Testing (accessed 8.29.13).

Pelc R., Fujita R.M., 2002. Renewable energy from the ocean. Mar. Policy 26, 471–479. doi:10.1016/S0308-597X(02)00045-3

Peterson, E.W., Hennessey, J.P., 1978. On the Use of Power Laws for Estimates of Wind Power Potential. J. Appl. Meteorol. 17, 390–394. doi:10.1175/1520-0450(1978)017<0390:OTUOPL>2.0.CO;2

Polagye, B., Thomson, J., 2010. Screening for Biofouling and Corrosion of Tidal Energy Device Materials: In-situ results for Admiralty Inlet, Puget Sound, Washington (Technical Memorandum). Northwest National Marine Renewable Energy Center, University of Washington, Seattle, WA, United States.

Pope, A., Harper, J.J., 1966. Low-speed wind tunnel testing. John Wiley & Sons, New York.

Powell, C.A., Michels, H.T., 2006. Review of Splash Zone Corrosion and Biofouling of C70600 Sheathed steel during 20 years exposure, in: EuroCorr. pp. 24–28.

Prandtl, L., Tietjens, O., 1931. Hydro-und Aeromechanik: nach Vorlesungen von L. Prandtl. J. Springer.

Prasad, A., 2000. Particle image velocimetry. Curr. Sci. 79, 51–60.

Prasad, A.K., 2000. Stereoscopic particle image velocimetry. Exp. Fluids 29, 103–116.

Rabah, K.V.O., Osawa, B.M., 1996. Design and field testing Savonius wind pump in East Africa. Int. J. Ambient Energy 17, 89–94.

Raciti Castelli, M., Englaro, A., Benini, E., 2011. The Darrieus wind turbine: Proposal for a new performance prediction model based on CFD. Energy 36, 4919–4934. doi:10.1016/j.energy.2011.05.036

Rauen, W.B., Lin, B., Falconer, R.A., 2008. Transition from wavelets to ripples in a laboratory flume with a diverging channel. Int. J. Sediment Res. 23, 1–12. doi:10.1016/S1001-6279(08)60001-3

Recharge, 2012. DeltaStream firm gets UK funding to monitor environmental impact - Recharge News [WWW Document]. URL http://www.rechargenews.com/news/wave_tidal_hydro/article1292811.ece (accessed 8.30.13).

Reupke, P., Probert, S.D., 1991. Slatted-blade Savonius wind-rotors. Appl. Energy 40, 65–75. doi:10.1016/0306-2619(91)90051-X

Roache, P.J., Ghia, K.N., White, F.M., 1986. Editorial policy statement on the control of numerical accuracy. J. Fluids Eng. 108, 2.

Roberge, P., 2013a. Erosion corrosion [WWW Document]. Corros. Dr. URL http://corrosion-doctors.org/Forms-Erosion/erosion.htm (accessed 8.30.13).

Roberge, P., 2013b. Types of Water [WWW Document]. Corros. Dr. URL http://corrosion-doctors.org/Corrosion-by-Water/Types-of-water.htm (accessed 8.30.13).

Ross, I., Altman, A., 2011. Wind tunnel blockage corrections: Review and application to Savonius vertical-axis wind turbines. J. Wind Eng. Ind. Aerodyn. 99, 523–538. doi:10.1016/j.jweia.2011.02.002

Saha, U.K., Rajkumar, M.J., 2006. On the performance analysis of Savonius rotor with twisted blades. Renew. Energy 31, 1776–1788. doi:10.1016/j.renene.2005.08.030

Saha, U.K., Thotla, S., Maity, D., 2008. Optimum design configuration of Savonius rotor through wind tunnel experiments. J. Wind Eng. Ind. Aerodyn. 96, 1359–1375. doi:10.1016/j.jweia.2008.03.005

Savonius, S.J., 1931. The S-rotor and its applications. Mech. Eng. 53, 333–338.

Scarano, F., Riethmuller, M.L., 2000. Advances in iterative multigrid PIV image processing. Exp. Fluids 29, S051–S060. doi:10.1007/s003480070007

Schneeberger, M., VA TECH HYDRO, 2008. Sihwa tidal-turbines and generators for the world's largest tidal power plant.

Scotrenewables, 2013. SR250 Testing [WWW Document]. Scotrenewables Tidal Power Ltd. URL http://scotrenewables.com/ (accessed 9.17.13).

Sea Generation Ltd., 2008. Delay in commissioning one of SeaGen's rotors | Marine Current Turbines [WWW Document]. URL http://www.marineturbines.com/3/news/article/11/delay_in_commissioning_one_of_seagen_s_rotors/ (accessed 8.30.13).

Sheldahl, R.E., Feltz, L.V., Blackwell, B.F., 1978. Wind tunnel performance data for two- and three-bucket Savonius rotors. J. Energy 2, 160–164.

Shiono, M., Suzuki, K., Kiho, S., 2002. Output characteristics of Darrieus water turbine with helical blades for tidal current generations, in: Proceedings of the Twelfth International Offshore and Polar Engineering Conference. Presented at the International Offshore and Polar Engineering Conference, Kitakyushu, Japan, pp. 859–864.

Siemens, 2012. Hat Trick for SeaGen Tidal Current Turbine [WWW Document]. URL http://www.siemens.com/press/en/feature/2012/energy/2012-11-seagen.php (accessed 8.30.13).

Siemens UK, 2013. Wales gives consent to pioneering tidal array scheme [WWW Document]. URL http://www.siemens.co.uk/en/news_press/index/news_archive/2013/skerries-tidal-array-consent-granted-wales.htm (accessed 11.17.13).

Slagter, W., 2011. Cutting Design Costs: How Industry leaders Benefit from Fast and Reliable CFD.

Snohomish County Public Utility District, 2012. Admiralty Inlet Tidal Energy Project.

Stallard, T., Collings, R., Feng, T., Whelan, J.I., 2011. Interactions Between Tidal Turbine Wakes: Experimental Study of a Group of 3-Bladed Rotors, in: 9th EWTEC. Presented at the European Wave and Tidal Energy Conference, Southampton, UK.

Starling, M., 2009. Guidelines for reliability, maintainability and survivability of marine energy conversion systems: marine renewable energy guides. European Marine Energy Centre, Orkney.

Sun, X., Chick, J.P., Bryden, I.G., 2008. Laboratory-scale simulation of energy extraction from tidal currents. Renew. Energy 33, 1267–1274. doi:10.1016/j.renene.2007.06.018

Sun, X., Luo, D., Huang, D., Wu, G., 2012. Numerical study on coupling effects among multiple Savonius turbines. J. Renew. Sustain. Energy 4, 053107. doi:10.1063/1.4754438

Tabassum, S.A., Probert, S.D., 1987. Vertical-axis wind turbine: A modified design. Appl. Energy 28, 59–67. doi:10.1016/0306-2619(87)90041-9

TATA Steel, BCSA, SCI, 2013a. Corrosion of Structural Steel [WWW Document]. http://www.steelconstruction.info. URL http://www.steelconstruction.info/Corrosion_of_structural_steel#Time_of_wetness (accessed 8.30.13).

TATA Steel, BCSA, SCI, 2013b. Paint Coatings [WWW Document]. http://www.steelconstruction.info. URL http://www.steelconstruction.info/Paint_coatings (accessed 8.30.13).

TATA Steel, BCSA, SCI, 2013c. Corrosion Protection [WWW Document]. http://www.steelconstruction.info. URL http://www.steelconstruction.info/Corrosion_protection#Hot-dip_galvanizing (accessed 8.30.13).

TATA Steel, BCSA, SCI, 2013d. UK Steel Construction Information [WWW Document]. http://www.steelconstruction.info. URL http://www.steelconstruction.info/ (accessed 8.30.13).

The Crown Estate, 2013. Leasing round and projects [WWW Document]. URL http://www.thecrownestate.co.uk/energy-infrastructure/wave-and-tidal/pentland-firth-and-orkney-waters/leasing-round-and-projects/ (accessed 9.23.13).

The Royal Society, 2010. Climate change: A Summary of the Science.

The Scottish Government, 2012. Renewable Energy [WWW Document]. URL http://www.scotland.gov.uk/Topics/Statistics/Browse/Business/TrenRenEnergy (accessed 9.25.13).

The United Kingdom Hydrographic Office, 1993. Admiralty Tidal Stream Atlas.

Thomson, J., Polagye, B., Richmond, M., Durgesh, V., 2010. Quantifying turbulence for tidal power applications, in: OCEANS 2010. pp. 1–8.

Tidal device deal for Sound of Islay, 2013. . BBC.

Tidal Energy Ltd, 2009. DeltaStream Demonstrator Project, Ramsey Sound, Pembrokeshire. Non-Technical Summary. Tidal Energy Ltd, Cardiff.

Tidal Energy Pty Ltd, 2013. Davidson-Hill turbine [WWW Document]. URL http://tidalenergy.net.au/media.html (accessed 9.17.13).

Tidal Flow Power Ltd., 2013. Development [WWW Document]. Tidal Flow Power Ltd. URL http://tidalflowpower.com/page4.html (accessed 11.27.13).

Tidal Lagoon Swansea Bay, 2013a. Lagoon Map [WWW Document]. URL http://www.tidallagoonswanseabay.com/assets/images/lagoon_map.jpg (accessed 8.29.13).

Tidal Lagoon Swansea Bay, 2013b. Tidal Lagoon Swansea Bay [WWW Document]. URL http://www.tidallagoonswanseabay.com/ (accessed 8.29.13).

Tidal Sails AS, 2013. Development [WWW Document]. URL http://tidalsails.com/development/ (accessed 8.30.13).

TIDENG, 2013. The rotor [WWW Document]. URL http://www.tideng.com/Tideng/Tideng.html (accessed 9.17.13).

Ting, O.S., Potty, N.S., Shahir Liew, M., 2011. Prediction of corrosion rates in marine and offshore structures, in: National Postgraduate Conference (NPC), 2011. Presented at the National Postgraduate Conference (NPC), 2011, pp. 1–6. doi:10.1109/NatPC.2011.6136376

Tougaard, J., Carstensen, J., Damsgaard Henriksen, O., Teilmann, J., 2003. Short-term effects of the construction of wind turbines on harbour porpoises at Horns Reef (No. HME/362-02662). TechWise A/S, Hedeselskabet, Roskilde.

Trade, G.B.D. of, 2007. Meeting the energy challenge: a White Paper on energy. TSO Shop.

UK Government, 2013. Increasing the use of low-carbon technologies [WWW Document]. URL https://www.gov.uk/government/policies/increasing-the-use-of-low-carbon-technologies/supporting-pages/the-renewables-obligation-ro (accessed 11.13.13).

United Nations, 2013. Kyoto Protocol [WWW Document]. URL http://unfccc.int/kyoto_protocol/items/2830.php (accessed 9.25.13).

University of Alberta, 2013. EarthScienceNHS - Tides [WWW Document]. URL https://earthsciencenhs.wikispaces.com/Tides (accessed 8.29.13).

University of Southampton, 2008. Tidal-current Energy Device Development and Evaluation Protocol (No. URN 08/1317). UK Government.

University of Strathclyde, 2013. Oscillating Hydrofoil [WWW Document]. Mar. Curr. Resour. Technol. Methodol. URL http://www.esru.strath.ac.uk/EandE/Web_sites/05-06/marine_renewables/technology/oschydro.htm (accessed 8.30.13).

Untaroiu, A., Wood, H.G., Allaire, P.E., Ribando, R.J., 2011. Investigation of Self-Starting Capability of Vertical Axis Wind Turbines Using a Computational Fluid Dynamics Approach. J. Sol. Energy Eng. 133, 041010–041010. doi:10.1115/1.4004705

US Department of Energy, 2013. Top 9 Things You Didn't Know about Carbon Fiber | Department of Energy [WWW Document]. URL http://energy.gov/articles/top-9-things-you-didn-t-know-about-carbon-fiber (accessed 8.30.13).

Ushiyama, I., Nagai, H., Mino, M., 1982. The optimum design configurations of savonius wind turbines, in: IECEC '82; Proceedings of the Seventeenth Intersociety Energy Conversion Engineering Conference. Presented at the IECEC '82; Proceedings of the Seventeenth Intersociety Energy Conversion Engineering Conference, pp. 2096–2101.

Vahdati, M., Nobile, R., Barlow, J., Mewburn-Crook, A., 2011. Dynamic stall for a Vertical Axis Wind Turbine in a two-dimensional study, in: Proceedings of WREC 2011. Presented at the World Renewable Energy Congress, Linköping University, Sweden.

Valdès, L.-C., Raniriharinosy, K., 2001. Low technical wind pumping of high efficiency. Renew. Energy 24, 275–301. doi:10.1016/S0960-1481(00)00201-9

Vance, T., 2013. Antifouling Coatings for Marine Renewable Devices. Wind Wave CONNECT.

Vestas, 2006. Life cycle assessment of offshore and onshore sited wind power plants based on Vestas V90-3.0MW turbines. Elsam Engineering, Randers, Denmark.

Wahl, T.L., 2000. Analyzing ADV data using WinADV, in: Proc., Joint Conf. on Water Resources Engineering and Water Resources Planning and Management. Presented at the Water Resources Engineering and Water Resources Planning and Management, Minneapolis, Minnesota, pp. 1–10.

Wahl, T.L., 2012. WinADV [WWW Document]. US Dep. Inter. - Bur. Reclam. URL http://www.usbr.gov/pmts/hydraulics_lab/twahl/winadv/ (accessed 11.27.13).

Wall Street Journal, 2013. UK Government: Renewables to Deliver Over 30% of Electricity Supply by 2020. Wall Str. J.

Welsh Government, 2012. Energy Wales: A Low Carbon Transition (No. WG14605). Crown Estate?

Westerweel, J., 1997. Fundamentals of digital particle image velocimetry. Meas. Sci. Technol. 8, 1379. doi:10.1088/0957-0233/8/12/002

Whelan, J.I., Graham, J.M.R., Peiró, J., 2009. A free-surface and blockage correction for tidal turbines. J. Fluid Mech. 624, 281–291. doi:10.1017/S0022112009005916

Widdows J., Brinsley M., 2002. Impact of biotic and abiotic processes on sediment dynamics and the consequences to the structure and functioning of the intertidal zone. J. Sea Res. 48, 143–156. doi:10.1016/S1385-1101(02)00148-X

Wilcox, D.C., 1994. Turbulence modeling for CFD. DCW industries La Cañada.

Wilson, R.E., Lissaman, P.B.S., 1974. Applied aerodynamics of wind power machines. [Corvallis, Or., Oregon State University].

World Nuclear Association, 2013. World Nuclear Association [WWW Document]. URL http://www.world-nuclear.org/ (accessed 8.29.13).

Wu, H., Chen, L., Yu, M., Li, W., Chen, B., 2012. On design and performance prediction of the horizontal-axis water turbine. Ocean Eng. 50, 23–30. doi:10.1016/j.oceaneng.2012.04.003

Wyre Tidal Energy, 2013. La Rance Barrage [WWW Document]. URL http://www.wyretidalenergy.com/tidal-barrage/la-rance-barrage (accessed 8.29.13).

Xia, J., Falconer, R.A., Lin, B., 2010a. Impact of different tidal renewable energy projects on the hydrodynamic processes in the Severn Estuary, UK. Ocean Model. 32, 86–104. doi:10.1016/j.ocemod.2009.11.002

Xia, J., Falconer, R.A., Lin, B., 2010b. Impact of different operating modes for a Severn Barrage on the tidal power and flood inundation in the Severn Estuary, UK. Appl. Energy 87, 2374–2391. doi:10.1016/j.apenergy.2009.11.024

Xia, J., Falconer, R.A., Lin, B., Tan, G., 2012. Estimation of annual energy output from a tidal barrage using two different methods. Appl. Energy 93, 327–336. doi:10.1016/j.apenergy.2011.12.049

Yang, B., Lawn, C., 2011. Fluid dynamic performance of a vertical axis turbine for tidal currents. Renew. Energy 36, 3355–3366. doi:10.1016/j.renene.2011.05.014

Yang, B., Lawn, C., 2013. Three-dimensional effects on the performance of a vertical axis tidal turbine. Ocean Eng. 58, 1–10. doi:10.1016/j.oceaneng.2012.09.020

Yang, B., Shu, X.W., 2012. Hydrofoil optimization and experimental validation in helical vertical axis turbine for power generation from marine current. Ocean Eng. 42, 35–46. doi:10.1016/j.oceaneng.2012.01.004

Yuen, K., Thomas, K., Grabbe, M., Deglaire, P., Bouquerel, M., Osterberg, D., Leijon, M., 2009. Matching a Permanent Magnet Synchronous Generator to a Fixed Pitch Vertical Axis Turbine for Marine Current Energy Conversion. IEEE J. Ocean. Eng. 34, 24–31. doi:10.1109/JOE.2008.2010658

Zhao, Z., Zheng, Y., Xu, X., Liu, W., Hu, G., 2009. Research on the improvement of the performance of savonius rotor based on numerical study, in: International Conference on Sustainable Power Generation and Supply, 2009. SUPERGEN ’09. Presented at the International Conference on Sustainable Power Generation and Supply, 2009. SUPERGEN ’09, pp. 1–6. doi:10.1109/SUPERGEN.2009.5348197

# 15 Appendix A

## 15.1 Technology Review

The following table is the result of a review of both a selection of the global VATTs under development and the tidal turbines currently being tested in UK waters. Due to the commercial sensitivity of the technologies, typically only general information is available from the developer's website and press releases; only a select few developers published results in scientific journals. For completion of an overall tidal turbine technology review there are turbines that were undergoing development at the initiation of this review in 2010 but as of 01/07/2013 development was halted, either due to technical or economic constraints. The review is accurate as of 01/07/2013. A more comprehensive list (but no details) of all known tidal turbines under development can be found on the EMEC website.

## 15.2 A global review of a selection of VATTs under development:

### 15.2.1 Davidson-Hill Venturi Turbine

*Website:* *http://tidalenergy.net.au/*

| | |
|---|---|
| *Type:* | VATT |
| *Company:* | Tidal Energy Pty Ltd |
| *Country:* | Australia |
| *Image/s:* | 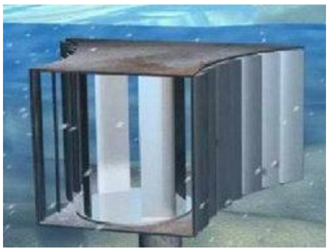 |

**Device Characteristics:**

- 4 arm Darrieus style turbine
- Turbine housed within a uniquely shaped venture duct.
- Duct yaws to the flow direction
- Duct enables efficiencies of up to 0.60 to be achieved; with the device claiming to be have the highest efficiency of any ducted/non-ducted turbine
- Holders of the world record for largest increase in performance relative to freestream conditions: An increase of 384%.
- No specific turbine details available

**Field Prototypes:**

- Field-testing has been undertaken in South West Queensland, Australia on a large prototype device in 2005.
- The venturi shroud comes in 5 different sizes from 1.5 to 10m in diameter.

### 15.2.2 Blue Energy Turbine

*Website:* http://www.bluenergy.com/

*Type:* VATT

*Company:* Blue Energy Canada Inc.

*Country:* Canada

*Image/s:*

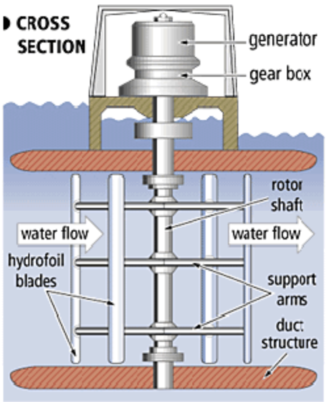

**Device Characteristics:**

- Darrieus style design
- Fixed 4 bladed hydrofoil
- Cut in speed of 1ms$^{-1}$
- Housed within ducted caisson
- Caisson supports the turbine as well as acting as a platform to bear the dry machinery room above the water level.
- Blue Energy Tidal Bridge Power System-device units interlock forming a bridge
- Bridge can create high blockage ratio across a channel; inducing a static head-augmenting device performance

**Field Prototypes:**

- Scale testing was undertaken in 2006 & 2007 in collaboration with the University of British Columbia.
- Extensive field-testing was undertaken in the 1980s on small-scale prototypes of the turbine.
- Completed preliminary design for a 10m diameter turbine
- Currently raising funds for a commercial demonstration prototype.

### 15.2.3 Kobold Turbine

*Website:* *www.pontediarchimede.it (under maintenance)*

*Type:* VATT

*Company:* Ponte di Archimede Int.

*Country:* Italy

*Image/s:*

**Device Characteristics:**

- Darrieus design
- Global Efficiency of $C_p$=0.23
- High torques enabling self-starting capability
- Omni directional

**Field Prototypes:**

- The ENERMAR Project

Deployed on floating buoy in the Messina Strait, Italy in 2001.

Estimating a total extractable energy of ≈398GWh

### 15.2.4 EnCurrent Vertical Axis Turbine

*Website:* *www.newenergycorp.ca*

*Type:* VATT

*Company:* New Energy Corporation

*Country:* Canada

*Image/s:*

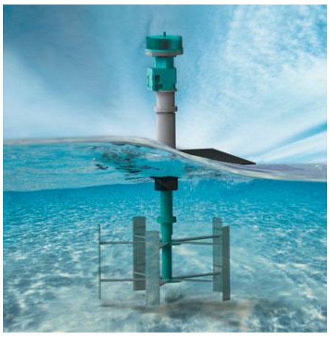

**Device Characteristics:**

- Darrieus Design
- Number of blades is site specific
- $C_p \approx 0.35$-0.40
- Rated at a TSR≈2 -2.5
- Developed in collaboration with the National Research Council of Canada.
- Company aims to offer off the shelf tidal power generation systems ranging from 5kW-250kW devices; with all devices currently encompassed within a floating configuration.
- Gearbox and generator are housed above the water surface

**Field Prototypes:**

- Early testing included both laboratory and field-testing.
- Both 5kW and 25kW systems were field tested.
- Velocities tested at in the field were 1.5, 1.9 & $2.35ms^{-1}$ for combinations of ducted and non-ducted configurations.
- Successfully tested at the City of Calgary's Bonnybrook Wastewater Treatment Plant and in an irrigation channel east of Calgary.
- In the process of implementing the first tidal energy commercialization project in Canada; labeled "The Canoe Pass Tidal Commercialization Project" in a stretch of water labeled the Canoe Pass off the east coast of Vancouver. Project to include 2 x 250kW devices.

### 15.2.5 FlipWing & C-12 Canal Turbine

*Website:* *http://hydrovolts.com*

*Type:* THATT

*Company:* Hydrovolts, Inc.

*Country:* USA

*Image/s:*

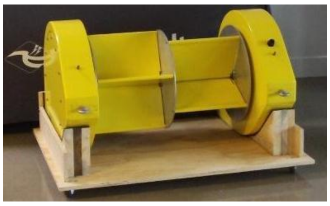

**FlipWing Turbine**

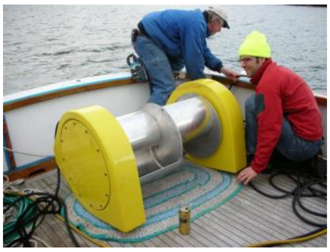

**Savonius Turbine**

**Device Characteristics:**

- Generator is attached to the unit, therefore can be submerged or buoyant.
- Claims to be fish friendly, since the blades spin with the water current.
- The turbine is scalable in the form of chains. Whereby numerous units can be interlocked.
- Patent pending FlipWing design is based upon the blades producing positive torque as the move downstream but open on the upstream stroke, considerably reducing their resistance; leading to a pressure differential across the axis of 95%.
- Savonius style found to perform at higher efficiencies and therefore used instead of the FlipWing

**Field Prototypes:**

- No field-testing of FlipWing only a Savonius 2 stage design-C-12 Canal Turbine
- Company promoting off the shelf tidal turbines, ranging from small to large-scale deployment.
- Permanent magnet generator with gearing system
- Flow speeds between 1.5-3m/s
- 20 year lifetime
- Dimensions:
  - 6’ tall
  - 13’wide
  - 8’ deep
  - 6000lbs dry weight
- Suggested applications include irrigation canals, slipways and outfalls.

### 15.2.6 Hunter Turbine

*Website:* *http://tidalflowpower.com*

*Type:* VATT
*Company:* TidalFlow Power Ltd.
*Country:* UK

*Image/s:*

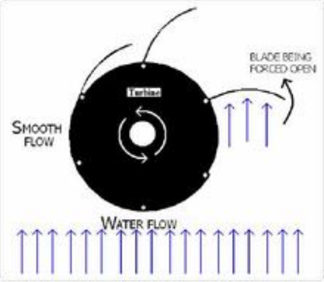

**Device Characteristics:**

- Drag type turbine
- Developed at Queen Mary, University of London
- $C_p$/TSR=0.15/0.67 at 3.5m/s
- Consists of curved blades hinged to a central drum
- Blades are opened when subjected to positive pressure, which then drive the turbine
- Blades closed against the drum when the pressure on the blades becomes negative

**Field Prototypes:**

- Only laboratory testing conducted to date
- Plans for 10kW, 100kW and 1MW scale testing based on investment.

(Li and Calisal, 2010; Yang and Lawn, 2011)

### 15.2.7 SKWID

*Website:* *http://www.modec.com/fps/skwid/index.html*

*Type:* VATT
*Company:* MODEC
*Country:* Japan

*Image/s:*

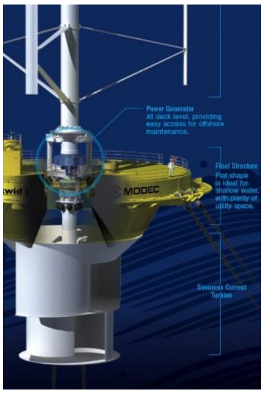

**Device Characteristics:**

- Savonius style
- 15m Diameter
- Designed to harness tidal currents in addition to providing start up torque to a Darrieus wind turbine
- Also acts as a self-righting ballast for the hybrid device

**Field Prototypes:**

- Sea trials to be conducted off Saga, Kyushu in Japan.
- No further detail available

## 15.3 Tidal turbines that have undergone testing in UK waters:

### 15.3.1 Hammerfest Strom Tidal Turbine

*Website:* *http://www.hammerfeststrom.com/*

*Type:* HATT

*Company:* Hammerfest Strom UK Ltd *(Main shareholder Andritz Hydro)*

*Image/s:*

**HS1000**

**Device Characteristics:**

- HS300 & HS1000 models; the latter essentially being a scaled up version of the first.
- 3 Bladed hydrofoil design
- Mounted on a triangular frame

**Field Prototypes:**

- HS300, deployed in Kvalsund, Finnmark, Norway in 2003. Has been fully tested regarding deployment, operation, maintenance and re-deployment; proving to be a success.
- World's first grid connected tidal turbine
- The 1MW HS1000 installed at the Fall of Warness site, EMEC during summer 2011.
- Installed in collaboration with Scottish Power Renewables who conducted the EIA study.
- 25 year design life
- Designed for maintenance every 5 years
- Both turbines designed for flows in excess of 2.5m/s

### 15.3.2 SeaFlow

*Website:* www.marineturbines.com/

*Type:* HATT

*Company:* Marine Current Turbines Ltd (MCT)

*Image/s:*

**Device Characteristics:**

- Twin bladed hydrofoil design
- Pitch controlled blades-can be pitched through 180°; enabling generation from bi-directional flow
- Can achieve a $C_p>0.48$
- Supported via a tubular steel monopole. Allowing rotors to be moved up and down for ease of maintenance.

**Field Prototypes:**

- 300kW device
- Installed 3km North-East off Lynmouth on the North Devon Coast.
- Installed May 2003
- Decommissioned in October 2009.

### 15.3.3 CoRMaT 2nd Generation

*Website:* *http://www.nautricity.com/*

*Type:* HATT

*Company:* Nautricity Ltd

*Image/s:*

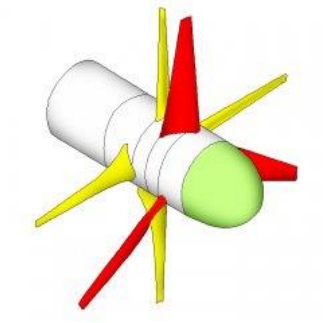

**At EMEC**

**Device Characteristics:**

- 2 contra rotating 3 bladed hydrofoil rotors situated on the same hub.
- Claims to double the relative rotational speed compared to single rotating rotor: Driving a contra-rotating generator, negating the need for a gearbox.
- No pitch control
- Potential increased array density due to reduced wake effect

**Field Prototypes:**

- Undergone 1/70th scale testing in large tanks
- 1/7th scale testing at sea with power capture performance of $Cp/\lambda = 0.42/7$
- 1.7th scale tested in the Clyde river forstructural loadings and material robustness
- Prototype testing in the sound of Islay
- To undergo proof-of-concept testing in London Thames alongside the HQS Wellington, moored at Temple Steps.
- Aims to potentially site numerous devices along the Thames from Westminster to Margate.
- Given the go-ahead for investigating potentially deploying 6 devices in the Mull of Kintyre off the west coast of Scotland.
- Test of a scaled turbine at the EMEC scaled test berths in 2013

### 15.3.4 Tocardo

*Website:* *http://www.tocardo.com/*

*Type:* HATT

*Company:* Tocardo Tidal Turbines

*Image/s:*

**Device Characteristics:**

- 2 bladed design
- T100, T200, T500, T1000 generations
- Permanent magnet direct drive generator
- Patented bi-directional reversible rotor blade design

**Field Prototypes:**

- Proof of concept testing in 2005
- In 2008 the demonstrator T100 device was installed in sluice of the Afsluitdijk near Den Oever and connected to the grid. Produces enough energy for 15 households.
- T500 in final stages of development, testing scheduled for 2014

### 15.3.5 Deltastream

*Website:* *http://www.tidalenergyltd.com*

*Type:* HATT

*Company:* Tidal Energy Ltd (TEL) *(Main Funder and driving force Eco2)*

*Image/s:*

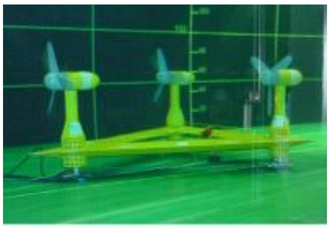

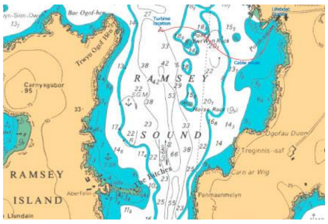

**Ramsey Sound test site**

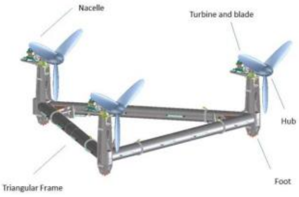

**Device Characteristics:**

- Three 3 bladed HATTs situated on a single triangular frame base
- Three independent turbines ensures constant generation during downtime of a single turbine
- Fixed pitch and thrust limiting blades
- Gravity based mooring.
- Automatic hydraulic yawing
- Electrical and control equipment mounted on the main base frame
- Patent filed for a variable swept area through a contracting/expanding device to alter the blade angular orientation.
- Patent filed for the seabed penetrating gravity support structure-rock feet; negating the need for drilling or piling of the sea bed.

**Field Prototypes:**

- From 2009 to 2012 a scaled model was tested by Cranfield University in France.
- 1.2MW device, consisting of 3 x 400kW rotors, to be installed in Ramsey Sound, West Wales in 2013/2014, for a 1 year trial period
- Ramsey sound exhibits peak spring flows of around 3m/s
- Site is sheltered from prevailing wind and wave conditions as well as no commercial fishing occurring at the site.
- Minimum clearance of 11.9m between blade tip and water surface at low tide
- Initially turbines with 12m diameter blades to be tested, with full scale 15m blades installed later during the testing period
- Initially only one 400kW to be installed with the aim to for full scale testing later in the year.
- Licenses for the site granted from DECC and the Welsh Assembly Government in March 2011.
- Environmental survey to be subsidized by the Carbon Trust and the results made available to the public.

### 15.3.6 SeaGen

*Website:* www.seageneration.co.uk/

*Type:* HATT

*Company:* Marine Current Turbines Ltd (MCT)

*Image/s:*

**Device Characteristics:**

- Evolution of SeaFlow turbine
- Twin turbine design connected via a hydrodynamic arm either side of the supporting structure
- Each turbine consists of 2 hydrofoils
- Connected to the UK electricity grid and recognized by OFGEM.
- Can generate up to 10MWh per tide
- Supported via a tubular steel monopole. Allowing rotors to be moved up and down for ease of maintenance.

**Field Prototypes:**

- Twin 16m diameter rotors.
- Rated at 1.2MW for a flow of 2.4m/s.
- Installed in Strangford Lough, April 2008.
- 5-year installation period.

### 15.3.7 Neptune Proteus

*Website:* http://www.neptunerenewableenergy.com/tidal_technology.phph

*Type:* VATT

*Company:* Neptune Renewable Energy Ltd
IN LIQUIDATION

*Image/s:*

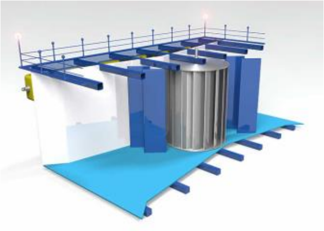

**Device Characteristics:**

- NP1000 is a 6m x 6m vertical axis turbine, housed in a bi-directional venturi diffusing buoyant duct.
- Previous testing and theoretical work estimates $C_P$>0.45
- Design is focused on deployment in estuarine locations.

**Field Prototypes:**

- Completed 1/10th, 1/40th & 1/100th scale testing.
- 3 months tow testing trial in 2009.
- Full scale testing in the Humber Estuary.
  - 150 tonnes & 20m in length.
  - Should generate 1000Mwh/year.
  - Failed to generate predicted power output and directors concluded it was not commercially viable to pursue with the development of the turbine

### 15.3.8 Open Hydro

*Website:* *http://www.openhydro.com/home.html*

*Type:* HATT

*Company:* Open Hydro Group Ltd (59.7% holding by DCNS)

*Image/s:*

**Device Characteristics:**

- Open centered turbine
- Low rotational speed
- Lubricant free operation
- Claims to minimize risk to marine life
- Low mechanical noise
- Gravity base mooring.

**Field Prototypes:**

- First tidal turbine to be tested at EMEC Fall of Warness site, installed in 2006
- 6m-diameter test unit, 250kW capacity. Was the first to generate electricity to the grid in the UK.
- On a twin piled structure, allows further generations to be tested easily.
- In 2009, deployed first commercial scale 1MW device in the waters of the Bay of Fundy,Nova Scotia, Canada on behalf of Nova Scotia Power.
- The 400tonne device was lowered to the seabed via the purpose built Open Hydro Installer barge.
- Reported that in the summer of 2010, the demonstration device had to be lifted for maintenance since all of its blades had been removed.
- 1MW device subsequently installed on a gravity base in EMEC adjoining the previous test rig.
- Close to deploying 7th iteration of the design in EMEC.

### 15.3.9 G-TT

*Website:* *http://www.green-tide.com/home*

*Type:* HATT

*Company:* Green tide turbines

*Image/s:*

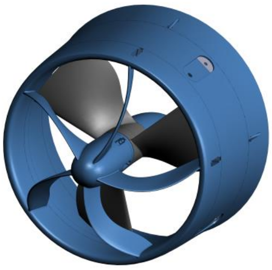

**Device Characteristics:**

- Noise reduction technology
- Ducted turbine:
  - Turbulence mitigation
  - Cost Reduction –smaller turbine blades
  - Reduced blade stresses
  - Reliability, allows fixed pitch blades to be used working at effectively the same efficiency as variable pitch blades

**Field Prototypes:**

- Sizes range from 2-5kW to a 720kW device.
- 720kW device – consisting of 2 12.8 diameter turbines aligned in a pair

### 15.3.10 Tidal Generation

*Website:* *http://www.tidalgeneration.co.uk/*

*Type:* HATT

*Company:* Tidal Generation Ltd (Wholly owned by Alstom)

*Image/s:*

**Device Characteristics:**

- 3 Bladed turbine fixed on a steel tripod foundation-fixed via a patented fast drilling and piling technique.
- Patented thruster system for yawing of the turbine to both the flood and ebb tide.
- Pitch controlled
- The nacelle rotates to the flow direction negating the need for accurate placement.
- Unit is buoyant therefore can be towed to and from location.

**Field Prototypes:**

- 500kW prototype testing at EMEC in September 2010
- 1MW prototype based upon on the 500kW device was installed at EMEC in early 2013 using the existing foundation in collaboration with the Energy Technologies Institute (ETI).
- Rated speed of 2.7m/s
- Cut-in speed 1.0m/s
- Planned 18 month test period
- 18m diameter
- 21m long nacelle
- Nacelle weighs 135tonnes (not including turbine support structure)
- Operating at a depth of 40m
- Generated at full capacity of 1MW and over 10GWh of electricity

### 15.3.11 Kepler Energy

*Website:* *http://www.keplerenergy.co.uk/*

*Type:* THAT

*Company:* Oxford University

*Image/s:*

**Device Characteristics:**

- Designed for use in low velocity flows
- 50% higher output than traditional propeller style turbines due to greater swept area
- Suited to blocked flow conditions
- No Gearing or pitch change mechanisms
- Bi-directional

**Field Prototypes:**

- Currently undergoing laboratory testing (McAdam et al., 2013a, 2013b, 2013c, 2010)
- Typical full scale rotor to be 10m in diameter, 125m long (2 x 60m long turbines with a generator in the middle) in a depth of 20m
- To be rated at 4.4MW for a flow speed of 2m/s

### 15.3.12 AR1000

*Website:* *http://atlantisresourcesltd.com/*

*Type:* *HATT*

*Company:* Atlantis Resources Ltd.

*Image/s:*

**Device Characteristics:**

- Two turbines fixed on a common nacelle-allowing bi-directional power generation
- Fixed pitch blades-eliminating need for nacelle rotation
- Rated at 1MW for a flow speed of 2.6m/s

**Field Prototypes:**

- Installed the AR1000 in the EMEC test facility in 2011
- Rated at 1MW for a flow speed of 2.65m/s.
- 18m rotor diameter
- 22.5m high
- Hub-height above seabed 13.5
- Weighs 1300 tonnes
- Sits on a gravity base with a total height of 22.5m
- Further testing on drive train and control system conducted at NAREC
- GRP blades, steel structure and nacelle.
- Consent granted by the Scottish Government for a 398MW tidal array in the Pentland Firth–to be installed in stages, beginning with a 9MW array.

### 15.3.13 HyTide

*Website:* http://www.voith.com

*Type:* HATT

*Company:* Voith Hydro Ocean Current Technologies (80:20 collaboration with RWE Innogy Venture Capital Fund)

*Image/s:*

**Device Characteristics:**

- 3 bladed turbine
- Direct drive-negating the need for gearing
- Design focused on minimizing the risk of failure and avoiding maintenance intensive parts
- Symmetric blade profile for bidirectional generation-eliminating need for yaw and pitch alterations
- **Field Prototypes:**
- In 2011 a 1/3rd scale turbine was successfully tested near the South Korean island of Jindo.
- 110kW rated device at a current speed of 2.9m/s
- Rotor diameter of 5.3m
- 1MW prototype of the HyTide to be tested in EMEC at the Fall of Warness site in 2013
- Supported on a 23m high mono-pile
- Rotor diameter of 16m
- Rated at 1MW for a current speed of 2.9m/s

### 15.3.14 Swan Turbine

*Website:* http://www.swanturbines.co.uk

*Type:* HATT

*Company:* Swanturbines *(Formed Cygnus Energy, to commercialize the technology)*

*Image/s:*

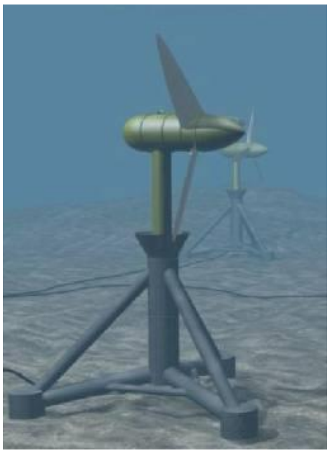

**Device Characteristics:**

- 3 bladed hydrofoil design
- Aimed at minimizing failure rates
- Reducing the risks entailed with installation and maintenance through providing a novel installation and removal technique – supporting structure installed first and the nacelle is placed afterwards
- Patented yawing system
- Gearless system

**Field Prototypes:**

- Proof of concept testing conducted at Swansea University on a 1/60th blade prototype.
- Tow testing of 1/20th scale prototype in 2001
- Gearless generator dry tested at NarREC under partial load
- Developing inshore turbines, Cygnet ISTT at ½ scale funded by SMART Scotland

### 15.3.15 TidEl

*Website:* *http://www.smd.co.uk/products/renewables/list.htm*

*Type:* HATT

*Company:* SMD Hydrovision

*Image/s:*

**Device Characteristics:**

- Twin contra rotating turbines attached by a cross beam.
- Fixed pitch blades
- Fixed by mooring chains to seabed
- Mooring system allows rotors to align themselves downstream of tidal flow without any external intervention

**Field Prototypes:**

- 1/10 scale in NAREC
- Full scale prototype will consist of 2 x 500kW turbines
- Will be rated at 1MW for a 2.3m/s flow rate, with a cut in speed of 0.7m/s
- Blades will have a diameter of 15m.
- No details of site location

### 15.3.16 SR250

*Website:* http://www.scotrenewables.com

*Type:* HATT

*Company:* Scotrenewables Tidal Power Ltd

*Image/s:*

**Device Characteristics:**

- Floating twin-turbine (counter-rotating)
- Hydraulically retractable legs –used during towing for installation or maintenance as well as automatically retracting rotors during storm conditions.
- Streamline design – storm waves pass over smoothly
- Passive yaw system
- Fixed pitch blades
- Rapid mechanical and electrical connection/disconnection.

**Field Prototypes:**

- 1/5th Prototype tested at Burra Sound
- 250kW Prototype deployed in early 2011 for an 18 month testing period at the Fall of Warness site at EMEC.
- 80 tonnes, 33m length, twin 8m diameter rotor
- Successful power generation in September 2011, with the device currently exceeding expectations. Surpassed its rated power, achieving a peak power export of 273kW, equating to 110% rated power.
- Obtained funding of £8.84 million for the design, construction, installation and testing of a new SR2000 2MW prototype, scheduled for Spring 2014 completion. £1.24 million of the funding was awarded by the Scottish Governments WATERS 2 scheme. The SR2000 will be optimised for a 20 year commercial life.

### 15.3.17 TIDENG Offshore

*Website:* *http://www.tideng.com/Tideng/Tideng.html*

*Type:* THAT

*Company:* TIDENG

*Image/s:*

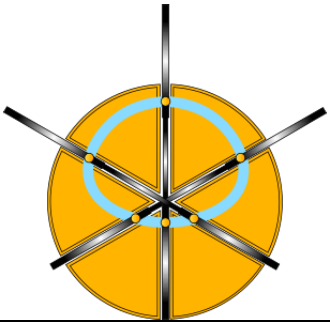

**Device Characteristics:**

- Consists of 6 flat rectangular blades (“wings”) on an axis.
- During a full rotation half the blades are in a generating position, whereas the other half are withdrawn from the flow to reduce friction.
- Bi-directional
- Concrete Base optimally shaped to accelerate the flow 1.3-2 times, depth dependent

**Field Prototypes:** N/A

### 15.3.18 Triton

*Website:* http://www.tidalstream.co.uk

*Type:* Turbine Support

*Company:* TidalStream Limited

*Image/s:*

**Device Characteristics:**

- 2nd Generation Tidal Energy Platform
- Ability to support up to 10MW from a range of turbines from 3rd party developers
- Semi-submersible spar buoys attached to a rigid swing-arm tether
- Platform can be towed to the site already assembled
- Ballasting and de-ballasting allows buoys to be submerged or above the surface allowing easy maintenance to be undertaken

**Field Prototypes:**

- 1/10th Scale model testing in the Thames, London
- Further testing to be conducted in 2011

### 15.3.19 Evo Pod

*Website:* *http://www.oceanflowenergy.com*

*Type:* HATT

*Company:* Oceanflow Energy

*Image/s:*

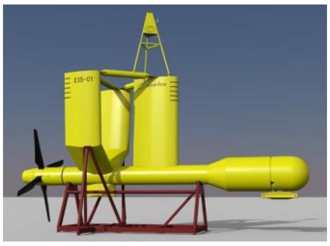

**Device Characteristics:**

- Mono, twin or multiple turbines using traditional 3 or 4 bladed HATT design
- Floating structure
- Surface piercing streamline struts and a deep lying nacelle ensure minimum motion from wave action is caused.
- Tethered to seabed using catenary spread mooring system with simple pin-pile and gravity anchors
- Swivel mooring system for turbine alignment

**Field Prototypes:**

- Completed 1/40th scale testing at Newcastle University in 2006.
- Completed 1/10th scale tesing in Strangford Narrows, Northern Ireland of single turbine device
- 1kW device installed in 2008 with testing continuing until 2011.
- Plan to deploy a ¼ scale twin turbine device with a rated power output of 37kW in Sanda Sound, South Kintyre in 2013 and will be grid connected.
- Funded by Scottish Enterprise WATERS grant
- Turbine diameter of 4.5m.

### 15.3.20 TidGen

*Website:* *http://www.orpc.co/default.aspx*

*Type:* THAT

*Company:* ORPC

*Image/s:*

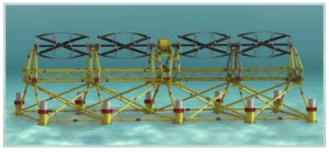

**Device Characteristics:**

- Gorlov Style device
- Unit style device, can be stacked in deeper waters
- Designed to harness power in water depths of 15-30m.

**Field Prototypes:**

- Each turbine unit has a capacity of 150kW
- Barge mounted test in 2010 in the Bay of Fundy
- TidGen Cobscook Bay Project:
  - US first commercial grid connected tidal turbine
  - Flow speed of roughly 3m/s
  - 1 unit consists of 2 x 150kW turbines, first of which installed in early 2013.
  - Aim to generate up to 3MW with a series of devices

### 15.3.21 Deep Green

*Website:* *http://www.minesto.com/*

*Type:* Kite

*Company:* Minesto Ltd

*Image/s:*

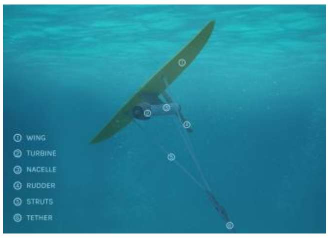

**Device Characteristics:**

- Kite-style turbine
  - Consists of a wing and turbine tethered to the ocean floor
- Operates in low velocities, since kite is able to travel up to ten times faster than the speed of the water
- Gearless system
- Low maintenance cost

- **Field Prototypes:**
- Example of scaled turbine:
  - Minesto DG-14 is an 850kW device, rated for a speed of 1.7m/s. Wing span of 14m and a rotor diameter of 1.15m.
- Scaled device tested in Strangford Lough in 2011/2012
- Obtained lease from Crown Estate and consent to test a quarter scale turbine at Strangford Lough
- Targeted Wales for deployment of full scale turbine
- Aim to deploy 3MW array in 2015

# Appendix B

## 1.1 PIV Investigation

Particle Image Velocimetry (PIV) is a technique for measuring fluid flow and unlike commonly used flow measurement apparatus such as Acoustic Doppler Velocimeters (ADVs) which result in point measurements of velocity, PIV has the ability to undertake global velocity measurements. In addition PIV is a non-intrusive method, measuring the velocities of small seeding particles from images captured by a camera as opposed to an intrusive probe. PIV has transformed the qualitative analysis of particle flow visualisation to that of a quantifiable flow analysis. PIV has widely been used to capture two velocity components, namely streamwise velocity component U, and spanwise velocity component V, of fluid flow, although stereoscopic techniques can be utilised to obtain the third component W. The results of PIV are comparable to output of computational fluid dynamics, i.e. the ability to plot large eddy simulations and real-time velocity vector/ contour maps (Dobrev and Massouh, 2012).

This study will apply the PIV method to analyse the wake of various scaled Savonius turbines. The conventional Savonius turbine was designed by Sigurd. J. Savonius (1931), at the beginning of the 20th century, to harness wind energy; it is a vertical axis (also referred to as a cross flow) tidal turbine. The simple design consists of two semi-circular vertical offset opposing sections (buckets) such that they form the letter S, see Figure 130. The study will be based on analysing the wake of Savonius turbines of varying scales, with variable turbine D. This will result in turbines with four different blockage factors, see equation (1), in the spanwise direction as shown in Table 37. The turbines will be analysed in a static state at angles of 0° and 90°at each scale, to represent the maximum and minimum blockage each turbine configuration would experience in a revolution. The PIV analysis has been conducted as a 2D study.

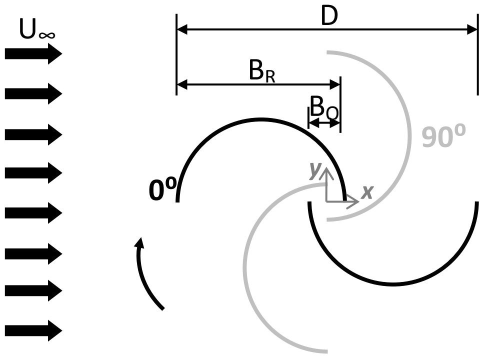

**Figure 130 Savonius Schematic**

$$Blockage\ Factor\ BF\ [\%] = \frac{Flume\ Width}{Turbine\ Diameter} \tag{71}$$

**Table 37 Details of scaled Savonius turbines**

| Test | D<br>[m] | $B_D$<br>[m] | $B_O$<br>[m] | BF<br>[%] |
|---|---|---|---|---|
| A | 0.06 | 0.035 | 0.010 | 20.0 |
| B | 0.10 | 0.060 | 0.018 | 33.3 |
| C | 0.12 | 0.070 | 0.020 | 40.0 |
| D | 0.15 | 0.085 | 0.025 | 50.0 |

**Note: Flume details can be found in Section 2.2**

## 1.2 PIV Theory

The basic principle of a PIV system is the acquisition of a velocity flow field from images of flow on a chosen plane, in which small seeding particles are illuminated. A typical PIV system comprises of several sub-systems: A tracer particle seeded flow, a high sensitivity CCD camera, a light source for illumination of the tracer particles on a chosen plane and a computer for data acquisition and extraction of information of tracer particle positions (A. Prasad, 2000). The post processing of these images using specialist PIV software will calculate the velocity magnitudes of the particles and produce a vector field. The target area for the PIV images is illuminated via a light sheet emitting light pulses at a given interval: A high sensitivity CCD camera, positioned perpendicular to the light sheet, captures images of the target area for each light pulse. The PIV analysis software uses two successive image frames and measures the distance travelled by particles from one frame to the next. The velocity is indirectly calculated from the distance travelled in a given time period of a tracer particle in successive images. For a displacement D, over a time period $\Delta t = t_2 - t_1$, the velocity v of the tracer particle is given as:

$$D(X; t', t'') = \int_{t_1}^{t_2} v[X(t), t]dt \qquad \textbf{(72)}$$

Equation (72) implies that an average velocity, v, is calculated over the particle displacement and not an exact representation. However, this is acceptable provided the spatial and temporal scales of the flow are large with respect to the spatial resolution, the exposure time delay, and dynamics of the tracer particles (Westerweel, 1997). After sequences of images are captured, each image frame is sub-divided into zones known as interrogation windows, measured by number of pixels. The interrogation windows from both images are cross-correlated for successive images to find a signal peak, which corresponds to the average particle displacement for that particular interrogation window and all the tracer particles within. Enhanced accuracy is achieved through sub pixel interpolation. Subsequently the interrogation windows are moved across the entire image frames to form a global velocity vector map over the images, as seen in Figure 138b. Although the sampling within the image window is random with regards to tracer particle locations, since the interrogation windows are square in shape the resulting vector map is formed upon a uniform grid across the images. The lower bound of interrogation window size is determined by the requirement that it should contain at least 5 to 10 particle images with an ideal particle image diameter of around 2 pixels (A. Prasad, 2000). The resolution of the vector flow field is proportional to the interrogation window size. Although decreasing the interrogation window size will improve the resolution, the interrogation window size is limited by the recommendation of ensuring the displacement of the particles in the x and y directions are no greater than 25% of the interrogation window x and y dimensions; any larger and the signal to noise ratio begins to degrade, due to in plane loss of particles between pairs of images. The maximum measured velocity is dictated by the displacement of particles being greater than the extents of the interrogation window.

## 1.3 PIV Set-up

The research was carried out in a horizontal recirculating flume in the hydraulics laboratory of Cardiff University School of Engineering. The working section is 0.3m wide, 10m in length and a maximum depth of 0.32m; x, y and z are the streamwise, spanwise and vertical coordinates, respectively. The flow is controlled via a centrifugal pump with a maximum flow rate of $0.03m^3/s$ and the water level is controlled via a weir downstream. The PIV system used in this study is a custom system, consisting of a: Baumer TXG14F CCD camera with a 1392 x 1040 pixel sensitivity, focal length, f, of 9mm, f number of f1.4 and a maximum frequency of 30fps ($\Delta t = 1/30\,s$), a Polytec BVS-11 Wotan Flash stroboscope and trigger box, fibre optic cable, linelight and cylindrical lens, as seen in Figure 131a & Figure 133. Image capturing was controlled using custom edited software supplied by Dantec Dynamics.

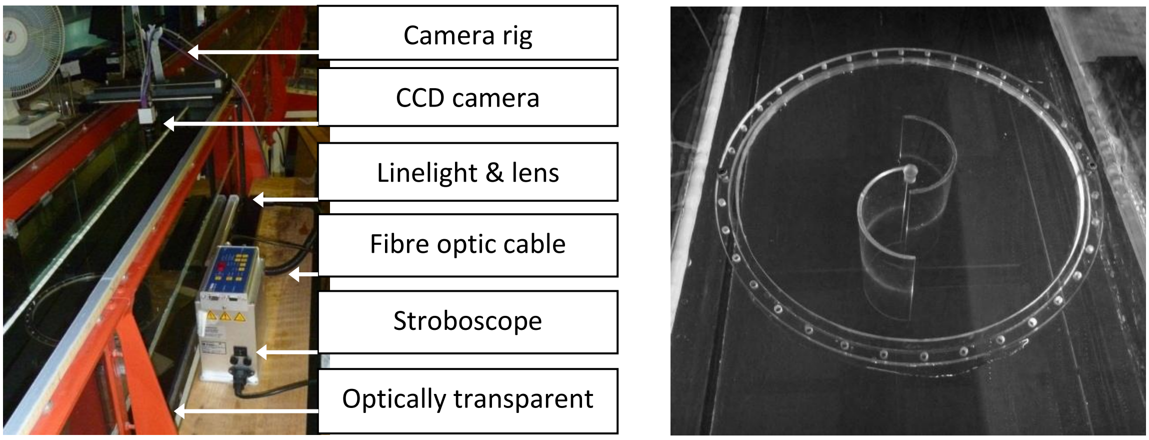

**(a)** **(b)**

**Figure 131 PIV system (a) laboratory set-up (b) Example of installed turbine and fixing**

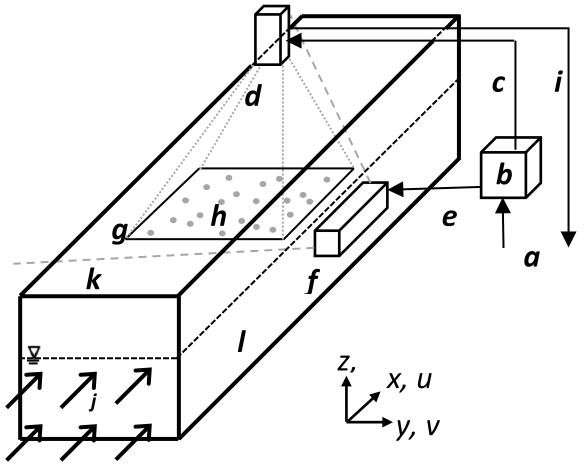

| | |
|---|---|
| a | PC |
| b | Stroboscope |
| c | Trigger cable |
| d | CCD Camera |
| e | Fibre optic cable |
| f | Linelight |
| g | Image window |
| h | Illuminated tracer particles |
| i | Gigabit Ethernet cable |
| j | Incoming flow |
| k | Emitted light plane |
| l | Optically transparent section |

**Figure 132 Schematic of PIV laboratory set-up**

The light sheet used to illuminate the image window is created using a combination of a linelight and cylindrical lens. The cylindrical lens is used to focus the expanding linelight into an ideally collimated light sheet, i.e. light sheet of constant thickness $\Delta z_{ls}$. The light sheet was focused to a distance equal to the width of the flume and a $\Delta z_{ls}$ of around 5-10mm was achieved. The camera depth of field δz was set to roughly the same value as $\Delta z_{ls}$; ideally $\delta z \geq \Delta z_{ls}$ to reduce the error of capturing out of focus particles

### 1.3.1 Image Acquisition

The study will analyse the wake region behind four different scaled static Savonius turbines along a horizontal plane in the streamwise direction. Initial trials of the system with no object in the flow discovered that the free surface posed a problem with regards to capturing clear images due to excessive diffraction caused by surface waves. This resulted in the installation of a Perspex ceiling in the streamwise direction into the flume that would eradicate any free surface effects, see Figure 131b.

The Perspex ceiling was fitted at a height of 0.25m above the flume bed and secured in place using a hybrid polymer based sealant. The Perspex section was 2.4m in length, with the front 0.1m curved upwards to prevent flooding of the Perspex ceiling. The location of the turbines was 0.7m downstream from the front edge of the Perspex. Each turbine, with blades also created from Perspex would be glued to a Perspex circular cap. The circular cap would then fit onto a circular hole in the Perspex ceiling at the location for the turbines. Subsequently the cap can be screwed in place at the desired angle, since each cap possesses fixing points at every 10°, see in Figure 131b. The light sheet was located at mid depth of the flow, z=0.125m, for each image acquisition; again to reduce wall effects from the base of the flume and the Perspex ceiling.

During trial tests the captured images displayed inconsistent light levels. It appeared that the light sheet intensity would not extend the full width of the flume, leaving the image with dark corners on the opposite side to the light source leading to particles remaining undetected during analysis. Similar issues arose whilst capturing images alongside the flume support structure. To eradicate these issues, two sets of images would be captured for each image location. For each set the light source would be on the opposite side of the flume. During analysis, these images would be split along the centreline of the flume, X=0m, and subsequently stitched together.

### 1.3.2 PIV Analysis Software - Fluere

The chosen software to perform the analysis on the PIV results was Fluere (Lynch. K. P., 2011). Fluere is open source software and is based upon the established iterative image deformation algorithm described by (Scarano and Riethmuller, 2000).

The analysis will be based on a split frame mode, which requires separate image files of equal dimensions for processing. The images sequence chosen for the split frame analysis was a step of 1 and a stride of 1. "Step in the file list will indicate to the software the number of files between adjacent image first frames. The stride in the file list indicates the separation in files between frame A and B." A step and stride of 1 results in a sequence $I_1$ & $I_2$, $I_2$ & $I_3$, etc. Equation (73) gives the discrete form of the cross-correlation function used by Fluere. In which CC is the correlation plane, Ia is the interrogation window from the first image, Ib is the interrogation window from the second image, p and q are the shift of the windows relative to each other and M and N pixel interrogation windows in the x and y direction respectively. Further details on the analysis can be found in (Lynch. K. P., 2011).

$$CC[p,q] = \frac{1}{M \times N} \sum_{i=1}^{M} \sum_{j=1}^{N} I_A[i,j] I_B[i+p, j+q] \tag{73}$$

### 1.3.3 Magnification

The magnification, M, is determined in this case by the desired image size. The aim is to capture the entire width of the flume in one image and traverse the flume, in the x-direction, to capture the entire length. Problems occurred while trying to capture the entire flume width due to the interference of the flume walls due to perspective, which caused the height of the side walls to be captured on the image as a thick boundary as opposed to a straight divide. As a result the image width was decreased until no interference was present, resulting in an image width of 26.9cm in the y-direction and length of 19cm in the x-direction. As a result the CCD camera was positioned at a vertical distance of 20.5cm from the light sheet. The chosen image length in the streamwise direction results in the length of the test section being divided into 13 equal windows. An overlap of 10% of the window length is present between successive images, included to provide a smoother transition between neighbouring flow fields during analysis (Dobrev and Massouh, 2012).

The processing software, Fluere, specifies distance as units of pixels. In order to convert the pixel displacement to a physical velocity, calibration was required. This was achieved through placing a ruler within the test section in the centre of the light sheet. The camera is then focused as sharp as possible on the ruler markers, a set of images were then acquired and analysed. The focus level achieved in the calibration was kept constant throughout the remainder of the study. Since calibration is a vital component of PIV, it was performed at 2 separate locations to instil confidence in the results, as seen in Figure 133; resulting in a calibration of 5.3 pixels/mm.

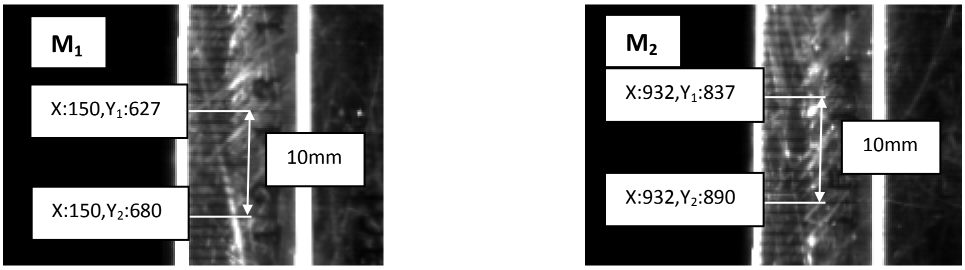

**(a)** **(b)**

**Figure 133 Calibration for PIV software (a) $M_1$ (b)$M_2$**

$$M_1 = \frac{Y_2 - Y_1}{y_2 - y_1} = \frac{(680 - 627)pixels}{10mm} = 5.3\,pixels/mm \tag{74}$$

$$M_2 = \frac{Y_2 - Y_1}{y_2 - y_1} = \frac{(890 - 837)pixels}{10mm} = 5.3\,pixels/mm \tag{75}$$

### 1.3.4 Interrogation window size

For a magnification $M$, time between exposures $\Delta t$ and an expected bulk velocity, U, in the object plan, the minimum interrogation window size, $I_w$, can be calculated from:

$$I_w \geq \frac{MU\Delta t}{0.25} \tag{76}$$

$U$ can be taken from the ADV readings carried out during the validation phase, thus being 0.11m/s for freestream flow at the future location of the turbines. At the location of the flow constriction either side of the turbines, the bulk flow in the wake region will be a reduced value and therefore the estimation of the minimum interrogation window size is a conservative value.

$$I_w \geq \frac{5.3 \times 110 \times (1/30)}{0.25} \therefore I_w \geq 77\,pixels \tag{77}$$

### 1.3.5 Sampling Period

An initial study was required to determine the number of images needed in order to capture a time-averaged flow field at each location. An average flow field for each location is required to enable all locations to be stitched together in the analysis to provide a total view of the time-averaged wake for each of the scaled turbines and angular positions. For this study no turbine was in situ and the future location of the turbines within the test section was used to capture the images. The images were acquired at the maximum sampling frequency of 30Hz, determined by the maximum setting of the CCD camera. From 160 images onwards there was marginal change in the velocity, therefore 160 images were taken at a sampling rate of 30Hz, to give a sampling period of 5.3s.

## 1.4 Data Capture Procedure

**Table 38 Window locations for Figure 134**

| Window | ≤ x(cm) ≤ | | Window | ≤ x(cm) ≤ | |
|---|---|---|---|---|---|
| **1** | -66.25 | -39.35 | **8** | 56.95 | 83.85 |
| **2** | -48.65 | -21.75 | **9** | 74.55 | 101.45 |
| **3** | -31.05 | -4.15 | **10** | 91.95 | 118.85 |
| **4** | -13.45 | 13.45 | **11** | 109.55 | 136.45 |
| **5** | 4.15 | 31.05 | **12** | 127.15 | 154.05 |
| **6** | 21.75 | 48.65 | **13** | 144.75 | 171.65 |
| **7** | 39.35 | 66.25 | | | |

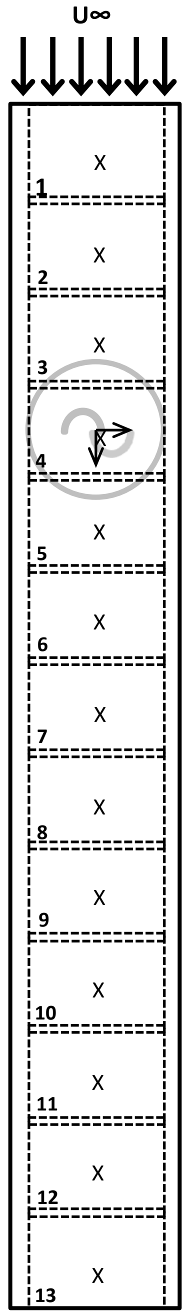

**Figure 134 Windows of test section**

1. To begin the system is initialised through ensuring that:
   - The line-light is connected to the stroboscope;
   - The camera trigger is connected to the stroboscope;
   - Power supply to camera and stroboscope are connected;
   - Network cable between PC and the camera is connected.
2. Next the equipment is positioned accordingly:
   - The camera is positioned at the location for image 1(see Figure 134).
   - Line-light is positioned to correspond with centreline of image
   - Mirrors are positioned on the opposite side of the flume to the line-light. The mirrors provide two purposes, eradicating external light from the current image and to reflect the line light to provide a consistent light sheet across the image enabling a full image of particles to be captured. Without the mirrors dark corners can appear on the image on the opposite side to the line light in which the particles cannot be detected by the PIV software.
3. Camera software is opened and camera initialised. Depending on external light levels, the exposure and gain settings on the camera software are altered to produce an image with a sharp contrast between the dark background and bright particles
4. Once the settings are confirmed the images can be captured. The default for file names is as follows:
   D(bucket diameter)_A(turbine angle)_X(camera location)_(Image number)
   - E.g. D35_A90_X715_5_1

6. As images are being saved a random selection of 10 images are processed using Fluere. This is to ensure that the images captured are of acceptable quality.

The quality measured by whether or not a whole image of vectors has been processed as seen in Figure 138b (picture of full image of vectors compared to partially full)

The process is then repeated as the camera is moved into position for image 2. Once the process has traversed the length of the test section and captured each image the process is repeated with the line light positioned on the opposite side to the flume and the mirrors moved accordingly.

## 1.5 RESULTS

### 1.5.1 Validation

Validation of the PIV system was achieved through comparison with results of a Nortek ADV. A flow field was captured using the PIV system at the future location of the turbines. For the captured flow field a series of test points were collected by the ADV along a regular grid, see Figure 135. In order to test the PIV's system capabilities the test was run for a freestream condition as well as around a blunt obstacle in order to validate the PIV's ability to capture velocity gradients. Three sets of data were collected using the PIV system for both freestream and object in-situ conditions. The ADV samples at a rate of 200Hz and a sampling period of 60s was used. A laboratory study by (A. S. Bahaj et al., 2007), in addition to studies conducted at Cardiff University using an ADV have shown that a 60s sampling period will produce representative average velocities. The velocity for each point was obtained through calculating the velocity magnitude from the U and V components and averaging each point for the sampling period. Figure 136 and Figure 137 show the results for both with and without the rectangular block in situ.

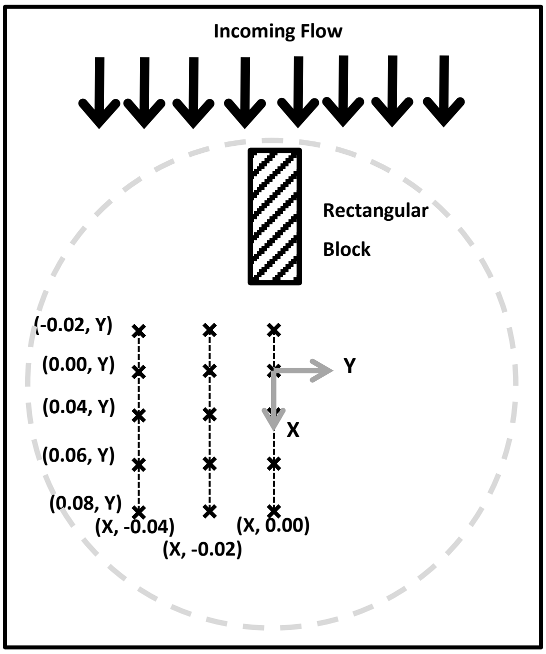

Figure 135 Location of sample points for PIV validation

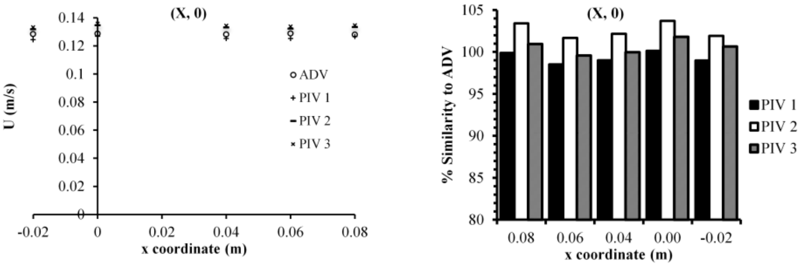

(a) (b)

**Figure 136 (a) ADV vs. PIV results (b)% Similarity of PIV to ADV data**

Figure 136 shows that for freestream conditions all three sets of PIV velocity values are within ±4% of the ADV values. Figure 137a shows that where the flow is close to freestream conditions the three sets of PIV measurements are within ±3% of the ADV values, similar to Figure 136. For Figure 137b PIV 1 achieves the lowest validation value of around 90% similarity to the ADV values whereby the PIV 3 results are within ±2.5% of the ADV values. Figure 137c shows that the results for PIV 1 are within ±4% of the AVD values, however the results for PIV 1 and 2 show that the values converge to 100% with increasing distance from the object but majority lie within ±10% of the ADV values with the lowest value being 17% lower than the ADV value for PIV 3.

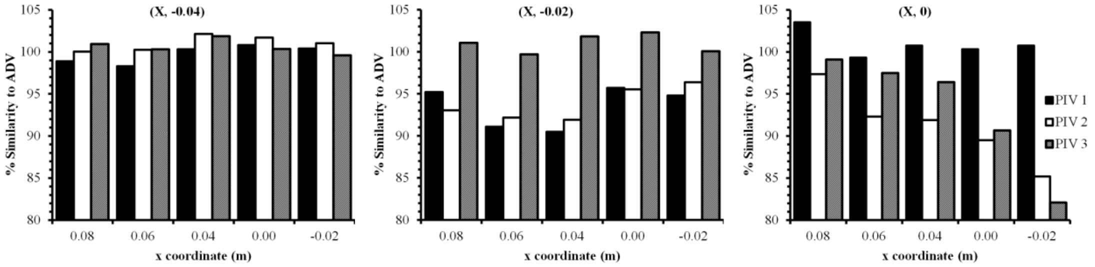

(a) (b) (c)

**Figure 137 % Similarity of PIV to ADV data for various locations (a) X, -0.04 (b) X, -0.02 (c) X, 0**

## 1.5.2 Wake Study

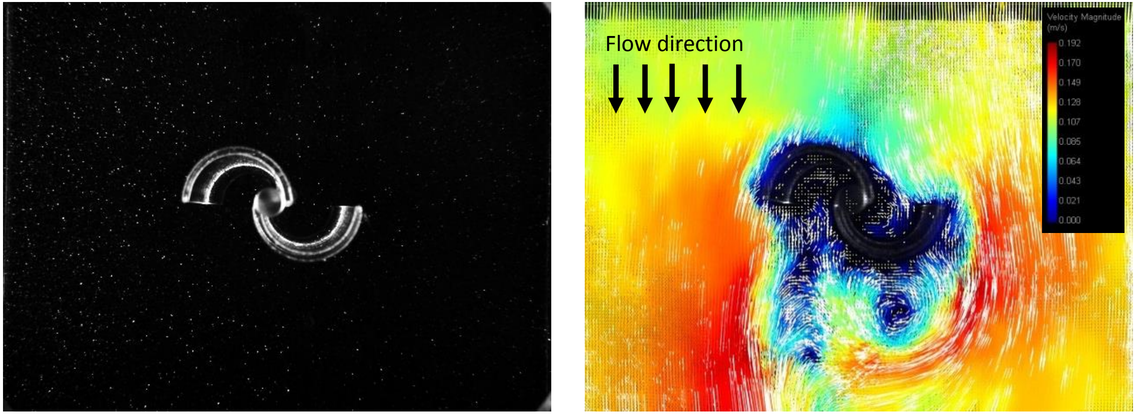

(a) (b)

**Figure 138 (a) Raw PIV image, (b) Processed PIV image**

Complete flow fields consisting of all the aligned images were captured for the four different scaled Savonius turbines at angles of $0^0$ and $90^0$. The flow speed for the tests was set to 0.11m/s and kept constant for the duration of the tests. Figure 138a illustrates that particles have been highlighted and distributed homogeneously throughout the whole image and Figure 138b illustrates a complete superimposed velocity vector field on to the raw image. Figure 138b has captured the reduced flow speed prior to the turbine (indicated in shades of blue) and the subsequent reduced flow speed apparent in the wake of the turbine, it has also captured the flow acceleration either side of the turbine (indicated by shades of red). For each scaled turbine and for both the angles of $0^0$ and $90^0$ the aligned images were processed using Fluere to obtain the vector fields and then analysed using TechPlot in order to stitch together adjacent images to produce a full contour plot of the flow field for each configuration.

Figure 140 illustrates the complete flow field for each of the configurations with a maximum velocity equal to the freestream velocity of the tests (used to highlight the wake region). All plots use non-dimensionalised velocities (using the freestream velocity) and length scales (using the specific turbine diameter).

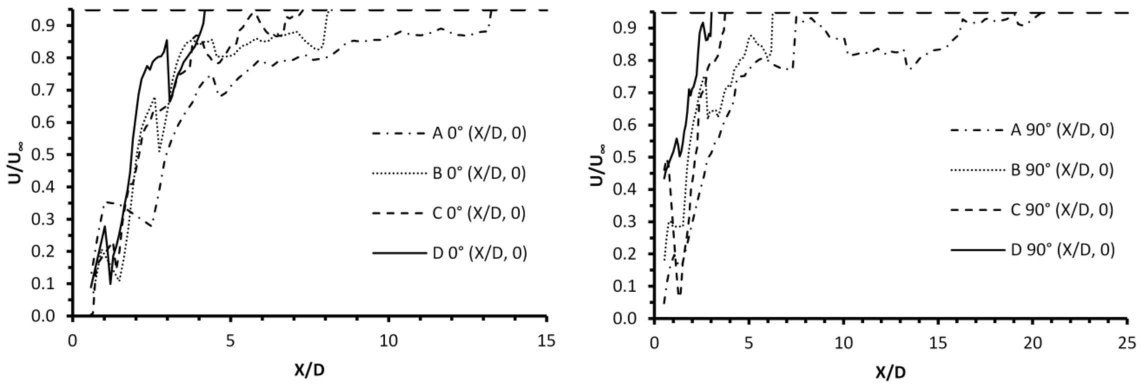

**(a)** **(b)**

**Figure 139 Non-dimensional wake comparison for various scaled turbines at (a) $0^0$ and (b) $90^0$**

In

Figure 140 the white bands where no data is available immediately above and below the turbines are the locations of the rim of the circular cap and therefore no data can be processed due to the interference of the shadow in the captured images. Figure 139 shows the centreline velocities in the wake of each of the turbine configurations for both angles of $0^0$ and $90^0$; these figures illustrate the extent of the wakes of the turbines. A turbine's wake is said to have dissipated once 95% of the freestream velocity has been achieved, which is the upper limit on Figure 139a and Figure 139b. Table 39 includes the distances downstream at which the flow has recovered to freestream velocities (i.e. achieved 95% of the freestream velocity) for each of the turbine configurations. Both Figure 139a and Figure 139b show that the wake deficit is at a maximum immediately behind the turbines and decreases as the distance downstream increases. In Figure 139b it can be seen that A is very close to achieving $U/U_\infty=0.95$ at $X/D\approx7$ however it does result with eventually surpassing $U/U_\infty=0.95$ at $X/D=20.4$.

**Table 39 Wake length at $U/U_\infty=0.95$ for all tests at (X, 0)**

| Test | Turbine diameter, D (m) | Angle ($^0$) | X/D | Test | Turbine diameter, D (m) | Angle ($^0$) | X/D |
|---|---|---|---|---|---|---|---|
| A | 0.06 | 0 | 13.4 | C | 0.12 | 0 | 7.28 |
|  | 0.06 | 90 | 20.4 |  | 0.12 | 90 | 3.78 |
| B | 0.1 | 0 | 8.2 | D | 0.15 | 0 | 4.22 |
|  | 0.1 | 90 | 6.28 |  | 0.15 | 90 | 3.055 |

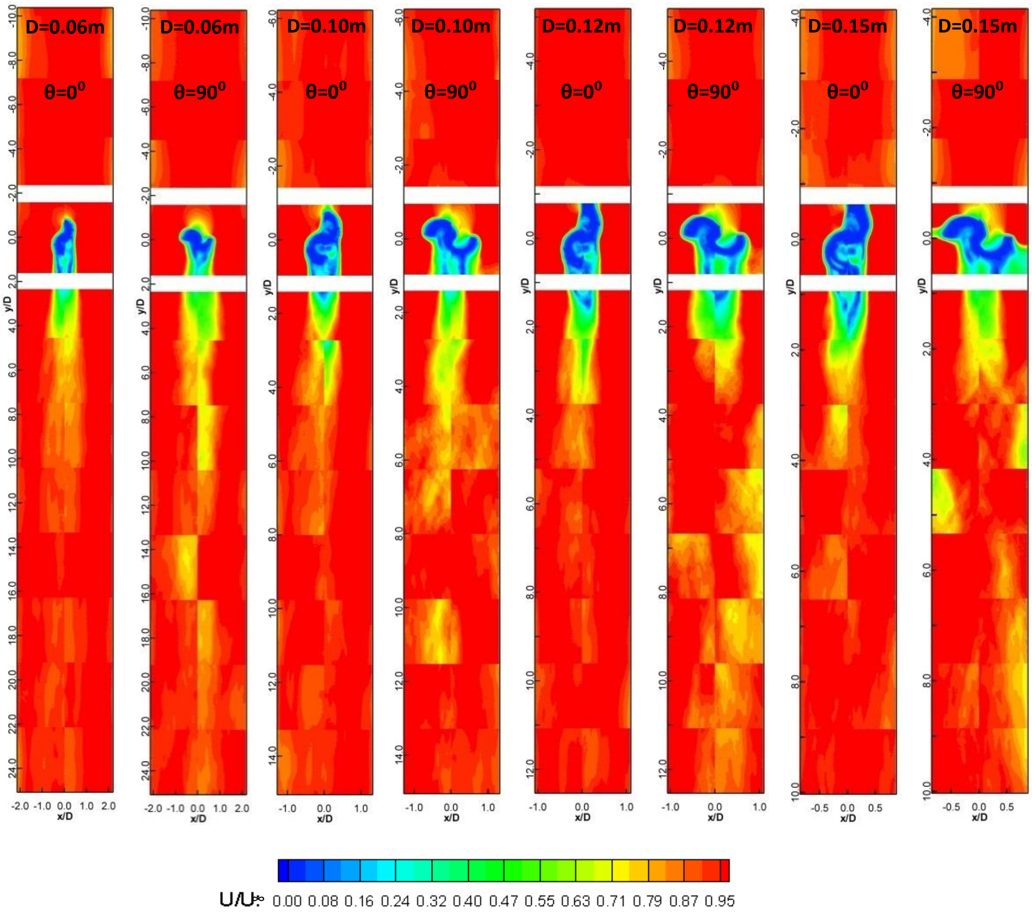

**Figure 140 PIV visualization of the highlighted downstream wake for each of the scaled turbines at $0^0$ and $90^0$**

## 1.6 DISCUSSION & CONCLUSIONS

In this study the PIV technique was adopted in order to characterize the wake properties of four different scaled Savonius turbines at azimuth angles of $0^0$ and $90^0$ for each of the scales in a hydraulic flume that posed the issue of blockage effects. The PIV system was successfully validated against ADV data for a test scenario with a rectangular block in situ, with Figure 136 and Figure 137 illustrating that the PIV is within 10% of the ADV results for both freestream conditions and with the rectangular block in situ.

Understanding the wake properties of a turbine is essential when discussing installing an array of turbines. Choosing the location to place a turbine downstream from another is based upon the wake length of the first turbine, since the energy available is reduced within the wake region the turbine must be placed where the wake is deemed to have dissipated and conditions close to freestream conditions have returned. Freestream conditions in this study were deemed to be when $U/U_{\infty}=0.95$ was reached.

In an unblocked environment (i.e. no side wall effects), the larger the blockage effect, see equation (1), the longer the corresponding wake, however this study has proved that in a blocked environment the opposite occurs: An increase in turbine blockage produces reduced wake lengths as seen in Table 39. Table 39 shows that for $0^{o}$ the wake decreases from X/D = 13.4 for the smallest turbine diameter, D=0.06m to X/D = 4.22 for the largest turbine diameter, D=0.15m. Similarly for $90^{o}$ the wake decreases from X/D = 20.4 for D=0.06m to X/D = 3.055 for D=0.15m.

An explanation for this effect is due to the turbine blockage causing flow acceleration between the turbine and the flume walls. This acceleration aids in hastening the breakdown of the wake through enhanced lateral turbulent mixing, as discussed by Giles et al., (2011) and Myers et al., (2008). The enhanced lateral turbulent mixing is due to the turbulent shear stress on the interface between the accelerated flow either side of the turbine and the flow through the turbine acting in such a way that it decelerates the bypass flow and accelerates the lower speed wake flow (Nishino and Willden, 2012). The effect leads to a reduction in the wake length.

Similar to the work carried out by Chen and Liou, (2011) and Ross and Altman, (2011) this study reiterates the assertion that it is key to understand and account for blockage effects through appropriate corrections when conducting and disseminating the results of flume experiments of marine current turbines. This study also suggests that there is potential to investigating the increased power output (from the accelerated flow compared to freestream conditions) and array density (larger blockage, shorter wake) that could be achieved through locating Savonius turbines within a ducted environment with a large blockage effect.

Future work will be based upon using the above results to validate CFD models.

# Appendix C

---

## Performance Summary of Physical Testing

| Turbine Configuration | $U_\infty$ *m/s* | $C_p$ - | $\lambda$ - | $C_t$ - | P *W* | RPM - | T *Nm* | $\omega$ *rad/s* |
|---|---|---|---|---|---|---|---|---|
| **Cardiff University Flume (CU)** | | | | | | | | |
| **C3** | ***0.76*** | 0.123 | 0.395 | 0.312 | 2.703 | 14.349 | 1.799 | 1.503 |
| | ***0.93*** | 0.123 | 0.347 | 0.355 | 4.947 | 15.405 | 3.067 | 1.613 |
| | ***1.07*** | 0.119 | 0.399 | 0.297 | 7.248 | 20.401 | 3.393 | 2.136 |
| | ***1.22*** | 0.118 | 0.343 | 0.345 | 10.738 | 20.009 | 5.125 | 2.095 |
| **C4** | ***0.76*** | 0.117 | 0.415 | 0.283 | 2.574 | 15.058 | 1.632 | 1.577 |
| | ***0.93*** | 0.120 | 0.406 | 0.295 | 4.803 | 18.023 | 2.545 | 1.887 |
| | ***1.07*** | 0.126 | 0.393 | 0.320 | 7.676 | 20.057 | 3.654 | 2.100 |
| | ***1.22*** | 0.132 | 0.441 | 0.299 | 11.968 | 25.703 | 4.447 | 2.692 |
| **C5** | ***0.76*** | 0.083 | 0.417 | 0.199 | 1.814 | 15.123 | 1.145 | 1.584 |
| | ***0.93*** | 0.089 | 0.393 | 0.226 | 3.566 | 17.442 | 1.952 | 1.827 |
| | ***1.07*** | 0.095 | 0.478 | 0.198 | 5.786 | 24.399 | 2.264 | 2.555 |
| | ***1.22*** | 0.097 | 0.351 | 0.276 | 8.789 | 20.465 | 4.101 | 2.143 |
| **C4O** | ***0.76*** | 0.071 | 0.392 | 0.182 | 1.564 | 14.224 | 1.050 | 1.49 |
| **C3+3** | ***0.76*** | 0.122 | 0.413 | 0.295 | 2.669 | 15.004 | 1.698 | 1.571 |
| | ***0.93*** | 0.118 | 0.421 | 0.280 | 4.722 | 18.674 | 2.415 | 1.956 |
| | ***1.07*** | 0.125 | 0.413 | 0.301 | 7.612 | 21.107 | 3.444 | 2.210 |
| | ***1.22*** | 0.117 | 0.433 | 0.270 | 10.611 | 25.219 | 4.018 | 2.641 |
| **Savonius** | ***0.76*** | 0.225 | 0.999 | 0.225 | 4.928 | 36.233 | 1.299 | 3.794 |
| | ***0.93*** | 0.239 | 0.834 | 0.287 | 9.597 | 37.027 | 2.475 | 3.877 |
| | ***1.07*** | 0.261 | 0.831 | 0.314 | 15.975 | 42.444 | 3.594 | 4.445 |
| | ***1.22*** | 0.266 | 1.051 | 0.253 | 24.138 | 61.217 | 3.765 | 6.411 |
| **Savonius (Closed flaps)** | ***0.76*** | 0.154 | 0.878 | 0.175 | 3.373 | 31.845 | 1.012 | 3.335 |
| | ***0.93*** | 0.167 | 0.884 | 0.189 | 6.706 | 39.257 | 1.631 | 4.111 |
| | ***1.07*** | 0.159 | 1.038 | 0.154 | 9.747 | 53.019 | 1.756 | 5.552 |
| | ***1.22*** | 0.181 | 1.007 | 0.180 | 16.408 | 58.656 | 2.671 | 6.142 |
| **Savonius (Open Flaps)** | ***0.76*** | 0.103 | 0.626 | 0.165 | 2.263 | 22.707 | 0.952 | 2.378 |
| **IFREMER** | | | | | | | | |
| **C4** | ***0.75*** | 0.067 | 0.346 | 0.194 | 1.410 | 12.388 | 1.087 | 1.297 |
| **C4 2 stage 45° offset** | | 0.064 | 0.405 | 0.158 | 2.685 | 14.494 | 1.769 | 1.518 |
| **Savonius** | | 0.098 | 0.692 | 0.142 | 2.065 | 24.766 | 0.796 | 2.594 |
| **Savonius (Closed flaps)** | | 0.057 | 0.783 | 0.073 | 1.200 | 28.034 | 0.409 | 2.936 |
| **Savonius (Open flaps)** | | 0.046 | 0.528 | 0.087 | 0.969 | 18.898 | 0.490 | 1.979 |